

AD-784 327

THEORETICAL STUDIES OF HIGH-POWER
ULTRAVIOLET AND INFRARED MATERIALS

Marshall S. Sparks, et al

Xonics, Incorporated

Prepared for:

Defense Supply Service
Advanced Research Projects Agency

30 June 1974

DISTRIBUTED BY:

NTIS

National Technical Information Service
U. S. DEPARTMENT OF COMMERCE
5285 Port Royal Road, Springfield Va. 22151

Unclassified

Security Classification

AD 784-327

DOCUMENT CONTROL DATA - R & D		
(Security classification of title, body of abstract and indexing annotation must be entered when the overall report is classified)		
1. ORIGINATING ACTIVITY (Corporate author) Xonics, Incorporated 6837 Hayvenhurst Avenue Van Nuys, California 91406		2a. REPORT SECURITY CLASSIFICATION Unclassified
		2b. GROUP N/A
3. REPORT TITLE THEORETICAL STUDIES OF HIGH-POWER ULTRAVIOLET AND INFRARED MATERIALS		
4. DESCRIPTIVE NOTES (Type of report and inclusive dates) Third Technical Report, 7 December 1973 through 30 June 1974		
5. AUTHOR(S) (First name, middle initial, last name) Marshall S. Sparks, Carl J. Duthler		
6. REPORT DATE 30 June 1974	7a. TOTAL NO. OF PAGES 245	7b. NO. OF REFS 112
8a. CONTRACT OR GRANT NO. DAHC15-73-C-0127	9a. ORIGINATOR'S REPORT NUMBER(S)	
b. PROJECT NO.		
c.	9b. OTHER REPORT NO(S) (Any other numbers that may be assigned this report)	
d.	ARPA Order No. 1969, Amendment No. 3	
10. DISTRIBUTION STATEMENT This document may be further distributed by any holder only with specific prior approval of the Defense Supply Service - Washington, D. C.		
11. SUPPLEMENTARY NOTES Sponsored by Advanced Research Projects Agency		12. SPONSORING MILITARY ACTIVITY Defense Supply Service - Washington Room 1D245, The Pentagon Washington, D. C. 20310
13. ABSTRACT A calculation of the intrinsic reflectance R of aluminum in the vuv indicates that the value of R = 0.92 observed under optimum conditions is very close to the calculated intrinsic limit and that the present value of $I_f = 20 \text{ MW/cm}^2$ for melting is within a factor of three of the intrinsic limit. It is unlikely that a vuv metallic reflector better than aluminum will be found. There are very few candidate transparent materials for the vuv, and their absorption coefficients are large (0.1 to 1 cm^{-1}), surely due to imperfections. Nevertheless, multilayer-dielectric reflectors and total-internal-reflection devices are more promising than metallic reflectors (without multilayer coatings). Total-internal-reflection devices are analyzed in some detail. Calculations indicate that for a single 10 nsec-duration xenon-laser pulse, the failure intensity I_f is: $\sim 20 \text{ MW/cm}^2$ for melting of a 100 A-thick film of aluminum on magnesium fluoride; $\sim 70 \text{ MW/cm}^2$ for optical distortion by two-photon heating in windows and total-internal-reflection devices; $\sim 200 \text{ MW/cm}^2$ for surface damage; $\sim 1 \text{ GW/cm}^2$ for thermal fracture by two-photon heating; $\sim 1 \text{ GW/cm}^2$ for fracture from enhanced stimulated Raman scattering in Raman active materials; $\sim 500 \text{ MW/cm}^2$ for optical distortion by one-photon heating with absorption coefficient $\beta = 0.1 \text{ cm}^{-1}$; and $\sim 100 \text{ GW/cm}^2$ for thermal fracture by one-photon heating with $\beta = 0.1 \text{ cm}^{-1}$. The failure intensities for thermal fracture and optical distortion are in general orders of magnitude lower in cw and repeated-pulse operation than those given (for a single 10 nsec pulse). A preliminary estimate of two-photon absorption in LiF gives $\beta = 1 \text{ cm}^{-1}$ for intensity $I \cong 2 \text{ GW/cm}^2$ at the photon energy $\hbar\omega = 7.2 \text{ eV}$ of the xenon laser. A study of the absorption and scattering by rough metallic surfaces, which includes surface plasmon coupling and effects of non-normal incidence, indicates which of the normal-incidence results of Ritchie and coworkers is correct and identifies the error in the other. The Raman-scattering process		

DD FORM 1 NOV 65 1473

Unclassified

Security Classification

Reproduced by
NATIONAL TECHNICAL
INFORMATION SERVICE
U S Department of Commerce
Springfield VA 22151

14 KEY WORDS	LINK A		LINK B		LINK C	
	ROLE	WT	ROLE	WT	ROLE	WT
ultraviolet absorption ultraviolet reflectors LiF, MgF ₂ , CaF ₂ , Al ₂ O ₃ laser damage alkali halides extrinsic ultraviolet absorption two-photon absorption stimulated-Raman-scattering instability optical materials theoretical study ultraviolet windows Lax-Burstein infrared absorption aluminum reflectance <u>ABSTRACT (Continued)</u> has a sharp-threshold parametric instability that affords explanations of long-standing anomalies in stimulated scattering and possibly self-focusing experiments. The low theoretical threshold intensity ($\sim 1 \text{ GW/cm}^2$ typically) for the instability indicates that this instability should be important in laser damage. Analysis of a one-dimensional shell model suggests that the Lax-Burstein contribution to infrared absorption is greater than the anharmonic-potential contribution at $10.6 \mu\text{m}$ in candidate window materials.						

THEORETICAL STUDIES OF HIGH-POWER
ULTRAVIOLET AND INFRARED MATERIALS

M. Sparks, Principal Investigator, 213 / 787-7380

C. J. Duthler, Principal Scientist, 213 / 787-7380

Xonics, Incorporated
Van Nuys, California 91406

Third Technical Report
30 June 1974

Contract No. DAHC15-73-C-0127
Effective Date of Contract: 7 December 1972
Contract Expiration Date: 6 December 1974

Prepared for
Defense Supply Service - Washington, D. C.

Sponsored by Advanced Research Projects Agency
ARPA Order No. 1969, Amendment No. 3; Program Code No. 4D10

This research was supported by the Advanced Research Projects Agency of the Department of Defense and was monitored by the Defense Supply Service-Washington, D. C. under Contract No. DAHC15-73-C-0127. The views and conclusions contained in this document are those of the authors and should not be interpreted as necessarily representing the official policies, either expressed or implied, of the Advanced Research Projects Agency or the U. S. Government.

TABLE OF CONTENTS

	<u>Page</u>
Preface	vii
A. Introduction and Summary	1
B. Intensity Limits of High-Intensity Vacuum Ultraviolet Materials	9
I. Introduction	10
II. Mirror Damage	16
III. Thermally Induced Optical Distortion and Fracture in Transparent Materials	20
IV. Two-Photon Absorption	24
V. Enhanced Stimulated Raman Scattering	25
VI. Other Failure Modes	27
VII. Precautions	28
C. Multiphoton Absorption	31
I. Introduction	32
II. First-Order Approximation to β	34
III. Three-Photon and General n-Photon Absorption	36
D. Calculated Reflectance of Aluminum in the Vacuum Ultraviolet	39
I. Introduction and Summary	40
II. Calculation of Absorptance	43
E. Total-Internal-Reflection Devices	50
I. Introduction	50
II. Total-Internal-Reflection Elements	51
III. Output Coupling	60
IV. Material Failure	63

TABLE OF CONTENTS (Cont'd)

	<u>Page</u>
F. The Scattering and Absorption of Electromagnetic Radiation by a Semi-Infinite Crystal in the Presence of Surface Roughness	65
I. Introduction	67
II. Scattering of Electromagnetic Radiation by a Rough Surface	73
III. Absorption of Electromagnetic Radiation by a Rough Surface	92
IV. The Contribution to the Roughness Induced Absorption from Coupling to Surface Polaritons	105
V. Numerical Studies of Roughness Induced Scattering and Absorption	117
Appendix	124
G. Infrared Absorption by the Higher-Order-Dipole-Moment Mechanism	155
I. Introduction	156
II. Model	160
III. n-Phonon Summation Process	165
IV. Frequency Dependence of Absorption	171
V. Discussion of Results	174
H. Stimulated Raman and Brillouin Scattering: Parametric Instability Explanation of Anomalies	189
I. Extrinsic Absorption in 10.6 μm Laser Window Materials	199
I. Introduction	200
II. Conical Surface-Damage Pits	201
III. Molecular-Ion Impurities	210
J. Erratum: High-power 2- to 6- μm Window-Material Figures of Merit with Edge Cooling and Surface Absorption Included	223
K. List of Recent Publications	235

LIST OF ILLUSTRATIONS

<u>Section</u>	<u>Figure</u>	<u>Title</u>	<u>Page</u>
E	1	Crossed roof prism optical cavity	52
	2	Optical cavity constructed from a corner cube and flat	55
	3	TIR elements with three internal reflections	56
	4	TIR elements with three internal reflections, A. Similar element with greater spatial beam separation, B	57
	5	TIR elements with two and four internal reflections . .	58
	6	Frustrated total internal reflection output coupling . .	61
	7	Output coupling by transmission	62
F	1	The scattering geometry employed	147
	2	The variation of the scattering functions $R(s \rightarrow s)$ and $R(s \rightarrow p)$ with angle of incidence for a 7 eV photon incident on aluminum	148
	3	The variation of the scattering functions $R(p \rightarrow s)$ and $R(p \rightarrow p)$ with angle of incidence for a 7 eV photon incident on aluminum	149
	4	The variation of the scattering functions $R(s)$ and $R(p)$ with angle of incidence for a 7 eV photon incident on aluminum	150
	5	The variation of $R(s)$ with frequency for several angles of incidence at 7 eV for aluminum	151
	6	The functions A_{sp} and A_{pp} as functions of the angle of incidence for a photon of $\hbar\omega = 7$ eV incident on aluminum	152
	7	The functions A_{sp} and A_{pp} as functions of the angle of incidence for a photon of energy $\hbar\omega = 9$ eV incident on aluminum	153
	8	The variations with frequency at normal incidence of A_{sp} , A_{ss} and the analytic approximation to the roughness induced absorption cross section.	154

LIST OF ILLUSTRATIONS (Cont'd)

<u>Section</u>	<u>Figure</u>	<u>Title</u>	<u>Page</u>
G	1	Two-phonon summation processes: (a) Lax-Burstein nonlinear-dipole-moment mechanism, and (b) anharmonic-potential mechanism	180
	2	Simple model for Lax-Burstein effect	181
	3	Schematic illustration of diamond showing that symmetry is necessary to prevent diamond from being a polar crystal	182
	4	Schematic illustration of the decrease in dipole moment p as x increases according to Mills and Maradudin and the contrasting increase in p from the present model	183
	5	The four diagrams contributing to the Hamiltonian for the anharmonic-potential process	184
	6	Effect on absorption of including both the Lax-Burstein and anharmonic mechanisms	185
	7	Large peak in $\beta_{anh}(\omega)$, at $\omega/\omega_f \cong 1.5$, that would result if ω_{eq} were in the two-phonon region	186
	8	Construction showing that if the first observed minimum of $\beta(\omega)$ were at ω_{eq} , the resulting maximum (at $\omega/\omega_f \cong 1.6$) would resemble a two-phonon absorption peak	187
	9	Experimental absorption curves for comparison with the heavy curve of Fig. G8 resulting from the LB-anisotropy crossover at $\omega_{eq} = 1.3 \omega_f$	188
H	1	Schematic illustration of the Stokes intensity I_S for three limiting values of incident laser intensity I_{Li}	194
	2	Comparison of experimental points from Ref. 7 with theoretical curve.	195

LIST OF ILLUSTRATIONS (Cont'd)

<u>Section</u>	<u>Figure</u>	<u>Title</u>	<u>Page</u>
I	1	Sketch of inclusion of radius a at a distance d below the plane surface	203
	2	Tensile stresses and cone half angle as a function of inclusion depth	205
	3	Cone-producing fracture for crack nucleation at inclusion surface (A) and at plane surface (B)	207
	4	Semi-log plot of absorption in alkali halides as a function of frequency	211
	5	Orientation of NO_2^- impurity in KCl at low temperature	213
	6	Calculated absorption coefficient of a KCl crystal containing 0.3 ppm NO_2^-	217
	7	Calculated absorption coefficient of a KCl crystal containing 0.03 ppm HCO_3^-	218
	8	Calculated absorption coefficient of a KCl crystal containing 0.3 ppm $\text{SO}_4^{2-}:\text{M}_g^{2+}$	219
	9	Calculated absorption coefficient of a KCl crystal containing a few impurities	220
J	1	Corrected diameter dependence of the pulse and cw powers transmitted by BaF_2 at $3.8\text{ }\mu\text{m}$	226

PREFACE

This Third Technical Report describes the work performed on Contract DAHC15-73-C-0127 on Theoretical Studies of High-Power Ultraviolet and Infrared Window Materials during the period from December 7, 1973 through June 30, 1974. The work on the present contract is a continuation of that of the previous Contract DAHC15-72-C-0129.

The following investigators contributed to this report:

Mr. H. C. Chow, research associate

Dr. C. J. Duthler, principal research scientist

Dr. A. M. Karo, consultant, Lawrence Livermore Laboratory,
Livermore, California

Dr. A. A. Maradudin, consultant, University of California, Irvine, California

Dr. D. L. Mills, consultant, University of California, Irvine, California

Dr. L. J. Sham, consultant, University of California, San Diego, California

Dr. M. Sparks, principal investigator

Previously reported results are not repeated in the present report, with the exception of Section J, where the previous results were included for the convenience of the reader in considering the changes reported in that section. The emphasis of the program during the report period has been on ultraviolet materials, although some time was spent on finishing the infrared-materials projects.

A. INTRODUCTION AND SUMMARY

The emphasis of the program has shifted from infrared materials to ultraviolet materials during the current reporting period. The motivation for the study is the realization that the operation and application of recently developed high-intensity vacuum ultraviolet sources are expected to be severely limited by the lack of satisfactory optical components.

It appears that we are beginning a new era of materials development in the vacuum ultraviolet. The output power of the first xenon vuv lasers was limited by the materials problem of the melting of the partially transparent aluminum film used as the cavity mirror. Since orders of magnitude greater power would be feasible if suitable mirrors were available, there is great interest in obtaining improved reflectors. Transparent materials for high-power use as windows, lenses, and possibly other optical components also are of interest.

In going from the visible to the vacuum ultraviolet to the X-ray region, the problem of obtaining mirrors with high reflectance and low absorptance and windows with low absorptance becomes more difficult. In the visible region there are rather wide choices of mirror and window materials. In the vacuum ultraviolet (vuv) region there are only a few acceptable materials, as discussed below, and in the X-ray region, there are no materials with high normal-incidence-reflectivity or low loss. Since the greatest current need and greatest promise of obtaining significant improvements lie in the vacuum ultraviolet region, the emphasis at the beginning of the program is focused there.

Sec. A

The problems of obtaining high-power materials in the vuv are more difficult and quite different from those in the infrared. It appears that transparent materials can withstand greater intensities than metallic reflectors can, in contrast to the IR case. Thus, dielectric reflectors and total-internal-reflection devices are expected to be important. The choice of vuv materials is greatly restricted. Only aluminum is available as a metallic reflector, and its absorptance is orders of magnitude greater than the values for good reflectors in the infrared region. There are only a small number of transparent materials with bandgap E_g greater than, say, 9 eV, and most of these are unsatisfactory for use as practical optical components. The optical tolerances are much more severe in the vuv, and the paucity of materials makes it difficult to obtain satisfactory antireflection and protection coatings.

In order to obtain an overview of the materials problems of high-intensity reflectors, windows, and other optical components, the major anticipated problems were considered briefly, then a number of the most pressing problems were considered in some detail. As a result, we have obtained conclusions of which effects are most likely to limit the performance of high-intensity vuv materials, of which problems to emphasize in the present program, and of which areas of experimental and theoretical investigations would be the most useful in the near future.

First consider metallic reflectors. There are two contributions to the absorptivity of a metal: The Drude absorptivity from the free electron character of the metal and the interband absorptivity. In order for the Drude reflectivity to be great, the plasma frequency of the metal must be large compared to the optical frequency. (Metals are transparent for optical frequencies greater than the plasma frequency.) The plasma wavelengths and energies ($\hbar\omega_p$) of a number of metals are as follows:

Sec. A

<u>Material</u>	<u>λ_p (nm)</u>	<u>$\hbar\omega_p$ (eV)</u>
Al	81.4	15.2
Mg	117	10.6
Tl	122	10.1
Zn	127	9.7
Cd	146	8.5
Li	155	8.0
Na	210	5.9
Ag	254	4.9
Au	306	4.0
K	315	3.9
Rb	340	3.6
Cs	362	3.4

Of the above materials, aluminum has the highest plasma frequency. In fact, aluminum has the largest metallic reflectivity in the vuv. However for use at the xenon laser frequency, 7.2 eV, the condition that $\omega \ll \omega_p$ is only approximately satisfied. It is estimated that the Drude contribution to the absorptivity of aluminum at 7.2 eV is 0.02. Other materials listed above with plasma frequencies greater than 7.2 eV have much lower reflectance than aluminum because of both a larger Drude absorption (from lower plasma frequency and lower conductivity) and a larger interband absorption. Silver, which is a commonly used metallic reflector in the visible, has a plasma frequency of 4.9 eV; consequently it would be transparent in the vuv except for interband absorption.

With extreme care, values of reflectance as great as $R = 92$ percent have been obtained for aluminum in the range from 6-10 eV. Without special precautions,

Sec. A

reflectivities of only $R = 40$ percent and even lower are obtained. To obtain the highest reflectivity it is necessary to deposit the aluminum on a supersmooth substrate (roughness $\sim 10 \text{ \AA}$) under ultrahigh vacuum conditions ($P \sim 10^{-9}$ Torr). Rough substrates result in a broad absorption band extending from $\sim 130 \text{ nm}$ to $\sim 180 \text{ nm}$, which is attributed to absorption by surface plasmons. To maintain the high reflectivity, the aluminum must be overcoated with MgF_2 or some other transparent material to prevent oxidation. Absorption by oxidized films, which is not completely understood, will be considered in the next report period.

In this report we have considered two limiting aspects of the reflectivity of aluminum. The absorption and scattering by rough surfaces is considered in Section F. Section D presents a calculation of the intrinsic reflectance of aluminum. It is found that the reflectance of $R = 92$ percent observed in the best samples is very close to the calculated intrinsic limit. The general problem of damage to optical components is considered in Section B.

In view of the high intrinsic absorptivity and the extreme difficulty in preparing the best aluminum reflectors, it is clear that dielectric reflectors, either in the form of thin-film stacks or total-internal-reflection devices, are needed to obtain a reflector with substantially higher damage resistance. Mechanisms limiting the transmission of transparent materials also are considered in this report.

Clearly in order for a dielectric material to be transparent, it must have a large bandgap $E_g > \hbar\omega$, where ω is the laser frequency, so that direct one-photon absorption across the bandgap does not occur. In fact, it is desirable that $E_g > 2\hbar\omega$ in order to avoid two-photon absorption. Bandgaps of several materials are listed below:

Sec. A

LiF	~13	SrF ₂	>9	NaBr	7.7
MgF ₂	~11	BaF ₂	>9	SiO ₂	~7.7
KF	10.9	NaCl	8.6	MgO	7.3
NaF	>10.5	KCl	8.5	KI	>6.2
RbF	10.4	LiBr	~8.5	LiI	>5.9
CsF	10	Al ₂ O ₃	8.3	NaI	>5.8
LiCl	~10	RbCl	8.2	Diamond	5.33
CaF ₂	~10	KBr	7.8		

The onset of one-photon absorption in these materials can occur at 1-2 eV below E_g due to exciton absorption. Materials that are transparent in the vuv are composed of elements from the edges of the periodic table (generally alkali halides and alkaline-earth fluorides). Of these, light elements tend to have larger bandgaps than heavy elements. Lithium fluoride has the largest known bandgap, $E_g \cong 13$ eV. Unfortunately this is less than two times the xenon-laser frequency, so that there is no material which is not limited by two-photon absorption. All alkali fluorides and alkaline-earth fluorides, along with most alkali chlorides, have sufficiently large bandgaps that one-photon absorption does not occur at the xenon-laser frequency.

In contrast to infrared materials, the intrinsic absorption coefficient of vuv materials decreases much more rapidly in the tail of the fundamental absorption. In the Urbach-tail region, the absorption coefficient β decreases exponentially with decreasing frequency, having a typical value of 7 to 8 orders-of-magnitude decrease per electronvolt. Hence in the vuv, it is possible to use materials to within roughly 1 eV of the first exciton peak. This makes possible the use of several

materials with desirable physical and chemical properties. For example, with respect to mechanical strength, resistance to water vapor, and resistance to color center formation, the alkaline-earth fluorides are superior to the alkali fluorides. However, a careful comparison of two-photon absorption must be made, and the possibility of damage in alkaline-earth fluorides from enhanced stimulated Raman scattering must be investigated.

Presently the best available alkali fluorides and alkaline-earth fluorides have absorption coefficients at 7.2 eV ranging from 10^{-1} cm^{-1} to 1 cm^{-1} due to impurity absorption. There is little good data available on the intrinsic absorption of sapphire. In view of its very desirable physical and chemical properties, the possible use of sapphire with xenon lasers should be investigated.

In this report, the general mechanisms and thresholds for damage in transparent materials are considered in Section B. It is found that with a single 10 nsec duration xenon-laser pulse, the failure intensity I_f is $\sim 20 \text{ MW/cm}^2$ for melting of a 100 Å-thick film of aluminum on magnesium fluoride; $\sim 70 \text{ MW/cm}^2$ for optical distortion by two-photon heating in windows and total-internal-reflection devices; $\sim 200 \text{ MW/cm}^2$ for surface damage; $\sim 1 \text{ GW/cm}^2$ for thermal fracture by two-photon heating; $\sim 1 \text{ GW/cm}^2$ for fracture from enhanced stimulated Raman scattering in Raman active materials; $\sim 500 \text{ MW/cm}^2$ for optical distortion by one-photon heating with absorption coefficient $\beta = 0.1 \text{ cm}^{-1}$; and $\sim 100 \text{ GW/cm}^2$ for thermal fracture by one-photon heating with $\beta = 0.1 \text{ cm}^{-1}$. The failure intensities for thermal fracture and optical distortion are in general orders of magnitude lower in cw and repeated-pulse operation than those given (for a single 10 nsec pulse). Multilayer dielectric reflectors have greater theoretical values of I_f , but technical problems also should be considered.

Sec. A

A report of work in progress on the theory of two-photon absorption is presented in Section C. A first estimate is that in LiF the absorption coefficient has the value $\beta = 1 \text{ cm}^{-1}$ for intensity $I \approx 2 \text{ GW/cm}^2$ at the photon energy $\hbar\omega = 7.2 \text{ eV}$ of the xenon laser. With this value of β , it is shown in Section B that the optical distortion caused by two-photon heating of transparent optical components has the lowest failure threshold of all processes considered. In view of the importance of the two-photon absorption, an improved calculation was undertaken and is currently in progress. Should other lasers become available with frequencies such that $2\hbar\omega$ is less than the electronic bandgap, thereby eliminating the two-photon absorption, then multiphoton absorption should be negligible since it is shown that three- and higher-order processes are negligible.

The theory of stimulated Raman scattering is considered in Section H. The Raman and Brillouin processes have important sharp-threshold parametric instabilities that afford explanations of long-standing anomalies in stimulated scattering and self-focusing experiments. Below the threshold intensity I_c , the gain is nonexponential and greater than that of previous theories of stimulated scattering, and at the threshold the Stokes intensity increases nearly discontinuously. Typically, $I_c \sim 10^9 \text{ W/cm}^2$ for a number of gases, liquids, and solids. The theoretical results agree well with previous experimental results. The extension of these results to the vuv is considered in Section B, where it is shown that at intensities of the order of I_c this enhanced stimulated Raman scattering can cause material failure.

In Section E several total-internal-reflection devices and optical cavities are considered. Laser cavities made from total-internal-reflection elements have the advantages of alignment stability and possible variable output coupling using frustrated total internal reflection.

Sec. A

Multilayer dielectric reflectors, including thin-film stacks of dielectrics, multilayer overcoating on metallic reflectors, and stacks including metallic films will be considered in the following report. Grazing-incidence reflectors have not been considered because the technical problems associated with the large number of reflections needed to turn a beam through a large angle make this reflector less promising than the others considered.

B. INTENSITY LIMITS OF HIGH-INTENSITY VACUUM ULTRAVIOLET MATERIALS*

M. Sparks and C. J. Duthler

Xonics, Incorporated, Van Nuys, California 91406

The output intensity I of current xenon lasers is limited by melting of the thin aluminum-film cavity mirrors. Calculations explain the experimental value of $I \cong 20 \text{ MW/cm}^2$ for a 10 nsec pulse and show that this value is only a factor of ~ 3 below the intrinsic limit. Multilayer dielectric reflectors and total-internal-reflection devices may withstand intensities that are ~ 10 times greater than 20 MW/cm^2 according to the calculations (which are sufficiently accurate only to serve as estimates until measurements are available). Calculated intensities I_f at which transparent materials fail in a single 10 nsec pulse are: $\sim 70 \text{ MW/cm}^2$ for optical distortion by two-photon heating in windows and total-internal-reflection devices; $\sim 200 \text{ MW/cm}^2$ for surface damage; $\sim 1 \text{ GW/cm}^2$ for thermal fracture by two-photon heating; $\sim 1 \text{ GW/cm}^2$ for fracture from enhanced stimulated Raman scattering in Raman active materials; $\sim 500 \text{ MW/cm}^2$ for optical distortion by one-photon heating with absorption coefficient $\beta = 0.1 \text{ cm}^{-1}$; and $\sim 100 \text{ GW/cm}^2$ for thermal fracture by one-photon heating with $\beta = 0.1 \text{ cm}^{-1}$. The failure intensities for thermal fracture and optical distortion are in general orders of magnitude lower in cw and repeated-pulse operation than those given (for a single 10 nsec pulse). Multilayer dielectric reflectors have greater theoretical values of I_f , but technical problems also should be considered.

I. INTRODUCTION

Recently developed high-intensity sources of vacuum ultraviolet (vuv) radiation¹⁻⁵ will undoubtedly create interest in materials for high-intensity vuv use. The output power of the first xenon vuv lasers was limited by the materials problem of the melting of the partially transparent aluminum film used as the cavity mirror. Since orders-of-magnitude greater power would be feasible if suitable mirrors were available, there is great interest in obtaining improved reflectors. Transparent materials for high-power use as windows, lenses, reflecting devices, and possibly other optical components also are of even greater interest.

In the present paper, a number of mechanisms by which reflectors and transparent optical components can fail in high-intensity systems are examined theoretically. The purposes of the analyses are to obtain estimates of the maximum intensities at which such systems can operate, to delineate the most important failure mechanisms, to determine areas in which research is needed, and to otherwise determine how materials and the systems operation could be improved. The mechanisms considered include: melting of the aluminum film on the laser-cavity mirrors; thermally induced optical distortion resulting from the absorption in the aluminum; fracture and thermally induced optical distortion from two-photon absorption and from extrinsic linear (one photon) absorption in transparent materials; fracture or melting from enhanced stimulated Raman scattering; and surface-damage mechanisms. The emphasis is on the xenon-laser wavelength 174 nm (7.2 eV), but the analyses are valid for the region of interest from ~ 100 to ~ 200 nm.

Table BI contains a list of the intensities at which system failure occurs for these various failure mechanisms for a single 10 nsec pulse with $h\nu = 7.2$ eV. Other conditions and assumptions incorporated into the calculations are discussed in Sec. VII, where potential difficulties in misusing the values are emphasized. The limiting intensity $I_f = 20 \text{ MW/cm}^2$ for the laser mirrors is set by the melting of the aluminum film, as already mentioned. See Sec. II. It is shown that it is highly unlikely that it would be possible to obtain an order-of-magnitude improvement in the metallic-film cavity mirrors, and obtaining an increase even by a factor of three would be extremely difficult.

This small value of intensity $I_f \approx 20 \text{ MW/cm}^2$ at which the metallic reflectors fail motivated an investigation of total-internal-reflection devices (Sec. E) and dielectric stacks (following report). However, the problems of transparent materials for high-power vuv use also are severe. There are only a handful of materials with values of the electronic bandgap E_g sufficiently great for use at 7.2 eV. For example, LiF, MgF_2 , CaF_2 , BaF_2 , BeO, NaF, KF, RbF, and CsF have $E_g > 9.2$ eV. The last four of these materials are not expected to be useful as practical high-power vuv windows. The values of E_g for SiO_2 and diamond are too small for use at 7.2 eV. The absorption edge of sapphire (at ~ 8.5 eV) was originally considered to be too close to 7.2 eV for use in the xenon-laser systems. This may well be true, but the superior physical properties of sapphire and the fact that intrinsic "Urbach-tails" are so steep (typically $\sim 10^8 \text{ cm}^{-1}/\text{eV}$ reduction in the optical absorption coefficient β) suggests that this conclusion be reexamined. The results will be given in the following technical report. It is not known if the problems of vuv generation of color centers and the resulting increased absorption and of surface contamination in LiF can be overcome.

Sec. B

Table BI. Values of parameters used in calculating the values of intensity I_f in Table BII. The calculated values of ΔT_f and ΔT_0 also are included.

Material	C J/cm ³ K	K W/cm K	α 10 ⁻⁵ K ⁻¹	n	σ k psi	E 10 ⁷ psi	$\partial_n/\partial T$ 10 ⁻⁵ K ⁻¹	$\partial_n T$ 10 ⁻⁵ K ⁻¹	ΔT_f K	ΔT_0 K
LiF	4.12	0.11	3.23	1.44	1.6	1.5	-1.1	0.8	7	0.14
MgF ₂	3.14	~0.2 [*]	1.37	1.46	7.6	2.45	+0.2 [†]	1.0	45	0.11

^{*} Values between 0.1 and 0.3 appear in the literature

[†] Average of ordinary and extraordinary values at 0.40 μ m

The mechanism having the lowest failure intensity $I_f \cong 70 \text{ MW/cm}^2$ for transparent materials is thermally induced optical distortion with the temperature rise caused by two-photon absorption. Thermally induced optical distortion⁶ is a result of the uneven heating of the material by the vuv radiation. Differences in temperature across the material cause changes in the index of refraction and in the sample thickness which distort the optical beam. See Sec. III. The above value of $I_f = 70 \text{ MW/cm}^2$ suggests that a factor of 4 increase in I_f could be obtained by using a total-internal-reflection device in place of the metallic mirror. However, it should be emphasized that the uncertainty in the calculated value of $I_f = 70 \text{ MW/cm}^2$ is great, say a factor of 10-100, which puts the difference in I_f between a factor of ~ 10 lost to a factor of $\sim 10^3$ gained. This failure mechanism is reversible; that is, the optical component is not destroyed, and the failure is self healing as the temperature returns to a constant value. As discussed in Sec. III, the threshold for thermally induced optical distortion in dielectric reflectors is much greater than in windows and total-internal-reflection devices.

The failure mechanism having the next highest value of I_f is laser-induced surface damage,⁷ which is irreversible and occurs at $I_f \cong 200 \text{ MW/cm}^2$. Thus, if the value of I_f for the two-photon absorption were in error by a factor of three on the low side, or if the system could tolerate the optical distortion, the system performance would then be limited to $I_f = 200 \text{ MW/cm}^2$ by the surface-damage mechanism. Since this latter limit is extrinsic, that is, set by imperfections such as inclusions, it is possible in principle to increase this threshold value by improving the materials. The difficulty of the technical problems of such improvement is underscored by the fact that a single imperfection could cause failure.

Sec. B

The next two (irreversible) damage thresholds, both having $I_f \cong 1 \text{ GW/cm}^2$, are stimulated Raman scattering (Sec. V) and fracture resulting from two-photon heating. Since MgF_2 and CaF_2 are Raman active while LiF is not, LiF will have a higher threshold intensity in the cases where I_f is limited by the enhanced stimulated Raman process.

Next consider the usual linear (one-photon) extrinsic absorption, which is quite large. Current measured values are of the order of $\beta \cong 0.1\text{--}1 \text{ cm}^{-1}$, as discussed in Sec. I. In order to keep $I_f \cong 70 \text{ MW/cm}^2$, which is the limit set by optical distortion from two-photon heating, the value of β for linear absorption should be $\lesssim 1 \text{ cm}^{-1}$, as seen in Table BI. This large value of $\beta \cong 1 \text{ cm}^{-1}$ (compared with $\sim 10^{-4} \text{ cm}^{-1}$ for good IR materials), indicates that even though the current measured values of β are very large, improving materials to reduce the values of β may not result in improved systems performance. Reducing the one-photon absorption to values below the two-photon absorption would not result in an increase in the values of I_f .

In repeated-pulse systems, heating becomes relatively more important, and such small values of β would be required to keep $I_f \cong 70 \text{ MW/cm}^2$. For example, for 100 pp sec for 5 sec, $\beta \cong 10^{-4} \text{ cm}^{-1}$ gives $I_f \cong 80 \text{ W/cm}^2$. For continuous operation of repeated-pulse systems, the methods of cooling the material become important in determining the values of I_f , and the analyses of cw IR systems⁶ should be useful. The two-photon heating could be reduced in principle by using a higher repetition rate of less intense pulses.

From these results, the following conclusions can be drawn: Measurements and improved calculations of the values of β for two-photon absorption

Sec. B

are important since the two-photon absorption is the most severe system limitation according to the preliminary estimates. The importance of these investigations is emphasized by the great uncertainty in the estimated value of β for two-photon absorption. Dielectric-stack and total-internal-reflection devices should withstand greater intensities than metallic reflectors without failing irreversibly and probably without failing reversibly, and multilayer-dielectric reflectors should withstand even greater intensities. Programs to determine the sources of the large extrinsic linear absorption coefficients and to improve the materials to reduce the values of β would be useful in general and especially for repeated-pulse systems.

II. MIRROR DAMAGE

The cavity mirrors in current xenon lasers are thin aluminum films on magnesium fluoride substrates.¹⁻⁴ The thickness ℓ of the aluminum is adjusted to a value, of the order of 100 Å, to give approximately five percent transmittance. The laser power currently is severely restricted by the mirrors, the aluminum coating being melted off the substrate.

The experimental value of the energy in a 10 nsec pulse at which the mirrors are destroyed was estimated to be 20 mJ (incident on the mirror, or ~ 1 mJ outside the cavity).⁸ The damaged area is of the order of 0.25 cm^2 , giving $I_f \cong 8 \text{ MW/cm}^2$. The following theoretical estimate of I_f for melting of the aluminum film agrees with the experimental value to within the accuracies of the absorptance A , thermal conductivity K (values from 0.1 to 0.3 W/cmK for MgF_2 in the literature), pulse length and shape, and the experimental error.

Consider a 10 nsec pulse incident on $\sim 100 \text{ Å}$ of aluminum (melting temperature 660°C, or $T_m \cong 640 \text{ K}$ above ambient, heat of fusion = 1.07 kJ/cm^3 , $A = 0.2$) deposited on MgF_2 (heat capacity $C = 3.14 \text{ J/cm}^3 \text{ K}$, $K \cong 0.2 \text{ W/cmK}$, linear thermal expansion coefficient $\alpha = 13.7 \times 10^{-6} \text{ K}^{-1}$). During the pulse duration t_{pulse} , the heat diffuses into the MgF_2 a distance d , which is related to t_{pulse} by the standard result $t_{\text{pulse}} = 4Cd^2/\pi K$; thus

$$d \cong (\pi K t_{\text{pulse}} / 4C)^{1/2} = 2 \times 10^{-5} \text{ cm} \quad (2.1)$$

for $t_{\text{pulse}} = 10^{-8} \text{ sec}$. The numerical factor $4/\pi$ was chosen to give the exact result⁹ for the temperature rise at the surface of the sample. The 100 Å thickness

Sec. B

of the aluminum is negligible with respect to d . The temperature rise is obtained as follows: Consider the volume $A_{su} d$, where A_{su} is the surface area illuminated. The energy put into this volume by the laser beam is AFA_{su} , where $F = It_{pulse}$ is the fluence, or the incident energy density. The resulting temperature rise ΔT is obtained by dividing this energy by the heat capacity of the volume, which is $CA_{su} d$. Thus,

$$AF/Cd = \Delta T \quad (2.2)$$

Setting ΔT equal to the melting temperature T_m , measured with respect to the sample temperature before irradiation by the laser, and substituting (2.1) into (2.2) and solving for $I_f = F/t_{pulse}$ gives

$$I_f = (T_m/2A)(\pi CK/t_{pulse})^{1/2} = 20 \text{ MW/cm}^2 \quad (2.3)$$

The corresponding fluence has the value $F_f = 0.2 \text{ J/cm}^2$. It is perhaps worth pointing out that both $I_f (\sim t_{pulse}^{-1/2})$ and $F \sim t_{pulse}^{1/2}$ depend on t_{pulse} ; i. e., the failure depends on both the intensity and the pulse length. By contrast, the total heat absorbed is proportional to F (independent of t_{pulse} for a given value of F), and the two-photon absorption coefficient is proportional to I (independent of F for a given value of I).

The heat of fusion of the thin aluminum film is negligible since 10^{-3} J/cm^2 in 100 Å supplies the heat of fusion of $1.07 \times 10^3 \text{ J/cm}^3$. This value of $F = 10^{-3} \text{ J/cm}^2$ is much less than $F_f = 0.2 \text{ J/cm}^2$. Since the MgF_2 is in compression (with stress $\sigma \cong -1.4 \alpha E T_m \cong -3 \times 10^5 \text{ psi}$, where $E = 2.4 \times 10^7 \text{ psi}$ is the Young's modulus), the MgF_2 substrate should not fracture at the melting point of the aluminum for a

Sec. B

uniformly illuminated surface. A radial temperature distribution can give rise to azimuthal tensile stresses, but these are expected to be small with respect to those generated by the axial temperature distribution for $d = 0.2 \mu\text{m}$ and a beam diameter of $\sim 1 \text{ cm}$.

Next it will be shown that the value of I_f determined by thermally induced optical distortion resulting from the absorption by the metallic film is slightly greater than the value for the aluminum melting. The amount of optical distortion that can be tolerated obviously varies from system to system, and the value of I_f could be computed for given system specifications. Since we are not considering a specific system, a reasonable criterion for the failure of a system is that the optical path difference $\delta \ell_{\text{op}}$ between a center ray and a ray at the edge of the beam of diameter D be equal to $\frac{1}{8} \lambda$:

$$\delta \ell_{\text{op}} = \lambda/8 \quad . \quad (2.4)$$

For example, the angle through which a ray bends is $\phi = d\ell_{\text{op}}/d\rho$, where ρ is the radial circular cylindrical coordinate. With $\ell_{\text{op}} = \text{constant} \pm \delta \ell_{\text{op}} (\rho/\frac{1}{2}D)^2$, the value of $|\phi|$ is $|\phi| = 8\delta \ell_{\text{op}} \rho/D^2$. The focal length f , which is the distance from the optical element at which the ray crosses the optic axis, is, in the small angle approximation, $f = \rho/\phi = D^2/8\delta \ell_{\text{op}}$. Setting the focal length equal to the Rayleigh range, D^2/λ , gives (2.4), which is the same criterion used in previous analyses of infrared-window materials.⁶ For a metallic reflector, $\delta \ell_{\text{op}} = 2h$, where h is the rise (bulge at the center). With $h \cong \alpha \Delta T d(1+\nu)$ and $\Delta T \cong I A t_{\text{pulse}}/dC$, (2.4) gives

$$\begin{aligned} I_f &= \lambda C / 16 \alpha (1 + \nu) t_{\text{pulse}} A \\ &= 100 \text{ MW/cm}^2 \quad . \end{aligned} \quad (2.5)$$

Sec. B

The factor $(1 + \nu)$, where ν is the Poisson ratio, accounts for the bulging induced by the radial compression.

Surface damage thresholds I_f for vuv mirrors are not known, but they should be considerably greater than the values of 20 and 100 MW/cm² for melting and optical distortion.

Great increases in the value of I_f for metallic reflectors are not expected. A factor of 10 appears extremely unlikely, and a factor of three would require a substantial research program. The calculation of Sec. D indicates that the absorptance A of aluminum at 7.2 eV is 8%. The lowest value measured to date, which was also $A = 8\%$, was the result of extensive programs involving rapid deposition of aluminum at high vacuum onto supersmooth substrates followed directly by overcoating with a protective layer of material such as MgF₂. Since the value of A for the currently used aluminum films is believed to be 20%,¹⁰ the maximum possible reduction in A is a factor of ~ 3 .

Since interband transitions are the dominant source of absorption at $\hbar\omega = 7.2$ eV, reducing the temperature, purifying the metal, or improving the surface are not expected to reduce A significantly below the value of 8%, as discussed in Sec. D. It is not likely that a metal with absorptance in the vacuum ultraviolet lower than that of aluminum will be found. The plasma frequency ω_p must be high, and most metals have too small a value of ω_p . The few with large ω_p have greater absorption from interband transitions. Great increases in the thermal properties of the substrate are not expected. The choice of transparent materials is limited as discussed in Sec. I, and the values of $C = 3.14$ J/cm² K and $K \cong 0.2$ W/cm K for MgF₂ are large.

III. THERMALLY INDUCED OPTICAL DISTORTION AND FRACTURE IN TRANSPARENT MATERIALS

The criterion (2.4) and that of Ref. 6 give the same result for thermally induced optical distortion in a plane parallel window of thickness ℓ ; that is, the temperature rise ΔT of the center of the window with respect to its rim temperature must be less than ΔT_0 , where

$$\Delta T_0 = \lambda / 8 \ell \left| \partial_n T \right| \quad (3.1)$$

with $\partial_n T \equiv (\partial_n / \partial T)_\sigma + \alpha(1 + \nu)(n - 1)$, where the subscript σ denotes constant stress, n is the index of refraction, and a stress-optic term S that is typically small has been neglected in (3.1). The derivation of (3.1) is simple. The value of the change of optical path $\delta \ell_{op}$ in (2.4) is $\delta \ell_{op} = \ell \delta n + (n-1)\delta \ell$, where $\delta n = \Delta T \partial_n / \partial T$ and $\delta \ell = \ell \alpha \Delta T(1 + \nu)$ for a window of index of refraction n in air with $n_{air} \cong 1$. As before, the factor $(1 + \nu)$ accounts for the change in thickness caused by the compression from the restraint of the warm center of the window by the cooler rim. Substituting this expression for $\delta \ell_{op}$ into (2.4) gives (3.1) directly.

The expression

$$\Delta T_{fr} = 2\sigma / \alpha E, \quad (3.2)$$

(where σ is the strength of the material and E is Young's modulus) for the temperature rise that causes thermally induced fracture in windows will be used formally for total-internal reflectors and dielectric-stack reflectors. This result, which is derived in Ref. 6, is reasonable since the stress resulting from a temperature

difference ΔT is of order $\alpha E \Delta T$, and the azimuthal stress $\sigma_{\phi\phi}$ becomes positive (tensile) at large values of the radial coordinate ρ .

Values of the material parameters and of ΔT_0 and ΔT_{fr} are listed in Table BII for LiF and MgF_2 . The values of ΔT_{fr} are independent of wavelength, while the values of ΔT_0 are much smaller in the ultraviolet than in the infrared. The factor of λ in ΔT_0 in (3.1) arises because there is less diffraction at higher frequencies, roughly speaking, and in order to take advantage of this fact, stricter optical tolerances are required in the vuv.

The value of intensity I_f corresponding to ΔT [given by (3.1) or 3.2)] is obtained from (2.5). The appropriate value of absorptance A is $A = \beta \ell$ for the case of $\beta \ell \ll 1$; then $I(\ell) = I(0) \exp(-\beta \ell) \cong I(0) [1 - \beta \ell]$, and $A \equiv [I(0) - I(\ell)]/I(0) \cong \beta \ell$. From (2.5) with $A = \beta \ell$, the critical intensity is

$$I_f = C \Delta T / \beta t_{\text{pulse}} \quad (3.3)$$

Values of I_f calculated from (3.3) with ΔT given by (3.1) and by (3.2) are listed in Table BI for LiF and MgF_2 for various values of β . These results, derived for plane windows, also serve as reasonable estimates for total-internal-reflection devices. However, the theoretical values of I_f for dielectric reflectors are greater since the high intensity penetrates only a small distance into the material. This reduces the severity of the thermally induced optical distortion and thermal fracture problems. The optical pathlength through the thin heated layer in the multilayer dielectric reflector is much less than that in a window or total-internal-reflection device, and the stresses in the thin layer resulting from the unheated bulk of the multilayer dielectric reflector tend to prevent fracture.

Sec. B

Table BII. Calculated values of intensity I_f at which metals and transparent optical components fail by various mechanisms.

Failure Mechanism	Failure Intensity CW/cm ²	
	LiF	MgF ₂
Transparent Materials		
two-photon heating to $\Delta T = \Delta T_0^*$	0.07	0.07
surface damage	0.2	0.2
two-photon heating to $\Delta T = \Delta T_{fr}^*$	0.6	1.4
enhanced stimulated Raman scattering	$\gg 1$	~ 1
linear absorption to $\Delta T = \Delta T_0^*$		
$\beta = 1 \text{ cm}^{-1}$	0.06	0.04
$\beta = 0.1 \text{ cm}^{-1}$	0.6	0.4
$\beta = 10^{-2} \text{ cm}^{-1}$	6	4
linear absorption to $\Delta T = \Delta T_f^*$		
$\beta = 1 \text{ cm}^{-1}$	3	14
$\beta = 0.1 \text{ cm}^{-1}$	30	140
$\beta = 10^{-2} \text{ cm}^{-1}$	300	1.4×10^3
Partially Transmitting Film	aluminum on MgF ₂	
film burn off	0.02	
mirror thermal distortion	0.1	

* These estimates are for windows and total-internal-reflection devices. The values for dielectric reflectors are orders of magnitude greater, as discussed in Sec. III.

Sec. B

As a rough approximation of thermally induced optical distortion, the value of ΔT_0 can be calculated from (3.1) with $\ell = \ell_F + d$, where ℓ_F is the thickness of the multilayer dielectric coating and d is the thermal diffusion distance. (See Sec. II.) With $\ell_F + d$ of the order of $0.5 \mu\text{m}$ and $\partial_{nT} \approx 10^{-5} \text{K}^{-1}$ from Table BI, (3.1) gives $\Delta T_0 \approx 4,250 \text{K}$. The material would of course fail by some other mechanism, such as melting, before reaching this great temperature, but the point is that I_f is much greater than in the case of a window. For a low value of $\Delta T = 10 \text{K}$, for example, (4.2) below gives $I_f = 3 \text{GW/cm}^2$, compared with 0.07GW/cm^2 for a window. The technical problems of multilayer dielectric stacks are not simple to solve, but successful units for use at 7.2eV have been constructed.

In passing it is mentioned that thermal distortion is important in frustrated total internal reflection, which could be used to obtain a variable output from a total-internal-reflection cavity.

IV. TWO-PHOTON ABSORPTION

Estimates of the values of I_f resulting from two-photon absorption are not as accurate as those for the melting of the aluminum and for the optical distortion resulting from the absorption by the aluminum. The estimated value of the absorption coefficient β for two-photon absorption in LiF from Sec. D is

$$\beta = [1/(2 \text{ GW/cm}^2)] \times 1 \text{ cm}^{-1} . \quad (4.1)$$

Work on improving the estimate is currently underway. As already mentioned, measurements of the two-photon optical absorption are needed.

The critical intensity I_f for failure by two-photon heating is obtained by substituting β from (4.1) into (3.3) and solving for I_f , which gives

$$I_f = (C \Delta T t_{\text{pulse}}^{-1} 2 \text{ GW/cm})^{1/2} . \quad (4.2)$$

Values of I_f calculated from (4.2) for ΔT given by (3.1) and by (3.2) are listed in Table BI for LiF and MgF_2 and are discussed in Sec. I.

V. ENHANCED STIMULATED RAMAN SCATTERING

It was recently proposed that the nearly discontinuous increase in the Stokes intensity I_S at a critical value I_R of the laser intensity I_L observed in a number of solids, liquids, and gases is a result of a parametric instability in the three-Boson Stokes scattering process. The instability is analogous to those in other three-Boson processes such as ferromagnetic parallel pumping,¹¹ premature saturation of the main resonance and subsidiary resonance absorption in ferromagnetic resonance,¹¹ and the instability in the two-phonon summation infrared absorption process.¹² The parametric instability in the Raman process causes nearly complete conversion from laser to Stokes radiation in a very short distance when $I_L > I_R$. Since one phonon is created for each Stokes photon created and the absorption distance can be short, the temperature rise can be sufficiently great to fracture or melt the crystal.

If experimental investigations verify the validity of the enhanced stimulated Raman scattering (ESRS) theory, it appears that this process could be important in laser damage in Raman active crystals, such as MgF_2 . The estimates below indicate that ESRS limits I_f to a value below that for fracture by two-photon absorption.

For $I_L > I_R$, essentially all of the laser radiation is converted to Stokes radiation in a short distance ℓ_R according to the theory. For diamond for example, $\ell_R \cong 5 \mu m$ for $I_L = I_R$ and $\ell_R \cong 0.02 \mu m$ for $I_L = 10 I_R$. Thus, for some value of $I_L \sim I_R$, $\ell_R < d$, where d is the heat-diffusion distance for the 10 nsec pulse. Then the volume heated in converting I_L to I_S is $A_S d$, where A_S is the area illuminated. The energy added to this volume is $I t_{pulse} A_S \omega_f / \omega_L$,

Sec. B

where ω_f is the Raman frequency and ω_L is the laser frequency. The factor ω_f/ω_L arises from the fact that one phonon of energy $\hbar\omega_f$ is created for every laser photon annihilated. Dividing this energy by the heat capacity $CA_S d$ gives the temperature rise ΔT :

$$\Delta T = I_R t_{\text{pulse}} \omega_f / \omega_L C d . \quad (5.1)$$

The value of I_R is not known for MgF_2 . However, for the few solids for which I_R has been calculated, the values are a few GW/cm^2 . Since $I_R \sim 1/\omega$, a value of $1 \text{ GW}/\text{cm}^2$ is reasonable. For MgF_2 with this value of I_R , $t_{\text{pulse}} = 10^{-8} \text{ sec}$, $\omega_f = 410 \text{ cm}^{-1}$, $\omega_L = 5.81 \times 10^4 \text{ cm}^{-1}$ (7.2 eV), $C = 3.14 \text{ J}/\text{cm}^3 \text{ K}$, and $d = 2 \times 10^{-5} \text{ cm}$, (5.1) gives $\Delta T = 10^3 \text{ K}$, which should be sufficient to damage the crystal. Thus, crystal damage is expected at intensities equal to or possibly somewhat greater than, I_R .

VI. OTHER FAILURE MODES

The transparent-material irreversible-failure mechanism having the lowest threshold, $I_f \cong 200 \text{ MW/cm}^2$, is laser surface damage. Extensive studies performed at 0.69 and $1.06 \mu\text{m}$ show that the damage thresholds of transparent materials typically are of the order of 2 J/cm^2 for 10 nsec pulses,⁷ or 200 MW/cm^2 as already mentioned. The threshold for selected small areas of the surface or the bulk of the sample can be considerably greater, which indicates the extrinsic nature of the damage mechanism and the possibility that higher values are in principle possible. The effect of changing the frequency from the visible and near infrared to the vuv is not known. For inclusions near the surface, for example, both the diameter to wavelength ratio and the ω dependence of the absorption coefficient are important. Since neither the diameter distribution nor the absorption coefficient are known usually, it is not possible to determine the effect of the increased frequency. Nevertheless, it would be surprising if the vuv damage threshold were not at least as low as those at the longer wavelengths: Almost every type of inclusion is expected to be strongly absorbing in the vuv, and the reduction in the absorption cross section for $ka \ll 1$, where a is the radius of the inclusion, occurs at smaller values of a since $\lambda = 2\pi/k$ is smaller.

The linear absorption at 174 nm of LiF and MgF_2 typically is large, with $\beta = 0.1\text{--}1 \text{ cm}^{-1}$ as typical values, as mentioned earlier. Such large values of β surely are the results of extrinsic processes. The sources of these imperfection processes are not known. Almost any macroscopic inclusion will have a large absorption coefficient as already mentioned, and small amounts of inclusion could give rise to substantial absorption.¹³ There are, of course, many types of absorbing centers and other possible sources of β . This very important problem of the sources of the large extrinsic absorption in the vuv is currently being studied.

VII. PRECAUTIONS

The values of the I_f discussed above and listed in Table BII are essentially figures of merit. As such, they are subject to the usual possibilities of misuse. The values are not universal numbers which can be applied to any system. They were derived under the idealized conditions listed below, and the actual value of intensity at which a given specific system will fail will not be equal to any I_f listed in Table BII in general because the actual operating conditions may differ from those used in the calculations.

A single 10 nsec pulse was considered. As discussed in Sec. I, the results for continuous, quasicontinuous (continuously pulsed system), or multiply pulsed operation are in general quite different from the single 10 nsec-pulse results listed. The photon energy is assumed to be 7.2 eV. The expression for the optical-path difference $\delta \ell_{op} = \lambda/8$ in (2.4) was used formally for total-internal-reflection devices as well as for plane windows and plane dielectric stacks. This is a typical criterion, but the requirement for a specific system may be different. The temperature rise ΔT_f at which a plane window will fracture was used formally for total-internal-reflection devices as well as for plane windows. In all calculations involving the temperature rise, it was assumed that the laser-intensity profile was a Gaussian truncated at $1/e$. Truncation at $1/e^2$ would change the values of ΔT_f and ΔT_0 somewhat.

The calculated value of I_f for melting of the metallic reflector should be accurate to within a factor of two or so. The estimated values of I_f for the other processes are considerably less accurate. The inaccuracy in the value of the two-photon absorption coefficient may be as great as two orders of magnitude.

Sec. B

There are wide variations in the measured values of damage thresholds. The intrinsic values for the alkali halides are believed to be of the order of 10^{10} W/cm^2 , which corresponds to 100 J/cm^2 for a 10 nsec pulse. This value is 50 times greater than the value of 2 J/cm^2 chosen as representative of usual experimental values.

REFERENCES

* This section will be submitted for publication in the J. Appl. Phys.

1. N. Basov, V. Denilychev, and Y. Popov, Sov. J. Quantum Electron. 1, 18 (1971).
2. P. W. Hoff, J. C. Swingle, and C. K. Rhodes, Appl. Phys. Lett. 23, 245 (1973).
3. J. B. Gerardo and A. W. Johnson, J. Appl. Phys. 44, 4120 (1973).
4. W. M. Hughes, J. Shannon, A. Kolb, E. Ault, and M. Bhaumik, Appl. Phys. Lett. 23, 385 (1973).
5. D. M. Bloom, J. T. Yardley, J. F. Young, and S. E. Harris, Appl. Phys. Lett. 24, 427 (1974); It is now possible to obtain 10^6 - 10^7 watts in picosecond pulses tunable from 100 to 200 nm and focusable to 10^{12} - 10^{13} W/cm². S. Harris, private communication.
6. M. Sparks, J. Appl. Phys. 42, 5029 (1971).
7. See for example several papers in "Laser Induced Damage in Optical Materials," ed. A. J. Glass and A. H. Gunther, NBS Spec. Pub. 387 (1973).
8. Paul Hoff, private communication.
9. M. Sparks, J. Appl. Phys. 44, 4137 (1973).
10. Acton Research Corporation, Box 304, 525 Main Street, Acton, Massachusetts 01720, Product Data Sheet No. 210, unpublished.
11. M. Sparks, Ferromagnetic-Relaxation Theory (McGraw-Hill, New York, 1964).
12. M. Sparks and H. C. Chow, Phys. Rev., in press.
13. M. Sparks and C. J. Duthler, J. Appl. Phys. 44, 3038 (1973).

C. MULTIPHOTON ABSORPTION^{*}

An estimate of the strength of the two-photon absorption in lithium fluoride indicates that the absorption coefficient has the value $\beta = 1 \text{ cm}^{-1}$ for intensity $I \cong 2 \text{ GW/cm}^2$ at the photon energy $\hbar\omega = 7.2 \text{ eV}$ of the xenon laser. With this value of β , it is shown in Sec. B that the optical distortion caused by two-photon heating of transparent optical components has the lowest failure threshold of all processes considered. In view of the importance of the two-photon absorption, an improved calculation was undertaken and is currently in progress. Should other lasers become available with frequencies such that $2\hbar\omega$ is less than the electronic bandgap, thereby eliminating the two-photon absorption, then multiphoton absorption should be negligible since it is shown that three- and higher-order processes are negligible.

I. INTRODUCTION

In this section estimates of the two-photon and general n -photon absorption in wide-bandgap insulators are made. The motivation for the study is that failure of transparent materials in high-intensity ultraviolet systems is expected to be strongly related to the value of the optical absorption coefficient β . Thermally induced fracture and thermally induced optical distortion resulting from optical absorption are two examples of such failure. The estimates obtained here are used in Sec. B in a study of failure of vuv materials.

Braunstein,¹ Loudon,² Braunstein and Ockman,³ and others⁴ have developed theories of two-photon absorption, with emphasis on the absorption edge. For materials that are useful in high-intensity systems, the photon energy typically is well above the two-photon absorption edge. For example, for LiF in xenon-laser systems, twice the photon energy is $2\hbar\omega = 14.4 \text{ eV}$, and the bandgap E_g is of order 13 eV. The present calculation includes the effects of being above the absorption edge.

The estimates of Braunstein¹ for relatively narrow bandgap ($E_g \cong 1 \text{ eV}$) semiconductors gave $\beta \cong 10^{-5} \text{ cm}^{-1}$ for intensity $I \sim 10 \text{ W/cm}^2$, or $\beta = 1 \text{ cm}^{-1}$ for $I = 1 \text{ MW/cm}$. The two-photon absorption coefficient β is proportional to I , of course. If the two-photon absorption were this great for the wide-bandgap materials of interest for use in the vuv, the performance of windows and other transparent optical elements in high-intensity systems would be severely limited. Thus, an order-of-magnitude estimate of β for LiF, which has the greatest bandgap of any practical material, was made in order to verify that the two-photon absorption is indeed important. The results indicate that β is over three orders of magnitude

smaller than Braunstein's estimated value for semiconductors. Even this much smaller value is sufficiently great to make the two-photon absorption one of the most important factors in system failure, as shown in Sec. B.

These results clearly indicate the need for experimental studies of two-photon absorption coefficients and for improved theoretical estimates of the value of β . The improved calculations are in progress, and the preliminary results are that

$$\beta = (I/I_1) \text{ cm}^{-1} ; \quad I_1 = 2 \text{ GW/cm}^2 . \quad (1.1)$$

This value must be considered as tentative, pending experimental results and completion of the calculations.

The band structure and wave functions are needed in order to calculate the two- and general n -photon absorption. There is not agreement in the literature even on the value of the band gap of LiF, and the wave functions are usually less reliable than the energies. Thus, it appears that an accurate first-principle calculation of β for multiphoton absorption is not realistic at present. Nevertheless, the analysis here, which is based on a simple model that contains the essential physics, should give the value of β correct to within an order of magnitude or so.

In Sec. III it is shown that three- and higher-order-photon absorption is negligible. Thus, if it is possible to operate at a frequency below the two-photon absorption edge, then multiphoton absorption should be negligible.

II. FIRST-ORDER APPROXIMATION TO β

The formal expression for the absorption coefficient β , which is easily obtained from standard perturbation theory,^{1,2} is

$$\beta = \frac{4\pi\epsilon^{1/2}}{\hbar c n_L} \sum_i \sum_f \delta(\tilde{E}) \left| \sum_h \frac{\mathcal{K}_{fh} \mathcal{K}_{hi}}{E_f - E_h - \hbar\omega} \right|^2 \quad (2.1)$$

where ϵ is the dielectric constant, n_L is the number of photons, δ is the Dirac delta function, $\tilde{E} \equiv E_f - E_i - 2\hbar\omega$, \mathcal{K}_{fh} and \mathcal{K}_{hi} are the matrix elements for the transitions, and E_f , E_i , and E_h are the electronic energies of the final, initial, and intermediate states, respectively. In the initial state i , the valence bands are full and the conduction bands are empty. In the final and intermediate states f and h there is one electron in a conduction band and one hole in a valence band.

For the case of a single intermediate conduction band h above the lowest conduction band c , with spherical bands in the effective mass approximation and with matrix elements independent of wavevector \underline{k} , and with the oscillator strength f_{ij} defined by

$$|\langle i | \hat{\mathbf{w}} \cdot i\hbar \nabla | j \rangle|^2 = \frac{3}{2} m E_{ij} f_{ij} \quad (2.2)$$

where E_{ij} is the energy difference between electronic states i and j , (2.1) reduces to

$$\beta = \frac{18\sqrt{2}\pi e^4 \epsilon f_{hv} f_{hc}}{c^2 m^{1/2} (\alpha_v + \alpha_c)^{3/2} (\hbar\omega)^3} \frac{(2\hbar\omega - E_g)^{1/2} E_{hv} E_{hc}}{[E_{hv} + \frac{\alpha_h \alpha_v}{\alpha_v + \alpha_c} (2\hbar\omega - E_g) - \hbar\omega]^2} \quad (2.3)$$

where v and c denote the valence and conduction band, respectively, and the α 's are the inverse effective masses normalized to m ; that is, $\alpha = m(\partial^2 E / \partial k^2) / \hbar$.

By setting $\omega_1 = \omega_2$ in Braunstein's result and using (2.2), the equivalence of (2.3) and Braunstein's result is easily demonstrated.

Equation (2.3) can be written in the convenient form

$$\beta = \frac{f_{hv} f_{hc} \epsilon}{(\alpha_v + \alpha_c)^{3/2}} \frac{E_{hv} E_{hc} (2\hbar\omega - E_g)^{1/2} (1 \text{ Ry})^{5/2}}{(\hbar\omega)^3 [E_{hv} - \hbar\omega + (2\hbar\omega - E_g) \alpha_h \alpha_v (\alpha_v + \alpha_c)^{-1}]^2} \frac{1}{I_0} \times 1 \text{ cm}^{-1} \quad (2.4)$$

where, with a_0 defined as the Bohr radius,

$$I_0 \equiv \hbar c^2 / a_0^3 (144 \pi \text{ cm}) = 1.4 \text{ GW/cm}^2 .$$

For f 's and α 's equal to unity and $E_{hv} = 2 \text{ Ry}$, $E_{hc} = E_g = 1 \text{ Ry}$, $\hbar\omega = (7.2 / 13.6) \text{ Ry}$, and $\epsilon = (1.44)^2$, (2.4) gives

$$\beta = (1 / 1.2 \text{ GW/cm}^2) \times 1 \text{ cm}^{-1} .$$

In setting both oscillator strengths equal to unity, the preliminary results of the detailed calculation are anticipated. Since the transition would be classified as "allowed-forbidden" by Braunstein and Ockman, one of the oscillator strengths would have been small. The detailed calculation indicates that both transitions are strong.

The preliminary result of the considerably more involved calculation in progress gives (1.1), which is in good agreement with the rough estimate. This result (1.1) is used in Sec. B in calculating failure intensities.

III. THREE-PHOTON AND GENERAL n -PHOTON ABSORPTION

It is essentially obvious even before performing calculations that the absorption by the three-photon process is much weaker than that of the two-photon process and that higher-order processes are weaker still. The general argument is that n -photon absorption in gases becomes important for large values n at intensities that are orders of magnitude greater than the intensities that can exist in solids without failure. At lower intensities, the higher-order processes become weaker rapidly as I is decreased.

The following order-of-magnitude estimate confirms this conjecture. For $n = 3$, the expression for β in (2.1) contains an extra factor F , which is the square of a matrix element divided by the square of an energy denominator. The Hamiltonian is

$$\mathcal{H} = (e/mc) \mathbf{A} \cdot \mathbf{p} \quad (3.1)$$

with $\mathbf{p} = i\hbar \nabla$ and

$$\mathbf{A} = \sum_{\mathbf{q}} \left(\frac{2\pi\hbar c}{qV} \right)^{1/2} a_{\mathbf{q}} e^{i\mathbf{q} \cdot \mathbf{r}} \hat{\mathbf{w}}_{\mathbf{q}} + \text{c.c.} \quad (3.2)$$

where V is the volume of the crystal, $\hat{\mathbf{w}}_{\mathbf{q}}$ is the unit polarization vector, and the other symbols have their standard meanings. Thus,

$$F \cong \frac{e^2}{m^2 c^2} \left(\frac{2\pi\hbar c}{qV} \right)^2 n_L |p_{ij}|^2 / E_{\text{den}}^2 \quad (3.3)$$

where E_{den} is the energy denominator and $|p_{ij}|^2$ is given by the left-hand side of (2.2). From (3.3), (2.2), $\omega = cq\epsilon^{-1/2}$, and $I = \hbar\omega cn_L/V\epsilon^{1/2}$, we find

$$F \cong \frac{3\pi f_{ij} c^2 E_{ij} I}{m c \omega^2 E_{den}^2}$$

which can be written in the convenient form

$$F = f_{ij} \frac{E_{ij} (1 \text{ Ry})^3}{(\hbar \omega E_{den})^2} \frac{I}{I_F} \quad (3.4)$$

where

$$I_F \equiv m c (1 \text{ Ry})^3 / 3\pi \hbar^2 c^2 = 1.2 \times 10^{16} \text{ W/cm}^2 .$$

Since a typical value of the coefficient of I/I_F in (3.4) is ~ 10 , the value of F is

$$F \cong 10^{-6}$$

for $I = 1 \text{ GW/cm}^2$. Thus, $\beta \cong 5 \times 10^{-7} \text{ cm}^{-1}$ for $I = 1 \text{ GW/cm}^2$, and three-photon absorption is negligible as expected.

REFERENCES

*This section represents work in progress.

1. R. Braunstein, Phys. Rev. 125, 475 (1962).
2. R. Loudon, Proc. Phys. Soc. 80, 952 (1962).
3. R. Braunstein and N. Ockman, Phys. Rev. 134, A499 (1964).
4. J. J. Hopfield, J. M. Worlock, and K. Park, Phys. Rev. Lett. 11, 414 (1963);
J. J. Hopfield and J. M. Worlock, Phys. Rev. 137, A1455 (1965); G. D. Mahan,
Phys. Rev. Lett. 20, 332 (1968); G. D. Mahan, Phys. Rev. 170, 825 (1968).

D. CALCULATED REFLECTANCE OF ALUMINUM IN THE VACUUM ULTRAVIOLET*

H. C. Chow

Department of Physics, University of California, Los Angeles, California 90024, and
Xonics, Incorporated, Van Nuys, California 91406

and

M. Sparks

Xonics, Incorporated, Van Nuys, California 91406

A calculation of the absorptance A of aluminum in the vacuum ultraviolet (vuv) indicates that the lowest values measured to date, $A = 0.08-0.10$ for $\hbar\omega = 3-12$ eV, are very near the intrinsic limit. Operating at low temperature, purifying the metal, or improving the surface are not expected to decrease A by more than ~ 0.02 , and metallic reflectors better than aluminum are not likely to be found. Thus, values of $A < 0.06$ for metals without reflection-enhancing coatings are not likely to be attained in the vuv, and lasers with such reflectors will continue to be limited by the performance of the reflectors.

I. INTRODUCTION AND SUMMARY

The recent development of xenon lasers¹⁻⁴ and other high-intensity vacuum ultraviolet (vuv) sources⁵ has stimulated interest in mirrors for high-power ultraviolet use. The importance of the mirror problem is illustrated by the fact that the output power of the first xenon lasers was limited by melting of the partially transparent aluminum film used as the cavity mirror. Orders of magnitude greater power would be feasible if suitable reflectors were available.

In order to have high reflectance in the vuv, the plasma frequency ω_p must be high. The few metals with large ω_p have greater absorption from interband transitions than does aluminum. Thus, aluminum is important in the vuv since it has the highest known metallic reflectance there and it appears unlikely that a metal with higher reflectance will be found. Since the lowest absorptance A of aluminum measured to date is not sufficient for current needs, the calculation of A reported here was made in order to determine if a program to decrease the absorptance should be undertaken. It might be expected that the absorptance could be decreased since the great differences in the vuv values of A measured by different investigators and by the same investigator on different samples suggest that the intrinsic limit may not have been reached. However, the calculation indicates that this is not the case. The lowest measured values of A are very close to the theoretical limit.

Measured values of the reflectance in aluminum in the vuv were quite low^{6,7} prior to recent improvement programs.⁸⁻¹⁰ By obtaining supersmooth surfaces (by depositing on fire-polished pyrex substrates,⁹ for example), by improving deposition conditions (ultrahigh vacuum and rapid deposition) to remove oxygen

and perhaps otherwise improve the films, and by overcoating the metal with a dielectric such as MgF_2 to reduce the deleterious effects of oxidation, the reflectance R was increased to 90-92 percent on the frequency range 3 to 12 eV. Such high values of R are not obtained without great care, and they have been achieved only in a few samples.

Since heating of the aluminum is the factor controlling the maximum intensity in current lasers as mentioned above, it is important to know if the absorptance A can be reduced below the current minimum observed value of 8 percent. In particular, the broad weak absorption peak with a maximum⁹ of $A = 0.10$ (10 percent) at $\hbar\omega = 10$ eV would appear to result from the coupling of the incident photon field to surface plasmons, this coupling being the result of the residual roughness remaining on the "supersmooth" surface. Rougher surfaces result in similar, but much greater, absorption peaks, and overcoating with magnesium fluoride shifts the peak to the xenon-laser photon energy of 7 eV.

The calculations discussed below were motivated by the questions of whether or not this explanation of the peak was correct and, what is of greater practical interest, if the surface-plasmon absorption and perhaps other extrinsic sources of absorption could be eliminated, how small would the resulting intrinsic value of A be? The results of the present calculations indicate that the theoretical values of the absorptance range from 8 to 10 percent on the frequency range 3-12 eV, the agreement with the lowest experimental values reported to date being within one percent ($|\Lambda_{\text{exp}} - \Lambda_{\text{th}}| \leq 0.01$) over this range of $\hbar\omega$. The peak in A at 10 eV is not present in the theoretical values, which further suggests that the residual surface-plasmon coupling is responsible for this peak in $A(\omega)$.

Since a central result of the calculations is that the absorptivity of the best samples measured to date are near the theoretical limit, little improvement over the lowest measured absorptance $A = 0.08-0.10$ is expected. An improvement by a factor of approximately three over the value of $A = 0.2$ for currently available reflectors is possible, but not simple technically. Since most of the intrinsic absorption is a result of interband transitions, which are independent of the electron relaxation frequency in the vuv, reducing the temperature, purifying the metal, or improving the surface are not expected to reduce A significantly.

The possible use of total-internal-reflection devices, multilayer dielectric reflectors, or reflection-enhancing dielectric coated metals rather than simple metallic reflectors has been discussed elsewhere.¹¹

II. CALCULATION OF ABSORPTANCE

Ehrenreich, Philipp, and Segall¹² pointed out the importance of parallel-band transitions in explaining the observed reflectance of aluminum. They associated the absorption peak at 1.5 eV with the parallel-band structure (away from symmetry points), which contribute appreciably to the joint density of states. This idea was further explored by Harrison¹³ and others. Using a pseudopotential approach, Harrison identified the positions for absorption edges for aluminum and found them to occur at 0.4 eV and 1.59 eV, which compare favorably with the experimentally determined values of 0.5 eV¹⁴ and 1.5 eV.¹⁵ This parallel-band effect, together with the usual interband transitions considered earlier,¹⁵ was included in the general theory of Ashcroft and Sturm for optical properties of polyvalent metals.¹⁶ Excellent agreement was found between the Ashcroft-Sturm theory and aluminum reflectance data up to 4 eV. However, no detailed comparison was made in the 4-15 eV region of current interest. The purpose of this note is to report the results of this comparison. The theoretical results cited above¹²⁻¹⁶ are sufficient for the present calculations.

The results of Ashcroft and Sturm for the interband contribution from one reciprocal lattice vector \tilde{K} to the imaginary part ϵ_2 of the dielectric constant is

$$\epsilon_2(\omega)^{(K)} = \frac{4\pi\sigma_a a_0 K (2U_K/\hbar\omega)^2}{\omega [1 - (2U_K/\hbar\omega)^2]^{1/2}} \quad (1)$$

for $U_K < \hbar\omega < \hbar\omega_0$, and is

$$\epsilon_2(\omega)^{(K)} = \frac{2\pi\hbar m\sigma_a a_0 K (2U_K/\hbar\omega)^2 (\hbar\omega_0 + \hbar\omega)(\hbar\omega_1 - \hbar\omega)}{(\hbar\omega)^2 (\hbar K)^2 [1 - (2U_K/\hbar\omega)^2]^{1/2}} \quad (2)$$

for $\hbar\omega_0 < \hbar\omega < \hbar\omega_I$. Here U_K is the magnitude of the Fourier component of the pseudopotential characterizing the strength of the Bragg reflection in the plane defined by \underline{K} , $\sigma_a = e^2/24\pi\hbar a_0 = 5.48 \times 10^{14} \text{ sec}^{-1}$, a_0 is the Bohr radius, $\hbar\omega_0 = \epsilon_K (2k_F/K - 1)$, $k_F = mv_F/\hbar$ is the Fermi wavevector, $\epsilon_K = \hbar^2 K^2/2m$, $\hbar\omega_I = 2\epsilon_K + \hbar\omega_0$, and m is the mass of the electron. The total interband contribution $\epsilon^I_2(\omega)$ of the six equivalent (200) planes and eight equivalent (111) planes in the first Brillouin zone plus the usual intraband (Drude) contribution $\epsilon^f_2(\omega)$ is

$$\epsilon_2(\omega) = 6\epsilon_2^{(200)}(\omega) + 8\epsilon_2^{(111)}(\omega) + \epsilon_2^f(\omega), \quad (3)$$

where

$$\epsilon_2^f(\omega) \cong \omega_p^2/\omega^3 \tau (1 + 1/\omega^2 \tau^2) \cong \omega_p^2/\omega^3 \tau,$$

with τ the relaxation time of the electrons.

In restricting ourselves to the optical properties in the 3-12 eV region, we assume that the real part of the dielectric constant assumes its asymptotic Drude form

$$\epsilon_1(\omega) = 1 - \omega_p^2/\omega^2. \quad (4)$$

The value used for the calculations is $\hbar\omega_p = 15.3 \text{ eV}$. The justification for using this Drude approximation is that it agrees with the values extracted from reflectance data by Ehrenreich, Philipp, and Segall¹² to within the accuracy of reading their curves, as expected. In this region, the interband contribution to ϵ_1 is negligible. Since the theoretical interband results become independent of the electron relaxation time τ for $\hbar\omega \gtrsim 3 \text{ eV}$ for the value of τ used by Ashcroft and Sturm, neglecting the damping in ϵ^I_2 should be an excellent approximation unless τ exhibits an unexpected extreme frequency dependence.

Sec. D

The absorptance of aluminum was calculated with the use of (1)-(4) and the standard formula¹⁷ for the reflectance R , which can be written as

$$A \equiv 1 - R = \frac{4n}{(n+1)^2 + k^2} \quad (5)$$

where $n = \left\{ \frac{1}{2} [(\epsilon_1^2 + \epsilon_2^2)^{1/2} + \epsilon_1] \right\}^{1/2}$, $k = \left\{ \frac{1}{2} [(\epsilon_1^2 + \epsilon_2^2)^{1/2} - \epsilon_1] \right\}^{1/2}$, and scattering is neglected. The values of the parameters used in the calculations are listed in Table DI, and the results of the calculation of A are exhibited in Table DII.

As mentioned above, the Drude contribution to A from the intraband transitions is smaller than that of the interband transitions. The accuracy of the result for the small intraband contribution is rather low as a result of the common problem that the value of the electron relaxation frequency $\Gamma \equiv 1/\tau$ typically is greater than the value obtained from the dc conductivity. The value $\Gamma = 2.0 \times 10^{14} \text{ sec}^{-1}$ used in the calculations is that determined by Ehrenreich, Philipp, and Segall¹² from the values of R in the infrared. The value of Γ obtained from the dc conductivity is $\Gamma = 1.3 \times 10^{14} \text{ sec}^{-1}$. The surface scattering term¹⁸ $\Gamma_S = \frac{3}{8} v_f \delta$, where $\delta = c/\omega_p = 125 \text{ \AA}$ is the skin depth, is equal to $4.0 \times 10^{13} \text{ sec}^{-1}$, giving $\Gamma_{dc} + \Gamma_S = 1.7 \times 10^{14} \text{ sec}^{-1}$, which is only slightly less than the value of $2.0 \times 10^{14} \text{ sec}^{-1}$ required to fit the IR data. Furthermore, it is not unlikely that in a given sample the IR and vuv values could be different. The accuracy of Γ should be greater than $(2.0 - 1.3)/2.0$, or 35%, which gives an error in the contribution to A from ϵ_2^f of less than ± 0.009 for $\hbar\omega = 3$ to 12 eV .

The accuracy of the interband contribution to A is more difficult to estimate. A major factor is the accuracy of the values of U_K , particularly U_{200} since its

Sec. D

Table DI. Values of parameters used in the calculation of the absorptance Λ .

Other values are $k_f = 1.75 \times 10^8 \text{ cm}^{-1}$, $E_f = 11.6 \text{ eV}$, $a = 4.04 \times 10^{-8}$, and $1/\tau = 1.95 \times 10^{14} \text{ sec}^{-1}$ (or $\hbar\Gamma \equiv \hbar/\tau = 0.128 \text{ eV}$).

parameter K	Ka	K 10^8 cm^{-1}	$2 U_K$ eV	ϵ_K eV	$\hbar\omega_0$ eV	$\hbar\omega_1$ eV
200	4π	3.11	1.60	36.6	4.59	77.8
111	$2\pi\sqrt{3}$	2.69	0.500	27.5	8.22	63.2

Table DII. Calculated values of absorptance A and calculated values of parameters used in obtaining A.

$\hbar\omega$	$\epsilon_2^{(200)}$	$\epsilon_2^{(111)}$	ϵ_2^I	ϵ_2^f	ϵ_1	n	k^2	A percent	A ^I percent
2	3.97	0.208	25.5	3.75	-57.5	1.87	61.0	10.8	9.8
3	0.834	0.0605	5.49	1.11	-25.0	0.655	25.4	9.3	7.8
4	0.325	0.0254	2.15	0.469	-13.6	0.354	13.7	9.1	7.5
5	0.153	0.0129	1.023	0.240	-8.36	0.218	8.41	8.8	7.2
6	0.0792	0.0075	0.535	0.139	-5.50	0.143	5.52	8.4	6.7
7	0.0457	0.0047	0.312	0.0875	-3.78	0.103	3.79	8.2	6.5
8	0.0285	0.0032	0.196	0.0586	-2.66	0.0779	2.66	8.1	6.4
9	0.0188	0.0021	0.130	0.0411	-1.85	0.0628	1.85	8.4	6.5
10	0.0130	0.0015	0.0898	0.0300	-1.34	0.0517	1.34	8.4	6.4
11	0.0094	0.0010	0.0643	0.0225	-0.935	0.0448	0.937	8.8	6.6
12	0.0069	0.0007	0.0475	0.0173	-0.626	0.0409	0.628	9.6	7.1
13	0.0052	0.0006	0.0359	0.0136	-0.385	0.0398	0.386	10.9	8.0
14	0.0040	0.0004	0.0277	0.0109	-0.194	0.0436	0.196	13.6	10
15	0.0032	0.0003	0.0218	0.0088	-0.027	0.0833	0.034	27.6	21

Sec. D

contribution to ϵ_2^I is greater than that of U_{111} as seen in Table DII. A reasonable value of the accuracy of the U_K is 10 percent, considering that the values of U_K appropriate to the greater values of $\hbar\omega$ may be different from the previous low- $\hbar\omega$ values and that the difference may be relatively less important when averaged over all transitions. A 10 percent error in U_K results in ~ 20 percent error in A , as shown below. Thus, the value of $A^I = 0.065$ at 7 eV is expected to be accurate within $\pm 0.065(0.2) \cong \pm 0.01$ for $\hbar\omega = 3$ to 12 eV. The resulting overall accuracy of ± 0.02 in A cannot be considered as a precise value, of course, but significantly greater errors are not expected.

It can be seen that the error in A^I is approximately twice that in U_K as follows: For $\hbar\omega = 3$ to 12 eV, $\epsilon_2^I \sim U_K^2$ according to (1) and (2), and the expression for n and k^2 under (5) reduce to $n \cong \epsilon_2 / 2 |\epsilon_1|^{1/2}$ and $k^2 \cong |\epsilon_1|$. Then (5) gives

$$A \cong 2 \epsilon_2 / |\epsilon_1|^{1/2} (1 + |\epsilon_1|) .$$

With $U_K = U_{K0} + \delta U_K$, $A^I \sim \epsilon_2^I \sim U_{K0}^2 [1 + 2(\delta U_K / U_{K0})]$.
QED.

By lowering the temperature, Γ can be reduced, and it should be possible to eliminate the small intraband contribution to A . The resulting interband values of A^I (obtained by replacing $\epsilon_2^I + \epsilon_2^f$ by ϵ_2^I) listed in Table DII are lower than the values of $A \equiv A^{(I+f)}$ by 0.015 to 0.029 for $\hbar\omega = 3$ to 13 eV. Thus, only a small reduction in A would result from eliminating the intraband contribution by lowering the temperature, as mentioned above.

REFERENCES

* This section represents work in progress.

1. N. Basov, V. Denilychev, and Y. Popov, *Sov. J. Quantum Electron.* 1, 18 (1971).
2. P. W. Hoff, J. C. Swingle, and C. K. Rhodes, *Appl. Phys. Lett.* 23, 245 (1973).
3. J. B. Gerardo and A. W. Johnson, *J. Appl. Phys.* 44, 4120 (1973).
4. W. M. Hughes, J. Shannon, A. Kolb, E. Ault, and M. Bhaumik, *Appl. Phys. Lett.* 23, 385 (1973).
5. L. M. Bloom, J. T. Yardley, J. F. Young, and S. E. Harris, *Appl. Phys. Lett.* 24, 427 (1974); It is now possible to obtain 10^6 - 10^7 watts in picosecond pulses tunable from 100 to 200 nm and focusable to 10^{12} - 10^{13} W/cm². S. Harris, private communication.
6. G. B. Sabine, *Phys. Rev.* 55, 1064 (1939).
7. M. Banning, *J. Opt. Soc. Am.* 32, 98 (1942).
8. R. P. Madden, L. R. Canfield, and G. Hass, *J. Opt. Soc. Am.* 53, 620 (1963).
9. B. P. Feuerbacher and W. Steinmann, *Opt. Commun.* 1, 81 (1969).
10. H. E. Bennett, M. Silver, and E. J. Ashley, *J. Opt. Soc. Am.* 53, 1089 (1963).
11. See Sec. E and C. J. Duthler and M. Sparks, unpublished.
12. H. Ehrenreich, H. R. Philipp, and B. Segall, *Phys. Rev.* 132, 1918 (1963).
13. W. A. Harrison, *Phys. Rev.* 147, 467 (1966).
14. L. W. Bos and D. W. Lynch, *Phys. Rev. Lett.* 25, 156 (1970).
15. P. N. Butcher, *Proc. Phys. Soc. (London)* A64, 765 (1951).
16. N. W. Ashcroft and K. Sturm, *Phys. Rev. B* 3, 1898 (1971).
17. F. Wooten, *Optical Properties of Solids* (Academic, New York, 1972).
18. T. Holstein, *Phys. Rev.* 88, 1427 (1952); R. B. Dingle, *Physica* 19, 729 (1953).

E. TOTAL-INTERNAL-REFLECTION DEVICES

I. INTRODUCTION

As has been pointed out in previous sections, the intrinsic absorption of aluminum or other metals is great, thus preventing the use of metallic reflectors as cavity mirrors in vuv lasers at high intensities. The reflectivity of an aluminum mirror can be increased by constructing a multilayer stack of thin aluminum layers and approximately quarter-wave layers of MgF_2 .¹⁻³ However, the absorption is decreased only by a small factor while orders-of-magnitude decrease is needed.

Therefore we are led to consider reflectors made from dielectric materials which can take the form of either thin-film stacks or total-internal-reflection (TIR) devices. Presently, absorption in all candidate materials for use at 174 nm wavelength is impurity limited.⁴ As these materials are improved, it is expected that the absorption will be reduced to very low levels as has been achieved with transparent infrared laser materials.

A limiting factor in multilayer dielectric reflectors is that there are relatively few materials available which have sufficiently large bandgaps to be transparent in the vuv. Consequently, the choice of refractive indices is limited, especially for the high-index materials. In addition, the optical quality (absorption and scattering) of high-refractive-index materials presently is worse than that of low-index materials such as LiF and MgF_2 . In spite of these difficulties and possible technical problems, multilayer dielectric reflectors have advantages as discussed in Sec. B. They will be discussed in the following technical report.

II. TOTAL-INTERNAL-REFLECTION ELEMENTS

A total-internal-reflection device can be constructed from the best optical material available regardless of its refractive index (as long as the refractive index is large enough for internal reflection to occur). We have designed several TIR devices and optical cavities which are described below.

Perhaps the best design is one utilizing crossed roof prisms that has been described previously by Gould et al.⁵ In order to visualize the optical path and the insensitivity of this cavity design to misalignment, a crossed roof reflector interferometer has been sketched in Fig. E1a. A ray in the cavity follows the closed geometrical path shown in the figure by the dashed line. This path is similar to that in an ordinary Fabry-Perot interferometer constructed with flat mirrors.

The crossed roof reflector cavity, however, does not suffer the alignment difficulties that are encountered with the flat Fabry-Perot interferometer. The roof reflector cavity is automatically in alignment. If the left reflector is rotated by the angle ψ , the rays will still follow a similar closed path parallel to the horizontal axis between the reflectors. Rotation of the left reflector by the angle ϕ will result in the optical path being tilted by ϕ to the horizontal. With the angle β deviating from 90° , the path will no longer be closed but will be rotated about the horizontal axis by $2(\beta - 90^\circ)$ for each round trip.

Two disadvantages of the plane Fabry-Perot are still preserved in this design. Diffraction losses will be greater than those that would be obtained with a spherical cavity. However with the dimensions used in present xenon-laser cavities, diffraction losses should be completely negligible. (For a 20 cm length

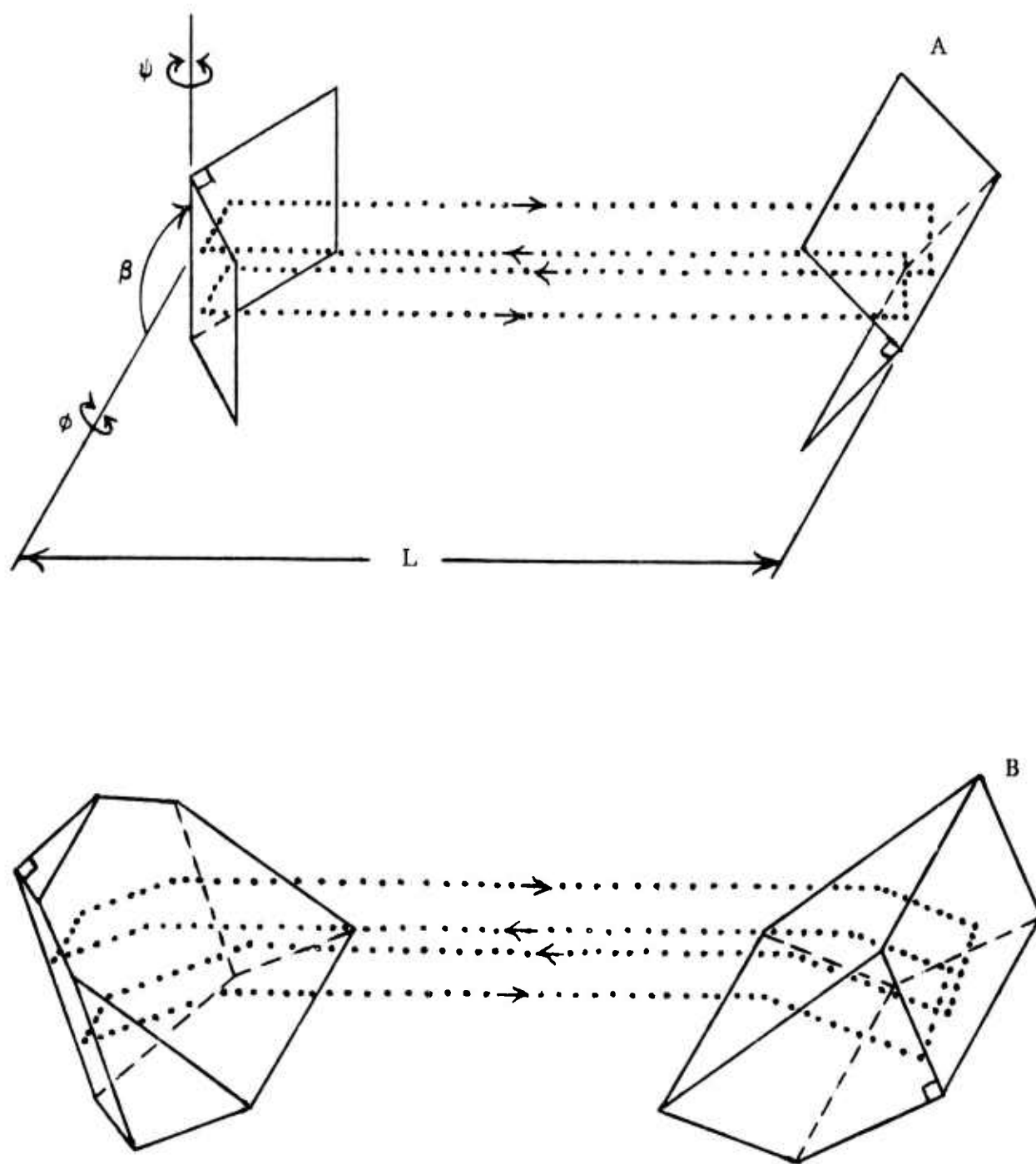


Fig. E1. Crossed roof prism optical cavity (after Gould, et al).

Sec. E

cavity with 2 cm diameter, flat mirrors, diffraction losses will be of the order of 10^{-7} per transit. The second difficulty is that paraxial rays will be lost due to walk-off from the mirrors. Both of these difficulties can be remedied by using roof reflectors with roof angles slightly less than 90° . In this case, the rays will tend to walk toward the axis of the cavity.⁶

A cavity constructed from simple roof prisms would be similar to Fig. E1a except that the roof reflectors are replaced by roof prisms and that the reflections are now total internal reflections. An undesirable feature of simple roof prisms is that there are additional partial reflections from the front faces of the prisms which are out of phase with the total internal reflections. The unwanted partial reflections can be eliminated by cutting the front faces of the prisms at Brewster's angle as is shown in Fig. E1b. (The roof axis must also be tilted to allow for refraction when passing through the Brewster face.) The cavity in Fig. E1b will have very little loss for vertically polarized rays.

In order for internal reflection to occur, the angle of incidence (measured from the normal to the reflecting plane) must be greater than the critical angle

$$i_c = \sin^{-1}(n_{\text{ext}}/n_{\text{int}})$$

where n_{int} is the refractive index of the TIR element and n_{ext} is the refractive index of the medium outside the element. Using $n_{\text{int}} = 1.444$ for MgF_2 and $n_{\text{int}} = 1.460$ for LiF at $\lambda = 174$ nm with $n_{\text{ext}} = 1$, we obtain $i_c = 43.8^\circ$ and $i_c = 43.2^\circ$, respectively. With the roof prism cavity the angle of incidence is 45° which is greater than i_c . There are two possible difficulties. First, the angle of incidence could be less than i_c due to misalignment or due to using a roof angle less than 90° . Second, the critical angle could be less than 43° if the

external medium has a refractive index greater than unity. These difficulties can be overcome either by using a material of higher refractive index (which may be more absorbing), or by using devices having more than two internal reflections.

Another type of TIR cavity that has been previously described in the literature is one made from corner cube reflectors.⁷ Although this cavity has retro-reflective properties as does the crossed roof prism resonator, the polarization properties are less desirable. It has been shown that there are six independent, elliptical eigenpolarization vectors in a corner cube cavity.⁸ Hence, it is not possible to reduce unwanted reflections from the cube faces by cutting the faces at Brewster's angle.

There is a situation where the corner cube retroreflector could be more desirable than a roof prism. This is where a totally internal reflection device is used along with a totally or partially reflecting flat to form an optical cavity as is sketched in Fig. E2. In this case the self-alignment property is preserved with the corner cube because it is exactly retroreflective. A single roof prism is retroreflective in one plane while acting as a plane mirror in the other plane. The undesirable polarization properties and unwanted reflections from the entrance face are still present in the single corner-cube cavity.

There are many other TIR devices with Brewster-angle entrance faces that can be designed. Examples of elements with three internal reflections are shown in Figs. E3 and E4. Elements with two and four internal reflections are shown in Fig. E5. For a chosen number of internal reflections there are four possible ways to cut the Brewster-angle surfaces: For the Brewster-angle surface perpendicular

Sec. E

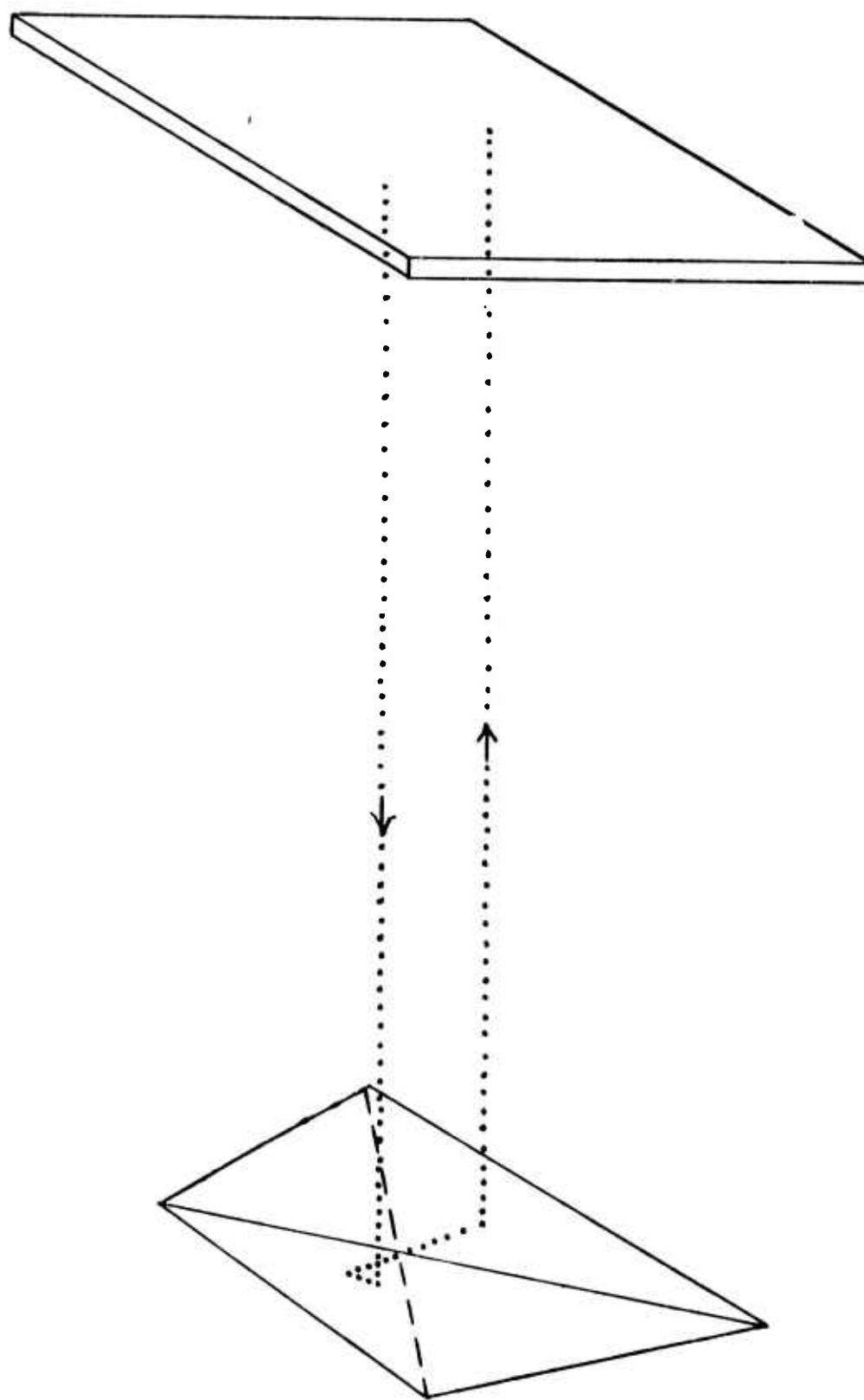


Fig. E2. Optical cavity constructed from a corner cube and flat.

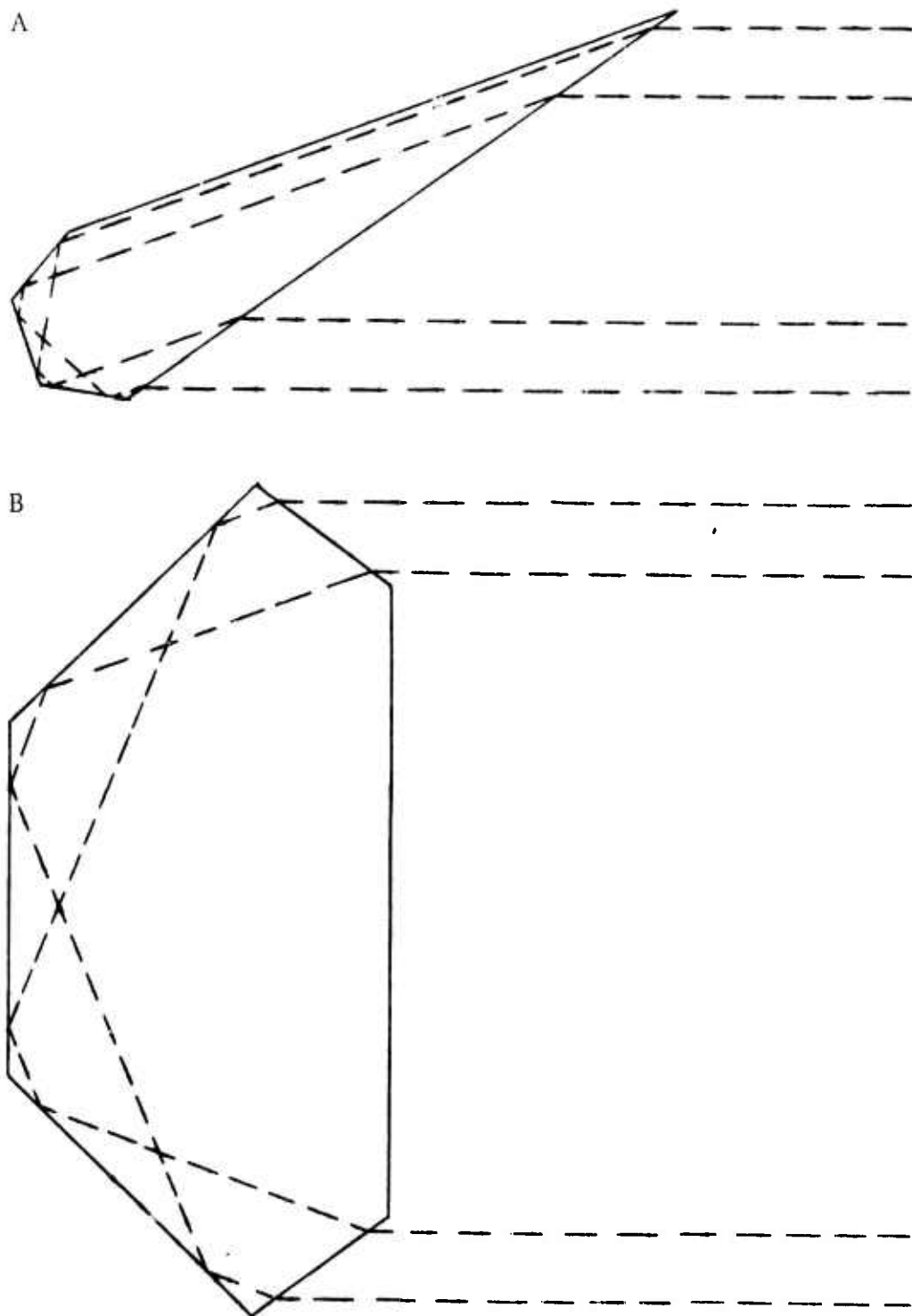


Fig. E3. TIR elements with three internal reflections.

Sec. E

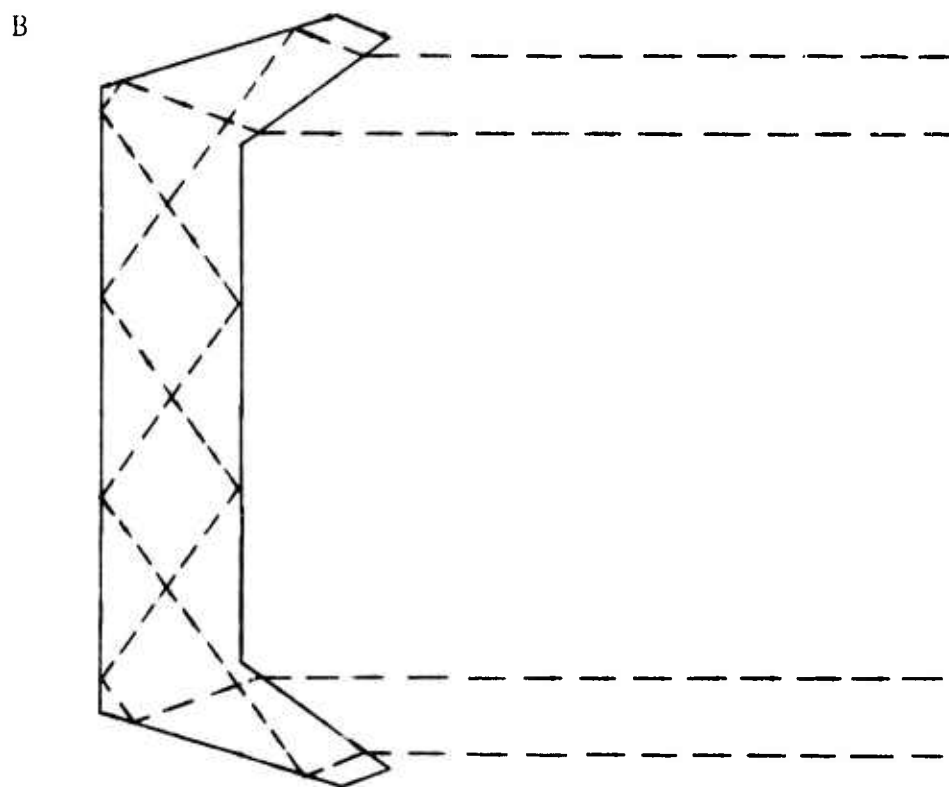
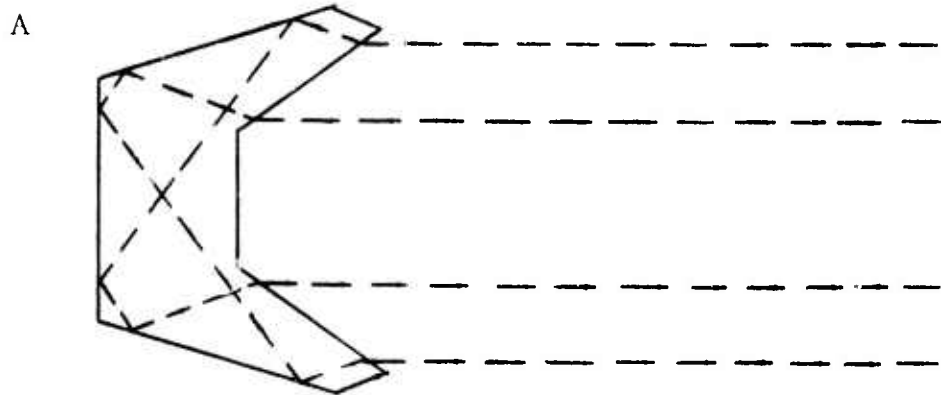


Fig. E4. TIR elements with three internal reflections, A. Similar element with greater spatial beam separation, B.

Sec. E

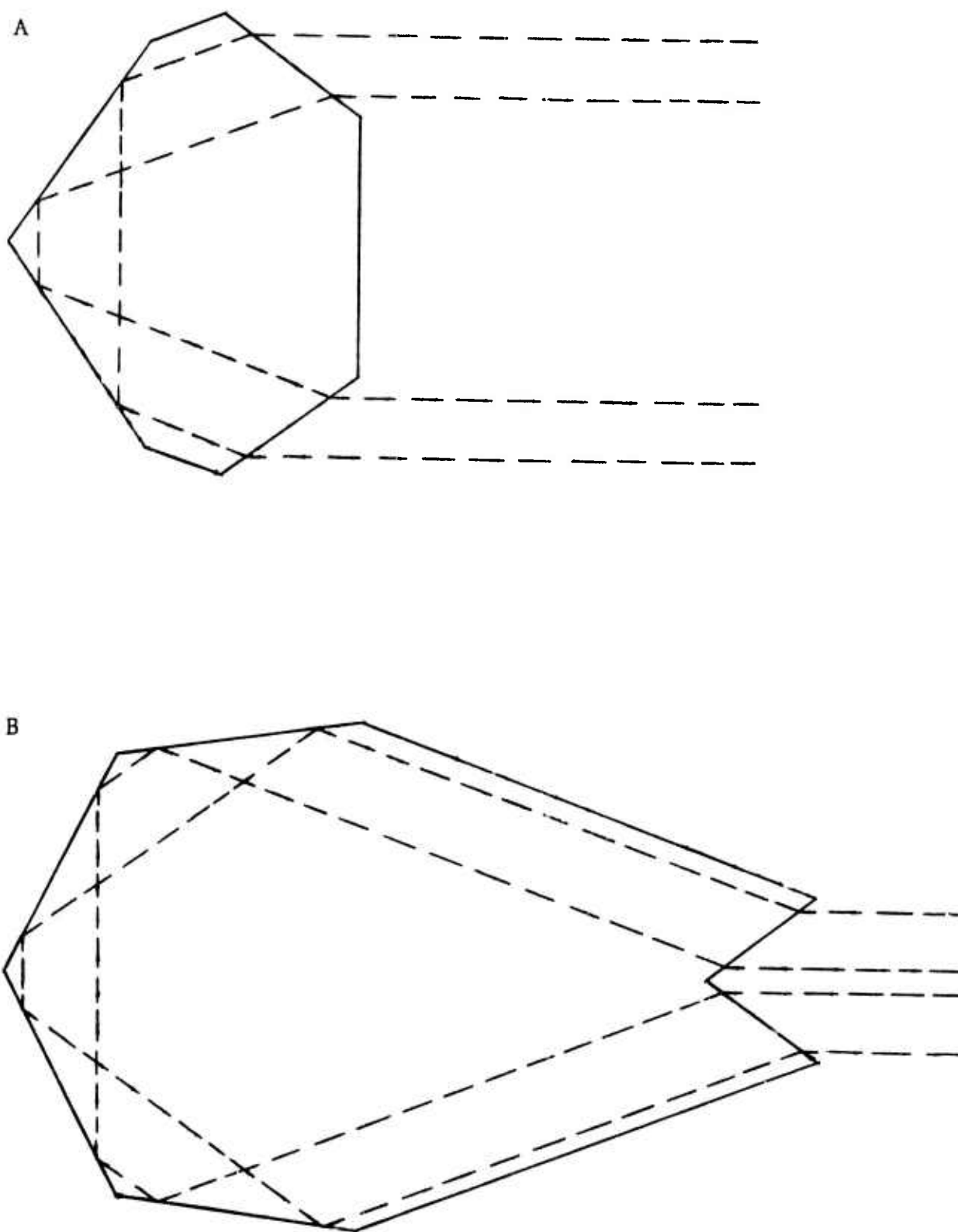


Fig. E5. TIR elements with two and four internal reflections.

Sec. E

to the reflection plane, the Brewster surface can either be a single plane as in Fig. E3a, or intersecting planes as in Figs. E3b and E4a. In addition, a single Brewster face could be cut at the Brewster angle to the reflection plane.

All TIR elements with three or more reflections will have spatially separated beams, except for the intersecting Brewster faces cut as in Figs. E4a and E5b. Elements with an even number of internal reflections and a single Brewster surface will be retroreflective, while those with an odd number will act as a plane mirror. For elements with intersecting Brewster faces, these reflection rules are approximate.

An approximately retroreflective cavity similar to that shown in Fig. E1b can be constructed from TIR elements having four internal reflections. However, since one of the elements will have spatially separated beams, the axis of the cavity will be inactive.

Spatially separated beams may be useful in some cases such as for a ring laser. Even greater spatial separation can be obtained using elements similar to Fig. E4b.

III. OUTPUT COUPLING

Output coupling from a cavity constructed with total-internal-reflection elements can be achieved by two means. First, variable output coupling can be obtained using adjustable frustrated total internal reflection (FTIR). Second, the surface of a TIR device can be modified so that partial or total transmission occurs at a small area near the cavity axis, in analogy with a spherical mirror which contains a hole in the center.

Some FTIR output couplers are shown in Fig. E6. The principle of these devices is that when a second surface is brought near a surface at which TIR is taking place, the reflection will no longer be total, but transmission through the gap will occur. The amount of transmission will vary from 100% with the gap distance $d = 0$ to less than 10% with $d = \lambda$ (assuming the output coupler and TIR device are made of the same material). Hence variable output can be obtained by adjusting the spacing d , perhaps piezoelectrically. The exact dependence of the transmission on d is discussed in Refs. 9 and 10.

The scheme shown in Fig. E6a results in two output beams.¹¹ These can be made parallel by using the arrangement shown in Fig. E6b.^{9,12,13} The element in Fig. E6c is similar to E6b except that it is reportedly easier to align.¹³ The elements in E6a-6c all have an exit face which is normal to the output beam which will result in unwanted reflections. This can be remedied by using a Brewster-angle output face as is shown in Fig. E6d for the element in E6b.

Roof prisms that have been modified to transmit rays near the optical axis are shown in Fig. E7. Part of the roof of the element in Fig. E7a has been cut normal to the beam. It may instead be desirable to cut this surface at Brewster's angle as is shown in Fig. E7b to avoid reflection, which also results in a horizontal output beam.

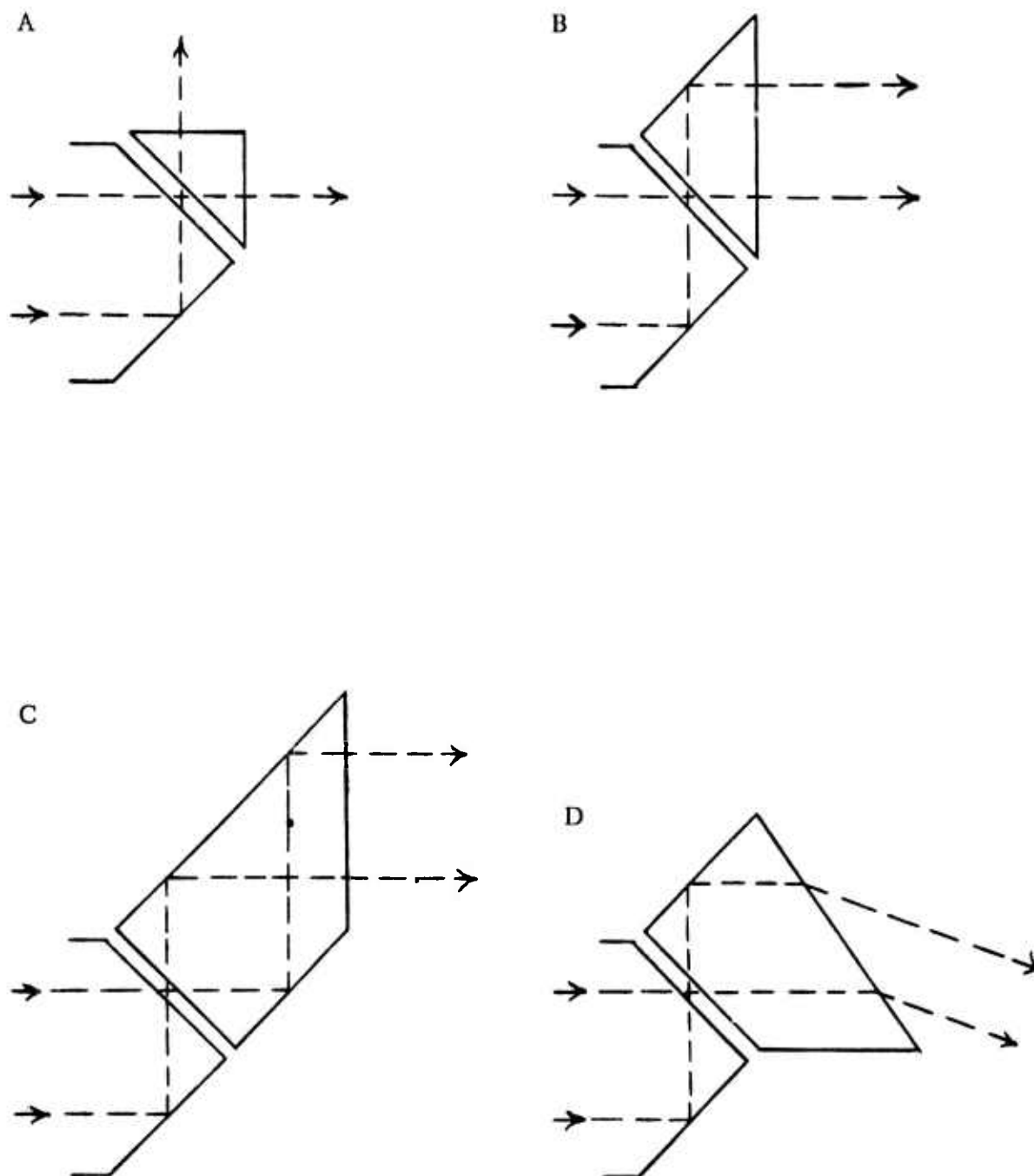


Fig. E6. Frustrated total internal reflection output coupling.

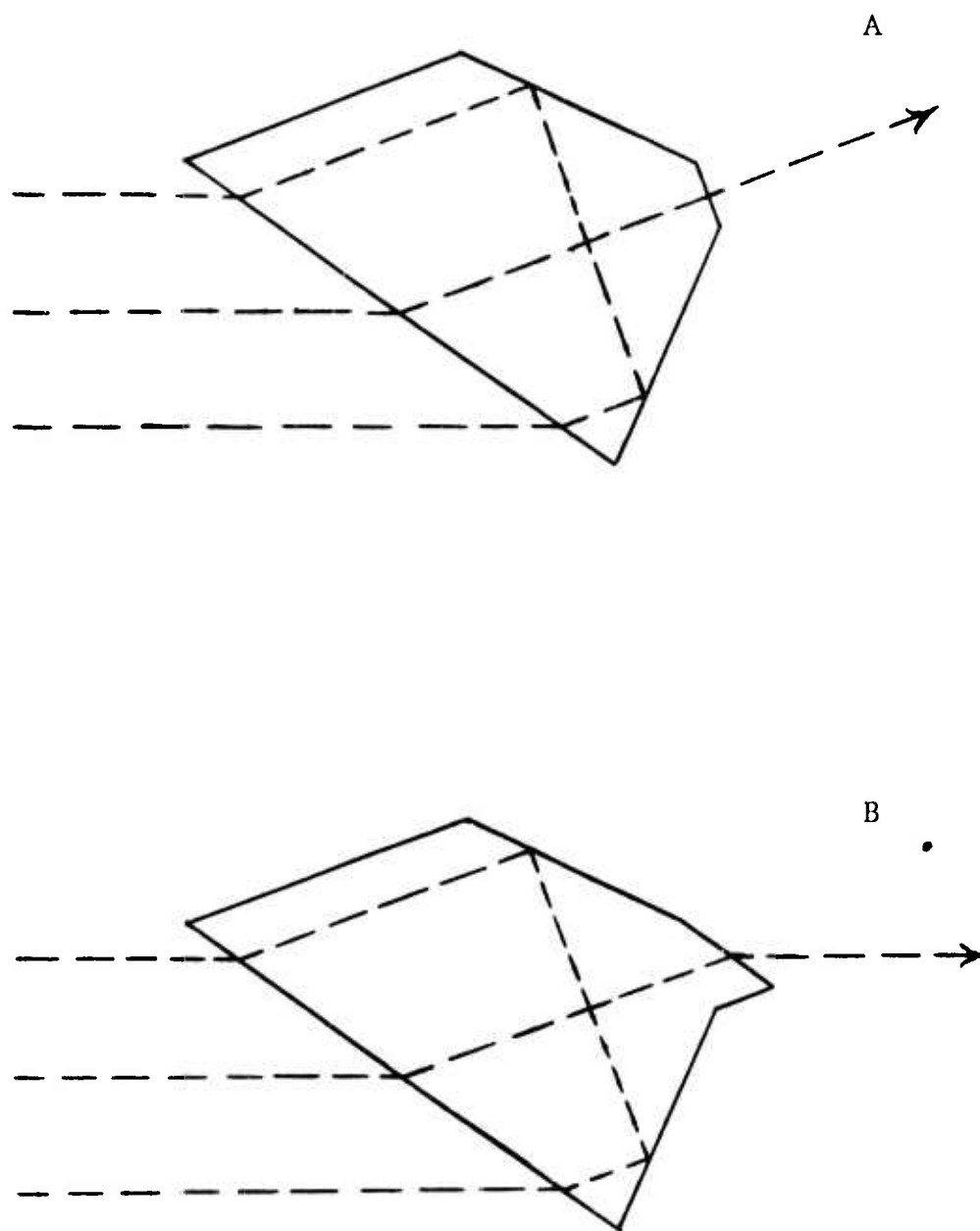


Fig. E7. Output coupling by transmission.

IV. MATERIAL FAILURE

Beside actual material damage (fracture or surface damage) to TIR elements, thermally induced optical distortion can also be a problem. Optical distortion will be especially troublesome with FTIR output coupling, where the coupling can be changed considerably if the surface elements expand a small fraction of a wavelength.

TIR elements will be subject to the same failure mechanisms as windows such as bulk or surface inclusion damage, impurity absorption, two-photon absorption, etc. An advantage of TIR elements over thin-film reflectors is that absorbed energy is distributed throughout the bulk of the element rather than in a thin film. The long path length through a TIR element (of the order of a few centimeters) requires that the absorption be kept to a very low level. Absorption coefficients $\beta \approx 0.1$ to 1 cm^{-1} that are observed at 174 nm in presently available materials⁴ will result in roughly 60% ($\approx 1 - 1/e$) absorption per pass. Clearly, orders of magnitude improvement in β is needed. These problems are discussed further in Sec. B.

REFERENCES

1. E. Spiller, Appl. Opt. 13, 1209 (1974); Optik 39, 118 (1973).
2. E. T. Fairchild, Appl. Opt. 12, 2240 (1973).
3. G. Hass and L. Hadley, in American Institute of Physics Handbook, D. E. Gray, Ed. (McGraw-Hill, New York, 1972), Chap. 6g.
4. T. Tomiki and T. Miyata, J. Phys. Soc. Japan 27, 658 (1969).
5. G. Gould, S. Jacobs, P. Rabinowitz, and T. Shultz, Appl. Opt. 1, 533 (1962).
6. L. Ronchi, Appl. Opt. 12, 93 (1973).
7. P. Rabinowitz, S. Jacobs, T. Shultz, and G. Gould, J. Opt. Soc. Am. 52, 452 (1962).
8. E. R. Peck, J. Opt. Soc. Am. 52, 253 (1962).
9. I. N. Court and F. K. von Willisen, Appl. Opt. 3, 719 (1964).
10. N. J. Harrick, Internal Reflection Spectroscopy (Interscience, New York, 1967).
11. L. Bergstein, W. Kahn, and C. Shulman, Proc. Inst. Radio Engrs. 50, 1833 (1962).
12. H. A. Daw, J. Opt. Soc. Am. 53, 915 (1963).
13. E. L. Steele, W.C. Davis, and R. L. Treuthart, Appl. Opt. 1, 5 (1966).

Sec. F

F. THE SCATTERING AND ABSORPTION OF ELECTROMAGNETIC
RADIATION BY A SEMI-INFINITE CRYSTAL IN THE
PRESENCE OF SURFACE ROUGHNESS*

A. A. Maradudin and D. L. Mills
Department of Physics
University of California
Irvine, California 92664

and

Xonics Corporation
Van Nuys, California 91406

Technical Report No. 74-18

* This section will be published in the Phys. Rev. (in press).

ABSTRACT

In this paper, we present a theoretical description of the scattering and absorption of electromagnetic radiation induced by roughness on the surface of a semi-infinite crystal. We approach the problem by the use of scattering theory applied to the classical Maxwell equations. We obtain formulas for the roughness induced scattering from the surface of an isotropic dielectric for both s and p polarized waves incident on the surface at a general angle of incidence. When the real part of the dielectric constant of the material is negative and its imaginary part small (as in a simple nearly free electron metal), we extract from the expressions for the total absorption rate that portion which describes roughness induced absorption by surface polaritons (surface plasmons). We compare our results with those recently published by Ritchie and collaborators for the case of normal incidence, and we present a series of numerical studies of the roughness induced scattering and absorption rates in aluminum.

I. Introduction

Our purpose in the present paper is to present a theoretical discussion of the effects of surface roughness on the interaction of incident electromagnetic radiation with the surface of a semi-infinite crystal. In the presence of roughness, which will be present on even the most carefully prepared sample, the incident radiation may be scattered away from the specular direction, either into the vacuum above the sample, or into the crystal, where it is absorbed if the sample is thick. Thus, the presence of roughness decreases the value of the measured reflection coefficient below the value appropriate to the idealized semi-infinite crystal with a perfectly smooth surface. In a simple metal, for which the real part of the dielectric constant is negative and its imaginary part small, one physical process that makes an important contribution to the absorption rate is the roughness-induced coupling of the incident electromagnetic wave to surface polaritons (surface plasmons)⁽¹⁾, which exist in the frequency region below $\omega_p/\sqrt{2}$, where ω_p is the bulk plasma frequency.

Over the past several years, several theoretical investigations of these phenomena have appeared.⁽²⁾⁻⁽⁶⁾ In these papers, attention is confined to the case of normal incidence. With one exception⁽⁶⁾, the authors have examined only the properties of the simple free electron metal, which is described by the (real) dielectric constant $\epsilon = 1 - \omega_p^2/\omega^2$. We feel it desirable to extend these discussions to the case of non-normal incidence, so the relative effect of surface roughness on incident radiation

of s and p polarization can be compared. Furthermore, even in simple metals such as aluminum, the dielectric constant may have an appreciable imaginary part in some frequency regions, and the real part of the dielectric constant need not be negative always.

Also, if one examines the recent papers of Ritchie and his collaborators,⁽⁴⁾⁻⁽⁶⁾ one sees that in one of them,⁽⁵⁾ the expressions obtained for the surface roughness induced scattering and absorption of radiation normally incident on the sample differ substantially from the results of the other two papers.^{(4),(6)} The question of which set of results is correct remains.

The remarks of the two preceding paragraphs suggest that the theoretical description of the surface roughness induced scattering and absorption of electromagnetic radiation remains incomplete at the present time. It is for this reason that we have chosen to examine these questions.

In some of the papers cited earlier, the analysis proceeds by the use of the formalism of second quantization. The quanta associated with the incident and scattered waves, as well as those associated with the surface polaritons, are described by introducing appropriate annihilation and creation operators. This formalism, while elegant, is difficult in practice to generalize to the case where all of the modes have a finite lifetime as a consequence of the imaginary part of the dielectric constant.

We view the problem as a problem in classical electromagnetic theory, and we choose to work directly with Maxwell's equations. We formally expand the dielectric constant in a Taylor series in the amplitude $\zeta(x,y)$ of the surface roughness, and use a method described earlier⁽⁷⁾ to convert Maxwell's equations to integral form, with the term proportional to $\zeta(x,y)$ treated by the methods of scattering theory. Within the first Born approximation, one obtains from this approach the contribution to the roughness-induced scattering and absorption rate proportional to ζ^2 , where ζ is the rms deviation of the rough surface from a perfect plane.

When our results at normal incidence are compared to the appropriate expressions in the recent work of Ritchie and co-workers,⁽⁴⁾⁻⁽⁶⁾ we find agreement with the results of the first⁽⁴⁾ and final⁽⁶⁾ papers, rather than with those of the second.⁽⁵⁾ We also believe that one assumption in reference 5 is not valid, and as a consequence the results there are not correct. A comment about this point may prove useful.

In reference 5, which confines its attention to the simple free electron metal, the calculation proceeds by introducing a transformation to a curvilinear coordinate system within which the rough surface is mapped into a smooth plane. By transforming the field variables and coordinates, the Hamiltonian H is broken up into a part H_0 , independent of the roughness amplitude $\zeta(x,y)$, and a part H_1 , of first order in this parameter, with higher order terms ignored. The part H_1 is treated via the Golden Rule of perturbation theory. Since H_0 has the form of a

Hamiltonian of a semi-infinite solid with a plane interface, it is presumed that the eigenstates of H_0 are those associated with the plane surface problem in a flat space. However, the transformation from the initial flat space to the curvilinear coordinate system is non-unitary in nature.

The commutation relations between the field amplitudes and their canonically conjugate momenta are not left invariant by this transformation. The commutation relations in the new space contain contributions proportional to the roughness amplitude $\zeta(x,y)$ (or more precisely, to certain of its derivatives). Thus, while H_0 has the appearance of a Hamiltonian of a semi-infinite solid bounded by a plane surface, the equations of motion generated by it contain terms proportional to $\zeta(x,y)$, contrary to the assumption made by Elson and Ritchie. Thus, their calculation includes some terms proportional to the derivatives of $\zeta(x,y)$, but not all of them.

In their second paper⁽⁶⁾, Elson and Ritchie again use the transformation to a curvilinear coordinate system. However, as we do here, they work directly with the wave equation of electromagnetic theory. In this second work, the method generates all terms proportional to $\zeta(x,y)$.

The transformation to curvilinear coordinates, while it yields correct results when all terms of the same order in $\zeta(x,y)$ are retained in the theory, has one cumbersome feature, in our view. When applied to the slightly rough plane interface,

Sec. F

it converts a problem with a perturbation highly localized in the z coordinate (normal to the surface) into one which extends from $z = -\infty$ to $z = +\infty$. We use here the very simple and straightforward approach described earlier which allows us to work with a perturbation that is highly localized, and which also generates in a formal sense all contributions to the scattered fields which are of first order in $\zeta(x,y)$.

This paper is organized as follows. In section II, we derive expressions for the fraction of energy scattered from the surface into the vacuum outside the crystal by the roughness, for both s and p polarized radiation at non-normal incidence. In section III, we use the same form of scattering theory to obtain expressions for the fraction of energy scattered into the solid (absorbed) by the roughness. In section IV, we examine the structure of the expressions obtained in section III, and we obtain from them expressions for the contribution to absorption by roughness induced coupling to surface polaritons, when the real part of the dielectric constant is negative and its imaginary part small. In section III and section IV, we find that at non-normal incidence the Poynting vector has a non-zero time average parallel as well as perpendicular to the surface. To our knowledge, the properties of the component parallel to the surface have not been considered previously, and under circumstances described below, it may play a significant role in the absorption process. In section V, we present a series of numerical calculations carried out for parameters characteristic of aluminum. The purpose of these

calculations is to explore the predictions of the theory at non-normal incidence, and to explore to what extent the simple expressions derived in section IV describe the roughness induced absorption. Finally, in an Appendix, we derive the complete set of electromagnetic Green's functions required for the scattering theory presented in the text. These Green's functions are also useful for a variety of other problems, and it is therefore useful to present their full form.

II. Scattering of Electromagnetic Radiation by a Rough Surface

In this section we formulate the problem of the interaction of an incident electromagnetic wave with a rough surface, and obtain the cross sections for the scattering of s- and p-polarized incident radiation caused by the surface roughness. In the next section the general results obtained here will be applied to the determination of the fraction of the incident radiation absorbed by the medium bounded by the rough surface.

Let the height of the surface above the xy-plane be specified by the equation

$$z = \zeta(x, y). \quad (2.1)$$

Above this surface is vacuum, while the medium occupies the space below it, and is characterized by a (complex) frequency dependent dielectric constant, $\epsilon(\omega)$, which we assume to be isotropic. Thus, the dielectric constant of the system of medium plus adjacent vacuum can be written as

$$\epsilon(z; \omega) = \theta(z - \zeta(x, y)) + \epsilon(\omega)\theta(\zeta(x, y) - z), \quad (2.2)$$

where $\theta(z)$ is Heaviside's unit step function. We now expand $\epsilon(z; \omega)$ in powers of $\zeta(x, y)$:

$$\epsilon(z; \omega) = \epsilon_0(z; \omega) + [\epsilon(\omega) - 1]\zeta(x, y)\delta(z) + O(\zeta^2) \quad (2.3)$$

where

$$\begin{aligned} \epsilon_0(z; \omega) &= 1 & z > 0 \\ &= \epsilon(\omega) & z < 0 \end{aligned} \quad (2.4)$$

A surface, even a rough surface, represents a static scatterer of electromagnetic radiation. Thus, if in Maxwell's equation

$$\nabla \times \nabla \times \underline{\underline{E}} = - \frac{1}{c^2} \frac{\partial^2}{\partial t^2} \underline{\underline{D}} \quad (2.5)$$

we substitute

$$\underline{\underline{E}}(\underline{\underline{x}}; t) = \underline{\underline{E}}(\underline{\underline{x}}; \omega) e^{-i\omega t} \quad (2.6a)$$

$$\underline{\underline{D}}(\underline{\underline{x}}; t) = \underline{\underline{D}}(\underline{\underline{x}}; \omega) e^{-i\omega t} , \quad (2.6b)$$

and use the relation

$$\underline{\underline{D}}(\underline{\underline{x}}; \omega) = \epsilon(z; \omega) \underline{\underline{E}}(\underline{\underline{x}}; \omega) , \quad (2.7)$$

the equation for the Fourier coefficient of the electric field $\underline{\underline{E}}(\underline{\underline{x}}; \omega)$ can be written in the form

$$\nabla \times \nabla \times \underline{\underline{E}}(\underline{\underline{x}}; \omega) - \epsilon_0(z; \omega) \frac{\omega^2}{c^2} \underline{\underline{E}}(\underline{\underline{x}}; \omega) = \frac{\omega^2}{c^2} [\epsilon(\omega) - 1] \zeta(x, y) \delta(z) \underline{\underline{E}}(\underline{\underline{x}}; \omega) . \quad (2.8)$$

We now introduce the Green's function $D_{\mu\nu}(\underline{\underline{x}}, \underline{\underline{x}}'; \omega)$ as the solution of the equation

$$\sum_{\mu} \left\{ \epsilon_0(z; \omega) \frac{\omega^2}{c^2} \delta_{\lambda\mu} - \frac{\partial^2}{\partial x_{\lambda} \partial x_{\mu}} + \delta_{\lambda\mu} \nabla^2 \right\} D_{\mu\nu}(\underline{\underline{x}}, \underline{\underline{x}}'; \omega) = 4\pi \delta_{\lambda\nu} \delta(\underline{\underline{x}} - \underline{\underline{x}}') . \quad (2.9)$$

With the use of this function we can convert the partial differential equation (2.8) into an integral equation

$$E_{\mu}(\underline{x};\omega) = E_{\mu}^{(0)}(\underline{x};\omega) - \frac{\omega^2}{4\pi c^2} [\epsilon(\omega) - 1] \sum_{\nu} \int d^3x' D_{\mu\nu}(\underline{x},\underline{x}';\omega) \zeta(x',y') \times \\ \times \delta(z') E_{\nu}(\underline{x}';\omega), \quad (2.10)$$

where $E_{\mu}^{(0)}(\underline{x};\omega)$ is a solution of the corresponding homogeneous equation

$$\sum_{\nu} \left\{ \epsilon_{\nu}(\underline{z};\omega) \frac{\omega^2}{c^2} \delta_{\mu\nu} - \frac{\partial^2}{\partial x_{\mu} \partial x_{\nu}} + \delta_{\mu\nu} \nabla^2 \right\} E_{\nu}^{(0)}(\underline{x};\omega) = 0,$$

and describes specular reflection of the incident electromagnetic field from a plane surface. Since the right hand side of Eq. (2.10) is already of first order in the surface profile function $\zeta(x,y)$, the first Born approximation suffices to yield the scattered electric field

$$E_{\mu}^{(s)}(\underline{x};\omega) = E_{\mu}(\underline{x};\omega) - E_{\mu}^{(0)}(\underline{x};\omega) \quad (2.12)$$

to first order in $\zeta(x,y)$, and we find that

$$E_{\mu}^{(s)}(\underline{x};\omega) = - \frac{\omega^2}{4\pi c^2} [\epsilon(\omega) - 1] \sum_{\nu} \int d^3x' D_{\mu\nu}(\underline{x},\underline{x}';\omega) \times \\ \times \zeta(x',y') \delta(z') E_{\nu}^{(0)}(\underline{x}';\omega) \quad (2.13)$$

To proceed farther it is convenient to introduce the Fourier representations of $D_{\mu\nu}(\underline{x},\underline{x}';\omega)$ and $\zeta(x,y)$,

$$D_{\mu\nu}(\underline{x},\underline{x}';\omega) = \int \frac{d^2k_{\parallel}}{(2\pi)^2} e^{ik_{\parallel}(\underline{x}_{\parallel} - \underline{x}'_{\parallel})} d_{\mu\nu}(k_{\parallel}|\omega|zz') \quad (2.14)$$

$$\zeta(\underline{x}_{\parallel}) = \int \frac{d^2 k_{\parallel}}{(2\pi)^2} e^{i \underline{k}_{\parallel} \cdot \underline{x}_{\parallel}} \hat{\zeta}(\underline{k}_{\parallel}), \quad (2.15)$$

where $\underline{k}_{\parallel}$ and $\underline{x}_{\parallel}$ are two-dimensional vectors whose Cartesian components are $(k_x, k_y, 0)$ and $(x, y, 0)$, respectively. The form of the representation (2.14) is dictated by the fact that the system of medium plus vacuum characterized by the dielectric constant $\epsilon_0(z; \omega)$, Eq. (2.4), is invariant against an infinitesimal displacement parallel to the plane $z = 0$, but not perpendicular to it. If we also write the field $E_v^{(0)}(\underline{x}; \omega)$ in the form

$$E_v^{(0)}(\underline{x}; \omega) = e^{i \underline{k}_{\parallel}^{(0)} \cdot \underline{x}_{\parallel}} E_v^{(0)}(\underline{k}_{\parallel}^{(0)} | \omega | z), \quad (2.16)$$

where $\underline{k}_{\parallel}^{(0)}$ is the component of the wave vector of the incident radiation parallel to the surface, we can express the scattered field in the following form

$$E_{\mu}^{(s)}(\underline{x}; \omega) = - \frac{\omega^2}{16\pi^3 c^2} [\epsilon(\omega) - 1] \int d^2 k_{\parallel} e^{i \underline{k}_{\parallel} \cdot \underline{x}_{\parallel}} \hat{\zeta}(\underline{k}_{\parallel} - \underline{k}_{\parallel}^{(0)}) \times \\ \times \sum_v \int dz' d_{\mu v}(\underline{k}_{\parallel} | \omega | z z') \delta(z') E_v^{(0)}(\underline{k}_{\parallel}^{(0)} | \omega | z') \quad (2.17)$$

It might be thought that the integration over z' in this expression could be carried out directly in view of the presence of the δ -function in the integrand. However, as we will see explicitly below, the functions $d_{\mu v}(\underline{k}_{\parallel} | \omega | z z')$ and $E_v^{(0)}(\underline{k}_{\parallel}^{(0)} | \omega | z')$ can be discontinuous across the plane $z' = 0$. In evaluating the integral over z' we therefore use the rule that if $F(z')$ is a function of z' which possesses a (finite) jump discontinuity at $z' = 0$,

$$\int_{-\infty}^{\infty} F(z') \delta(z') dz' = \frac{1}{2} [F(0+) + F(0-)] , \quad (2.18)$$

a result which has its origin in the evenness of the δ -function, and its normalization to unity, and which clearly reduces to the usual one if $F(z')$ is continuous across $z'=0$. The result (2.18) enables us to represent the scattered field, Eq. (2.17), as

$$E_{\mu}^{(s)}(\underline{x}; \omega) = - \frac{\omega^2}{16\pi^3 c^2} [\epsilon(\omega) - 1] \int d^2 k_{\parallel} e^{i \underline{k}_{\parallel} \cdot \underline{x}_{\parallel}} \times \\ \times \hat{e}(\underline{k}_{\parallel} - \underline{k}_{\parallel}^{(0)}) \Lambda_{\mu}(\underline{k}_{\parallel} \underline{k}_{\parallel}^{(0)} \omega | z) , \quad (2.19)$$

where

$$\Lambda_{\mu}(\underline{k}_{\parallel} \underline{k}_{\parallel}^{(0)} \omega | z) = \frac{1}{2} \sum_{\nu} \left\{ d_{\mu\nu}(\underline{k}_{\parallel} \omega | z+) E_{\nu}^{(0)}(\underline{k}_{\parallel}^{(0)} \omega | +) + \right. \\ \left. + d_{\mu\nu}(\underline{k}_{\parallel} \omega | z-) E_{\nu}^{(0)}(\underline{k}_{\parallel}^{(0)} \omega | -) \right\} , \quad (2.20)$$

and the notation + and - denotes 0+ and 0-, respectively.

It is shown in the Appendix that the function $d_{\mu\nu}(\underline{k}_{\parallel} \omega | zz')$ can be expressed in terms of a simpler function $g_{\mu\nu}(\underline{k}_{\parallel} \omega | zz')$ according to

$$d_{\mu\nu}(\underline{k}_{\parallel} \omega | zz') = \sum_{\mu' \nu'} S_{\mu' \mu}(\underline{k}_{\parallel}) S_{\nu' \nu}(\underline{k}_{\parallel}) g_{\mu' \nu'}(\underline{k}_{\parallel} \omega | zz') , \quad (2.21)$$

where the 3×3 , real, orthogonal matrix $\underline{S}(\underline{k}_{\parallel})$ is given by

$$\underline{S}(\underline{k}_{\parallel}) = \frac{1}{k_{\parallel}} \begin{pmatrix} k_x k_y 0 \\ -k_y k_x 0 \\ 0 0 k_{\parallel} \end{pmatrix}, \quad \underline{S}^{-1}(\underline{k}_{\parallel}) = \frac{1}{k_{\parallel}} \begin{pmatrix} k_x -k_y 0 \\ k_y k_x 0 \\ 0 0 k_{\parallel} \end{pmatrix}. \quad (2.22)$$

In calculating both the scattering and absorption of electromagnetic radiation by a rough surface, we assume that the plane of incidence is the xz -plane. The vector $\underline{k}_{\parallel}^{(0)}$ is then given by

$$\underline{k}_{\parallel}^{(0)} = (k^{(0)}, 0, 0). \quad (2.23)$$

We will consider only incident radiation which is polarized either parallel to the plane of incidence (p-polarization) or perpendicular to it (s-polarization). It is then a straightforward matter to find the electric field $\underline{E}^{(0)}(\underline{x}; \omega) e^{-i\omega t}$ in the vacuum and in the medium. The results are:

$z > 0$:

$$E_x^{(0)}(\underline{x}; t) = i(k^{(0)} x - \omega t) \left\{ -ik_z^{(0)} z + \frac{k_z^{(1)} + \epsilon(\omega) k_z^{(0)}}{k_z^{(1)} - \epsilon(\omega) k_z^{(0)}} ik_z^{(0)} z \right\} E_x^{(1)} \quad (2.24a)$$

$$E_y^{(0)}(\underline{x}; t) = i(k^{(0)} x - \omega t) \left\{ -ik_z^{(0)} z + \frac{k_z^{(0)} + k_z^{(1)}}{k_z^{(0)} - k_z^{(1)}} ik_z^{(0)} z \right\} E_y^{(1)} \quad (2.24b)$$

$$E_z^{(0)}(\underline{x}; t) = i(k^{(0)} x - \omega t) \frac{k^{(0)}}{k_z^{(0)}} \left\{ -ik_z^{(0)} z - \frac{k_z^{(1)} + \epsilon(\omega) k_z^{(0)}}{k_z^{(1)} - \epsilon(\omega) k_z^{(0)}} ik_z^{(0)} z \right\} E_x^{(1)} \quad (2.24c)$$

$z < 0$:

$$E_x^{(0)}(\tilde{x}; t) = e^{i(k^{(0)}x - \omega t)} e^{ik_z^{(1)}z} \frac{2k_z^{(1)}}{k_z^{(1)} - \epsilon(\omega)k_z^{(0)}} E_x^{(1)} \quad (2.25a)$$

$$E_y^{(0)}(\tilde{x}; t) = e^{i(k^{(0)}x - \omega t)} e^{ik_z^{(1)}z} \frac{2k_z^{(0)}}{k_z^{(0)} - k_z^{(1)}} E_y^{(1)} \quad (2.25b)$$

$$E_z^{(0)}(\tilde{x}; t) = e^{i(k^{(0)}x - \omega t)} e^{ik_z^{(1)}z} \frac{-2k_z^{(0)}}{k_z^{(1)} - \epsilon(\omega)k_z^{(0)}} E_x^{(1)} \quad (2.25c)$$

The quantities $k_z^{(0)}$ and $k_z^{(1)}$ appearing in these expressions are defined by

$$k_z^{(0)} = \left(\frac{\omega^2}{c^2} - k^{(0)2} \right)^{\frac{1}{2}} \quad (2.26)$$

$$k_z^{(1)} = - \left(\epsilon(\omega) \frac{\omega^2}{c^2} - k^{(0)2} \right)^{\frac{1}{2}}, \quad (2.27)$$

where the negative sign for the square root in Eq. (2.27), together with the fact that $\text{Im } \epsilon(\omega) > 0$, leads to the result that $\text{Im } k_z^{(1)} < 0$. (We take the branch cut for the square root along the negative real axis.) In each of Eqs. (2.24) the first term on the right hand side represents the incident electric field, while the second represents the reflected field. The vector $\tilde{E}^{(1)}$ gives the amplitude of the incident field, and in writing Eqs. (2.24) - (2.25) we have used the fact that

$$E_z^{(1)} = \frac{k_z^{(0)}}{k_z^{(0)}} E_x^{(1)} \quad (2.28a)$$

$$= - \frac{k_z^{(0)}}{k_z^{(0)}} E_x^{(1)} \quad (2.28b)$$

for the incident and reflected fields, respectively.

It follows from Eqs. (2.24) - (2.25), and the definitions (2.6), (2.16), and (2.23) that the amplitudes $E_v^{(0)}(k_{\parallel}^{(0)}\omega|\pm)$ are given by

$$E_x^{(0)}(k_{\parallel}^{(0)}\omega|+) = E_x^{(0)}(k_{\parallel}^{(0)}\omega|-) = \frac{2k_z^{(1)}}{k_z^{(1)} - \epsilon(\omega)k_z^{(0)}} E_x^{(1)} \quad (2.29)$$

$$E_y^{(0)}(k_{\parallel}^{(0)}\omega|+) = E_y^{(0)}(k_{\parallel}^{(0)}\omega|-) = \frac{-2k_z^{(0)}}{k_z^{(1)} - k_z^{(0)}} E_y^{(1)} \quad (2.30)$$

$$E_z^{(0)}(k_{\parallel}^{(0)}\omega|+) = \frac{-2\epsilon(\omega)k_z^{(0)}}{k_z^{(1)} - \epsilon(\omega)k_z^{(0)}} E_x^{(1)} \quad (2.31a)$$

$$E_z^{(0)}(k_{\parallel}^{(0)}\omega|-) = \frac{-2k_z^{(0)}}{k_z^{(1)} - \epsilon(\omega)k_z^{(0)}} E^{(1)} \quad (2.31b)$$

The results obtained so far apply equally to the scattering and absorption of light by a rough surface. In the remainder of this section we confine our attention to the scattering problem.

Sec. F

In the scattering problem the coordinate z in Eqs. (2.19) - (2.21) must be positive. The results of the Appendix show us that for $z > 0$ the function $g_{\mu\nu}(k_{\parallel}\omega|z\pm)$ has the form

$$g_{\mu\nu}(k_{\parallel}\omega|z\pm) = e^{ik_z z} \hat{g}_{\mu\nu}(k_{\parallel}\omega|\pm), \quad (2.32)$$

where

$$k_z = \left(\frac{\omega^2}{c^2} - k_{\parallel}^2 \right)^{\frac{1}{2}} \quad \frac{\omega^2}{c^2} > k_{\parallel}^2 \quad (2.33a)$$

$$= i \left(k_{\parallel}^2 - \frac{\omega^2}{c^2} \right)^{\frac{1}{2}} \quad \frac{\omega^2}{c^2} < k_{\parallel}^2. \quad (2.33b)$$

The function $g_{\mu\nu}(k_{\parallel}\omega|z\pm)$ clearly satisfies the outgoing wave condition at infinity for $(\omega^2/c^2) > k_{\parallel}^2$, and describes exponentially decaying waves for $(\omega^2/c^2) < k_{\parallel}^2$. The nonvanishing functions $\hat{g}_{\mu\nu}(k_{\parallel}\omega|\pm)$ are given explicitly by

$$\hat{g}_{xx}(k_{\parallel}\omega|+) = \hat{g}_{xx}(k_{\parallel}\omega|-) = - \frac{4\pi i c^2}{\omega^2} \frac{k_{\parallel} k_z}{k_{\parallel} - \epsilon(\omega) k_z} \quad (2.34)$$

$$\hat{g}_{zx}(k_{\parallel}\omega|+) = \hat{g}_{zx}(k_{\parallel}\omega|-) = \frac{4\pi i c^2}{\omega^2} \frac{k_{\parallel} k_{\perp}}{k_{\parallel} - \epsilon(\omega) k_z} \quad (2.35)$$

$$\hat{g}_{yy}(k_{\parallel}\omega|+) = \hat{g}_{yy}(k_{\parallel}\omega|-) = \frac{4\pi i}{k_{\parallel} - k_z} \quad (2.36)$$

$$\hat{g}_{xz}(k_{\parallel} \omega | +) = - \frac{4\pi i c^2}{\omega^2} \frac{\epsilon(\omega) k_{\parallel} k_z}{k_1 - \epsilon(\omega) k_z} \quad (2.37a)$$

$$\hat{g}_{xz}(k_{\parallel} \omega | -) = - \frac{4\pi i c^2}{\omega^2} \frac{k_{\parallel} k_z}{k_1 - \epsilon(\omega) k_z} \quad (2.37b)$$

$$\hat{g}_{zz}(k_{\parallel} \omega | +) = \frac{4\pi i c^2}{\omega^2} \frac{\epsilon(\omega) k_{\parallel}^2}{k_1 - \epsilon(\omega) k_z} \quad (2.38a)$$

$$\hat{g}_{zz}(k_{\parallel} \omega | -) = \frac{4\pi i c^2}{\omega^2} \frac{k_{\parallel}^2}{k_1 - \epsilon(\omega) k_z} \quad (2.38b)$$

The quantity k_1 appearing in these equations is

$$k_1 = - \left(\epsilon(\omega) \frac{\omega^2}{c^2} - k_{\parallel}^2 \right)^{\frac{1}{2}}, \quad (2.39)$$

and $\Im m k_1 < 0$.

Combining Eqs. (2.20), (2.21), and (2.32), we can express $\Lambda_{\mu}(\underline{k}_{\parallel} \underline{k}_{\parallel}^{(o)} \omega | z)$ conveniently as

$$\Lambda_{\mu}(\underline{k}_{\parallel} \underline{k}_{\parallel}^{(o)} \omega | z) = e^{i k_z z} \bar{\lambda}_{\mu}(\underline{k}_{\parallel} \underline{k}_{\parallel}^{(o)} \omega) \quad (2.40)$$

where

$$\bar{\lambda}_{\mu}(\underline{k}_{\parallel} \underline{k}_{\parallel}^{(o)} \omega) = \sum_{\mu'} \lambda_{\mu'}(\underline{k}_{\parallel} \underline{k}_{\parallel}^{(o)} \omega) S_{\mu' \mu}(\underline{k}_{\parallel}) \quad (2.41)$$

with

$$\begin{aligned} \lambda_{\mu}(\underline{k}_{\parallel} \underline{k}_{\parallel}^{(o)} \omega) = \frac{1}{2} \sum_{\nu} \{ & \hat{g}_{\mu \nu}(k_{\parallel} \omega | +) \mathcal{E}_{\nu}^{(o)}(\underline{k}_{\parallel} \underline{k}_{\parallel}^{(o)} \omega | +) + \\ & + \hat{g}_{\mu \nu}(k_{\parallel} \omega | -) \mathcal{E}_{\nu}^{(o)}(\underline{k}_{\parallel} \underline{k}_{\parallel}^{(o)} \omega | -) \} \end{aligned} \quad (2.42)$$

Sec. F

and

$$e_{\mu}^{(o)}(\underline{k}_{\parallel} \underline{k}_{\parallel}^{(o)} \omega | \pm) = \sum_{\nu} S_{\mu\nu}(\underline{k}_{\parallel}) E_{\nu}^{(o)}(\underline{k}_{\parallel}^{(o)} \omega | \pm). \quad (2.43)$$

The scattered field amplitude (2.19) can now be written as

$$\underline{E}^{(s)}(\underline{x}; \omega) = \frac{-\omega^2}{16\pi^3 c^2} [\epsilon(\omega) - 1] \int d^2 k_{\parallel} e^{i \underline{k} \cdot \underline{x}} \zeta(\underline{k}_{\parallel} - \underline{k}_{\parallel}^{(o)}) \bar{\lambda}(\underline{k}_{\parallel} \underline{k}_{\parallel}^{(o)} \omega), \quad (2.44)$$

where \underline{k} is the three-dimensional vector

$$\underline{k} = \underline{k}_{\parallel} + \hat{z} k_z. \quad (2.45)$$

It must be kept in mind that k_z is a function of $\underline{k}_{\parallel}$ given by Eq. (2.33).

If we write the scattered magnetic field in the form

$$\underline{H}^{(s)}(\underline{x}; t) = \underline{H}^{(s)}(\underline{x}; \omega) e^{-i\omega t}, \quad (2.46)$$

then from the Maxwell equation $\nabla \times \underline{E} = -c^{-1}(\partial \underline{H} / \partial t)$ we find directly that

$$\underline{H}^{(s)}(\underline{x}; \omega) = -\frac{\omega}{16\pi^3 c} [\epsilon(\omega) - 1] \int d^2 k_{\parallel} e^{i \underline{k} \cdot \underline{x}} \zeta(\underline{k}_{\parallel} - \underline{k}_{\parallel}^{(o)}) \underline{k} \times \bar{\lambda}(\underline{k}_{\parallel} \underline{k}_{\parallel}^{(o)} \omega). \quad (2.47)$$

Sec. F

The complex Poynting vector for the scattered radiation is therefore given by

$$\begin{aligned} \underline{S} &= \frac{c}{8\pi} \underline{E}^{(s)}(\underline{x};t)^* \times \underline{H}^{(s)}(\underline{x};t) \\ &= \frac{\omega^3}{2048\pi^7 c^2} |\epsilon(\omega)-1|^2 \int d^2 k_{\parallel} \int d^2 k'_{\parallel} e^{-i(\underline{k}-\underline{k}') \cdot \underline{x}} \times \\ &\times \zeta(\underline{k}_{\parallel}-\underline{k}_{\parallel}^{(o)})^* \zeta(\underline{k}'_{\parallel}-\underline{k}_{\parallel}^{(o)}) \bar{\lambda}(\underline{k}_{\parallel}\underline{k}_{\parallel}^{(o)}\omega)^* \times (\underline{k}'_{\parallel} \bar{\lambda}(\underline{k}_{\parallel}\underline{k}_{\parallel}^{(o)})' \omega)). \quad (2.48) \end{aligned}$$

In order that we can compare our results with experimental data for a metal surface it is reasonable to assume that the surface profile function $\zeta(x,y)$ is a stationary stochastic process, and that our result (2.48) for the Poynting vector should be averaged over the probability distribution function for this process. In fact we have to average the product $\zeta(\underline{k}_{\parallel})\zeta(\underline{k}'_{\parallel})$. The averaging restores infinitesimal translational invariance parallel to the plane $z = 0$, and we have that

$$\langle \zeta(\underline{k}_{\parallel})\zeta(\underline{k}'_{\parallel}) \rangle = \frac{(2\pi)^2}{A} \delta(\underline{k}_{\parallel}+\underline{k}'_{\parallel}) \langle |\zeta(\underline{k}_{\parallel})|^2 \rangle, \quad (2.49)$$

where A is the area of the metal surface, and use has been made of the reality condition $\zeta(-\underline{k}_{\parallel}) = \zeta(\underline{k}_{\parallel})^*$. Following Elson and Ritchie⁽⁵⁾ we make the replacement

Sec. F

$$A^{-1} \langle |\hat{\xi}(\underline{k}_{\parallel})|^2 \rangle = \delta^2 g(k_{\parallel}) \quad , \quad (2.50)$$

where δ^2 is the mean square surface height variation, and the surface scattering factor $g(k_{\parallel})$ is assumed to depend only on the magnitude of $\underline{k}_{\parallel}$, but not on its direction. With the use of Eqs. (2.49) - (2.50) the spatial average of the Poynting vector (2.48) can be written

$$\begin{aligned} \langle \underline{S} \rangle = & \delta^2 \frac{\omega^3 |\epsilon(\omega) - 1|^2}{512\pi^5 c^2} \int d^2 k_{\parallel} g(|\underline{k}_{\parallel} - \underline{k}_{\parallel}^{(o)}|) \times \\ & \times \left\{ \underline{k}_{\parallel} \bar{\lambda}(\underline{k}_{\parallel} \underline{k}_{\parallel}^{(o)} \omega) \right|^2 - \bar{\lambda}(\underline{k}_{\parallel} \underline{k}_{\parallel}^{(o)} \omega) (\underline{k}_{\parallel} \cdot \bar{\lambda}(\underline{k}_{\parallel} \underline{k}_{\parallel}^{(o)} \omega)^*) \right\} \quad (2.51) \end{aligned}$$

where we have expanded the triple vector product. With the aid of the definitions (2.41) - (2.43), and the results given by Eqs. (2.34) - (2.38), it is straightforward to establish the two useful results

$$\underline{k}_{\parallel} \cdot \bar{\lambda}(\underline{k}_{\parallel} \underline{k}_{\parallel}^{(o)} \omega)^* = 0 \quad (2.52a)$$

$$|\bar{\lambda}(\underline{k}_{\parallel} \underline{k}_{\parallel}^{(o)} \omega)|^2 = |\lambda(\underline{k}_{\parallel} \underline{k}_{\parallel}^{(o)} \omega)|^2 \quad (2.52b)$$

The first of these is a consequence of the transverse nature of the scattered electric field. Thus the spatial average of the Poynting vector takes the simple form

$$\langle \tilde{S} \rangle = \delta^2 \frac{\omega^3 |\epsilon(\omega) - 1|^2}{512\pi^5 c^2} \int d^2 k_{\parallel} g(|\tilde{k}_{\parallel} - \tilde{k}_{\parallel}^{(o)}|) |\tilde{k}_{\parallel} \lambda(\tilde{k}_{\parallel} \tilde{k}_{\parallel}^{(o)} \omega)|^2, \quad (2.53)$$

which is manifestly real. The magnitude of the real part of the averaged Poynting vector describing radiation associated with wave vector components parallel to the surface between \tilde{k}_{\parallel} and $\tilde{k}_{\parallel} + d\tilde{k}_{\parallel}$ is therefore

$$\langle S(\tilde{k}_{\parallel}) \rangle d^2 k_{\parallel} = \delta^2 \frac{\omega^4 |\epsilon(\omega) - 1|^2}{512\pi^5 c^3} g(|\tilde{k}_{\parallel} - \tilde{k}_{\parallel}^{(o)}|) |\tilde{k}_{\parallel} \lambda(\tilde{k}_{\parallel} \tilde{k}_{\parallel}^{(o)} \omega)|^2 d^2 k_{\parallel}, \quad (2.54)$$

where we have used the result that $k = (k_{\parallel}^2 + k_z^2)^{\frac{1}{2}} = (\omega/c)$.

To proceed farther, we require the $\lambda_{\mu}(\tilde{k}_{\parallel} \tilde{k}_{\parallel}^{(o)} \omega)$. We first record the expressions for the quantities $\epsilon_{\mu}^{(o)}(\tilde{k}_{\parallel} \tilde{k}_{\parallel}^{(o)} \omega | \pm)$.

Combining Eqs. (2.22), (2.29) - (2.31), and (2.43) we obtain

$$\epsilon_x^{(o)}(\tilde{k}_{\parallel} \tilde{k}_{\parallel}^{(o)} \omega | \pm) = \frac{1}{k_{\parallel}} \left\{ \frac{2k_x k_z^{(1)}}{k_z^{(1)} - \epsilon(\omega) k_z^{(o)}} E_x^{(1)} - \frac{2k_y k_z^{(o)}}{k_z^{(1)} - k_z^{(o)}} E_y^{(1)} \right\} \quad (2.55)$$

$$\epsilon_y^{(o)}(\tilde{k}_{\parallel} \tilde{k}_{\parallel}^{(o)} \omega | \pm) = \frac{1}{k_{\parallel}} \left\{ \frac{-2k_y k_z^{(1)}}{k_z^{(1)} - \epsilon(\omega) k_z^{(o)}} E_x^{(1)} - \frac{2k_x k_z^{(o)}}{k_z^{(1)} - k_z^{(o)}} E_y^{(1)} \right\} \quad (2.56)$$

$$\epsilon_z^{(o)}(\tilde{k}_{\parallel} \tilde{k}_{\parallel}^{(o)} \omega | +) = \frac{-2\epsilon(\omega) k_z^{(o)}}{k_z^{(1)} - \epsilon(\omega) k_z^{(o)}} E_x^{(1)} \quad (2.57a)$$

$$\epsilon_z^{(o)}(\tilde{k}_{\parallel} \tilde{k}_{\parallel}^{(o)} \omega | -) = \frac{-2k_z^{(o)}}{k_z^{(1)} - \epsilon(\omega) k_z^{(o)}} E_x^{(1)}. \quad (2.57b)$$

Sec. F

Substitution of these results, together with Eqs. (2.34) - (2.38), into Eq. (2.42) yields the results

$$\lambda_x(k_{\parallel} k_{\parallel}^{(o)})_{\omega} = - \frac{k_z}{k_{\parallel}} \lambda_z(k_{\parallel} k_{\parallel}^{(o)})_{\omega} \quad (2.58)$$

$$\lambda_y(k_{\parallel} k_{\parallel}^{(o)})_{\omega} = \frac{-4\pi i}{k_1 - k_z} \frac{1}{k_{\parallel}} \left\{ \frac{2k_y k_z^{(1)}}{k_z^{(1)} - \epsilon(\omega) k_z^{(o)}} E_x^{(1)} + \frac{2k_x k_z^{(o)}}{k_z^{(1)} - k_z^{(o)}} E_y^{(1)} \right\} \quad (2.59)$$

$$\begin{aligned} \lambda_z(k_{\parallel} k_{\parallel}^{(o)})_{\omega} &= \frac{4\pi i c^2}{\omega^2} \frac{1}{k_1 - \epsilon(\omega) k_z} \frac{1}{k_z^{(1)} - \epsilon(\omega) k_z^{(o)}} \times \\ &\times \left\{ 2k_x k_1 k_z^{(1)} - k_{\parallel}^2 k^{(o)} \left[\epsilon^2(\omega) + 1 \right] \right\} E_x^{(1)} - \frac{4\pi i c^2}{\omega^2} \frac{k_1}{k_1 - \epsilon(\omega) k_z} \frac{2k_y k_z^{(o)}}{k_z^{(1)} - k_z^{(o)}} E_y^{(1)}. \end{aligned} \quad (2.60)$$

When we substitute Eqs. (2.58) - (2.60) into Eq. (2.54), the contribution from $|\lambda_x|^2 + |\lambda_z|^2$ corresponds to scattered radiation that is p-polarized; the contribution from $|\lambda_y|^2$ corresponds to scattered radiation that is s-polarized. Within each category the contribution containing $|E_x^{(1)}|^2$ corresponds to incident radiation which is p-polarized, while the contribution containing $|E_y^{(1)}|^2$ corresponds to incident radiation which is s-polarized. We can therefore decompose the differential Poynting vector (2.54) into contributions associated with the

scattering of incident radiation of a given polarization into radiation with prescribed polarization. Thus, in an obvious notation

$$\langle S(\underline{k}_{\parallel} | s \rightarrow p) \rangle d^2 k_{\parallel} = \delta^2 \frac{\omega^2 |\epsilon(\omega) - 1|^2}{8\pi^3 c} g(|\underline{k}_{\parallel} - \underline{k}_{\parallel}^{(o)}|) \frac{k_y^2 k_z^{(o)2}}{k_{\parallel}^2} \times$$

$$\times \frac{|\underline{k}_1|^2}{|k_1 - \epsilon(\omega) k_z|^2 |k_z^{(1)} - k_z^{(o)}|^2} |E_y^{(1)}|^2 d^2 k_{\parallel} \quad (2.61)$$

$$\langle S(\underline{k}_{\parallel} | s \rightarrow s) \rangle d^2 k_{\parallel} = \delta^2 \frac{\omega^4 |\epsilon(\omega) - 1|^2}{8\pi^3 c^3} g(|\underline{k}_{\parallel} - \underline{k}_{\parallel}^{(o)}|) \frac{k_x^2 k_z^{(o)}}{k_{\parallel}^2} \times$$

$$\times \frac{|E_y^{(1)}|^2}{|k_1 - k_z|^2 |k_z^{(1)} - k_z^{(o)}|^2} d^2 k_{\parallel} \quad (2.62)$$

$$\langle S(\underline{k}_{\parallel} | p \rightarrow s) \rangle d^2 k_{\parallel} = \delta^2 \frac{\omega^4 |\epsilon(\omega) - 1|^2}{8\pi^3 c^3} g(|\underline{k}_{\parallel} - \underline{k}_{\parallel}^{(o)}|) \frac{k_y^2 |k_z^{(1)}|^2}{k_{\parallel}^2} \times$$

$$\times \frac{|E_x^{(1)}|^2}{|k_1 - k_z|^2 |k_z^{(1)} - \epsilon(\omega) k_z^{(o)}|^2} d^2 k_{\parallel} \quad (2.63)$$

$$\langle S(\underline{k}_{\parallel} | p \rightarrow p) \rangle d^2 k_{\parallel} = \delta^2 \frac{\omega^2 |\epsilon(\omega) - 1|^2}{8\pi^3 c} g(|\underline{k}_{\parallel} - \underline{k}_{\parallel}^{(o)}|) \frac{1}{k_{\parallel}^2} \times$$

$$\times \frac{|k_x k_1 k_z^{(1)} - \frac{1}{2} k_{\parallel}^2 k^{(o)} (\epsilon(\omega) + 1)|^2}{|k_1 - \epsilon(\omega) k_z|^2 |k_z^{(1)} - \epsilon(\omega) k_z^{(o)}|^2} |E_x^{(1)}|^2 d^2 k_{\parallel} \quad (2.64)$$

Sec. F

We can simplify these results somewhat. We note first from Eqs. (2.24) and the scattering geometry depicted in Fig. 1, that the incident flux, per unit area of the surface is

$$S_s^{(o)} = \frac{c}{8\pi} \cos \theta_o |E_y^{(1)}|^2, \quad (2.65)$$

for s-polarized incident radiation, where θ_o is the angle of incidence, and

$$S_p^{(o)} = \frac{c}{8\pi} \frac{1}{\cos \theta_o} |E_x^{(1)}|^2, \quad (2.66)$$

for p-polarized incident radiation. We will normalize the expressions (2.61) - (2.64) by dividing Eqs. (2.61) and (2.62) by Eq. (2.65) and Eqs. (2.63) and (2.64) by Eq. (2.66). We also note that Eqs. (2.61) - (2.64) give the energy crossing unit area normal to the direction of \tilde{k} per unit time. We normalize the scattered flux to unit surface area by multiplying each of Eqs. (2.61) - (2.64) by $\cos \theta_s$, where θ_s is the polar scattering angle. We next note that

$$\begin{aligned} d^2 k_{\parallel} &= k_{\parallel} dk_{\parallel} d\varphi_s \\ &= \frac{\omega^2}{c^2} \cos \theta_s d\Omega_s, \end{aligned} \quad (2.67)$$

where $d\Omega_s = \sin \theta_s d\theta_s d\varphi_s$ is the element of solid angle about the scattering direction (θ_s, φ_s) . Finally, we note the geometrical relations

Sec. F

$$\begin{aligned}
 k_x &= \frac{\omega}{c} \sin \theta_s \cos \varphi_s & k &= \frac{\omega}{c} \\
 k_y &= \frac{\omega}{c} \sin \theta_s \sin \varphi_s & k^{(0)} &= \frac{\omega}{c} \sin \theta_o \\
 k_z &= \frac{\omega}{c} \cos \theta_s & k_z^{(0)} &= \frac{\omega}{c} \cos \theta_o
 \end{aligned} \tag{2.68}$$

$$k_1 = -\frac{\omega}{c} \left[\epsilon(\omega) - \sin^2 \theta_s \right]^{\frac{1}{2}}, \quad k_z^{(1)} = -\frac{\omega}{c} \left[\epsilon(\omega) - \sin^2 \theta_o \right]^{\frac{1}{2}}.$$

Again, we point out that the negative signs attached to the square roots in the expressions for k_1 and $k_z^{(1)}$ lead to the results $\text{Im } k_1 < 0$ and $\text{Im } k_z^{(1)} < 0$, required by the boundary conditions at infinity.

Combining the normalizations described above and the results given by Eqs. (2.67) and (2.68), with the results expressed by Eqs. (2.61) - (2.64), we obtain finally the cross sections for the scattering of radiation into unit solid angle about (θ_s, φ_s) :

$$\begin{aligned}
 \frac{df(k_{\parallel} | s \rightarrow p)}{d\Omega_s} &= \delta^2 \frac{\omega^4 |\epsilon(\omega) - 1|^2}{\pi^2 c^4} g(|\tilde{k}_{\parallel} - \tilde{k}_{\parallel}^{(0)}|) \cos \theta_o \cos^2 \theta_s \sin^2 \varphi_s \times \\
 &\times \frac{|\epsilon(\omega) - \sin^2 \theta_s|}{|\epsilon(\omega) \cos \theta_s + [\epsilon(\omega) - \sin^2 \theta_s]^{\frac{1}{2}}|^2 |\cos \theta_o + [\epsilon(\omega) - \sin^2 \theta_o]^{\frac{1}{2}}|^2}
 \end{aligned} \tag{2.69}$$

$$\frac{df(\underline{k}_{\parallel} | s \rightarrow s)}{d\Omega_s} = \delta^2 \frac{\omega^4 |\epsilon(\omega) - 1|^2}{\pi^2 c^4} g(|\underline{k}_{\parallel} - \underline{k}_{\parallel}^{(o)}|) \cos \theta_o \cos^2 \theta_s \cos^2 \varphi_s \times$$

$$\times \frac{1}{|\cos \theta_s + [\epsilon(\omega) - \sin^2 \theta_s]^{\frac{1}{2}}|^2 |\cos \theta_o + [\epsilon(\omega) - \sin^2 \theta_o]^{\frac{1}{2}}|^2} \quad (2.70)$$

$$\frac{df(\underline{k}_{\parallel} | p \rightarrow s)}{d\Omega_s} = \delta^2 \frac{\omega^4 |\epsilon(\omega) - 1|^2}{\pi^2 c^4} g(|\underline{k}_{\parallel} - \underline{k}_{\parallel}^{(o)}|) \cos \theta_o \cos^2 \theta_s \sin^2 \varphi_s \times$$

$$\times \frac{|\epsilon(\omega) - \sin^2 \theta_o|}{|\cos \theta_s + [\epsilon(\omega) - \sin^2 \theta_s]^{\frac{1}{2}}|^2 |\epsilon(\omega) \cos \theta_o + [\epsilon(\omega) - \sin^2 \theta_o]^{\frac{1}{2}}|^2} \quad (2.71)$$

$$\frac{df(\underline{k}_{\parallel} | p \rightarrow p)}{d\Omega_s} = \delta^2 \frac{\omega^4 |\epsilon(\omega) - 1|^2}{\pi^2 c^4} g(|\underline{k}_{\parallel} - \underline{k}_{\parallel}^{(o)}|) \cos \theta_o \cos^2 \theta_s \times$$

$$\times \frac{|\cos \varphi_s [\epsilon(\omega) - \sin^2 \theta_s]^{\frac{1}{2}} [\epsilon(\omega) - \sin^2 \theta_o]^{\frac{1}{2}} - \frac{1}{2} \sin \theta_o \sin \theta_s [\epsilon^2(\omega) + 1]|^2}{|\epsilon(\omega) \cos \theta_s + [\epsilon(\omega) - \sin^2 \theta_o]^{\frac{1}{2}}|^2 |\epsilon(\omega) \cos \theta_o + [\epsilon(\omega) - \sin^2 \theta_o]^{\frac{1}{2}}|^2} \quad (2.72)$$

III. Absorption of Electromagnetic Radiation by a Rough Surface

In the preceding section we have developed a formalism for treating the interaction of an electromagnetic wave with the rough surface of some medium, and applied it to the determination of the cross sections for the scattering of the electromagnetic wave by the surface roughness. In this section we apply the same formalism to the determination of the absorption of the electromagnetic wave by the medium arising from the surface roughness.

Our starting point is the expression for the scattered electric field given by Eqs. (2.19) - (2.21). In contrast with the scattering problem, in which it is the values of $g_{\mu\nu}(k_{\parallel}\omega|zz')$ for $z > 0$ that are required, in the absorption problem it is their values for $z < 0$, i.e., in the medium, that are required. From the results of the Appendix we find that for $z < 0$ we can write

$$g_{\mu\nu}(k_{\parallel}\omega|z\pm) = e^{ik_1 z} \hat{g}_{\mu\nu}(k_{\parallel}\omega|\pm), \quad (3.1)$$

where the coefficient functions $\hat{g}_{\mu\nu}(k_{\parallel}\omega|\pm)$ are given explicitly by

$$\hat{g}_{xx}(k_{\parallel}\omega|+) = \hat{g}_{xx}(k_{\parallel}\omega|-) = -\frac{4\pi ic^2}{\omega^2} \frac{k_1 k_z}{k_1 - \epsilon(\omega)k_z} \quad (3.2)$$

Sec. F

$$\hat{g}_{zx}(k_{||}\omega|+) = \hat{g}_{zx}(k_{||}\omega|-) = \frac{4\pi ic^2}{\omega^2} \frac{k_{||}k_z}{k_1 - \epsilon(\omega)k_z} \quad (3.3)$$

$$\hat{g}_{yy}(k_{||}\omega|+) = \hat{g}_{yy}(k_{||}\omega|-) = \frac{4\pi i}{k_1 - k_z} \quad (3.4)$$

$$\hat{g}_{xz}(k_{||}\omega|+) = - \frac{4\pi ic^2}{\omega^2} \frac{k_{||}k_1}{k_1 - \epsilon(\omega)k_z} \quad (3.5a)$$

$$\hat{g}_{xz}(k_{||}\omega|-) = \frac{4\pi ic^2}{\omega^2 \epsilon(\omega)} \frac{k_{||}k_1}{k_1 - \epsilon(\omega)k_z} \quad (3.5b)$$

$$\hat{g}_{zz}(k_{||}\omega|+) = \frac{4\pi ic^2}{\omega^2} \frac{k_{||}^2}{k_1 - \epsilon(\omega)k_z} \quad (3.6a)$$

$$\hat{g}_{zz}(k_{||}\omega|-) = \frac{4\pi ic^2}{\omega^2 \epsilon(\omega)} \frac{k_{||}^2}{k_1 - \epsilon(\omega)k_z} \quad (3.6b)$$

Thus we can write the function $\Lambda_{\mu}(k_{||}k_{||}^{(o)}\omega|z)$ entering Eq. (2.19) in the form

$$\Lambda_{\mu}(k_{||}k_{||}^{(o)}\omega|z) = e^{ik_1 z} \bar{\lambda}_{\mu}(k_{||}k_{||}^{(o)}\omega) \quad (3.7)$$

where $\bar{\lambda}_{\mu}(\underline{k}_{\parallel} \underline{k}_{\parallel}^{(0)} \omega)$ is again defined by Eqs. (2.41) - (2.43), with the only difference being that the functions $\hat{g}_{\mu\nu}(\underline{k}_{\parallel} \omega | \pm)$ appearing in Eq. (2.42) are now those given by Eqs. (3.2) - (3.6).

The scattered electric and magnetic fields are now given by

$$\underline{E}^{(s)}(\underline{x}; t) = -e^{-i\omega t} \frac{\omega^2}{16\pi^3 c^2} [\epsilon(\omega) - 1] \int d^2 k_{\parallel} e^{i\underline{k} \cdot \underline{x}} \hat{\zeta}(\underline{k}_{\parallel} - \underline{k}_{\parallel}^{(0)}) \bar{\lambda}(\underline{k}_{\parallel} \underline{k}_{\parallel}^{(0)} \omega) \quad (3.8)$$

$$\underline{H}^{(s)}(\underline{x}; t) = -e^{-i\omega t} \frac{\omega}{16\pi^3 c} [\epsilon(\omega) - 1] \int d^2 k_{\parallel} e^{i\underline{k} \cdot \underline{x}} \hat{\zeta}(\underline{k}_{\parallel} - \underline{k}_{\parallel}^{(0)}) \times \\ \times (\underline{k} \times \bar{\lambda}(\underline{k}_{\parallel} \underline{k}_{\parallel}^{(0)} \omega)) , \quad (3.9)$$

where the three-dimensional wave vector \underline{k} is now given by

$$\underline{k} = \underline{k}_{\parallel} + \hat{z} k_1 .$$

It should be kept in mind that k_1 is a function of $\underline{k}_{\parallel}$ through Eq. (2.39), and is complex,

$$k_1 = k_1^{(1)} - ik_1^{(2)} , \quad k_1^{(2)} > 0 . \quad (3.11)$$

The vector \underline{k} , therefore, is also complex.

The complex Poynting vector obtained by substituting Eqs. (3.8) - (3.9) into Eq. (2.48), and averaging the result with respect to the distribution function for the surface profile function $\zeta(x, y)$, now takes the form

Sec. F

$$\langle \underline{S}(z) \rangle = \delta^2 \frac{\omega^3 |\epsilon(\omega) - 1|^2}{512\pi^5 c^2} \int d^2 k_{\parallel} e^{2k_1^{(2)} z} g(|\underline{k}_{\parallel} - \underline{k}_{\parallel}^{(o)}|) \times$$

$$\times \left\{ k_{\parallel} |\bar{\lambda}(\underline{k}_{\parallel} \underline{k}_{\parallel}^{(o)} \omega)|^2 - \bar{\lambda}(\underline{k}_{\parallel} \underline{k}_{\parallel}^{(o)} \omega) (\underline{k}_{\parallel} \cdot \bar{\lambda}(\underline{k}_{\parallel} \underline{k}_{\parallel}^{(o)} \omega)^*) \right\} . \quad (3.12)$$

However, in the present case the scalar product $\underline{k}_{\parallel} \cdot \bar{\lambda}(\underline{k}_{\parallel} \underline{k}_{\parallel}^{(o)} \omega)^*$ does not vanish, and both terms in braces contribute to $\langle \underline{S}(z) \rangle$. It is therefore convenient to define two vectors $\underline{A}(\underline{k}_{\parallel} \underline{k}_{\parallel}^{(o)} \omega)$ and $\underline{B}(\underline{k}_{\parallel} \underline{k}_{\parallel}^{(o)} \omega)$ by

$$\underline{A}(\underline{k}_{\parallel} \underline{k}_{\parallel}^{(o)} \omega) = \underline{k}_{\parallel} |\bar{\lambda}(\underline{k}_{\parallel} \underline{k}_{\parallel}^{(o)} \omega)|^2 \quad (3.13)$$

$$\underline{B}(\underline{k}_{\parallel} \underline{k}_{\parallel}^{(o)} \omega) = \bar{\lambda}(\underline{k}_{\parallel} \underline{k}_{\parallel}^{(o)} \omega) (\underline{k}_{\parallel} \cdot \bar{\lambda}(\underline{k}_{\parallel} \underline{k}_{\parallel}^{(o)} \omega)^*) \quad (3.14)$$

With the aid of Eqs. (2.22) and (2.41) we can rewrite these vectors in terms of the functions $\lambda_{\mu}(\underline{k}_{\parallel} \underline{k}_{\parallel}^{(o)} \omega)$ as

$$A_x = k_x |\lambda|_{\parallel}^2, \quad A_y = k_y |\lambda|_{\parallel}^2, \quad A_z = k_1 |\lambda|_{\parallel}^2 \quad (3.15)$$

$$B_x = \frac{1}{k_{\parallel}} (k_x \lambda_x - k_y \lambda_y) (k_{\parallel} \lambda_x^* + k_1 \lambda_z^*) \quad (3.16a)$$

$$B_y = \frac{1}{k_{\parallel}} (k_y \lambda_x + k_x \lambda_y) (k_{\parallel} \lambda_x^* + k_1 \lambda_z^*) \quad (3.16b)$$

$$B_z = \lambda_z (k_{\parallel} \lambda_x^* + k_1 \lambda_z^*) \quad (3.16c)$$

We now require explicit expressions for the functions $\lambda_{\mu}(k_{\parallel} k_{\parallel}^{(o)} \omega)$ appearing in Eqs. (3.15) and (3.16). Combining Eqs. (2.42), (2.55) - (2.57), and (3.2) - (3.6), we find that

$$\lambda_x(k_{\parallel} k_{\parallel}^{(o)} \omega) = - \frac{k_1}{k_{\parallel}} \lambda_z(k_{\parallel} k_{\parallel}^{(o)} \omega) \quad (3.17)$$

$$\lambda_y(k_{\parallel} k_{\parallel}^{(o)} \omega) = \frac{-4\pi i}{k_1 - k_z} \frac{1}{k_{\parallel}} \left\{ \frac{2k_y k_z^{(1)}}{k_z^{(1)} - \epsilon(\omega) k_z^{(o)}} E_x^{(1)} + \frac{2k_x k_z^{(o)}}{k_z^{(1)} - k_z^{(o)}} E_y^{(1)} \right\} \quad (3.18)$$

$$\begin{aligned} \lambda_z(k_{\parallel} k_{\parallel}^{(o)} \omega) &= \frac{4\pi i c^2}{\omega^2} \frac{1}{k_1 - \epsilon(\omega) k_z} \frac{1}{k_z^{(1)} - \epsilon(\omega) k_z^{(o)}} \times \\ &\times \left\{ 2k_x k_z k_z^{(1)} - k^{(o)} k_{\parallel}^2 [\epsilon(\omega) + \epsilon^{-1}(\omega)] \right\} E_x^{(1)} - \\ &- \frac{4\pi i c^2}{\omega^2} \frac{k_z}{k_1 - \epsilon(\omega) k_z} \frac{2k_y k_z^{(o)}}{k_z^{(1)} - k_z^{(o)}} E_y^{(1)} . \end{aligned} \quad (3.19)$$

To obtain the power absorbed by the medium we need the real part of the complex Poynting vector (3.12). If we combine Eqs. (3.17) - (3.19) with Eqs. (3.15) - (3.16) we find that the real part of $\langle S(z) \rangle$ depends on the following quantities:

Sec. F

$$\operatorname{Re} [A_x - B_x] = k_x \left\{ \frac{k_{\parallel}^2 + \operatorname{Re}(k_1)^2}{k_{\parallel}^2} |\lambda_z|^2 + |\lambda_y|^2 \right\} - 2k_y \left(\frac{k_1^{(2)}}{k_{\parallel}} \right) \operatorname{Re}(i\lambda_y \lambda_z^*) \quad (3.20)$$

$$\operatorname{Re} [A_y - B_y] = k_y \left\{ \frac{k_{\parallel}^2 + \operatorname{Re}(k_1)^2}{k_{\parallel}^2} |\lambda_z|^2 + |\lambda_y|^2 \right\} + 2k_x \left(\frac{k_1^{(2)}}{k_{\parallel}} \right) \operatorname{Re}(i\lambda_y \lambda_z^*) \quad (3.21)$$

$$\operatorname{Re} [A_z - B_z] = k_1^{(1)} \left\{ \frac{k_{\parallel}^2 + |k_1|^2}{k_{\parallel}^2} |\lambda_z|^2 + |\lambda_y|^2 \right\} . \quad (3.22)$$

With these results we can now write down the components of the real part of $\langle S(z) \rangle$ in the case that the incident light is s-polarized. We have that

$$\begin{aligned} \operatorname{Re} \langle S_x(z) \rangle_s &= \delta^2 \frac{\omega^3 |\epsilon(\omega) - 1|^2}{8\pi^3 c^2} \frac{k_z^{(0)2} |E_y^{(1)}|^2}{|k_z^{(1)} - k_z^{(0)}|^2} \int d^2 k_{\parallel} e^{2k_1^{(2)} z} \times \\ &\times g(|k_{\parallel} - k_{\parallel}^{(0)}|) \frac{k_x}{k_{\parallel}^2} \left\{ \frac{k_y^2}{|k_1 - \epsilon(\omega)k_z|^2} \left[\frac{c^4}{\omega^4} [k_{\parallel}^2 + \operatorname{Re}(k_1^2)] |k_z|^2 - \right. \right. \\ &\left. \left. - 2 \frac{c^2}{\omega^2} k_1^{(2)} \operatorname{Re} \left(i k_z^* \frac{k_1 - \epsilon(\omega)k_z}{k_1 - k_z} \right) \right] + \frac{k_x^2}{|k_1 - k_z|^2} \right\} \quad (3.23) \end{aligned}$$

$$\operatorname{Re} \langle S_y(z) \rangle_s = 0 \quad (3.24)$$

Sec. F

$$\begin{aligned} \text{Re}\langle S_z(z) \rangle_S &= \delta^2 \frac{\omega^3 |\epsilon(\omega) - 1|^2}{8\pi^3 c^2} \frac{k_z^{(0)2} |E_y^{(1)}|^2}{|k_z^{(1)} - k_z^{(0)}|^2} \int d^2 k_{\parallel} e^{2k_1^{(2)} z} \times \\ &\times g(|k_{\parallel} - k_{\parallel}^{(0)}|) \frac{k_1^{(1)}}{k_{\parallel}^2} \left\{ \frac{c^4}{\omega^4} \frac{(k_{\parallel}^2 + |k_1|^2) k_y^2 |k_z|^2}{|k_1 - \epsilon(\omega) k_z|^2} + \frac{k_x^2}{|k_1 - k_z|^2} \right\}. \quad (3.25) \end{aligned}$$

The vanishing of $\text{Re}\langle S_y(z) \rangle_S$ is due to the fact that the integrand of the expression for it is an odd function of k_y .

We can simplify Eqs. (3.23) - (3.25) by going to polar coordinates and setting

$$k_x = k_{\parallel} \cos \varphi_S, \quad k_y = k_{\parallel} \sin \varphi_S. \quad (3.26)$$

In this way we obtain

$$\begin{aligned} \text{Re}\langle S_x(z) \rangle_S &= \delta^2 \frac{\omega^3 |\epsilon(\omega) - 1|^2}{8\pi^3 c^2} \cos^2 \theta_0 \frac{|E_y^{(1)}|^2}{|k_z^{(1)} - k_z^{(0)}|^2} \int d^2 k_{\parallel} e^{2k_1^{(2)} z} \times \\ &\times g(|k_{\parallel} - k_{\parallel}^{(0)}|) k_{\parallel} \cos \varphi_S \left\{ \frac{c^2}{\omega^2} \frac{\sin^2 \varphi_S}{|k_1 - \epsilon(\omega) k_z|^2} \left[(k_{\parallel}^2 + |k_1|^2) |k_z|^2 - \right. \right. \\ &\left. \left. - 2k_1^{(2)} k_z^{(2)} k_{\parallel}^2 \theta(k_{\parallel}^2 - \frac{\omega^2}{c^2}) \right] + \frac{\omega^2}{c^2} \frac{\cos^2 \varphi_S}{|k_1 - k_z|^2} \right\} \quad (3.27) \end{aligned}$$

Sec. F

$$\begin{aligned} \text{Re}\langle S_z(z) \rangle_s &= \delta^2 \frac{\omega^3 |\epsilon(\omega) - 1|^2}{8\pi^3 c^2} \cos^2 \theta_0 \frac{|E_y^{(1)}|^2}{|k_z^{(1)} - k_z^{(0)}|^2} \int d^2 k_{\parallel} e^{2k_1^{(2)} z} \times \\ &\times g(|k_{\parallel} - k_{\parallel}^{(0)}|) k_1^{(1)} \left\{ \frac{c^2}{\omega^2} \sin^2 \varphi_s \frac{(k_{\parallel}^2 + |k_1|^2) |k_z|^2}{|k_1 - \epsilon(\omega) k_z|^2} + \frac{\omega^2}{c^2} \frac{\cos^2 \varphi_s}{|k_1 - k_z|^2} \right\}. \end{aligned} \quad (3.28)$$

In Eq. (3.27), $k_z^{(2)} = (k_{\parallel}^2 - (\omega^2/c^2))^{\frac{1}{2}}$, and the term in which it appears contributes only when $k_{\parallel}^2 > (\omega^2/c^2)$, as the presence of the Heaviside unit step function indicates.

Turning now to the case of p-polarized incident light we find that

$$\begin{aligned} \text{Re}\langle S_x(z) \rangle_p &= \delta^2 \frac{\omega^3 |\epsilon(\omega) - 1|^2}{8\pi^3 c^2} \frac{|E_x^{(1)}|^2}{|k_z^{(1)} - \epsilon(\omega) k_z^{(0)}|^2} \int d^2 k_{\parallel} e^{2k_1^{(2)} z} \times \\ &\times g(|k_{\parallel} - k_{\parallel}^{(0)}|) \frac{1}{k_{\parallel}} \left\{ \frac{1}{|k_1 - \epsilon(\omega) k_z|^2} \left[\frac{c^4}{\omega^4} (k_{\parallel}^2 + \text{Re}(k_1^2)) k_x \times \right. \right. \\ &\times |k_x k_z k_z^{(1)} - \frac{1}{2} k^{(0)} k_{\parallel}^2 (\epsilon(\omega) + \epsilon^{-1}(\omega))|^2 + 2 \frac{c^2}{\omega^2} k_y^2 k_1^{(2)} \times \\ &\times \left. \left. \text{Re} \left(i k_z^{(1)} \frac{k_1 - \epsilon(\omega) k_z}{k_1 - k_z} (k_x k_z^* k_z^{(1)*} - \frac{1}{2} k^{(0)} k_{\parallel}^2 (\epsilon^*(\omega) + \epsilon^{-1}(\omega)^*)) \right) \right] + \right. \\ &\left. + \frac{k_x k_y^2 |k_z^{(1)}|^2}{|k_1 - k_z|^2} \right\} \end{aligned} \quad (3.29)$$

$$\text{Re}\langle S_y(z) \rangle_p = 0 \quad (3.30)$$

Sec. F

$$\begin{aligned}
 \text{Re}\langle S_z(z) \rangle_p = & \delta^2 \frac{\omega^3 |\epsilon(\omega) - 1|^2}{8\pi^3 c^2} \frac{|E_x^{(1)}|^2}{|k_z^{(1)} - \epsilon(\omega)k_z^{(0)}|^2} \int d^2 k_{\parallel} e^{2k_1^{(2)}z} \times \\
 & \times g(|\tilde{k}_{\parallel} - \tilde{k}_{\parallel}^{(0)}|) \frac{k_1^{(1)}}{k_{\parallel}^2} \left\{ \frac{c^4}{\omega^4} (k_{\parallel}^2 + |k_1|^2) \frac{|k_x k_z k_z^{(1)} - \frac{1}{2}k^{(0)} k_{\parallel}^2 (\epsilon(\omega) + \epsilon^{-1}(\omega))|^2}{|k_1 - \epsilon(\omega)k_z|^2} + \right. \\
 & \left. + \frac{k_y^2 |k_z^{(1)}|^2}{|k_1 - k_z|^2} \right\} . \quad (3.31)
 \end{aligned}$$

The function $\text{Re}\langle S_y(z) \rangle_p$ vanishes for this geometry also, because the integrand in the expression for it is an odd function of k_y .

We have recorded here the expression for $\text{Re}\langle S_x(z) \rangle_p$ associated with p-polarized incident radiation for completeness. However, in what follows we will consider explicitly only the component $\text{Re}\langle S_z(z) \rangle_p$ induced by p-polarized incident radiation. With the use of Eqs. (3.26) we can write it as

$$\begin{aligned}
 \text{Re}\langle S_z(z) \rangle_p = & \delta^2 \frac{\omega^3 |\epsilon(\omega) - 1|^2}{32\pi^3 c^2} \frac{|E_x^{(1)}|^2}{|k_z^{(1)} - \epsilon(\omega)k_z^{(0)}|^2} \times \\
 & \times \left\{ 4 \frac{c^2}{\omega^2} |k_z^{(1)}|^2 \int d^2 k_{\parallel} e^{2k_1^{(2)}z} g(|\tilde{k}_{\parallel} - \tilde{k}_{\parallel}^{(0)}|) k_1^{(1)} \right. \\
 & \times \left[\frac{c^2}{\omega^2} \cos^2 \varphi_s \frac{(k_{\parallel}^2 + |k_1|^2) |k_z|^2}{|k_1 - \epsilon(\omega)k_z|^2} + \frac{\omega^2}{c^2} \frac{\sin^2 \varphi_s}{|k_1 - k_z|^2} \right] + \frac{c^2}{\omega^2} \sin^2 \theta_o |\epsilon(\omega) + 1|
 \end{aligned}$$

Sec. F

$$\begin{aligned}
& + \epsilon^{-1}(\omega) \left| \int d^2 k_{\parallel} e^{2k_1^{(2)} z} g(|\tilde{k}_{\parallel} - k_{\parallel}^{(0)}|) \frac{(k_{\parallel}^2 + |k_1|^2) k_{\parallel}^2 k_1^{(1)}}{|k_1 - \epsilon(\omega) k_z|^2} - \right. \\
& - 4 \frac{c^3}{\omega^3} \sin \theta_0 \int d^2 k_{\parallel} e^{2k_1^{(2)} z} g(|\tilde{k}_{\parallel} - k_{\parallel}^{(0)}|) \frac{(k_{\parallel}^2 + |k_1|^2) k_{\parallel} k_1^{(1)}}{|k_1 - \epsilon(\omega) k_z|^2} \times \\
& \times \cos \varphi_s \operatorname{Re} \left(k_z^* k_z^{(1)*} (\epsilon(\omega) + \epsilon^{-1}(\omega)) \right) \Big\} . \quad (3.32)
\end{aligned}$$

Having obtained the real part of the complex Poynting vector, averaged over the surface roughness, inside the medium, for both s- and p-polarized incident radiation, we now turn to a discussion of the physical significance of these quantities.

Let us denote by P_0 the energy incident per unit time on unit area of the surface. Explicit expressions for this quantity are given by Eqs. (2.65) and (2.66), for s- and p-polarized incident radiation, respectively. We then define the vector $\tilde{S}(z)$ by

$$\tilde{S}(z) = \frac{1}{P_0} \operatorname{Re} \langle \tilde{S}(z) \rangle , \quad (3.33)$$

where it should be kept in mind that in this section z is negative.

The z -component of the Poynting vector gives the energy crossing unit area perpendicular to the z -axis per unit time. To obtain the portion of the incident flux entering the medium

we clearly require the z-component of the Poynting vector evaluated at $z = 0^-$. If the incident beam strikes a rectangular area of the surface of linear dimensions L_x and L_y , then the total energy carried into the medium per unit time by the scattered waves is

$$\frac{dE_z}{dt} = S_z(0^-) E_0 \quad (3.34)$$

where

$$E_0 = L_x L_y P_0 \quad (3.35)$$

is the energy per unit time that strikes the area $L_x L_y$. Thus if we denote by f_z the fraction of the energy carried off by the scattered waves in the direction of the normal to the surface, we have

$$f_z = S_z(0^-) \quad (3.36)$$

Combining Eqs. (3.28) and (2.65) and Eqs. (3.32) and (2.66) according to Eqs. (3.33) and (3.36), we find that this fraction f_z is given by

$$f_z^{(s)} = \delta^2 \frac{\omega^3 |\epsilon(\omega) - 1|^2}{\pi^2 c^3} \frac{\cos \theta_0}{|k_z^{(1)} - k_z^{(0)}|^2} \int d^2 k_{\parallel} g(|\tilde{k}_{\parallel} - \tilde{k}_{\parallel}^{(0)}|) k_1^{(1)} \times$$

$$\times \left\{ \frac{c^2}{\omega^2} \sin^2 \varphi_s \frac{(k_{\parallel}^2 + |k_1|^2) |k_z|^2}{|k_1 - \epsilon(\omega) k_z|^2} + \frac{\omega^2}{c^2} \frac{\cos^2 \varphi_s}{|k_1 - k_z|^2} \right\} \quad (3.37)$$

Sec. F

for s-polarized incident radiation, and

$$\begin{aligned}
 f_z^{(p)} = & \delta^2 \frac{\omega^3 |\epsilon(\omega) - 1|^2}{4\pi^2 c^3} \frac{\cos \theta_o}{|k_z^{(1)} - \epsilon(\omega) k_z^{(0)}|^2} \left\{ 4 \frac{c^2}{\omega^2} |k_z^{(1)}|^2 \int d^2 k_{\parallel} \times \right. \\
 & \times g(|k_{\parallel} - k_{\parallel}^{(0)}|) k_1^{(1)} \left[\frac{c^2}{\omega^2} \cos^2 \varphi_s \frac{(k_{\parallel}^2 + |k_1|^2) |k_z|^2}{|k_1 - \epsilon(\omega) k_z|^2} + \frac{\omega^2}{c^2} \frac{\sin^2 \varphi_s}{|k_1 - k_z|^2} \right] + \\
 & + \frac{c^2}{\omega^2} \sin^2 \theta_o |\epsilon(\omega) + \epsilon^{-1}(\omega)|^2 \int d^2 k_{\parallel} g(|k_{\parallel} - k_{\parallel}^{(0)}|) \frac{(k_{\parallel}^2 + |k_1|^2) k_{\parallel}^2 k_1^{(1)}}{|k_1 - \epsilon(\omega) k_z|^2} - \\
 & - 4 \frac{c^3}{\omega^3} \sin \theta_o \int d^2 k_{\parallel} g(|k_{\parallel} - k_{\parallel}^{(0)}|) \frac{(k_{\parallel}^2 + |k_1|^2) k_{\parallel} k_1^{(1)}}{|k_1 - \epsilon(\omega) k_z|^2} \cos \varphi_s \times \\
 & \times \operatorname{Re} \left(k_z^* k_z^{(1)*} (\epsilon(\omega) + \epsilon^{-1}(\omega)) \right) \Big\} , \tag{3.38}
 \end{aligned}$$

for p-polarized incident radiation.

Turning now to the x-component of the Poynting vector, and consequently of the vector $\underline{S}(z)$, we see that $\operatorname{Re} \langle S_x(z) \rangle$ gives the energy traveling parallel to the surface which crosses unit area at a depth z per unit time. The total energy per unit time carried by the wave is therefore

$$\frac{dE_x}{dt} = L_{y_{-z}} \int_0^{\infty} dz \operatorname{Re} \langle S_x(z) \rangle = L_y P_{Q_{-z}} \int_0^{\infty} dz S_x(z) . \tag{3.39}$$

We divide this expression by E_0 to obtain the fraction f_x of the incident energy absorbed by the medium and carried off in the x -direction,

$$f_x = \frac{1}{L_x} \int_{-b}^0 dz S_x(z) \quad (3.40)$$

Thus the quantity $S_x(z)$ itself has no direct physical meaning. The physically meaningful quantity is f_x , which is obtained from $S_x(z)$. Combining Eqs. (3.27) and (2.65) with Eq. (3.40), we find for f_x the result

$$f_x^{(s)} = \frac{\delta^2}{L_x} \frac{\omega^3 |\epsilon(\omega) - 1|^2}{\pi^2 c^3} \frac{\cos \theta_0}{|k_z^{(1)} - k_z^{(0)}|^2} \int d^2 k_{\parallel} g(|k_{\parallel} - k_{\parallel}^{(0)}|) \frac{k_{\parallel} \cos \varphi_s}{2k_1^{(2)}} \times$$

$$\times \left\{ \frac{c^2}{\omega^2} \frac{\sin^2 \varphi_s}{|k_1 - \epsilon(\omega)k_z|^2} \left[(k_{\parallel}^2 + |k_1|^2) |k_z|^2 - 2k_1^{(2)} k_z^{(2)} k_{\parallel}^2 \theta(k_{\parallel}^2 - \frac{\omega^2}{c^2}) \right] + \right.$$

$$\left. + \frac{\omega^2}{c^2} \frac{\cos^2 \varphi_s}{|k_1 - k_z|^2} \right\} \quad (3.41)$$

for s -polarized incident radiation.

The numerical evaluation of the results of this and the preceding section will be carried out in the following two sections.

IV. The Contribution to the Roughness Induced Absorption from Coupling to Surface Polaritons

Many of the earlier theoretical studies ^(4.1) of the roughness-induced absorption confine their attention to the simple free electron metal, which is described by the dielectric constant $\epsilon(\omega) = 1 - \omega_p^2/\omega^2$. In the frequency region where $\epsilon(\omega) \leq -1$, surface polaritons may propagate along the interface between the crystal and the vacuum. ⁽⁸⁾ The waves are described by the dispersion relation

$$\frac{c^2 k_{\parallel}^2}{\omega^2} = \frac{\epsilon(\omega)}{\epsilon(\omega) + 1} \quad (4.1)$$

Notice that for the surface polariton $ck_{\parallel} > \omega$, a condition that must be satisfied if the surface wave is not to radiate its energy into the vacuum. Then in some of the earlier papers, the roughness induced absorption is presumed to arise from the roughness induced coupling of the incident wave to the surface polariton.

The purpose of the present section is to examine the general results of Section III when the real part $\epsilon^{(1)}(\omega)$ of the crystal is negative, and the imaginary part $\epsilon^{(2)}(\omega)$ is small. In this case, we find contributions to the absorption rate that may be identified with roughness induced coupling to surface polaritons. For small $\epsilon^{(2)}(\omega)$, we extract from the general expressions simple expressions for the contribution

described above. We do this for the cases of s and p-polarization at non-normal incidence. In Section V, we shall make a quantitative comparison between the results obtained in the present section, and numerical computations of the total absorption rate calculated from the general expressions given above. We do this for the case of aluminum metal, the material for which the approximate results should hold best. In their most recent paper⁽⁶⁾, Elson and Ritchie have carried out an analysis similar to the one presented here, although they confine their attention to the case of normal incidence, and they have not carried out numerical studies of the sort reported in Section V.

We begin with the general expression for the quantity $f_z^{(s)}$, the fraction of the energy of an incident wave with s-polarization absorbed by the roughness induced energy flow in the direction normal to the surface. We saw earlier that this quantity is given by

$$f_z^{(s)} = \text{Re} \langle S_z(o-) \rangle_s / P_o \quad (4.2a)$$

where

$$P_o = c |E_y^{(1)}|^2 \cos \theta_o / 8\pi \quad (4.2b)$$

We have the explicit form from Eq. (3.37):

Sec. F

$$f_z^{(s)} = \frac{\delta^2 \omega^3 |\epsilon(\omega) - 1|^2 \cos \theta_0}{\pi^2 c^3 |k_z^{(1)} - k_z^{(0)}|^2} \int d^2 k_{\parallel} g(|k_{\parallel} - k_{\parallel}^{(0)}|) k_1^{(1)} \times$$

$$\times \left\{ \frac{c^2}{\omega^2} \sin^2 \varphi_s \frac{(k_{\parallel}^2 + |k_1|^2) |k_z|^2}{|k_1 - \epsilon(\omega) k_z|^2} + \frac{\omega^2}{c^2} \frac{\cos^2 \varphi_s}{|k_1 - k_z|^2} \right\} \quad (4.3)$$

The first term in braces arises from scattering processes which transform the incident wave of s-polarization to a scattered wave with p-polarization, while the second term describes scattering of the initial wave into a scattered wave of s-polarization. It is the first term which contains a description of the roughness induced absorption by surface polaritons. This may be seen by noting that

$$\frac{1}{|k_1 - \epsilon(\omega) k_z|^2} = \frac{|k_1 + \epsilon(\omega) k_z|^2}{|k_1^2 - \epsilon^2(\omega) k_z^2|^2},$$

or after some small rearrangements,

$$\frac{1}{|k_1 - \epsilon(\omega) k_z|^2} = \frac{|k_1 + \epsilon(\omega) k_z|^2}{|\epsilon^2(\omega) - 1|^2} \frac{1}{|k_{\parallel}^2 - \frac{\omega^2}{c^2} \frac{\epsilon(\omega)}{\epsilon(\omega) + 1}|^2} \quad (4.4)$$

Thus, when the left hand side of Eq. (4.4) is considered as a function of k_{\parallel} , when $\epsilon^{(2)}(\omega)$ is small and $\epsilon^{(1)}(\omega)$ negative, a strong resonance at the surface plasmon wave vector (Eq. (4.1)) appears. We may obtain the contribution to $f_z^{(s)}$ from roughness induced coupling to surface polaritons by considering only the part that arises from this resonance. We proceed to obtain this portion in the limit $\epsilon^{(2)}(\omega) \rightarrow 0$, by replacing k_{\parallel} everywhere in slowly varying factors by the value

$$k_{sp} = \frac{\omega^2}{c^2} \frac{\epsilon^{(1)}(\omega)}{\epsilon^{(1)}(\omega) + 1} = \frac{\omega^2}{c^2} \frac{|\epsilon^{(1)}(\omega)|}{|\epsilon^{(1)}(\omega)| - 1}, \quad (4.5)$$

where, as the last step indicates, we confine our attention to frequency regions where $\epsilon^{(1)}(\omega) < 0$. With such an approximation applied to Eq. (4.4), one obtains

$$\frac{1}{|k_{\parallel} - \epsilon(\omega)k_z|^2} \cong \left(\frac{\omega}{c}\right)^2 \frac{4|\epsilon^{(1)}(\omega)|^2}{(|\epsilon^{(1)}(\omega)| - 1)^3 (|\epsilon^{(1)}(\omega)| + 1)^2} \frac{1}{|k_{\parallel}^2 - \frac{\omega^2}{c^2} \frac{\epsilon(\omega)}{\epsilon(\omega) + 1}|^2} \quad (4.6)$$

Notice also that when $\epsilon^{(2)}(\omega)$ is small and $\epsilon^{(1)}(\omega) < 0$,

Sec. F

$$k_1^{(1)} \cong - \frac{\omega^2}{2c^2} \frac{\epsilon^{(2)}(\omega)}{\left[k_{\parallel}^2 + \frac{\omega^2}{c^2} |\epsilon^{(1)}(\omega)| \right]^{\frac{1}{2}}}, \quad (4.7)$$

i.e. the quantity $k_1^{(1)}$ is proportional to $\epsilon^{(2)}(\omega)$ in this limit⁽⁹⁾.

When the approximations described above are carried out for all the factors in the appropriate term of Eq. (4.8), the results may be arranged to read (for small $\epsilon^{(2)}(\omega)$)

$$f_z^{(s)} = \frac{2\delta^2 \cos \theta_o}{\pi} \left(\frac{\omega}{c} \right)^6 \frac{|\epsilon^{(1)}(\omega)|^2}{\left(|\epsilon^{(1)}(\omega)| - 1 \right)^{9/2}} \epsilon^{(2)}(\omega) \times$$

$$\times \int_0^{2\pi} d\varphi_s \sin^2 \varphi_s g(|\hat{k}_{\parallel} k_{sp} - k_{\parallel}^{(o)}|) \int_0^{\infty} \frac{dk_{\parallel} k_{\parallel}}{|k_{\parallel}^2 - k_{sp}^2 - 1 \left(\frac{\omega}{c} \right)^2 \frac{\epsilon^{(2)}(\omega)}{(|\epsilon^{(1)}(\omega)| - 1)^2}|^2}.$$

(4.8)

To obtain this result, it is useful to note the identity (as $\epsilon^{(2)}(\omega) \rightarrow 0$ and with $\epsilon^{(1)}(\omega) < 0$)

$$|k_z^{(1)} - k_z^{(o)}|^2 = 1 + |\epsilon^{(1)}(\omega)|. \quad (4.9)$$

As $\epsilon^{(2)}(\omega) \rightarrow 0$, the integral over k_{\parallel} is readily evaluated to give the simple result

$$f_z^{(s)} = \left(\frac{\omega}{c}\right)^4 \delta^2 \cos \theta_0 \frac{|\epsilon^{(1)}(\omega)|^2}{(|\epsilon^{(1)}(\omega)|^2 - 1)^{5/2}} \int_0^{2\pi} \frac{d\varphi_s}{\pi} \sin^2 \varphi_s \times \\ \times g(|\tilde{k}_{\parallel} k_{sp} - \tilde{k}_{\parallel}^{(0)}|) . \quad (4.10)$$

At normal incidence, this result becomes equivalent to the result of Crowell and Ritchie⁽⁴⁾, who derived it through the use of quantum mechanical perturbation theory, and also with the recent results of Elson and Ritchie.⁽⁶⁾ It is interesting to note that in the classical theory, this contribution comes from a small "leak" of energy out of the surface polariton into the crystalline interior, due to the (assumed small) value of $\epsilon^{(2)}(\omega)$. This is evident from Eq. (4.7), where one sees that for each k_{\parallel} , the contribution to the time average of the Poynting vector in the direction normal to the crystal surface vanishes identically as $\epsilon^{(2)}(\omega) \rightarrow 0$. As we have seen, the integrated strength of all contributions to $f_z^{(s)}$ remains finite as $\epsilon^{(2)}(\omega) \rightarrow 0$.

We next examine the behavior of $f_x^{(s)}$, the fraction of the energy of the incident wave absorbed by the energy flow parallel to the surface. We shall find for $f_x^{(s)}$ a behavior that differs qualitatively from that of $f_z^{(s)}$, in the limit $\epsilon^{(2)}(\omega) \rightarrow 0$.

Sec. F

As explained earlier, if the incident beam illuminates a rectangular area of the surface with length L_x for the side parallel to the x axis and L_y for the side parallel to the y axis, then

$$f_x^{(s)} = \left(L_y \int_{-\infty}^0 dz \operatorname{Re} \langle S_x(z) \rangle \right) / (L_x L_y P_0) ,$$

where P_0 is given in Eq. (4.2b). Thus, we have

$$\begin{aligned} f_x^{(s)} = & \frac{\delta^2 \omega^3 |\epsilon(\omega) - 1|^2}{2\pi^2 c^3 L_x} \frac{\cos \theta_0}{|k_z^{(1)} - k_z^{(0)}|^2} \times \\ & \times \int \frac{d^2 k_{\parallel}}{k_1^{(2)}} g(|k_{\parallel} - k_{\parallel}^{(0)}|) k_{\parallel} \cos \varphi_s \left\{ \frac{c^2}{\omega^2} \frac{\sin^2 \varphi_s}{|k_1 - \epsilon(\omega) k_z|^2} \times \right. \\ & \times \left. \left[\left(k_{\parallel}^2 + |k_1|^2 \right) |k_z|^2 - 2k_1^{(2)} k_z^{(2)} k_{\parallel}^2 \theta \left(k_{\parallel}^2 - \frac{\omega^2}{c^2} \right) \right] + \frac{\omega^2}{c^2} \frac{\cos^2 \varphi_s}{|k_1 - k_z|^2} \right\} . \end{aligned} \quad (4.11)$$

As in the case of $f_z^{(s)}$, the term proportional to $|k_1 - \epsilon(\omega) k_z|^{-2}$ contains the contribution to the absorption that arises from the coupling of the incident wave to surface polaritons. We may proceed with the evaluation of $f_x^{(s)}$ exactly as before. We shall simply state the result as a consequence. However, before we do this, we make two general observations.

First, notice that $f_x^{(s)}$ is proportional to L_x^{-1} . The reason for this is that the incident wave illuminates a rectangular area of the surface with area $L_x L_y$, while the energy absorbed from the incident wave which flows parallel to the surface is carried in a small channel of dimensions $L_y \times$ (the skin depth). This is evident from the factor of $1/k_1^{(2)}$ in the integrand of Eq. (4.11). Because $f_x^{(s)}$ is inversely proportional to L_x , it will not appear in any calculation which assumes the incident wave to illuminate the whole surface, and then takes the limit as the surface area becomes infinite. Most of the quantum field theoretic treatments discussed in Section I fall into this class.

It is apparent also that in the limit as $\epsilon^{(2)}(\omega) \rightarrow 0$, the quantity $f_x^{(s)}$ will diverge as $\epsilon^{(2)}(\omega)^{-1}$. This is apparent at once because $k_{\parallel} \cos \varphi_s$ appears in Eq. (4.11) in place of the factor $k_1^{(1)}$ in Eq. (4.3). As we see from Eq. (4.7), as $\epsilon^{(2)}(\omega) \rightarrow 0$ (in a frequency region where $\epsilon^{(1)}(\omega) < 0$), the factor of $k_1^{(1)}$ introduces a factor of $\epsilon^{(2)}(\omega)$ into $f_z^{(s)}$, and as $\epsilon^{(2)}(\omega) \rightarrow 0$ this cancels the factor of $(\epsilon^{(2)}(\omega))^{-1}$ that arises from integration over the surface polariton resonance. We shall discuss the physical origin of the divergence below.

As remarked above, when $\epsilon^{(1)}(\omega) < 0$, and in the limit $\epsilon^{(2)}(\omega) \rightarrow 0$, one may evaluate the surface polariton contribution to $f_x^{(s)}$ exactly as before. Upon carrying out the calculation, we find

$$|f_x^{(s)}| = \frac{\delta^2 \omega^3 |\epsilon^{(1)}(\omega)|^{5/2} \cos \theta_0}{L_x c^3 (|\epsilon^{(1)}(\omega)| + 1) (|\epsilon^{(1)}(\omega)| - 1)^2} \frac{1}{\epsilon^{(2)}(\omega)} \times$$

$$\times \int_0^{2\pi} \frac{d\varphi_s}{\pi} \cos \varphi_s \sin^2 \varphi_s g(|\hat{k}_{\parallel} k_{sp} - \tilde{k}_{\parallel}^{(o)}|) \quad (4.12)$$

The physical meaning of this result becomes more apparent if we introduce the mean free path $\iota_{sp}(\omega)$ of the surface polariton. The mean free path is defined by

$$\frac{1}{\iota_{sp}(\omega)} = \Im(k_{\parallel}) \quad , \quad (4.13)$$

where $\Im(k_{\parallel})$ is the imaginary part of k_{\parallel} , calculated by inserting the complex dielectric constant in the right hand side of Eq. (4.1). As $\epsilon^{(2)}(\omega) \rightarrow 0$, and with $\epsilon^{(1)}(\omega)$ negative one has

$$\frac{1}{\iota_{sp}(\omega)} = \frac{\omega}{zc} \frac{\epsilon^{(2)}(\omega)}{|\epsilon^{(1)}(\omega)|^{1/2} (|\epsilon^{(1)}(\omega)| - 1)^{3/4}} \quad , \quad (4.14)$$

so that we have

$$|f_x^{(s)}| = \frac{\delta^2 \omega^4}{2c^4} \frac{|\epsilon^{(1)}(\omega)|^2 \cos \theta_0}{(|\epsilon^{(1)}(\omega)| + 1) (|\epsilon^{(1)}(\omega)| - 1)^{7/2}} \frac{\iota_{sp}(\omega)}{L_x}$$

$$\times \int_0^{2\pi} \frac{d\varphi_s}{\pi} \cos \varphi_s \sin^2 \varphi_s g(|\hat{k}_{\parallel} k_{sp} - \tilde{k}_{\parallel}^{(o)}|) \quad . \quad (4.15)$$

At normal incidence, $\tilde{k}_{\parallel}^{(o)} = 0$, and the angular integral on the right hand side of Eq. (4.15) vanishes.

The physical interpretation of the result in Eq. (4.15) is the following. The incident wave has frequency ω that matches that of a surface polariton (when $\epsilon^{(1)}(\omega) < 0$ as assumed here), but its wave vector component $k_{\parallel}^{(o)}$ in the plane of the surface does not, since necessarily $ck_{\parallel}^{(o)} < \omega$, while for surface polaritons $ck_{\parallel}^{(o)} > \omega$, as remarked above. The effect of the surface roughness is to mix into the incident wave a broad spectrum of spatial Fourier components k_{\parallel} , and the electric field at each k_{\parallel} oscillates with frequency ω . There is thus in the scattered field a component which matches both the frequency of the surface polariton and its wave vector, the latter computed from Eq. (4.1) with $\epsilon(\omega)$ replaced by $\epsilon^{(1)}(\omega)$. Thus, in the language of non-linear optics, the surface roughness induced interaction between the incident wave and the surface polariton is phase-matched. For the incident wave, k_{\parallel} is purely real, while the surface polariton has the finite mean free path $l_{sp}(\omega)$ parallel to the surface. Thus, the surface polariton mean free path $l_{sp}(\omega)$ plays the role of the coherence length of the phase-matched interaction, and the energy stored in the driven surface polariton is proportional to the coherence length.

We can see from the discussion of the preceding paragraph that the result displayed in Eq. (4.15) is valid only in one limit (which in many circumstances is the one relevant to experimental situations). If $\epsilon^{(2)}(\omega)$ is so small, or the incident beam so well focused, that $l_{sp}(\omega) > L_x$, then quite clearly the coherence length of the phase matched interaction becomes L_x .

Sec. F

rather than $\ell_{sp}(\omega)$. In our discussions, we have implicitly assumed L_x and L_y are both very large, and integrations over spatial coordinates parallel to the surface have been freely extended to $\pm \infty$. Had they been kept finite, then we would have found Eq. (4.15) valid only when $\ell_{sp}(\omega) < L_x$, and when $\ell_{sp}(\omega) > L_x$, the factor $\ell_{sp}(\omega)/L_x$ would have been replaced by unity. Throughout the visible range of frequencies and into the ultraviolet, $\epsilon^{(2)}(\omega)$ is large enough that the condition $\ell_{sp}(\omega) < L_x$ should be satisfied, unless the beam is focused very sharply. However, in the infrared, it has been demonstrated that $\ell_{sp}(\omega)$ can become very large⁽¹⁰⁾, and the limit $\ell_{sp}(\omega) > L_x$ may be appropriate most commonly here.

Notice that when $\ell_{sp}(\omega) > L_x$, $|f_x^{(s)}|$ and $f_z^{(s)}$ become comparable in magnitude, so both components of the Poynting vector must be considered when the total surface roughness induced absorption is calculated. When $\ell_{sp}(\omega) \ll L_x$, then $|f_x^{(s)}|$ is small in magnitude. However, the energy density stored in the surface polariton can be very large when $\epsilon^{(2)}(\omega)$ is small and this may lead to a number of physical effects, such as the diffuse scattering of the incident radiation through the surface polariton as an intermediate state, a phenomenon observed in a number of experiments⁽¹¹⁾. This question, along with related problems, is currently under investigation.

The discussion presented above is confined entirely to the case of s-polarized incident radiation. We conclude this section by stating the expression for the contribution from surface

Sec. F

polaritons to $f_z^{(p)}$, the fraction of the energy absorbed from the incident wave due to surface roughness that comes about because of the presence of $\langle S_z \rangle$. When $l_{sp}(\omega) \ll L_x$, this is the dominant contribution to the roughness induced absorption, as in the case of s-polarization.

We find, after a series of manipulations very similar to those above, that the surface polariton contribution to $f_z^{(p)}$ is

$$f_z^{(p)} = \delta^2 \left(\frac{\omega}{c} \right)^4 \frac{|\epsilon^{(1)}(\omega)| \cos \theta_o}{[|\epsilon^{(1)}(\omega)| \cos^2 \theta_o + \sin^2 \theta_o]} \frac{1}{[|\epsilon^{(1)}(\omega)| - 1]^{5/2}} \times$$

$$\times \int_0^{2\pi} \frac{d\varphi_s}{\pi} g(|\hat{k}_{\parallel} k_{sp} - k_{\parallel}^{(o)}|) \left[\cos \varphi_s (|\epsilon^{(1)}(\omega)|^2 + |\epsilon^{(1)}(\omega)| \sin^2 \theta_o)^{1/2} - \right.$$

$$\left. - \frac{1}{2} (1 + |\epsilon^{(1)}(\omega)|^2) \sin \theta_o \right]^2 . \quad (4.16)$$

V. Numerical Studies of Roughness Induced Scattering and Absorption

In this section, we explore the predictions of the results derived in Sections II - IV. The purpose of the calculations is to explore the dependence of the roughness induced scattering on the polarization of the incident wave, on polarization at normal incidence, and to test the accuracy of the simple results given by Eqs. (4.10) and (4.16) against the predictions for aluminum, both because it is the material which most closely approximates the nearly free electron metal for which one would expect Eqs. (4.10) and (4.16) to be valid, and because one can prepare films of this material with well characterized surface roughness. We refer the reader to the very complete study of aluminum films carried out by Endriz and Spicer as an example of such studies⁽¹²⁾.

In the numerical calculations reported below, we have presumed a gaussian distribution function for the surface roughness correlation function. More specifically, the correlation function $\langle \zeta(\underline{x}_{\parallel}) \zeta(\underline{0}) \rangle$ is related to the quantity $g(\underline{Q}_{\parallel})$ introduced in the preceding section in the following manner,

$$\langle \zeta(\underline{x}_{\parallel}) \zeta(\underline{0}) \rangle = \delta^2 \int \frac{d^2 Q_{\parallel}}{(2\pi)^2} g(\underline{Q}_{\parallel}) e^{i \underline{Q}_{\parallel} \cdot \underline{x}_{\parallel}} , \quad (5.1)$$

where if $g(\underline{Q}_{\parallel})$ is normalized so that

$$\int \frac{d^2 Q_{\parallel}}{(2\pi)^2} g(Q_{\parallel}) = 1 \quad , \quad (5.2)$$

then $\langle \zeta^2(\underline{Q}) \rangle = \langle \zeta^2 \rangle = \delta^2$, so the parameter δ is then the rms height of the surface roughness. In the calculations reported below, we have used a gaussian for $g(Q_{\parallel})$:

$$g(Q_{\parallel}) = \pi a^2 \exp \left(- \frac{a^2}{4} Q_{\parallel}^2 \right) \quad , \quad (5.3)$$

where a is a transverse correlation length. With this form of $g(Q_{\parallel})$, one finds

$$\langle \zeta(\underline{x}_{\parallel}) \zeta(\underline{Q}) \rangle = \delta^2 \exp \left(- x_{\parallel}^2 / a^2 \right) \quad . \quad (5.4)$$

The gaussian form for $g(Q_{\parallel})$ has the virtue that all the integrations over φ_s may be performed analytically, and expressed in terms of the modified Bessel functions $I_n(x)$. Thus, the numerical calculations involve only a single integration over θ_s in the case of the scattering calculation, or k_{\parallel} for the case of the absorption calculations. In our numerical calculations, we have chosen 500\AA as the value of the transverse correlation length a which enters $g(Q_{\parallel})$. The real and imaginary parts of $\epsilon(\omega)$ have been extracted from the analysis of the optical properties of aluminum by Ehrenreich, Philipp and Segall⁽¹³⁾.

Sec. F

We first consider the behavior of the roughness induced scattering of light from aluminum. If we let $f(s)$ and $f(p)$ denote the fraction of the energy scattered away from an incident wave of s and p polarization respectively, then we write

$$f(s) = f(s \rightarrow s) + f(s \rightarrow p) \quad (5.5a)$$

and

$$f(p) = f(p \rightarrow s) + f(p \rightarrow p) \quad (5.5b)$$

where $f(i \rightarrow j)$ denotes the fraction of the energy of the incident wave of polarization i scattered into the final state of polarization j . Of course,

$$f(i \rightarrow j) = \int d\Omega_s \frac{df(i \rightarrow j)}{d\Omega_s}, \quad (5.6)$$

where the integration is over solid angle with $0 \leq \theta_s \leq \pi/2$, and the $df(i \rightarrow j)/d\Omega_s$ are the differential scattering cross sections presented in Eqs. (2.69) - (2.72).

To present the results, it is useful to introduce dimensionless quantities $R(i \rightarrow j)$ related to the $f(i \rightarrow j)$ of Eq. (5.5) as follows:

$$f(i \rightarrow j) = 6^2 a^2 \left(\frac{\omega}{c}\right)^4 R(i \rightarrow j) \quad (5.6)$$

In Fig. 2, we show the variation with angle of incidence of the two functions $R(s \rightarrow s)$ and $R(s \rightarrow p)$, for a photon of energy 7eV incident on aluminum. The two functions are comparable in magnitude, and they both fall off smoothly and monotonically with angle of incidence.

In Fig. 3, we show the behavior of $R(p \rightarrow s)$ and $R(p \rightarrow p)$ again for $\hbar\omega = 7\text{eV}$ on aluminum. The behavior of $R(p \rightarrow p)$ is quite striking, since it exhibits the pronounced broad maximum centered about $\theta_0 \approx 50^\circ$.

In Fig. 4, we illustrate the variation with angle of incidence of the total reduced scattering efficiencies $R(s)$ and $R(p)$, defined by

$$R(s) = R(s \rightarrow s) + R(s \rightarrow p)$$

and

$$R(p) = R(p \rightarrow s) + R(p \rightarrow p) \quad .$$

The broad shoulder in $R(p)$ reflects the off-center maximum in $R(p \rightarrow p)$ illustrated in Fig. 3.

In Fig. 5, we show the variation of $R(s)$ with frequency, for three angles of incidence. The fact that $R(s)$ decreases substantially as ω increases means that the total scattering efficiency varies with frequency considerably more slowly than ω^4 . Of course, this comes about because $\epsilon(\omega)$ is strongly dependent on frequency in this region. Notice that at normal

incidence, $R(s)$ displays a feature at the bulk plasma frequency ω_p where $\epsilon^{(1)}(\omega) = 0$. This feature becomes small by the time $\theta_0 = 40^\circ$.

We next turn our attention to the roughness induced absorption cross section. We introduce dimensionless measures of the absorption rate A_{ij} similar to those employed in the scattering calculations through the relations

$$f_z^{(s)} = \delta^2 a^2 \left(\frac{\omega}{c} \right)^4 [A_{sp} + A_{ss}] \quad (5.7a)$$

and

$$f_z^{(p)} = \delta^2 a^2 \left(\frac{\omega}{c} \right)^4 [A_{ps} + A_{pp}] \quad (5.7b)$$

The function A_{ij} is a dimensionless measure of the contribution to the rate of absorption of radiation of polarization i through roughness induced coupling to final states of polarization j . In the general expression for $f_z^{(s)}$, A_{sp} comes from the contributions proportional to $\sin^2 \varphi_s$ while A_{ss} comes from those proportional to $\cos^2 \varphi_s$. In $f_z^{(p)}$, A_{ps} arises from the portion proportional to $\sin^2 \varphi_s$ and A_{pp} from the remainder.

In Fig. 6, we show the angular variation of A_{sp} and A_{pp} , for the case where $\hbar\omega = 7\text{eV}$. Note the similarity in the dependence on angle of incidence to the variation with θ_0 of the reduced scattering cross sections R_{sp} and R_{pp} . The solid lines in the figure are obtained by fully evaluating the integrals numerically,

and the dashed lines have been calculated from the approximate expressions presented in Eqs. (4.10) and (4.16). The agreement between the analytical approximation and the full calculation is remarkably good at 7eV although for reasons discussed below, we will see it is less good at both lower and higher photon energies. At 7eV, we find both A_{ss} and A_{ps} are quite small, of the order of two or three percent of A_{sp} and A_{pp} at all angles of incidence.

In Fig. 7, we present calculations similar to those in Fig. 6 for $\hbar\omega = 9\text{eV}$. The agreement between the analytic approximation and the full calculations is now less good than that at 7eV. We believe that the reason why this is so is apparent from the form of the integral over k_{\parallel} in Eq. (4.8). One sees that the width of the resonance in the integral scales as $\epsilon^{(2)}(\omega)/[|\epsilon^{(1)}(\omega)| - 1]^2$. As ω increases, $|\epsilon^{(1)}(\omega)|$ decreases until at $\approx 10.6\text{eV}$, the surface plasmon energy in aluminum, $|\epsilon^{(1)}(\omega)|$ approaches unity. Thus, even though $\epsilon^{(2)}(\omega)$ may be small, as ω increases the simple Lorentzian approximation to the structure of the integrand in the full expression for A_{ip} becomes less good. At 9eV, both A_{ss} and A_{ps} remain a very small fraction of the total absorption rate.

In Fig. 8, we present the frequency dependence of the various contributions to the roughness induced absorption rate, for the case of normal incidence. The results of the numerical calculations are shown as full lines, and the analytic approximation as a dashed line. The roughness induced absorption rate falls off

dramatically as one passes through the surface plasmon frequency at 10.6 eV, and one can see that while the analytic approximation represents the trend well, the agreement with the full calculations is semi-quantitative, with discrepancies of up to 50% in the range of energies displayed in Fig. 7. Note particularly that the analytic approximation falls below the full curves below 7eV. We ascribe this to the fact that at these lower energies, roughness induced absorption by free particle-hole pairs becomes a significant fraction of the total, so the picture which assigns all the absorption to roughness induced coupling to surface polaritons underestimates the total roughness induced absorption. In the figure, the importance of roughness induced coupling to single particle excitations is illustrated by the fact that A_{ss} now contributes to the absorption rate significantly, while above 7eV it represents a very small fraction of the total.

These calculations suggest that while the simple analytic expressions in Eqs. (4.10) and (4.16) provide reasonable semi-quantitative estimates of the roughness induced absorption rates, attempts to provide quantitative contact between theory and experiment should proceed with the use of the full expressions. In this regard, the calculations presented here should place the analytic approximations in a most favorable light, since aluminum is the metal most accurately approximated by the free electron model.

Appendix

In this Appendix we outline the derivation of the elements of the Green's function tensor $D_{\mu\nu}(\underline{x}, \underline{x}'; \omega)$, which is the solution of the equation

$$\sum_{\mu} \left\{ \epsilon_0(z; \omega) \frac{\omega^2}{c^2} \delta_{\lambda\mu} - \frac{\partial^2}{\partial x_{\lambda} \partial x_{\mu}} + \delta_{\lambda\mu} \nabla^2 \right\} D_{\mu\nu}(\underline{x}, \underline{x}'; \omega) = 4\pi \delta_{\lambda\nu} \delta(\underline{x} - \underline{x}'), \quad (\text{A.1})$$

where

$$\begin{aligned} \epsilon_0(z; \omega) &= 1 & z > 0 \\ &= \epsilon(\omega) & z < 0, \end{aligned} \quad (\text{A.2})$$

together with boundary conditions which will be specified below.

We begin by Fourier analyzing $D_{\mu\nu}(\underline{x}, \underline{x}'; \omega)$ and $\delta(\underline{x} - \underline{x}')$ according to

$$D_{\mu\nu}(\underline{x}, \underline{x}'; \omega) = \int \frac{d^2 k_{\parallel}}{(2\pi)^2} e^{i k_{\parallel} \cdot (\underline{x}_{\parallel} - \underline{x}'_{\parallel})} d_{\mu\nu}(k_{\parallel} | z z') \quad (\text{A.3})$$

$$\delta(\underline{x} - \underline{x}') = \delta(z - z') \int \frac{d^2 k_{\parallel}}{(2\pi)^2} e^{i k_{\parallel} \cdot (\underline{x}_{\parallel} - \underline{x}'_{\parallel})} \quad (\text{A.4})$$

where $\underline{k}_{\parallel}$ and $\underline{x}_{\parallel}$ are two-dimensional vectors given by $(k_x, k_y, 0)$ and $(x, y, 0)$, respectively. The decomposition (A.3) reflects the fact that the system for which the Green's function $D_{\mu\nu}(\underline{x}, \underline{x}'; \omega)$ is being sought retains infinitesimal translational invariance in

the x- and y-directions, even if it has lost it in the z-direction. Substitution of Eqs. (A.3) and (A.4) into Eq. (A.1) yields the following set of differential equations for the Fourier coefficients $d_{\mu\nu}(k_{\parallel}\omega|zz')$:

$$\begin{pmatrix} (\epsilon_0 \frac{\omega^2}{c^2} - k_y^2 + \frac{d^2}{dz^2}) & k_x k_y & -ik_x \frac{d}{dz} \\ k_x k_y & (\epsilon_0 \frac{\omega^2}{c^2} - k_x^2 + \frac{d^2}{dz^2}) & -ik_y \frac{d}{dz} \\ -ik_x \frac{d}{dz} & -ik_y \frac{d}{dz} & (\epsilon_0 \frac{\omega^2}{c^2} - k_{\parallel}^2) \end{pmatrix} \begin{pmatrix} d_{xx} & d_{xy} & d_{xz} \\ d_{yx} & d_{yy} & d_{yz} \\ d_{zx} & d_{zy} & d_{zz} \end{pmatrix} = 4\pi \delta(z - z') \begin{pmatrix} 1 & 0 & 0 \\ 0 & 1 & 0 \\ 0 & 0 & 1 \end{pmatrix}. \quad (A.5)$$

At this point it is convenient to exploit the isotropy of our system in the xy-plane by pre-multiplying and post-multiplying Eq. (A.5) by the matrices $\tilde{S}(k_{\parallel})$ and $\tilde{S}^{-1}(k_{\parallel})$, respectively, where

$$\tilde{S}(k_{\parallel}) = \frac{1}{k_{\parallel}} \begin{pmatrix} k_x & k_y & 0 \\ -k_y & k_x & 0 \\ 0 & 0 & k_{\parallel} \end{pmatrix}, \quad \tilde{S}^{-1}(k_{\parallel}) = \frac{1}{k_{\parallel}} \begin{pmatrix} k_x & -k_y & 0 \\ k_y & k_x & 0 \\ 0 & 0 & k_{\parallel} \end{pmatrix}. \quad (A.6)$$

(The matrix $\tilde{S}(k_{\parallel})$ is recognized as the matrix which rotates the vector $(k_x, k_y, 0)$ into the vector $(k_{\parallel}, 0, 0)$.) The result of this transformation is the simpler equation

$$\begin{pmatrix} \epsilon_0 \frac{\omega^2}{c^2} + \frac{d^2}{dz^2} & 0 & -ik_{\parallel} \frac{d}{dz} \\ 0 & \epsilon_0 \frac{\omega^2}{c^2} - k_{\parallel}^2 + \frac{d^2}{dz^2} & 0 \\ -ik_{\parallel} \frac{d}{dz} & 0 & \epsilon_0 \frac{\omega^2}{c^2} - k_{\parallel}^2 \end{pmatrix} \begin{pmatrix} g_{xx} & g_{xy} & g_{xz} \\ g_{yx} & g_{yy} & g_{yz} \\ g_{zx} & g_{zy} & g_{zz} \end{pmatrix} \\
 = 4\pi\delta(z - z') \begin{pmatrix} 1 & 0 & 0 \\ 0 & 1 & 0 \\ 0 & 0 & 1 \end{pmatrix} \quad (A.7)$$

for Fourier coefficients $g_{\mu\nu}(k_{\parallel}\omega|zz')$ which are related to the coefficients $d_{\mu\nu}(k_{\parallel}\omega|zz')$ by

$$d_{\mu\nu}(k_{\parallel}\omega|zz') = \sum_{\mu'\nu'} g_{\mu'\nu'}(k_{\parallel}\omega|zz') S_{\mu'\mu}(k_{\parallel}) S_{\nu'\nu}(k_{\parallel}) . \quad (A.8)$$

In what follows we will obtain only the coefficients $g_{\mu\nu}(k_{\parallel}\omega|zz')$.

We note first from Eq. (A.7) that the functions g_{yx} and g_{yz} satisfy homogeneous equations

$$\left(\epsilon_0 \frac{\omega^2}{c^2} - k_{\parallel}^2 + \frac{d^2}{dz^2} \right) g_{yx} = 0 \quad (\text{A.9a})$$

$$\left(\epsilon_0 \frac{\omega^2}{c^2} - k_{\parallel}^2 + \frac{d^2}{dz^2} \right) g_{yz} = 0 \quad . \quad (\text{A.9b})$$

The functions g_{xy} and g_{zy} satisfy a pair of coupled homogeneous equations

$$\left(\epsilon_0 \frac{\omega^2}{c^2} + \frac{d^2}{dz^2} \right) g_{xy} - ik_{\parallel} \frac{d}{dz} g_{zy} = 0 \quad (\text{A.10a})$$

$$-ik_{\parallel} \frac{d}{dz} g_{xy} + \left(\epsilon_0 \frac{\omega^2}{c^2} - k_{\parallel}^2 \right) g_{zy} = 0 \quad . \quad (\text{A.10b})$$

These four functions therefore vanish. We are thus left with the following sets of equations to solve:

$$\left(\epsilon_0 \frac{\omega^2}{c^2} - k_{\parallel}^2 + \frac{d^2}{dz^2} \right) g_{yy} = 4\pi\delta(z - z') \quad (\text{A.11})$$

$$\left(\epsilon_0 \frac{\omega^2}{c^2} + \frac{d^2}{dz^2} \right) g_{xx} - ik_{\parallel} \frac{d}{dz} g_{zx} = 4\pi\delta(z - z') \quad (\text{A.12A})$$

$$-ik_{\parallel} \frac{d}{dz} g_{xx} + \left(\epsilon_0 \frac{\omega^2}{c^2} - k_{\parallel}^2 \right) g_{zx} = 0 \quad (\text{A.12b})$$

$$\left(\epsilon_0 \frac{\omega^2}{c^2} + \frac{d^2}{dz^2} \right) g_{xz} - ik_{\parallel} \frac{d}{dz} g_{zz} = 0 \quad (\text{A.13a})$$

$$-ik_{\parallel} \frac{d}{dz} g_{xz} + \left(\epsilon_0 \frac{\omega^2}{c^2} - k_{\parallel}^2 \right) g_{zz} = 4\pi\delta(z - z') \quad (\text{A.13b})$$

From Eqs. (A.11) - (A.13) we see that we can regard the Green's functions g_{xx} , g_{yy} , and g_{xz} as the primary functions to be solved for, since the remaining functions g_{zx} and g_{zz} can be obtained from g_{xx} and g_{xz} , respectively.

We must now consider the boundary conditions which supplement the differential equations (A.11) - (A.13). They are of two types: (1) boundary conditions at $z = \pm \infty$, and (2) boundary conditions at the interface $z = 0$. For the former we assume either outgoing waves at infinity, or exponentially decaying waves at infinity, depending on the values of k_{\parallel} and ω . To obtain the boundary conditions at the interface $z = 0$ we proceed as follows.

It is straightforward to obtain from the Maxwell equations in the presence of an external current $\underline{j}^{\text{ext}}(\underline{x}, t)$, in a gauge in which the scalar potential $\varphi(\underline{x}, t)$ vanishes,

$$\nabla \times \underline{H} = \frac{4\pi}{c} \underline{j}^{\text{ext}} + \frac{1}{c} \dot{\underline{D}} \quad , \quad \nabla \times \underline{E} = - \frac{1}{c} \dot{\underline{H}} \quad (\text{A.14a})$$

$$\underline{\underline{H}} = \nabla \times \underline{\underline{A}} , \quad \underline{\underline{E}} = - \frac{1}{c} \dot{\underline{\underline{A}}} , \quad \varphi = 0 \quad (\text{A.14b})$$

$$\underline{\underline{B}} = \underline{\underline{H}} , \quad \underline{\underline{D}} = \epsilon_0 \underline{\underline{E}} , \quad (\text{A.14c})$$

that the vector potential $A_\alpha(\underline{x}, \omega)$ is related to the external current $j_\beta^{\text{ext}}(\underline{x}, \omega)$ by

$$A_\alpha(\underline{x}, \omega) = - \frac{1}{c} \sum_\beta \int d^3x' D_{\alpha\beta}(\underline{x}, \underline{x}'; \omega) j_\beta^{\text{ext}}(\underline{x}', \omega) , \quad (\text{A.15})$$

where $D_{\alpha\beta}(\underline{x}, \underline{x}'; \omega)$ is the same Green's function as appears in Eq. (A.1). It follows from Eqs. (A.14) that the electric and magnetic fields induced by the external current are given by

$$E_\alpha(\underline{x}, \omega) = - \frac{i\omega}{c^2} \sum_\beta \int d^3x' D_{\alpha\beta}(\underline{x}, \underline{x}'; \omega) j_\beta^{\text{ext}}(\underline{x}', \omega) \quad (\text{A.16})$$

$$H_\alpha(\underline{x}, \omega) = - \frac{1}{c} \sum_{\beta\gamma\delta} \epsilon_{\alpha\beta\gamma} \frac{\partial}{\partial x_\beta} \int d^3x' D_{\gamma\delta}(\underline{x}, \underline{x}'; \omega) j_\delta^{\text{ext}}(\underline{x}', \omega) .$$

(A.17)

The boundary conditions on $D_{\alpha\beta}(\underline{x}, \underline{x}'; \omega)$ follow from the continuity of the tangential components of $\underline{\underline{E}}$ and of $\underline{\underline{H}}$, and the normal components of $\underline{\underline{D}}$ and $\underline{\underline{H}}$ across the plane $z = 0$. Since $j_\beta^{\text{ext}}(\underline{x}, \omega)$ is arbitrary, we see that the following quantities must be continuous across the plane $z = 0$, for $\beta = x, y, z$:

$$D_{x\beta}(\underline{x}, \underline{x}'; \omega) , \quad D_{y\beta}(\underline{x}, \underline{x}'; \omega) , \quad \sum_{\gamma} \epsilon_{z\gamma}(\underline{x}; \omega) D_{\gamma\beta}(\underline{x}, \underline{x}'; \omega) \quad (A.18)$$

$$\frac{\partial}{\partial y} D_{z\beta}(\underline{x}, \underline{x}'; \omega) - \frac{\partial}{\partial z} D_{y\beta}(\underline{x}, \underline{x}'; \omega) \quad (A.19a)$$

$$\frac{\partial}{\partial z} D_{x\beta}(\underline{x}, \underline{x}'; \omega) - \frac{\partial}{\partial x} D_{z\beta}(\underline{x}, \underline{x}'; \omega) \quad (A.19b)$$

$$\frac{\partial}{\partial x} D_{y\beta}(\underline{x}, \underline{x}'; \omega) - \frac{\partial}{\partial y} D_{x\beta}(\underline{x}, \underline{x}'; \omega) . \quad (A.19c)$$

In writing the third of the quantities in (A.18) we have assumed, for greater generality, an arbitrary position-dependent dielectric tensor $\epsilon_{\alpha\beta}(\underline{x}; \omega)$ which, however, still possesses a discontinuity across the plane $z = 0$. The boundary conditions which follow from the continuity of the six quantities given by (A.18) and (A.19) are not all independent, however.

With the aid of Eq. (A.3) we find that these boundary conditions translate into the following conditions on the Fourier coefficients $d_{\mu\nu}(\underline{k}_{\parallel}\omega | zz')$. The quantities

$$d_{x\beta}(\underline{k}_{\parallel}\omega | zz') , \quad d_{y\beta}(\underline{k}_{\parallel}\omega | zz') , \quad \epsilon_0(z; \omega) d_{z\beta}(\underline{k}_{\parallel}\omega | zz') \quad (A.20a)$$

$$ik_y d_{z\beta}(\underline{k}_{\parallel}\omega | zz') - \frac{d}{dz} d_{y\beta}(\underline{k}_{\parallel}\omega | zz') \quad (A.20b)$$

$$\frac{d}{dz} d_{x\beta}(\underline{k}_{\parallel}\omega | zz') - ik_x d_{z\beta}(\underline{k}_{\parallel}\omega | zz') \quad (A.20c)$$

$$ik_x d_{y\beta}(\underline{k}_{\parallel\omega}|zz') - ik_y d_{x\beta}(\underline{k}_{\parallel\omega}|zz') \quad (\text{A.20d})$$

must be continuous across the plane $z = 0$. Note that the first two conditions imply the last, which will therefore be discarded in what follows. We have also assumed a z -dependent, scalar dielectric constant in writing these conditions, the situation appropriate to the problem at hand.

To obtain the boundary conditions on the functions $g_{\mu\nu}(\underline{k}_{\parallel\omega}|zz')$ for which we are solving, we must combine the conditions (A.20) with the inverse of Eq. (A.8),

$$g_{\mu\nu}(\underline{k}_{\parallel\omega}|zz') = \sum_{\mu'\nu'} S_{\mu\mu'}(\underline{k}_{\parallel}) S_{\nu\nu'}(\underline{k}_{\parallel}) d_{\mu'\nu'}(\underline{k}_{\parallel\omega}|zz') , \quad (\text{A.21})$$

and the differential equations (A.5). For example, we have that

$$g_{xx} = \frac{1}{k_{\parallel}} (k_x^2 d_{xx} + k_x k_y d_{xy} + k_x k_y d_{yx} + k_y^2 d_{yy}) .$$

Since each term on the right hand side is continuous across the plane $z = 0$, we obtain the boundary condition

$$g_{xx}|_{0-} = g_{xx}|_{0+} . \quad (\text{A.22a})$$

In addition, we have that

$$\begin{aligned}
\frac{d}{dz} g_{xx} &= \frac{k_x}{k_{\parallel}^2} (k_x \frac{d}{dz} d_{xx} + k_y \frac{d}{dz} d_{yx}) + \frac{k_y}{k_{\parallel}^2} (k_x \frac{d}{dz} d_{xy} + k_y \frac{d}{dz} d_{yy}) \\
&= \frac{1k_x}{k_{\parallel}^2} (-1k_x \frac{d}{dz} d_{xx} - 1k_y \frac{d}{dz} d_{yx}) + \\
&\quad + 1 \frac{k_y}{k_{\parallel}^2} (-1k_x \frac{d}{dz} d_{xy} - 1k_y \frac{d}{dz} d_{yy}) \\
&= \frac{1}{k_{\parallel}^2} (k_{\parallel}^2 - \epsilon_o(z; \omega) \frac{\omega^2}{c^2}) (k_x d_{zx} + k_y d_{zy}) ,
\end{aligned}$$

where we have used Eq. (A.5) in going from the second equation to the third. Multiplying both sides of this equation by $\epsilon_o(z; \omega) [k_{\parallel}^2 - \epsilon_o(z; \omega)(\omega^2/c^2)]^{-1}$ we obtain

$$\frac{\epsilon_o(z; \omega)}{k_{\parallel}^2 - \epsilon_o(z; \omega) \frac{\omega^2}{c^2}} \frac{d}{dz} g_{xx} = \frac{1}{k_{\parallel}^2} [k_x \epsilon_o(z; \omega) d_{zx} + k_y \epsilon_o(z; \omega) d_{zy}] .$$

According to (A.20a), the right hand side of this equation is continuous across the plane $z = 0$. Thus we obtain the second boundary condition

$$\frac{\epsilon_0}{k_{\parallel}^2 - \epsilon_0 \frac{\omega^2}{c^2}} \frac{d}{dz} g_{xx} \big|_{0-} = \frac{\epsilon_0}{k_{\parallel}^2 - \epsilon_0 \frac{\omega^2}{c^2}} \frac{d}{dz} g_{xx} \big|_{0+} . \quad (\text{A.22b})$$

In the same way we obtain the remaining boundary conditions

$$g_{yy} \big|_{0-} = g_{yy} \big|_{0+} \quad (\text{A.22c})$$

$$\frac{d}{dz} g_{yy} \big|_{0-} = \frac{d}{dz} g_{yy} \big|_{0+} \quad (\text{A.22d})$$

$$g_{xz} \big|_{0-} = g_{xz} \big|_{0+} \quad (\text{A.22e})$$

$$\frac{\epsilon_0}{k_{\parallel}^2 - \epsilon_0 \frac{\omega^2}{c^2}} \frac{d}{dz} g_{xz} \big|_{0-} = \frac{\epsilon_0}{k_{\parallel}^2 - \epsilon_0 \frac{\omega^2}{c^2}} \frac{d}{dz} g_{xz} \big|_{0+} . \quad (\text{A.22f})$$

Equations (A.22) constitute the boundary conditions at the plane $z = 0$ on the primary Green's functions g_{xx} , g_{yy} , and g_{xz} .

In solving the differential equations (A.11) - (A.13) the following two results are useful for obtaining the particular integrals:

$$\left(\frac{d^2}{dz^2} + \alpha^2 \right) \frac{e^{i\alpha|z-z'|}}{2i\alpha} = \delta(z - z') \quad (\text{A.23a})$$

$$\left(\frac{d^2}{dz^2} + \alpha^2 \right) \frac{1}{2} e^{i\alpha|z-z'|} \operatorname{sgn}(z-z') = \frac{d}{dz} \delta(z-z') \quad (\text{A.23b})$$

We illustrate the determination of the $g_{\mu\nu}(k_{\parallel}\omega|zz')$ by working out $g_{xz}(k_{\parallel}\omega|zz')$. We assume first that $z' < 0$. On combining Eqs. (A.13a) and (A.13b), and recalling Eq. (A.2), we find that the equations satisfied by this function are

$$\left(\frac{d^2}{dz^2} + k^2 \right) g_{xz} = 0 \quad z > 0 \quad (\text{A.24a})$$

$$\left(\frac{d^2}{dz^2} + k_1^2 \right) g_{xz} = ik_{\parallel} \frac{4\pi c^2}{\epsilon(\omega)\omega^2} \frac{d}{dz} \delta(z-z') \quad z < 0, \quad (\text{A.24b})$$

where we have introduced the functions

$$\begin{aligned} k &= \left(\frac{\omega^2}{c^2} - k_{\parallel}^2 \right)^{\frac{1}{2}} & \frac{\omega^2}{c^2} > k_{\parallel}^2 \\ &= i \left(k_{\parallel}^2 - \frac{\omega^2}{c^2} \right)^{\frac{1}{2}} & \frac{\omega^2}{c^2} < k_{\parallel}^2 \end{aligned} \quad (\text{A.25})$$

$$k_1^2 = - \left(\epsilon(\omega) \frac{\omega^2}{c^2} - k_{\parallel}^2 \right)^{\frac{1}{2}}. \quad (\text{A.26})$$

The choice of the sign in Eq. (A.26), together with the fact that $\operatorname{Im} \epsilon(\omega) > 0$, ensures that $\operatorname{Im} k_1 < 0$.

The solutions of Eqs. (A.24) can be written in the forms

$$g_{xz} = A e^{ikz} \quad z > 0$$

$$= ik_{\parallel} \frac{2\pi c^2}{\epsilon(\omega)\omega^2} e^{-ik_1|z-z'|} \text{sgn}(z-z') + B e^{ik_1 z} \quad z < 0,$$

which, in view of Eqs. (A.25) - (A.26), satisfy the boundary conditions at infinity. We now apply the boundary conditions (A.22e) and (A.22f) to obtain the following equations for the coefficients A and B,

$$A = B + 2\pi i \frac{k_{\parallel} c^2}{\epsilon(\omega)\omega^2} e^{ik_1 z'}$$

$$\frac{k_1 A}{k \epsilon(\omega)} = B - 2\pi i \frac{k_{\parallel} c^2}{\epsilon(\omega)\omega^2} e^{ik_1 z'}.$$

In obtaining the second equation we have assumed that $z' \neq 0$. We thus find that

$$A = - \frac{4\pi i k_{\parallel} c^2}{\omega^2} \frac{k}{k_1 - \epsilon(\omega)k} e^{ik_1 z'}$$

$$B = - \frac{2\pi i k_{\parallel} c^2}{\epsilon(\omega)\omega^2} \frac{k_1 + \epsilon(\omega)k}{k_1 - \epsilon(\omega)k} e^{ik_1 z'},$$

from whence it follows that

Sec. F

$$\begin{aligned}
 g_{xz}(k_{\parallel} \omega | zz') &= - \frac{4\pi i k_{\parallel} c^2}{\omega^2} \frac{k}{k_1 - \epsilon(\omega)} e^{ikz + ik_1 z'} \quad z > 0, z' < 0 \\
 &= - \frac{2\pi i k_{\parallel} c^2}{\epsilon(\omega) \omega^2} \left\{ \frac{k_1 + \epsilon(\omega)k}{k_1 - \epsilon(\omega)k} e^{ik_1(z+z')} - e^{-ik_1|z-z'|} \operatorname{sgn}(z-z') \right\} \\
 &\quad z < 0, z' < 0
 \end{aligned}$$

When $z' > 0$, the equations obeyed by $g_{xz}(k_{\parallel} \omega | zz')$ become

$$\left(\frac{d^2}{dz^2} + k^2\right) g_{xz} = \frac{4\pi i k_{\parallel} c^2}{\omega^2} \frac{d}{dz} \delta(z - z') \quad z > 0$$

$$\left(\frac{d^2}{dz^2} + k_1^2\right) g_{xz} = 0 \quad z < 0$$

The solutions satisfying the boundary conditions are

$$g_{xz}(k_{\parallel} | z z') = -\frac{2\pi i k_{\parallel} c^2}{\omega^2} \left\{ \frac{k_1 + \epsilon(\omega)k}{k_1 - \epsilon(\omega)k} e^{ik(z+z')} - e^{ik|z-z'|} \text{sgn}(z-z') \right\}$$

$$z > 0, z' > 0$$

$$= -\frac{4\pi i k_{\parallel} c^2}{\omega^2} \frac{k_1}{k_1 - \epsilon(\omega)k} e^{ik_1 z + ik z'} \quad z < 0, z' > 0$$

All of the remaining Green's functions can be obtained in the same way. The results of these calculations are summarized below.

$$g_{yy}(k_{\parallel} | z z') = \frac{4\pi i}{k_1 - k} e^{ikz + ik_1 z'} \quad z > 0, z' < 0$$

$$= \frac{2\pi i}{k_1} \left\{ \frac{k_1 + k}{k_1 - k} e^{ik_1(z+z')} + e^{-ik_1|z-z'|} \right\} \quad z < 0, z' < 0$$

$$= \frac{2\pi i}{k} \left\{ \frac{k_1 + k}{k_1 - k} e^{ik(z+z')} - e^{ik|z-z'|} \right\} \quad z > 0, z' > 0$$

$$= \frac{4\pi i}{k_1 - k} e^{ik_1 z + ikz'} \quad z < 0, z' > 0$$

$$g_{xz}(k_{\parallel} \omega | zz') = - \frac{4\pi i k_{\parallel} c^2}{\omega^2} \frac{k}{k_1 - \epsilon(\omega)k} e^{ikz + ik_1 z'} \quad z > 0, z' < 0$$

$$= - \frac{2\pi i k_{\parallel} c^2}{\epsilon(\omega) \omega^2} \left\{ \frac{k_1 + \epsilon(\omega)k}{k_1 - \epsilon(\omega)k} e^{ik_1(z+z')} - e^{-ik_1|z-z'|} \operatorname{sgn}(z-z') \right\} \quad z < 0, z' < 0$$

$$= - \frac{2\pi i k_{\parallel} c^2}{\omega^2} \left\{ \frac{k_1 + \epsilon(\omega)k}{k_1 - \epsilon(\omega)k} e^{ik(z+z')} - e^{ik|z-z'|} \operatorname{sgn}(z-z') \right\} \quad z > 0, z' > 0$$

$$= - \frac{4\pi i k_{\parallel} c^2}{\omega^2} \frac{k_1}{k_1 - \epsilon(\omega)k} e^{ik_1 z + ikz'} \quad z < 0, z' > 0$$

$$g_{zz}(k_{\parallel} \omega | zz') = \frac{4\pi i k_{\parallel}^2 c^2}{\omega^2} \frac{1}{k_1 - \epsilon(\omega)k} e^{ikz + ik_1 z'} \quad z > 0, z' < 0$$

$$= \frac{2\pi i k_{\parallel}^2 c^2}{k_1 \epsilon(\omega) \omega^2} \left\{ \frac{k_1 + \epsilon(\omega)k}{k_1 - \epsilon(\omega)k} e^{ik_1(z+z')} + e^{-ik_1|z-z'|} \right\} + \frac{4\pi c^2}{\epsilon(\omega) \omega^2} \delta(z-z')$$

$$z < 0, z' < 0$$

$$= \frac{2\pi i k_{\parallel}^2 c^2}{k \omega^2} \left\{ \frac{k_1 + \epsilon(\omega)k}{k_1 - \epsilon(\omega)k} e^{ik(z+z')} - e^{ik|z-z'|} \right\} + \frac{4\pi c^2}{\omega^2} \delta(z-z')$$

$$z > 0, z' > 0$$

$$= \frac{4\pi i k_{\parallel}^2 c^2}{\omega^2} \frac{1}{k_1 - \epsilon(\omega)k} e^{ik_1 z + ikz'} \quad z < 0, z' > 0$$

$$g_{xx}(k_{\parallel} \omega | zz') = - \frac{4\pi i c^2}{\omega^2} \frac{k k_1}{k_1 - \epsilon(\omega)k} e^{ikz + ik_1 z'} \quad z > 0, z' < 0$$

$$= - \frac{2\pi i k_1 c^2}{\epsilon(\omega) \omega^2} \left\{ \frac{k_1 + \epsilon(\omega)k}{k_1 - \epsilon(\omega)k} e^{ik_1(z+z')} - e^{-ik_1|z-z'|} \right\} \quad z < 0, z' < 0$$

$$= - \frac{2\pi i k c^2}{\omega^2} \left\{ \frac{k_1 + \epsilon(\omega)k}{k_1 - \epsilon(\omega)k} e^{ik(z+z')} + e^{ik|z-z'|} \right\} \quad z > 0, z' > 0$$

$$= - \frac{4\pi i k c^2}{\omega^2} \frac{k_1}{k_1 - \epsilon(\omega)k} e^{ik_1 z + ikz'} \quad z < 0, z' > 0$$

$$g_{zx}(k_{\parallel} \omega | zz') = \frac{4\pi i k_{\parallel} c^2}{\omega^2} \frac{k_1}{k_1 - \epsilon(\omega)k} e^{ikz + ik_1 z'} \quad z > 0, z' < 0$$

$$= \frac{2\pi i k_{\parallel} c^2}{\epsilon(\omega) \omega^2} \left\{ \frac{k_1 + \epsilon(\omega)k}{k_1 - \epsilon(\omega)k} e^{ik_1(z+z')} + e^{-ik_1|z-z'|} \operatorname{sgn}(z-z') \right\} \quad z < 0, z' < 0$$

$$= \frac{2\pi i k_{\parallel} c^2}{\omega^2} \left\{ \frac{k_1 + \epsilon(\omega)k}{k_1 - \epsilon(\omega)k} e^{ik(z+z')} + e^{ik|z-z'|} \text{sgn}(z-z') \right\}$$

$$z > 0, z' > 0$$

$$= \frac{4\pi i k_{\parallel} c^2}{\omega^2} \frac{k}{k_1 - \epsilon(\omega)k} e^{ik_1 z + ikz'}$$

$$z < 0, z' > 0$$

We conclude this Appendix by pointing out that in addition to the uses to which they are put in the present paper, the Green's functions $D_{\mu\nu}(\underline{x}, \underline{x}'; \omega)$, whose Fourier coefficients $g_{\mu\nu}(k_{\parallel} \omega | z z')$ have been presented here, also arise in the evaluation of thermodynamic and double-time Green's functions, and correlation functions of the electromagnetic fields in the layered medium for which the present calculations have been carried out. (14)

For example, we consider the retarded Green's function

$$D_{\alpha\beta}^R(\underline{x}_1, \underline{x}_2; t_1 - t_2) = -i \theta(t_1 - t_2) \langle [A_{\alpha}(\underline{x}_1 t_1), A_{\beta}(\underline{x}_2 t_2)] \rangle \quad (\text{A.27})$$

where $A(\underline{x}, t)$ is now the operator of the vector potential in the Heisenberg representation, and the angular brackets denote an average with respect to the canonical ensemble described by the Hamiltonian of the electromagnetic field. The Fourier transform of this Green's function can be written in the form

Sec. F

$$D_{\alpha\beta}^R(\underline{x}_1, \underline{x}_2; \omega) = \int_{-\infty}^{\infty} d(t_1 - t_2) e^{i\omega(t_1 - t_2)} D_{\alpha\beta}^R(\underline{x}_1, \underline{x}_2; t_1 - t_2)$$

$$= - \int_{-\infty}^{\infty} dx (1 - e^{-\beta \hbar x}) \frac{\rho_{\alpha\beta}(\underline{x}_1, \underline{x}_2; x)}{x - \omega - i\delta} \quad (\text{A.28})$$

where the spectral density $\rho_{\alpha\beta}(\underline{x}_1, \underline{x}_2; x)$ is given by

$$\rho_{\alpha\beta}(\underline{x}_1, \underline{x}_2; x) = \sum_{mn} \frac{e^{-\beta E_m}}{Z} \langle m | A_{\alpha}(\underline{x}_1) | n \rangle \langle n | A_{\beta}(\underline{x}_2) | m \rangle \delta(x - \frac{1}{\hbar}(E_n - E_m))$$

(A.29)

in terms of the eigenfunctions $|n\rangle$ and eigenvalues E_n of the system Hamiltonian; Z is the partition function. We can express the Fourier transforms of several useful correlation functions in terms of $\rho_{\alpha\beta}(\underline{x}_1, \underline{x}_2; x)$. For example, we have that

$$\int_{-\infty}^{\infty} d(t_1 - t_2) e^{i\omega(t_1 - t_2)} \langle A_{\alpha}(\underline{x}_1 t_1) A_{\beta}(\underline{x}_2 t_2) \rangle = 2\pi \rho_{\alpha\beta}(\underline{x}_1, \underline{x}_2; \omega) \quad (\text{A.30})$$

$$\int_{-\infty}^{\infty} d(t_1 - t_2) e^{i\omega(t_1 - t_2)} \langle E_{\alpha}(\underline{x}_1 t_1) E_{\beta}(\underline{x}_2 t_2) \rangle = 2\pi \frac{\omega^2}{c^2} \rho_{\alpha\beta}(\underline{x}_1, \underline{x}_2; \omega)$$

(A.31)

The spectral density $\rho_{\alpha\beta}(\underline{x}_1, \underline{x}_2; \omega)$ can be obtained in a standard fashion⁽¹⁵⁾. We introduce a function of the complex variable z by

$$\hat{D}_{\alpha\beta}(\underline{x}_1, \underline{x}_2; z) = - \int_{-\infty}^{\infty} dx (1 - e^{-\beta \hbar x}) \frac{\rho_{\alpha\beta}(\underline{x}_1, \underline{x}_2; x)}{x - z} \quad (\text{A.32})$$

which coincides with $D_{\alpha\beta}^R(\underline{x}_1, \underline{x}_2; \omega)$ for $\text{Im} z > 0$. (For $\text{Im} z < 0$ $\hat{D}_{\alpha\beta}(\underline{x}_1, \underline{x}_2; z)$ coincides with the Fourier transform of the advanced Green's function.) Then we have that

$$\rho_{\alpha\beta}(\underline{x}_1, \underline{x}_2; \omega) = \frac{1}{2\pi} \frac{1}{1 - e^{-\beta \hbar \omega}} \left[\hat{D}_{\alpha\beta}(\underline{x}_1, \underline{x}_2; \omega + i0) - \hat{D}_{\alpha\beta}(\underline{x}_1, \underline{x}_2; \omega - i0) \right]. \quad (\text{A.33})$$

The importance of the Green's functions $D_{\alpha\beta}(\underline{x}_1, \underline{x}_2; \omega)$ studied in this Appendix for such calculations lies in the fact that Dzyaloshinski and Pitayevski⁽¹⁶⁾ have established the relation

$$D_{\alpha\beta}^R(\underline{x}, \underline{x}'; \omega) = \hbar D_{\alpha\beta}(\underline{x}, \underline{x}'; \omega), \quad (\text{A.34})$$

from which $\hat{D}_{\alpha\beta}(\underline{x}, \underline{x}'; z)$ can be obtained, and hence the spectral density $\rho_{\alpha\beta}(\underline{x}, \underline{x}'; \omega)$ and other useful correlation functions.

REFERENCES

1. E. A. Stern and R. A. Ferrell, Phys. Rev. 111, 1214 (1958).
2. P. A. Fedders, Phys. Rev. 165, 580 (1968).
3. R. H. Ritchie and R. E. Wilems, Phys. Rev. 178, 372 (1968).
4. J. Crowell and R. H. Ritchie, J. Opt. Soc. Am. 60, 795 (1970).
5. J. M. Elson and R. H. Ritchie, Phys. Rev. B4, 4129 (1971).
6. J. M. Elson and R. H. Ritchie, Phys. Stat. Sol., (to be published). We are grateful to Dr. R. H. Ritchie for calling our attention to this work, and for providing us with a copy of it in advance of publication.
7. D. L. Mills, A. A. Maradudin and E. Burstein, Annals of Physics 56, 504 (1970).
8. See, for example, the discussions in reference (4) and reference (5).
9. The minus sign in Eq. (4.7) is a consequence of placing the crystal in the lower half space $z < 0$. Then inside the crystal, $\langle S_z \rangle$ is negative. In the subsequent discussion, we drop this minus sign.
10. J. Schoenwald, E. Burstein and J. Elson, Solid State Communications 12, 185 (1973).
11. D. Beaglehole and O. Hunderi, Phys. Rev. B2, 309 (1970); 2, 321 (1970), J. L. Stanford, J. Opt. Soc. Am. 60, 49 (1970).
12. J. G. Endriz and W. E. Spicer, Phys. Rev. B4, 4144 and 4159 (1971).
13. H. Ehrenreich, H. R. Phillipp and B. Segall, Phys. Rev. 132, 1918 (1963).

Sec. F

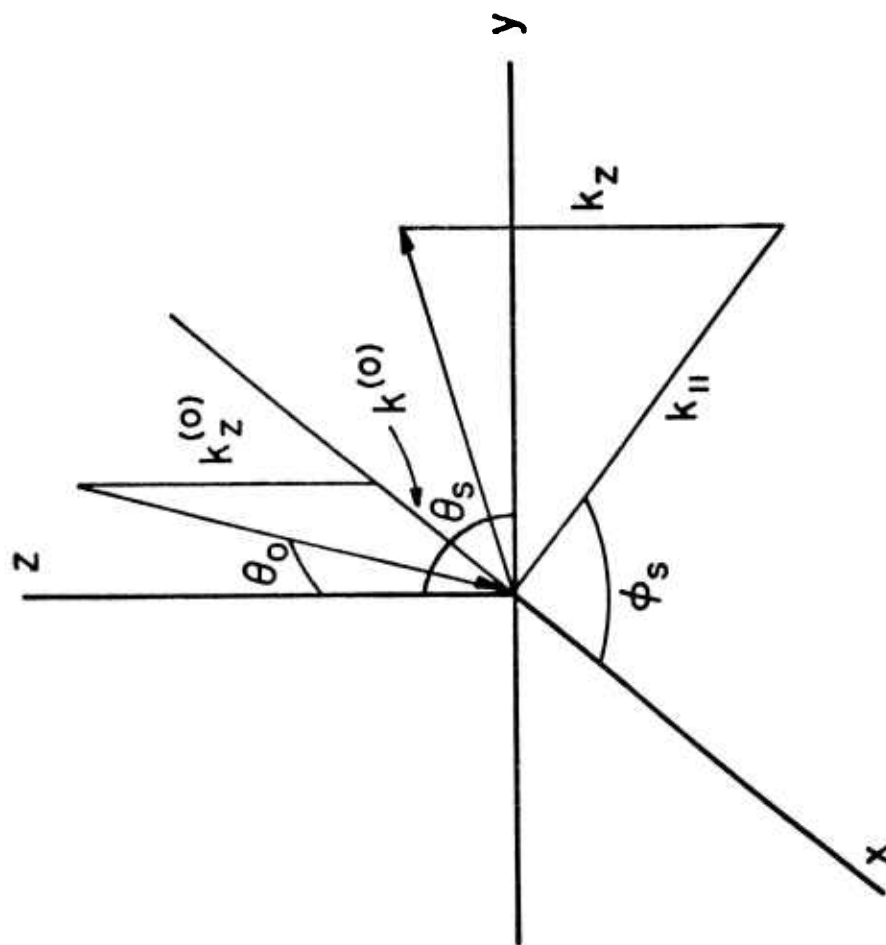
14. A. A. Abrikosov, L. P. Gorkov, and I. E. Dzyaloshinski,
Methods of Quantum Field Theory in Statistical Physics
(Prentice-Hall, Inc., Englewood Cliffs, N.J., 1963),
section 28.
15. D. N. Zubarev, Soviet Physics-Uspekhi 3, 320 (1960).
16. I. E. Dzyaloshinski and L. P. Pitayevski, Soviet Physics -
JETP 9, 1282 (1959).

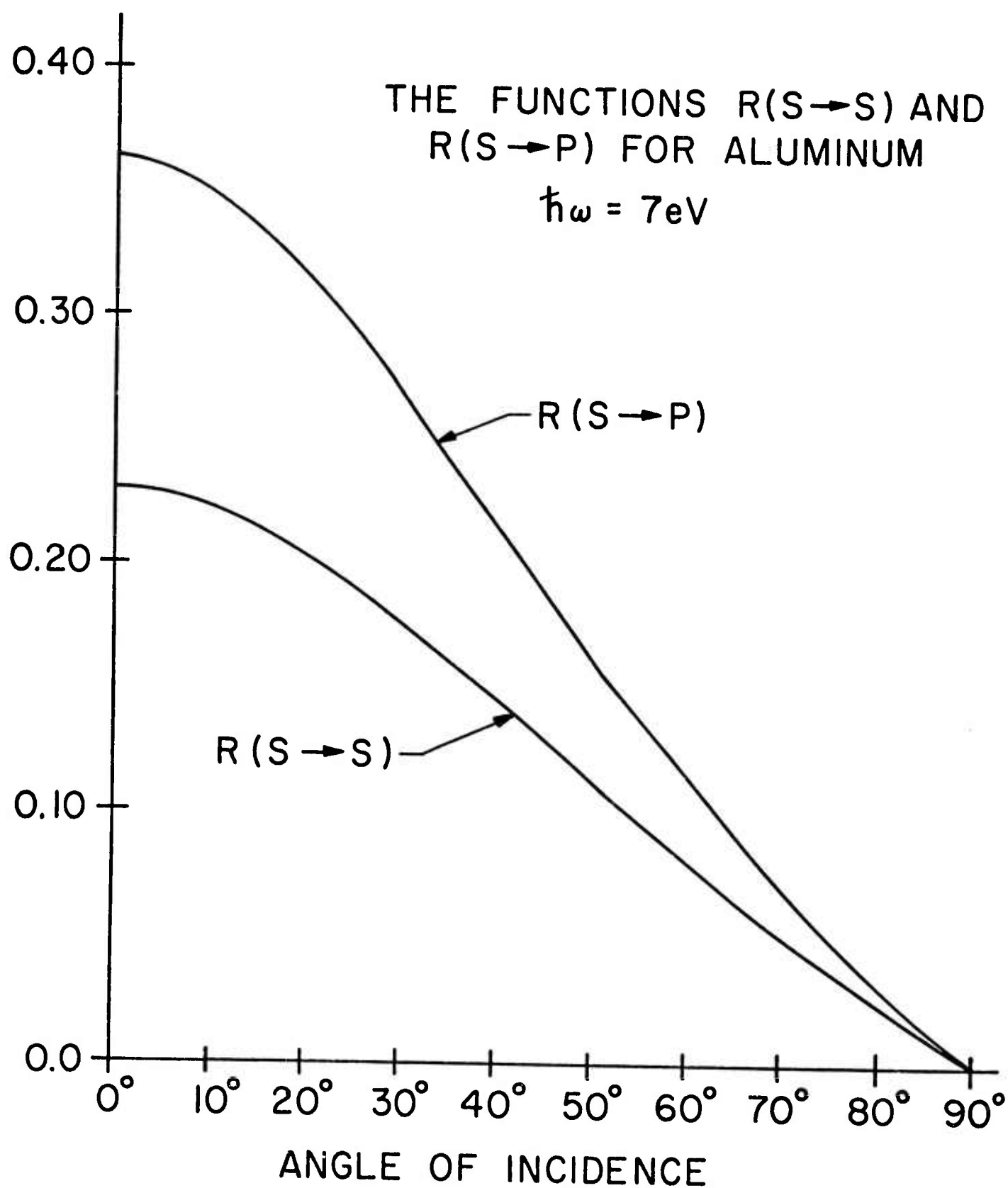
Figure Captions

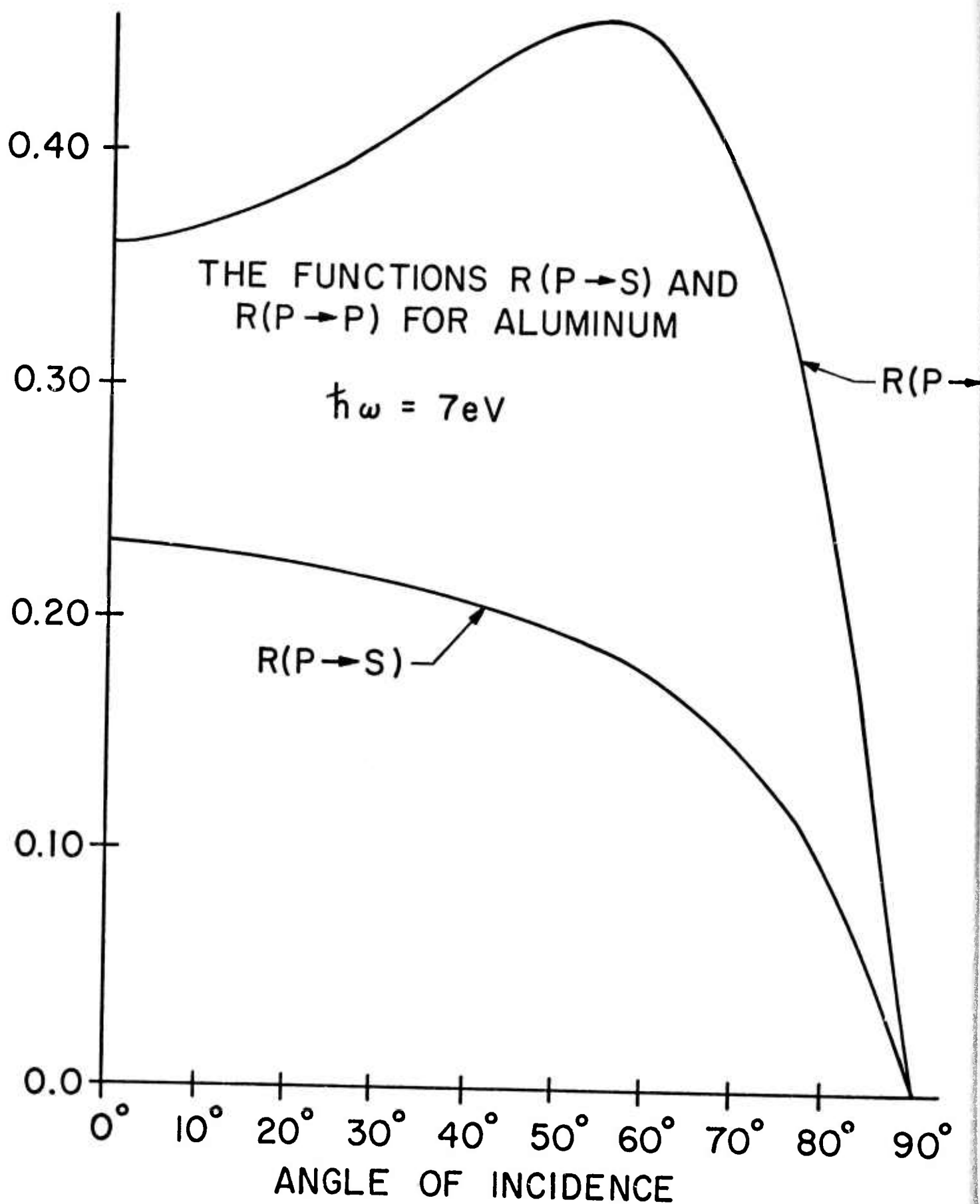
- Fig. 1. The scattering geometry employed in this paper.
- Fig. 2. The variation of the scattering functions $R(s \rightarrow s)$ and $R(s \rightarrow p)$ with angle of incidence, for a 7eV photon incident on aluminum. The transverse correlation length a has been chosen equal to 500\AA .
- Fig. 3. The variation of the scattering functions $R(p \rightarrow s)$ and $R(p \rightarrow p)$ with angle of incidence, for a 7eV photon incident on aluminum. The transverse correlation length a has been chosen equal to 500\AA .
- Fig. 4. The variation of the scattering functions $R(s)$ and $R(p)$ with angle of incidence, for a 7eV photon incident on aluminum. The transverse correlation a has been chosen equal to 500\AA .
- Fig. 5. The variation of $R(s)$ with frequency for several angles of incidence, at 7eV for aluminum. The transverse correlation length a has been chosen equal to 500\AA .
- Fig. 6. The functions A_{sp} and A_{pp} as functions of the angle of incidence, for a photon of $\hbar\omega = 7\text{eV}$ incident on aluminum. The solid line is a result of a numerical integration over the exact formulas, and the dashed lines are obtained from Eqs. (4.10) and (4.15). The transverse correlation length a has been chosen equal to 500\AA ,
- Fig. 7. The functions A_{sp} and A_{pp} as functions of the angle of incidence, for a photon of energy $\hbar\omega = 9\text{eV}$ incident on aluminum. The solid line is a result of a numerical

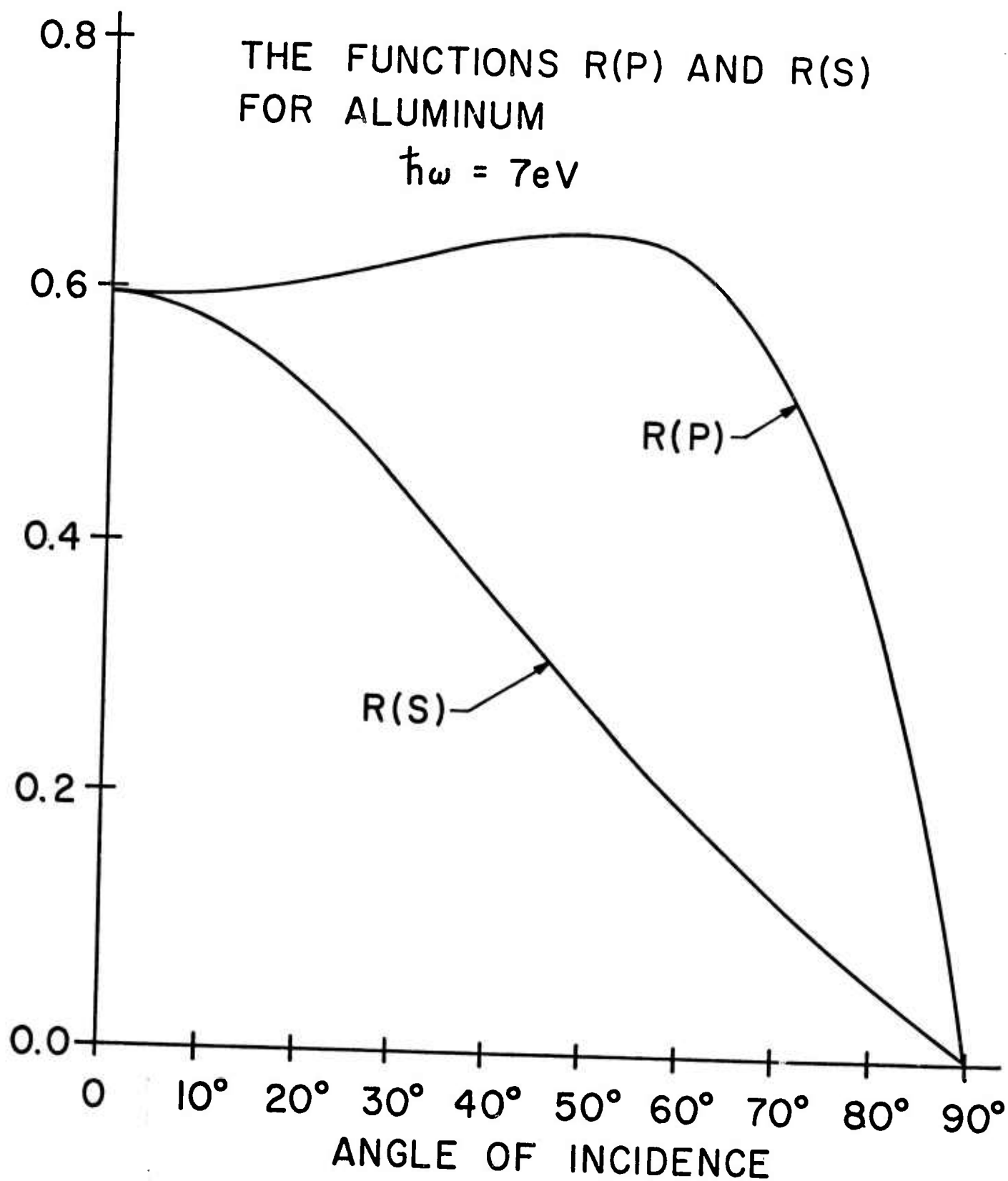
integration over the exact formula, and the dashed lines are obtained from Eqs. (4.10) and (4.15). The transverse correlation length a has been chosen equal to 500\AA .

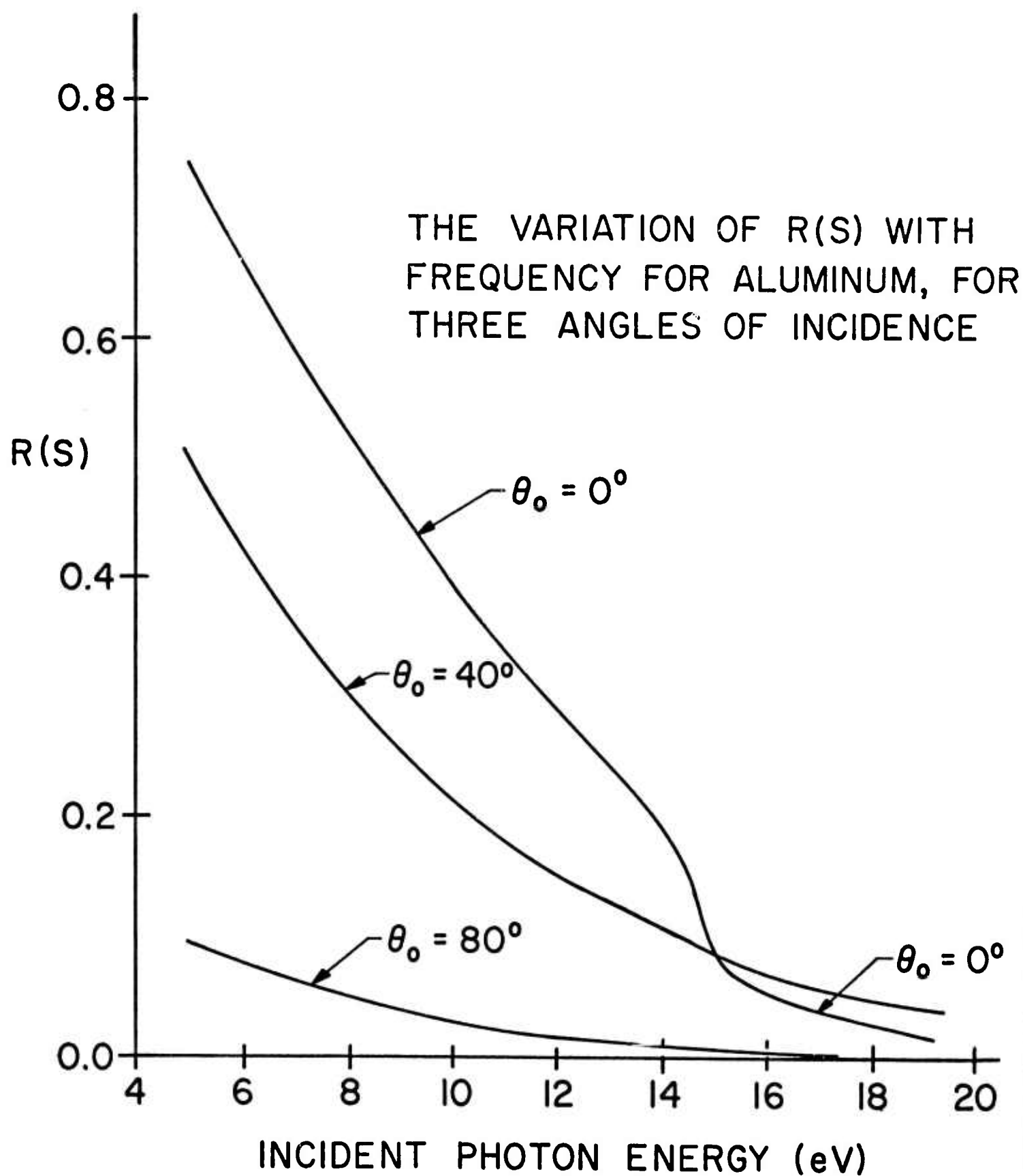
Fig. 8. The variation with frequency at normal incidence of A_{sp} , A_{ss} and the analytic approximation to the roughness induced absorption cross section. The calculations have been performed for an aluminum substrate with the transverse correlation length a equal to 500\AA .

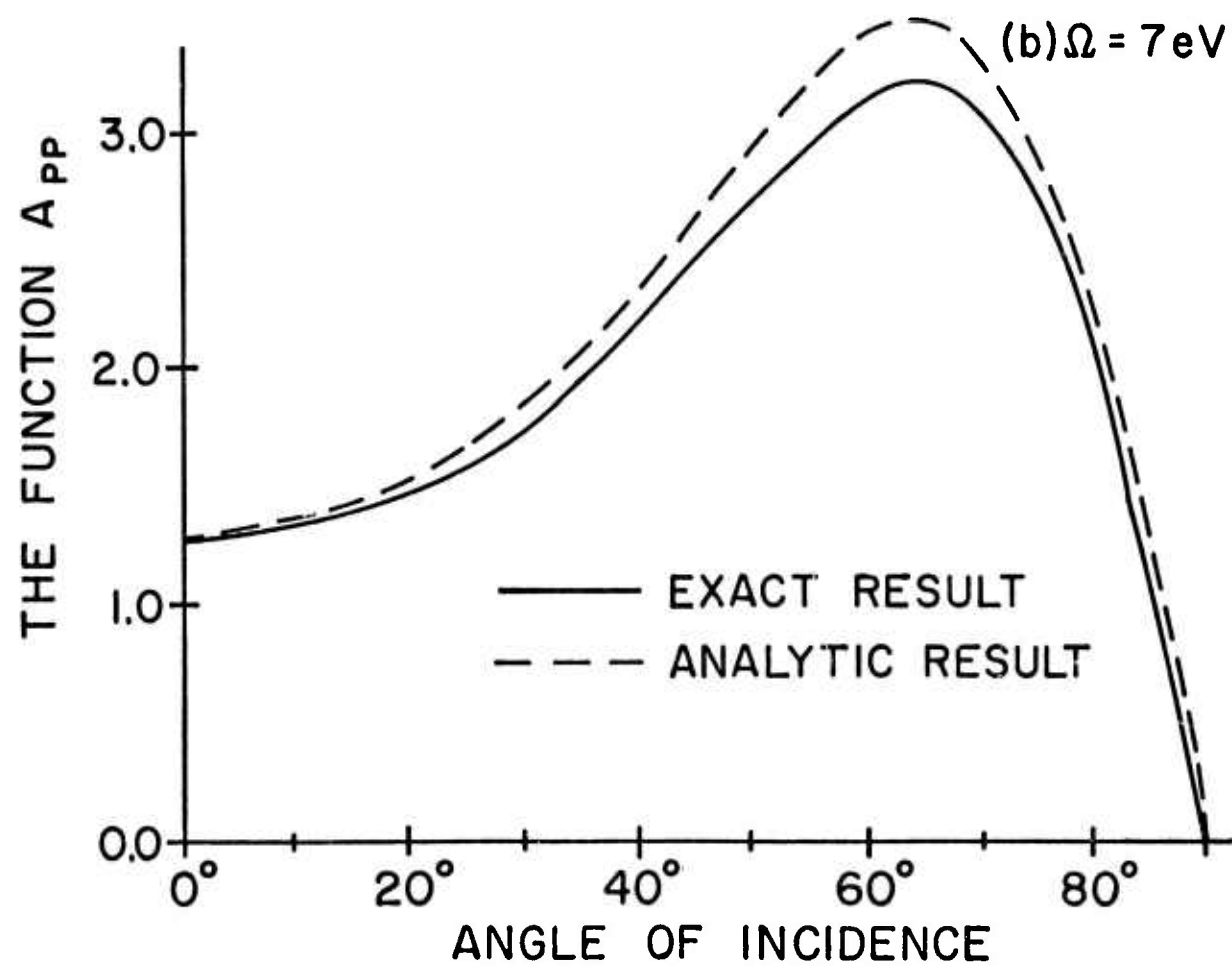
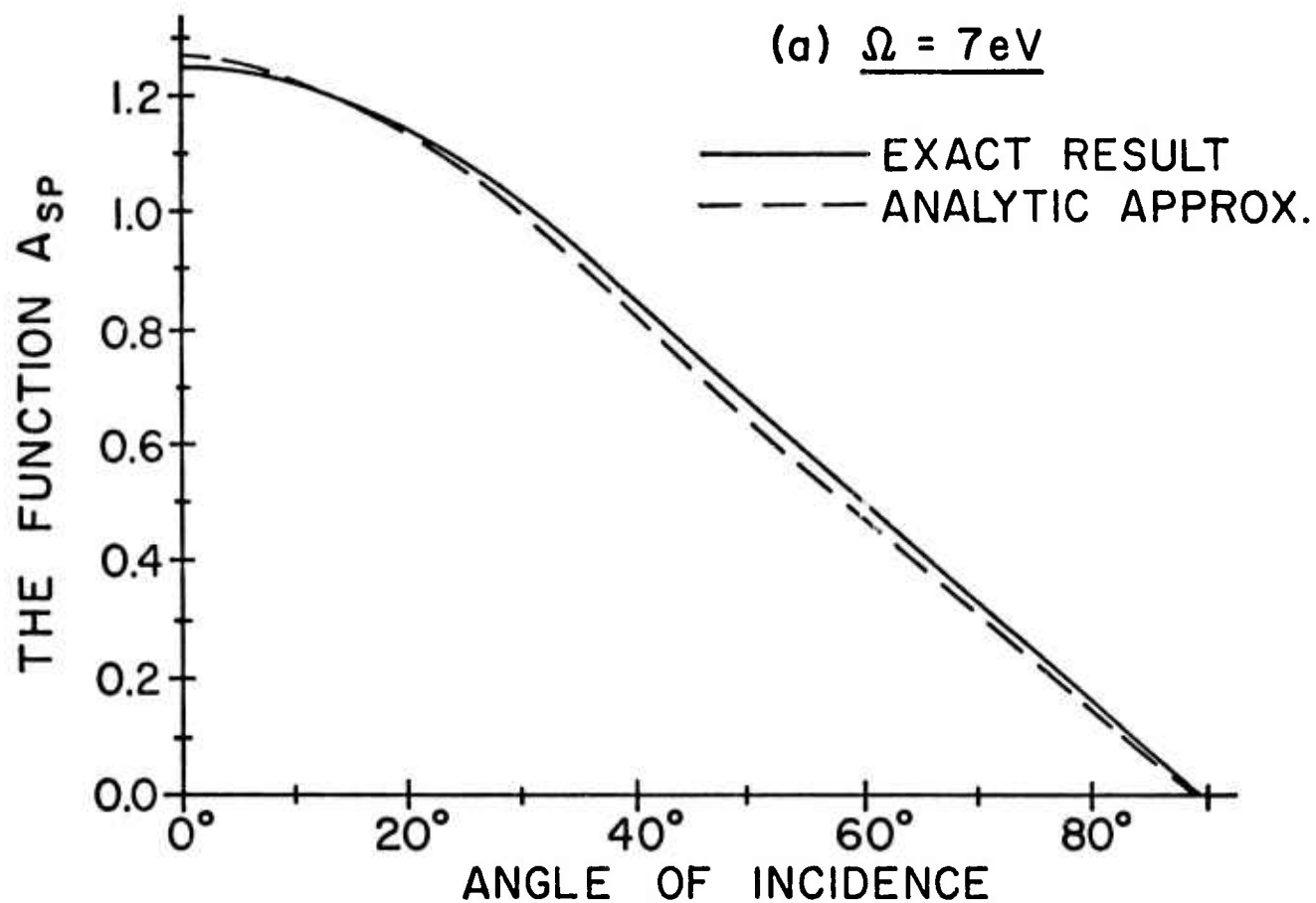


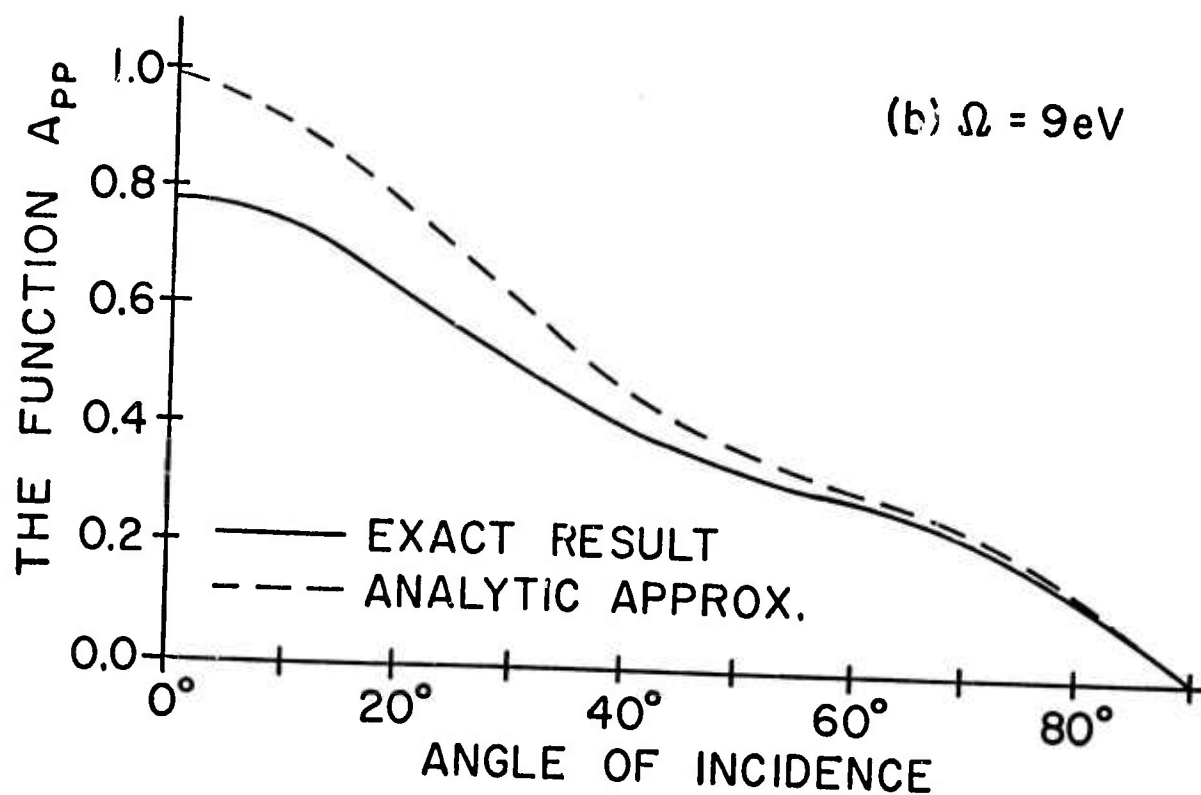
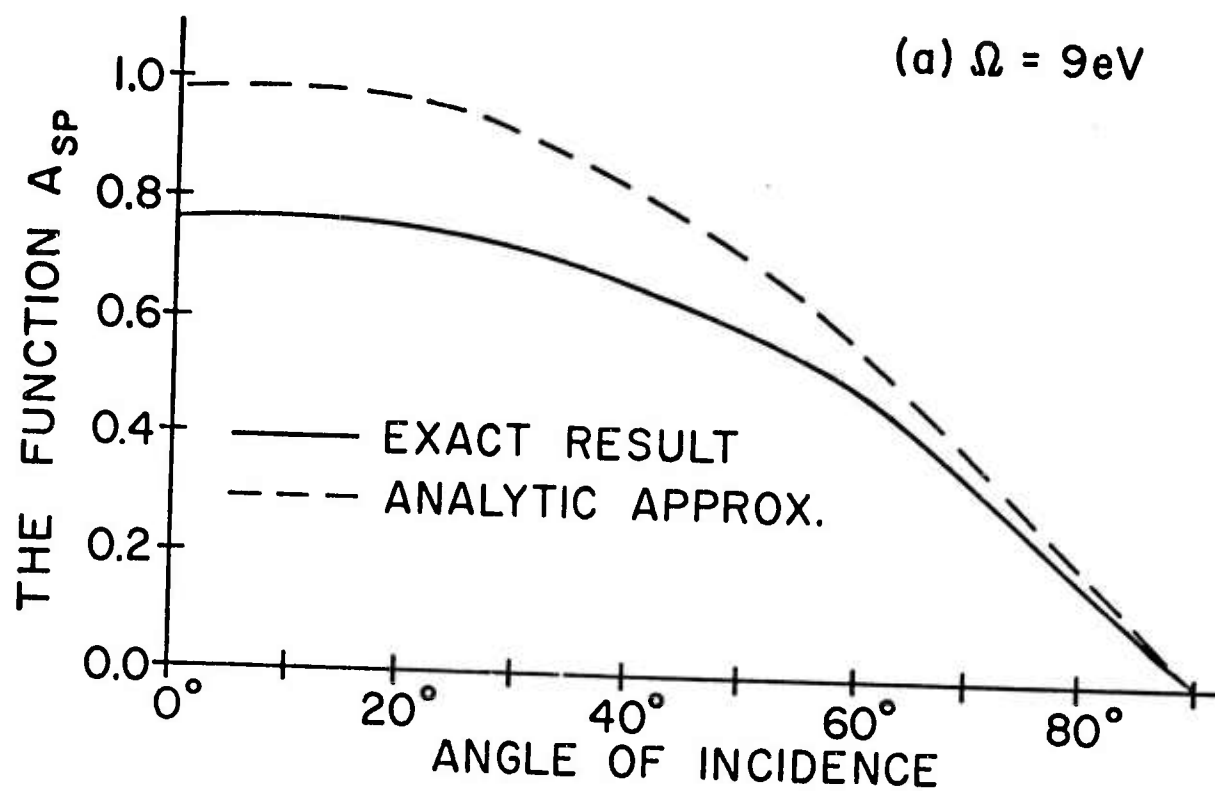


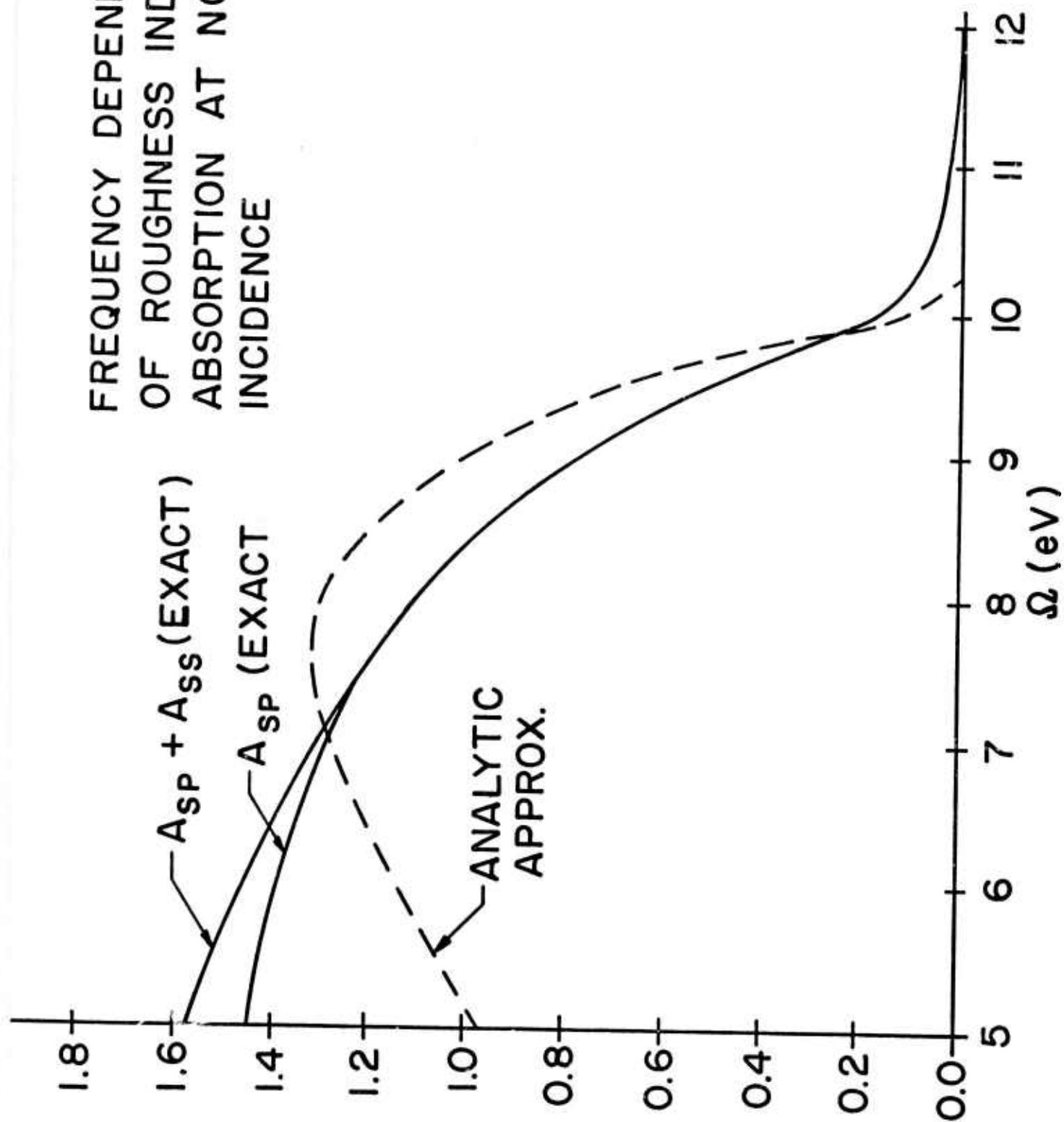










FREQUENCY DEPENDENCE
OF ROUGHNESS INDUCED
ABSORPTION AT NORMAL
INCIDENCE

G. INFRARED ABSORPTION BY THE HIGHER-ORDER-DIPOLE-MOMENT MECHANISM*

M. Sparks

Xonics, Incorporated, Van Nuys, California 91406

The simple model consisting of a one-dimensional chain of alternating rigid positive ions and shell-model negative ions connected by anharmonic forces gives insight into the Lax-Burstein nonlinear-dipole-moment mechanism (LB) of multiphonon absorption, especially in relation to the anharmonic-potential mechanism (AP) in polar crystals. The model and general considerations suggest that LB dominates AP in the high-frequency region of current interest and that the LB and AP Hamiltonians have opposite signs. The resulting minimum in the absorption coefficient β should be observable if it were in the region of exponential decay of $\beta(\omega)$. The most likely explanation for the apparent lack of the minimum in experiments is that it occurs at the observed minimum nearest the Reststrahlen peak in $\beta(\omega)$. Even though the accuracy of the results from the model is not expected to be great, the minimum is in the two-phonon region, though not as close to the peak as the first observed minimum. Since a larger value of LB corresponds to a minimum nearer the peak, this explanation results in theoretical values of β at high ω that are considerably greater than experimental values in the alkali halides. In spite of this difficulty, it is unlikely that LB is negligible in the high-frequency region if shell models are believable in general. Possibilities of a positive LB to AP ratio, which would alleviate the difficulty, are shown to exist but to be unlikely.

I. INTRODUCTION

The development of high-power $10.6\text{ }\mu\text{m}$ lasers has created considerable interest in infrared transmitting materials with ultrasnall absorption. The intrinsic absorption limit in the highly transparent region now appears to be set by multiphonon absorption in many materials, particularly the alkali halides. There are two sources of multiphonon absorption, the anharmonic-potential mechanism¹ and the Lax-Burstein nonlinear-dipole-moment mechanism,^{2,1} which are illustrated schematically in Fig. G1 for the two-phonon summation process. In nonpolar crystals, such as diamond, the anharmonic-potential mechanism is inoperative, and only the Lax-Burstein mechanism contributes to the multiphonon absorption. Until recently, it appeared that the Lax-Burstein mechanism was negligible in polar crystals, such as the alkali halides, although there were conflicting opinions.³

The recent interest in multiphonon absorption has also stimulated renewed interest in the Lax-Burstein mechanism in polar crystals.⁴⁻⁸ At our present state of knowledge, we are still not in a position to answer with certainty the question of which mechanism dominates in polar crystals. Theoretical calculations are necessarily based on models, and the results must be model dependent since the rigid-ion model gives no Lax-Burstein effect, for example. There is no obvious way to distinguish between the two experimentally. In view of the renewed attention to the Lax-Burstein mechanism, it is of interest to reexamine the effect from a simple point of view. Thus, the first purpose of the present paper is to examine the simplest model that contains the essential physics to produce the Lax-Burstein

effect, which has been treated in the past mostly by adding the appropriate terms to the Hamiltonian. The model, which is discussed in Sec. II, is a one-dimensional line of alternating rigid positive ions and simple-shell-model negative ions with one of the force constants anharmonic. Both the polarizability and anharmonicity are required in order to obtain a nonzero Lax-Burstein effect. Extensions of the model are discussed in Secs. II and III.

Although the detailed features of the results of such a simple model cannot be expected to give accurate numerical results for real crystals, and in spite of the difficulty of the model dependence of theoretical results already mentioned, the general results of the model do have important consequences for real materials. Both the relative magnitudes and signs of the Lax-Burstein and anharmonic Hamiltonians \mathcal{H}_{LB} and \mathcal{H}_{anh} are of interest. The absence of a resonance denominator in the Lax-Burstein Hamiltonian makes the Lax-Burstein contribution to the optical absorption coefficient β decrease less rapidly with increasing frequency ω so that the Lax-Burstein mechanism dominates at some sufficiently high frequency ω . At the fundamental resonance (at frequency ω_f) in the anharmonic-potential mechanism, the contribution β_{anh} to β from this process is much greater than the contribution β_{LB} from the Lax-Burstein process, which does not have a resonance. These two limits imply that $|\mathcal{H}_{LB}| = |\mathcal{H}_{anh}|$ at some frequency ω_{eq} that is greater than ω_f . Since values of ω_{eq} greater than $\sim 2.5 \omega_f$ are discussed and the high-frequency region is of great interest, an important feature of the calculations below is that they are not restricted to the two-phonon region, as were most previous treatments.

The model and general considerations of the Sziget effective charge,⁹ the polarizabilities of the ions, and shell model results for phonon dispersion relations suggest that ω_{eq} is sufficiently small that the Lax-Burstein mechanism dominates in the high-frequency region of current interest, typically $\omega \approx 7\omega_f$. Furthermore, the model predicts that the Hamiltonians for the two processes have different signs, which implies that there should be an observable minimum at $\omega = \omega_{eq}$ in the absorption coefficient. There are no changes in the parameters in the model that give a positive sign. Different models that could in principle, though apparently not in practice, give a positive sign are discussed in Sec. III. This negative sign poses a difficulty to any theory which predicts that $\beta_{LB} \gg \beta_{anh}$, since no such minimum has been observed. It is possible that the minimum occurs in the two-phonon region and is obscured by the two-phonon structure. Simple estimates in Sec. IV indicate that if this is indeed the case, then the theoretical values¹⁰ of β that contain no adjustable parameters are several orders of magnitude greater than the experimental values at high frequencies.

The frequency and temperature dependence of β cannot be used to determine which mechanism controls β . Both mechanisms give rise to a nearly exponential decrease in β with increasing ω . It has been pointed out previously¹⁰ that the explicit temperature dependence is the same for the two processes. The implicit temperature dependence resulting from wavevector-conservation effects¹⁰ and from the temperature dependence of the phonon frequencies and lattice constants¹¹ does give a slightly different temperature dependence for the two processes. However, at the present time it would be impossible to distinguish between the two on the basis of this rather small difference.

Sec. G

It is shown in Sec. II that the difference between the present negative sign of κ_{LB}/κ_{anh} and the positive sign suggested by Mills and Maradudin⁴ results from their assumption that charge flows from one ion to another as the spacing between the ions changes, in contrast to the present assumption of a polarization change with no net change in charge. The polarizable-ion model is more plausible than the charge-flow model, which involves the transfer of small fractions of the electron charge from one ion to another.

Using an analysis, quite different from the present one, of a one-dimensional model with both ions polarizable, Keating and Rupprecht⁷ concluded that the Lax-Burstein mechanism was negligible. Their results in the two-phonon region appear to be similar to the present results with $n = 2$. In Sec. III it is shown that their different conclusion results from their neglect of the frequency dependence of the ratio κ_{LB}/κ_{anh} .

The simplicity of the model and analysis affords intuitive explanations of the Szigeti effective charge, the fact that a crystal of uncharged atoms can be polar, the need for both anharmonicity and polarizability in order to have a Lax-Burstein effect.

II. MODEL

A simple model that gives the Lax-Burstein effect is a one-dimensional chain of alternating point-charge positive and simple-shell-model negative ions as shown in Fig. G2. The positive ions are rigid, that is unpolarizable, and have charge q . A negative ion consists of a massive positive core of charge q and a massless shell of charge $-2q$. The electronic excitations that would result from a small shell mass are not of interest here. The core is connected to the shell by a Hookian spring having spring constant g . That is, the force on the core is $-g\ell$, where ℓ is the relative displacement of the core and shell. The positive ions are connected to the shell of the negative ions by a nonlinear spring having force constant F and nonlinear force constants G_n . That is, the force on the shell from the left in Fig. G2 is

$$\text{force} = -Fx + G_2 x^2 + G_3 x^3 + \dots, \quad (2.1)$$

where $x = (u_0 - \ell) - u_-$ is the relative displacement of the positive ion and the shell of the negative ion. The equilibrium positions of the ions are r_i and $r_i \pm a$, and the displacements of the ion cores from equilibrium are $u_0 \equiv u(r_i)$ and $u_{\pm} \equiv u(r_i \pm a)$.

Bilz¹² calculated the phonon frequencies from this model without the anharmonicity (all $G_n = 0$). Previous absorption coefficient calculations have considered the two-phonon summation process. Since the general n -phonon process is of far greater current interest and the analysis is only slightly more complicated than that for $n = 2$, the case of general n is considered.

The net dipole moment ϑ of the chain determines the coupling to an applied electromagnetic field, as is well known and demonstrated explicitly for this

Sec. G

model in Sec. III. The contribution p_+ of a rigid positive ion to θ is $p_+ = qu_+$. The contribution p_- of the polarizable negative ions to θ contains a displacement term proportional u_0 plus a contribution from the relative displacement of the core and shell. In particular, $p_- = qu_0 - 2q(u_0 - \ell)$, where $u_0 - \ell$ is the displacement of the core. Thus,

$$p_- = -qu_0 + 2q\ell, \quad (2.2)$$

which shows that the u_0 term is the same as that of a rigid ion of charge $-q$ and the shell polarization term is $2q\ell$.

In the n -phonon region¹⁰ $[(n - \frac{1}{2})\omega_f < \omega < (n + \frac{1}{2})\omega_f]$, very roughly], all G_m with $m \leq n$ contribute to the absorption. However, it has been shown¹⁰ that the leading terms come from G_n . The value of ℓ can be determined from the condition that the sum of the forces on the massless shell be zero:

$$g\ell = -F(u_{+0} + \ell) + G_n(u_{+0} + \ell)^n - F(u_{-0} + \ell) - G_n(u_{-0} - \ell)^n,$$

where $u_{\pm 0} \equiv u_{\pm} - u_0$ and $u_{0-} \equiv -u_{-0}$. In keeping track of the signs of the G terms, it is useful to realize that the G_2 force tends to extend the springs when in either tension or compression. These equations can be rewritten as

$$\ell = -F_g(u_{+0} + u_{-0}) + G_{ng}[(u_{+0} + \ell)^n - (u_{0-} - \ell)^n], \quad (2.3)$$

where

$$F_g \equiv F/(g + 2F), \quad G_{ng} \equiv G_n/(g + 2F).$$

Sec. G

Since the G_{ng} term is small, the first approximation $\ell^{(1)}$ to ℓ is given by the first term on the right-hand side of (2.3)

$$\ell^{(1)} = -F_g (u_{+0} + u_{-0}) . \quad (2.4)$$

In the rigid-ion limit of g going to infinity, this gives $\ell^{(1)} = 0$. In order to obtain a reasonable fit to the phonon dispersion curves, the value of g is large; that is, $g \gg F$. Then $F_g \cong F/g \ll 1$, and (2.4) gives $|\ell^{(1)}| \ll |u_{+0} + u_{-0}|$, which means that the dipole moment associated with polarization of the negative ions is much less than that of the ionic displacements. In this case, the second approximation $\ell^{(2)}$ to ℓ is obtained by replacing ℓ by $\ell^{(1)}$ on the right-hand side of (2.3) and using $|\ell^{(1)}| \ll |u_{+0}|$, $|u_{-0}|$, which gives

$$\ell \cong \ell^{(2)} = -F_g (u_{+0} + u_{-0}) + G_{ng} (u_{+0}^n - u_{-0}^n) . \quad (2.5)$$

This result for ℓ , which is related to the dipole moment by (2.2), illustrates how a nonlinear-dipole moment arises for the simple shell model with anharmonic forces. Both the polarizability and the anharmonicity are required.

It is of interest that the model illustrates several interesting effects. First, it shows how crystals with no net charges on the ions can be polar, that is, have dipole moments linear in the displacements. Specifically, if the rigid ions in Fig. G2 are uncharged and the shell of the polarizable ion is singly charged (so that the ion has no net charge), then ℓ still has a term linear in the displacements according to (2.5). The corresponding dipole moment from (2.2) is nonzero. Diamond would be a polar crystal were it not for symmetry.

Sec. G

This is illustrated schematically in Fig. G3 where the two types of ions (both carbon, but on different sites) are equally polarizable so that the two ℓ 's add to zero.

Second, the model illustrates that the Szigeti effective charge⁹ q_S , which relates the dipole moment to the displacement u , is less than the ionic charge q . The dipole moment resulting from the displacement of the net charges of a pair of ions is qu_{+0} , while that of a shell is $2q\ell$, according to (2.2). From (2.5), $\sum_j 2q\ell_j = -4qF_g u_{+0} + \dots$. Thus the net dipole moment per pair of ions is $q_S u_{+0}$, where

$$q_S = q(1 - 4F_g) \quad (2.6)$$

is less than q . If the polarizability of the positive ion were greater than that of the negative ion, q_S would be greater than q . This is an alternative explanation to that of the electron cloud of the negative ion moving toward the positive ion as the positive ion moves toward the negative one.³

Third, the model indicates the source of the difference between the negative sign of $\mathcal{K}_{LB}/\mathcal{K}_{anh}$ obtained in Sec. III and positive sign suggested by Mills and Maradudin.⁴ Their suggestion is based on a flow of charge from one ion to another as the spacing between the ions is changed. They envision neutral atoms at infinite separation, which become charged as they are brought closer together. This gives a decrease (relative to the initial linear response) in the dipole moment p as the spacing x between the ions increases, which is easily shown to correspond to a positive sign of $\mathcal{K}_{LB}/\mathcal{K}_{anh}$. By contrast, the present model envisions charged ions at infinite separation, which become polarized but retain their

overall charges as they are brought closer together. This gives a decreasing value of p as x increases, which corresponds to a negative sign of $\mathcal{K}_{LB}/\mathcal{K}_{anh}$. The two situations are illustrated schematically in Fig. G4. The curve marked "present model" is the sum of two contributions. The first, marked "u," is the linear ionic term qx , and the second, marked " ℓ ," is the contribution from the polarization of the negative ion. Since the latter goes to zero as x goes to infinity and the two contributions have opposite signs, the sum increases more rapidly than that of the original linear response, as shown. In passing, notice that if the positive ion is polarizable, the contributions to the dipole moment from u and ℓ have the same signs, and the dipole moment decreases less rapidly at large u than at small u , in agreement with the Mills and Maradudin suggestion.

In searching for effects not contained in the simple model, the following features could be added to the model: long-range forces, shell to shell coupling, coupling of positive and negative cores, three dimensionality, polarizability of both ions, vertex corrections,¹⁰ nonzero masses of the shells, non-spherical and "breathing" shells, incorporation of other recent refinements in shell and deformation dipole models, and higher-order multipole moments of the polarizable ions.

Two such extensions, those of including a nonlinearity in the shell spring of Fig. G2 and of including the polarizability of the positive ions, are interesting because they can give the same signs for the Lax-Burstein and anharmonic-potential Hamiltonians. This has important consequences as discussed in Sec. IV. These extensions are discussed in Sec. III.

III. n-PHONON SUMMATION PROCESSES

In the two-phonon summation processes, a photon is annihilated and two phonons are created. In the Lax-Burstein nonlinear-dipole-moment mechanism, the interaction occurs at a single vertex, as illustrated in Fig. G1a. In the anharmonic-potential interaction, the photons couple to fundamental (Reststrahl) phonons which in turn couple to two other phonon modes.

In order to determine the relative importance of the two mechanisms, the absorption coefficients could be calculated and the two contributions compared. Fortunately, the easier procedure of comparing the Hamiltonians for the absorption processes can be carried out. The Hamiltonian for the Lax-Burstein process is the nonlinear-dipole-moment part of the usual Hamiltonian

$$\mathcal{H}_{PE} = - \sum_{j=1}^{2N} \underline{p}_j \cdot \underline{E} \equiv - \underline{\mathcal{P}} \cdot \underline{E} \quad , \quad (3.1)$$

where N is the number of unit cells (ion pairs), \underline{p}_j is the dipole moment of the j th ion, \underline{E} is the electric field, and $\underline{\mathcal{P}} = \sum \underline{p}_j$ is the total dipole moment of the sample. For the one-dimensional case, the vector scalar product $\underline{p}_j \cdot \underline{E}$ is the simple product $p_j E$. With $p_j = q u_{+j}$ for the positive ions and p_j for the negative ions given by (2.2) and (2.5) with the subscript j added, (3.1) gives

$$\mathcal{H}_{PE} = -q E \sum_{i=1}^N \left[\frac{1}{2} (u_{+0i} + u_{-0i}) + 2 G_{ng} (u_{+0i}^n - u_{-0i}^n) \right] \quad . \quad (3.2)$$

The linear term of order $F_g \ll 1$ was neglected in (3.2).¹³ The Lax-Burstein n-phonon Hamiltonian is the nonlinear part of (3.2)

$$\mathcal{H}_{LB} = -2q E G_{ng} \sum_{i=1}^N (u_{+0i}^n - u_{-0i}^n) \quad . \quad (3.3)$$

The Hamiltonian for the anharmonic-potential mechanism is obtained from second-order perturbation theory. The standard result is

$$\begin{aligned} \langle f | \mathcal{H}_{\text{anh}} | i \rangle &= \langle f | \mathcal{H}_{n+1} | n_f + 1, n_p - 1 \rangle \\ &\times \langle n_f + 1, n_p - 1 | \mathcal{H}_{\text{PE}}^{(1)} | i \rangle / \hbar (\omega - \omega_f) + 3 \text{ terms} \end{aligned} \quad (3.4)$$

where the initial state $|i\rangle = |n_f, n_p, n_Q, n_{-Q}\rangle$, the final state $|f\rangle = |n_f, n_p - 1, n_Q + 1, n_{-Q} + 1\rangle$, \mathcal{H}_{n+1} is the anharmonic potential for the n -phonon process, and n_f, n_p, n_Q , and n_{-Q} designate the numbers of f phonons, photons, Q phonons, and $-Q$ phonons, respectively. The other three terms in (3.4) correspond to the two time orderings of the vertices and the two directions of the f -phonon line, as illustrated in Fig. G5.

The Hamiltonian $\mathcal{H}_{\text{PE}}^{(1)}$ in (3.4) is given by the first term in (3.2). The anharmonic-interaction Hamiltonian \mathcal{H}_{n+1} is the sum over ion pairs of the $(n+1)^{\text{th}}$ -order anharmonic interaction in the Taylor expansion of the potential:

$$\mathcal{H}_{n+1} = [\phi_{n+1} / (n+1)!] \sum_{i=1}^N (u_{+0i}^{n+1} + u_{0-i}^{n+1}) \quad (3.5)$$

where ϕ_{n+1} is the $(n+1)^{\text{th}}$ derivative of the potential energy with respect to the relative displacements evaluated at equilibrium. In order to evaluate the matrix elements in (3.4), the displacements are expanded as¹

$$u(x_j) = \sum_Q w_{b\pm} (\hbar/2 \omega_Q N M)^{1/2} e^{i k r_j} A_Q, \quad (3.6)$$

where Q denotes the set of numbers (k, b) with k the wavevector and b the ⁺ branch (acoustical or optical), $w_{b\pm}$ are the polarization vectors, $A_Q = a_Q + a_{-Q}$

Sec. G

with a and a^\dagger the phonon annihilation and creation operators and $-Q \equiv (-k, b)$, and \pm denotes the positive or negative ions, respectively. The ion masses M are assumed to be equal for simplicity. The result (3.10) is valid for unequal masses.

When (3.6) and the expansion of E in photon creation and annihilation operators are substituted into the expressions for \mathcal{K}_{n+1} and $\mathcal{K}_{PE}^{(1)}$, the matrix elements can be evaluated. This can be avoided by noticing that in both \mathcal{K}_{n+1} and $\mathcal{K}_{PE}^{(1)}$, one of the A_Q must be A_f in order for the matrix element not to vanish. From (3.6) with $k \approx 0$ and $\omega_+ - \omega_- = \sqrt{2}$ for the fundamental mode,

$$u_{\pm 0i} = (\hbar/\omega N M)^{1/2} A_f + \text{terms with } Q \neq f.$$

Thus, (3.5) and (3.2) become

$$\mathcal{K}_{n+1} = [(n+1) \phi_{n+1} / (n+1)!] (\hbar/\omega M)^{1/2} A_f \sum_{i=1}^N (u_{+0i}^n - u_{0-i}^n) \quad (3.7)$$

and

$$\mathcal{K}_{PE}^{(1)} = -qE (\hbar N/\omega M)^{1/2} A_f. \quad (3.8)$$

The factor of $n+1$ in (3.7) accounts for the fact that each u in the $(n+1)^{\text{th}}$ -order expression in (3.5) contains an A_f in its expansion.

Using the well known matrix elements $\langle n_f - 1 | a_f | n_f \rangle = n_f^{1/2}$ and $\langle n_f + 1 | a_f^\dagger | n_f \rangle = (n_f + 1)^{1/2}$, summing the four terms in (3.4), and deleting $\langle f |$ and $| i \rangle$ in (3.4) gives

$$\mathcal{K}_{anh} = -2 \omega_f qE (\phi_{n+1}/n!) \sum_{i=1}^N (u_{+0i}^n - u_{0-i}^n) / M \omega (\omega^2 - \omega_f^2). \quad (3.9)$$

Sec. G

With $\phi_{n+1}/n! = -G_n$ (which follows from the result, force $= -d\phi/dx$) and $\omega_f^2 = 4F/M$, the ratio of \mathcal{K}_{LB} in (3.3) to \mathcal{K}_{anh} in (3.9) is

$$\mathcal{K}_{LB}/\mathcal{K}_{anh} = -4\omega(\omega^2 - \omega_f^2)\omega_f^{-3}(F/g) \quad (3.10)$$

Notice that the ratio is independent of the anharmonicity constant G_n . In particular, the negative sign in (3.10) is independent of the sign of the anharmonicity constant G_n . For the two-phonon region ($\omega < 2.5\omega_f$, very roughly), $|\mathcal{K}_{LB}/\mathcal{K}_{anh}| < 52 F/g$. Thus the Lax-Burstein mechanism would be negligible in the two-phonon region if $F/g \ll 1/52$ were satisfied.

Since (3.10) was derived for arbitrary n , it is valid for $\omega > 2.5\omega_f$. Thus for a sufficiently high frequency, the ratio $|\mathcal{K}_{LB}/\mathcal{K}_{anh}|$ becomes large, and the Lax-Burstein mechanism dominates.

As mentioned in Sec. II, a nonlinear spring constant in the shell spring g in Fig. G2 is of interest since it results in a positive value of $\mathcal{K}_{LB}/\mathcal{K}_{anh}$. Very briefly, if $G_n = 0$ and $G_{Sm} \neq 0$, where $G_{Sm} = -\phi_{Sm}/(m-1)!$, (2.3) is replaced by

$$g\ell - G_{S,n}\ell^n = -F(u_{+0} + u_{-0}) - 2F\ell$$

and (2.5) becomes

$$\ell \cong -F_g(u_{+0} + u_{-0}) + (G_{S,n}/g)[-F_g(u_{+0} + u_{-0})]^n.$$

Equation (3.8) is unchanged, (3.3) is replaced by

$$\mathcal{K}_{LB} = -2qE(G_{S,n}/g) \sum_{i=1}^N [-F_g(u_{+0i} + u_{-0i})]^n,$$

Sec. G

and (3.5) is replaced by

$$\begin{aligned}\mathcal{K}_{n+1} &= [\phi_{S,n+1}/(n+1)!] \sum_{i=1}^N l_i^{n+1} \\ &= [\phi_{S,n+1}/(n+1)!] \sum_{i=1}^N [-F_g(u_{+0i} + u_{-0i})]^{n+1}.\end{aligned}$$

With these results, the sign of $\mathcal{K}_{LB}/\mathcal{K}_{anh}$ in (3.10) is positive, rather than negative. It is emphasized that even though the anharmonicity in the shell spring does give rise to a positive value of $\mathcal{K}_{LB}/\mathcal{K}_{anh}$, it is not likely that $\mathcal{K}_{LB}/\mathcal{K}_{anh}$ will actually be positive since the negative contribution from the anharmonicity in the inter-ion force constants is expected to be greater. This is easily verified by making a simple estimate of the values of the parameters under the assumption that G_{Sn}/g is of the order of G_n/F . The key factor is that the anharmonic contribution of the inter-ion spring is greater than that of the shell spring since it is weaker than the shell spring, thereby having greater displacements with the corresponding greater anharmonic effects.

Another model that gives a positive value of $\mathcal{K}_{LB}/\mathcal{K}_{anh}$ is that of rigid negative ions and polarizable positive ions. This can be seen by replacing q by $-q$ on the ions at $r_i \pm a$ in Fig. C2 and replacing the charges $+q$ and $-2q$ on the nucleus and shell of the ion at r_i by $+2q$ and $-q$, respectively. Since the polarizabilities of the negative ions are usually greater than those of the positive ions (as is the case for all materials discussed in Sec. IV), including the polarizabilities of the positive ions is not expected to make $\mathcal{K}_{LB}/\mathcal{K}_{anh}$ positive.

Sec. G

At the risk of pushing a simple model too far, consider the size of F/g . For KCl with $M \cong 6 \times 10^{-23}$ g and $\omega_f = 2.7 \times 10^{13}$ sec⁻¹, the equation $F = M\omega_f^2$ gives $F = 1.1 \times 10^4$ dynes/cm. In a local field E_{loc} , the force compressing the shell spring is qE_{loc} , which is equal to the restoring force $g\ell$; thus $g = qE_{loc}/\ell$. The relation between E_{loc} and ℓ is obtained by equating the two expressions $2q\ell$ and αE_{loc} for the dipole moment of the chlorine ion, where $\alpha = 3.0 \times 10^{-24}$ cm³ is the polarizability of the ion. This gives $g = 2q^2/\alpha = 1.5 \times 10^5$ dynes/cm for $q = |e|$. Thus, $F/g = 1/15$.

With (3.10), this value of $F/g = 1/15$ indicates that $|\mathcal{K}_{LB}| = |\mathcal{K}_{anh}|$ at frequency $\omega_{eq} = 1.8\omega_f$. Thus, in the high frequency region $\omega \gtrsim 3\omega_f$, the Lax-Burstein mechanism dominates. It is encouraging that essentially the same values of F/g and ω_{eq} are obtained from (2.6). With $q_S/q \cong 0.8$ for KCl, (2.6) gives $F/g = 1/20$, and (3.10) gives $\omega_{eq} = 1.9\omega_f$. If the shell charge is changed, the results from (2.6) are unchanged, but the value of ω_{eq} obtained from the polarizability estimate becomes greater.

Keating and Rupprecht⁷ considered a one-dimensional diatomic chain with both ions polarizable. The simplicity of the model was lost in their treatment since the model was analyzed by relating it to a previous general treatment that was more involved than is needed here. They considered only the two-phonon region. Their conclusion that the Lax-Burstein mechanism was negligible, which contradicts the present results, was based on their approximation that $|\mathcal{K}_{LB}/\mathcal{K}_{anh}|$ is of order F/g . This approximation is fair for values of ω near ω_f , but is not good for larger values of ω . It is understandable that the frequency dependence of the ratio and its importance were overlooked since the interest in the higher-frequency regions was not as great in 1965 as it is at present.

IV. FREQUENCY DEPENDENCE OF ABSORPTION

The negative sign in (3.10) shows that β , which is proportional to $|\kappa_{LB} + \kappa_{anh}|^2$, has a zero at frequency ω_{eq} at which $\kappa_{LB} = -\kappa_{anh}$. At the fundamental resonance at $\omega = \omega_f$, $|\kappa_{anh}|^2 \gg |\kappa_{LB}|^2$. (Finite phonon lifetimes prevent κ_{anh} from diverging at $\omega = \omega_f$.) At sufficiently high frequency, $|\kappa_{LB}|^2 \gg |\kappa_{anh}|^2$, according to (3.10). Thus, if β is measured over some frequency range $\omega_f < \omega < m\omega_f$ and if a theory suggests that $|\kappa_{LB}|^2 \gg |\kappa_{anh}|^2$ at the high-frequency end $m\omega_f$ of the range, then the effect of the "zero" in β at $\omega = \omega_{eq}$ should be considered in the theory. An actual zero in β at $\omega = \omega_{eq}$ would not be observed, of course, as any one of a number of effects such as instrument resolution or other absorption processes would give rise to a nonzero value of β at $\omega = \omega_{eq}$.

According to (3.10), if ω_{eq} were in the exponential frequency region,¹⁰ the resulting deviation from an exponential decay of β would be readily observable, as seen in Fig. G6. The light solid curve is the theoretical curve of Sparks and Sham¹⁰ with only the anharmonic-potential mechanism included, and the heavy curve for the theory with both mechanisms included was obtained by multiplying the values of β from the light curve by $R(\omega, 3\omega_f)$ where

$$R(\omega, \omega_{eq}) \equiv \left| 1 + \frac{\kappa_{LB}}{\kappa_{anh}} \right|^2 = \left[1 - \frac{\omega(\omega^2 - \omega_f^2)}{\omega_{eq}(\omega_{eq}^2 - \omega_f^2)} \right]^2. \quad (4.1)$$

Comparison with (3.10) gives

$$\Gamma_g = \omega_f^3 / 4 \omega_{eq} (\omega_{eq}^2 - 1). \quad (4.2)$$

The gross features of the heavy curve in Fig. G6 agree well with the curves of Mills and Maradudin⁴ obtained for the quite different model of noninteracting anharmonic molecules. Since experimental results such as the heavy curve in Fig. G6 have not been observed, the simplified theory suggests that ω_{eq} is not in the exponential region. The dashed curve will be discussed in Sec. V.

The numerical estimate of Sec. III puts ω_{eq} in the two-phonon region, where β does show structure experimentally that could include the minimum; ω_{eq} could be at any of the minima in the two-phonon region. However, if the experimental values of β are divided by R in order to obtain β_{anh} , there results a fairly large peak in β_{anh} at $\omega = \omega_{eq}$ for all of the minima in KBr, KCl, NaCl, and LiF except the one nearest the fundamental resonance. An example of the peak is given in Fig. G7 for KCl. It is unlikely that β_{anh} would contain a large peak at $\omega = \omega_{eq}$ in all four materials. Thus, if ω_{eq} is in the observed region, it is most likely to be at the first minimum ω_{m1} .

Figure G8 illustrates the resulting $\beta(\omega)$ for $\omega_{eq} = \omega_{m1}$. The solid light curve of β_{anh} was obtained by dividing the experimental values¹⁴ of β by $R(\omega, 1.3\omega_f)$. In order to avoid the clutter of the multiphonon peaks, which lie in region S, and to illustrate the effect of the minimum, the experimental curve in this region S was replaced by a smooth curve that joins the experimental curve at the ends of S. The heavy curve was then obtained by multiplying the values of β from the light curve by R . The original experimental curve is of course retrieved outside the region S, and the heavy curve in the region S contains a minimum near $\omega = \omega_{eq} = 1.3\omega_f$ and a corresponding peak which result from the zero in R in (4.1). The actual zero was eliminated by arbitrarily

Sec. G

rounding the curve near $\omega = 1.3\omega_f$ as shown, in keeping with the discussion above. The structure near the zero at ω_{eq} , which is shown in the "unrounded" curve in the inset, is a very narrow slot. The central feature of the heavy curve is that the structure in region S resulting from the minimum is virtually indistinguishable from typical two-phonon structure, as shown in Fig. G9.

V. DISCUSSION OF RESULTS

The magnitude of F/g and the sign of $\mathcal{K}_{LB}/\mathcal{K}_{anh}$ are important in the comparison of β_{LB} and β_{anh} . With $\omega_{eq} = 1.3\omega_f$ from the previous section, (4.2) gives $F/g = 1/3.6$, which is considerably smaller than the estimated values of $1/15$ and $1/20$ from Sec. III. This may not be too serious since great accuracy cannot be expected from such a simple model. Furthermore, the similarity between the resulting heavy curve in Fig. G8 and the experimental curves of Fig. G9 is striking.

However, there is a somewhat more serious problem. The previous theoretical results¹⁰ for β_{anh} (which do not include the Lax-Burstein term) with no adjustable parameters were only slightly less than the experimental values over wide ranges of frequencies for KBr, KCl, NaCl, and LiF.¹⁵ If $\omega_{eq} = 1.3\omega_f$, then the Lax-Burstein mechanism dominates the anharmonic-potential mechanism, and the agreement between experiment and theory is considerably worse. For example, the theoretical value of $\beta_{anh} = 3 \times 10^{-5} \text{ cm}^{-1}$ for NaCl at $10.6 \mu\text{m}$ (i.e., $\omega/\omega_f = 5.75$) is a factor of 2×10^3 greater than the extrapolated experimental value of $\beta_{anh} = 1.5 \times 10^{-8} \text{ cm}^{-1}$ (obtained from $\beta_{anh} = \beta_{exp}/R(5.75\omega_f, 1.3\omega_f) = 6 \times 10^{-4}/4 \times 10^4$). It is of course possible that the previous theoretical values of β were too large, and the values including the Lax-Burstein term are correct.

It is important to notice that if the sign of $\mathcal{K}_{LB}/\mathcal{K}_{anh}$ were positive, the difficulties would not arise. For example, changing the sign of $\mathcal{K}_{LB}/\mathcal{K}_{anh}$ from negative to positive in (4.1) and keeping the same value of $\omega_{eq} = 3\omega_f$ used in Fig. G6 gives the dashed curve in Fig. G6. In fact, this theoretical result is in quite good agreement with the experimental curve (even though the value of $\omega_{eq} = 3\omega_f$

was chosen quite arbitrarily for the purpose of illustrating the dip in the solid curve). It is conceivable that for $\mathcal{K}_{LB}/\mathcal{K}_{anh}$ negative, the dip is removed for some presently unknown reason.

These difficulties are not unique to the present model. The proponents of a dominant Lax-Burstein effect in the alkali halides will have to address these problems in order to obtain a viable theory. The general features of the results above surely will apply to more sophisticated shell models, which are commonly used to fit experimental phonon dispersion relations. The fact that F/g is sufficiently large to give noticeable deviations in the phonon dispersion relations and in the Szigeti effective charge from rigid-ion results implies that the Lax-Burstein mechanism dominates in the observed high-frequency region discussed above. If F/g were completely negligible, there would be no such effects. According to (4.2), $F/g = 1.2 \times 10^{-3}$ for $\omega_{eq} = 6\omega_f$. The $k = 0$ intercept of the optical mode is at $(4F/M)^{1/2}$ for the rigid-ion model and is at $(4F^*/M)^{1/2}$, where $F^* = F/(1 + 2F/g)$, for the Bilz model¹² ($G_n = 0$ in the model of Sec. II). This gives a 10 percent frequency shift for $F/g = 1/10$ and only a 0.12 percent shift for $F/g = 1.2 \times 10^{-3}$. These results suggest that the value of ω_{eq} is well below $6\omega_f$.

One final observation about the sign of $\mathcal{K}_{LB}/\mathcal{K}_{anh}$ is that if the sign were positive for the case of $\omega^2 > \omega_f^2$ considered above, it would be negative for $\omega^2 < \omega_f^2$, according to (3.10). It might be expected that a minimum in $\beta(\omega)$ would then occur at some $\omega = \omega_{+eq} < \omega_f$. This is, however, not the case because $|\mathcal{K}_{LB}/\mathcal{K}_{anh}| = |4\omega(\omega^2 - \omega_f^2)\omega_f^{-3}(F/g)| < 1$ for reasonable values of F/g .

Summarizing briefly, the model and analysis are sufficiently simple to yield unambiguous general results that are expected to be common to other models. The results strongly suggest that the Lax-Burstein mechanism dominates the anharmonic-interaction mechanism in the high-frequency region of current interest. They also point out difficulties in any theory that predicts such a dominant Lax-Burstein mechanism. The most likely of the known possible solutions to the problem of the minimum in $\beta(\omega)$ at ω_{eq} not having been observed is that $\omega_{eq} = \omega_{m1}$. Other possibilities include a positive value of κ_{LB}/κ_{anh} or a negligible value of β_{LB} , either of which would require drastic changes in the results above. The model affords simple explanations of a number of effects, as listed in the introduction.

Conversations with Mr. Armando Moreira are gratefully acknowledged. Dr. C. J. Duthler made useful suggestions on the manuscript.

REFERENCES

This section will be published in the Phys. Rev. (in press).

1. M. Born and K. Huang, Dynamical Theory of Crystal Lattices (Oxford University Press, London, 1968).
2. M. Lax and E. Burstein, Phys. Rev. 97, 39 (1955); M. Born, Rev. Mod. Phys. 17, 245 (1945).
3. B. Szigeti, Lattice Dynamics, Proc. International Conference, Copenhagen, August 1963, Ed. R. F. Wallis (Pergamon Press, Inc., 1965), p. 405.
4. D. L. Mills and A. A. Maradudin, Phys. Rev., in press.
5. B. Bendow and S. C. Ying, Phys. Lett. 42A, 359 (1973).
6. C. Flytzanis, Phys. Rev. Lett. 29, 772 (1972).
7. P. N. Keating and G. Rupprecht, Phys. Rev. 138, A 866 (1965).
8. R. Geick, Phys. Rev. 138, A 1495 (1965).
9. B. Szigeti, Trans. Faraday Soc. 45, 155 (1949); B. Szigeti, Proc. Roy. Soc. (London), A 204, 51 (1950).
10. M. Sparks and L. J. Sham, Solid State Commun. 11, 1451 (1972); M. Sparks and L. J. Sham, Phys. Rev. Lett. 31, 714 (1973).
11. M. Sparks and L. J. Sham, Phys. Rev. Lett. 31, 714 (1973).
12. H. Bilz, Optical Properties of Solids, Ed. S. Nudelman and S. S. Mitra (Plenum Press, New York, 1969), p. 291.
13. Including the F_g term changes q to q^* in the linear terms $-\frac{1}{2} q E (u_{+0i} + u_{-0i})$, as discussed in Sec. II. However, q rather than q^* , appears in the Lax-Burstein terms $-2 q E G_{ng} (u_{+0i}^n - u_{-0i}^n)$.

Sec. G

14. The experimental curves in Figs. G6-G9 are the composite curves from M. Sparks, Xonics Final Technical Report, Contract No. DAH15-72-C-0129, December (1972), pp. 133, 134, and 149, which were compiled from a number of references.
15. A. Karo, M. Sparks, and L. J. Sham (unpublished).

Figure Captions

FIG. G1. Two-phonon summation processes: (a) Lax-Burstein nonlinear-dipole-moment mechanism, and (b) anharmonic-potential mechanism. Wavy lines represent photons and straight lines represent phonons.

FIG. G2. Simple model for Lax-Burstein effect.

FIG. G3. Schematic illustration of diamond showing that symmetry is necessary to prevent diamond from being a polar crystal.

FIG. G4. Schematic illustration of the decrease in dipole moment p as x increases according to Mills and Maradudin and the contrasting increase in p from the present model.

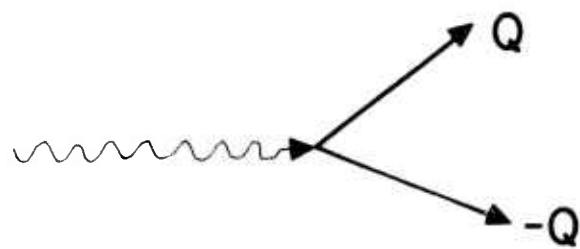
FIG. G5. The four diagrams contributing to the Hamiltonian for the anharmonic-potential process.

FIG. G6. Effect on absorption of including both the Lax-Burstein and anharmonic mechanisms. The negative sign of $\mathcal{K}_{LB}/\mathcal{K}_{anh}$ leads to the great deviation of the heavy curve from an exponential. The experimental curves for this and the following two figures are from p. 133 of Ref. 14.

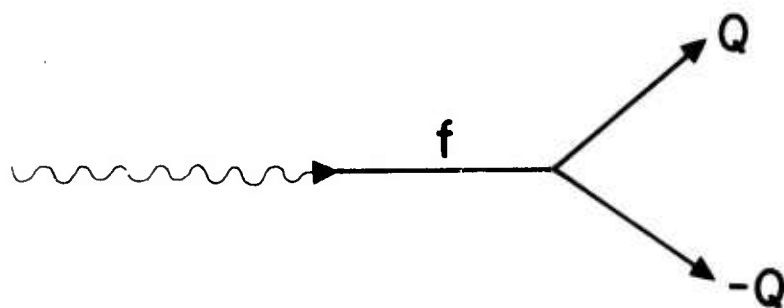
FIG. G7. Large peak in $\beta_{anh}(\omega)$, at $\omega/\omega_f \cong 1.5$, that would result if ω_{eq} were in the two-phonon region.

FIG. G8. Construction showing that if the first observed minimum of $\beta(\omega)$ were at ω_{eq} , the resulting maximum (at $\omega/\omega_f \cong 1.6$) would resemble a two-phonon absorption peak.

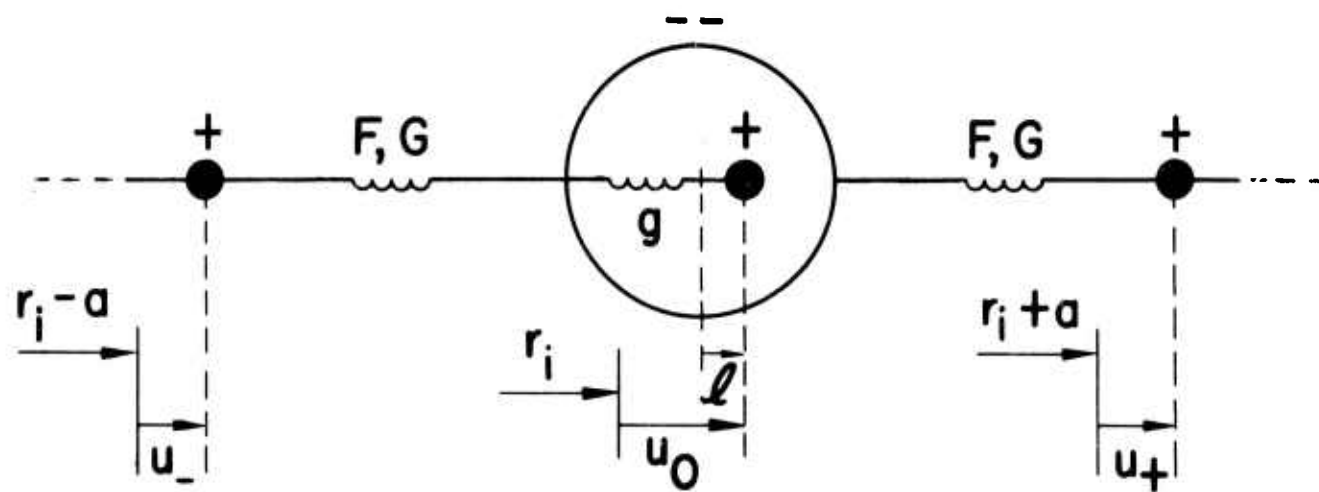
FIG. G9. Experimental absorption curves for comparison with the heavy curve of Fig. G8 resulting from the LB-anisotropy crossover at $\omega_{eq} = 1.3 \omega_f$. The curves are from p. 149 of Ref. 14.

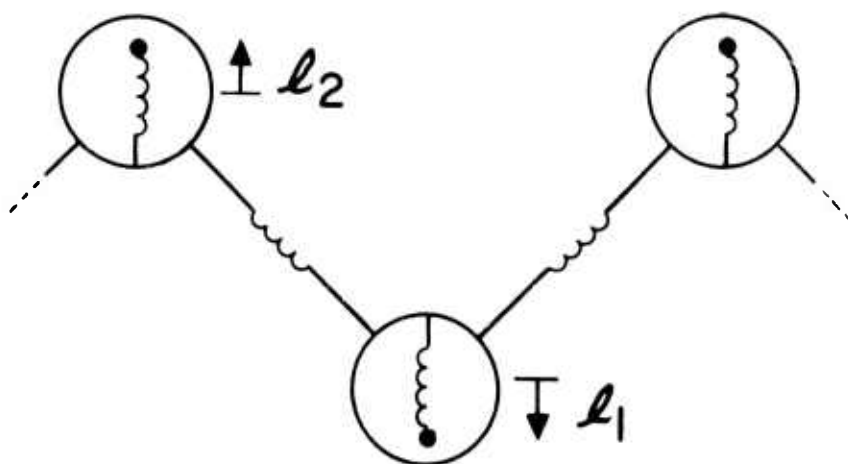


(a)

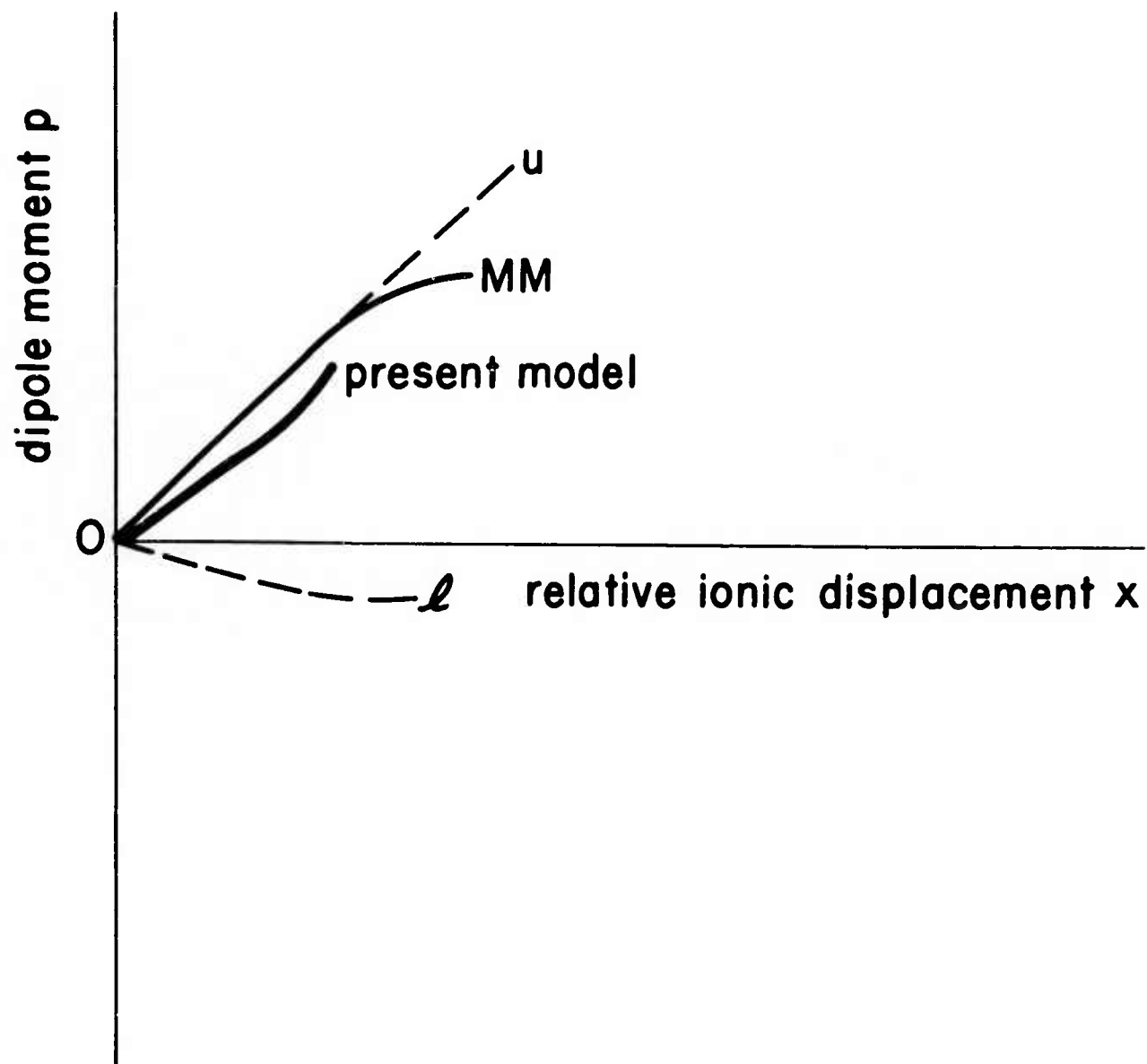


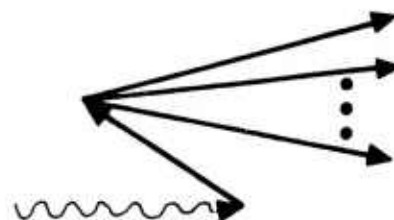
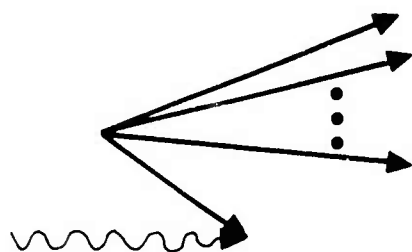
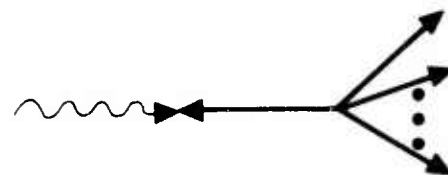
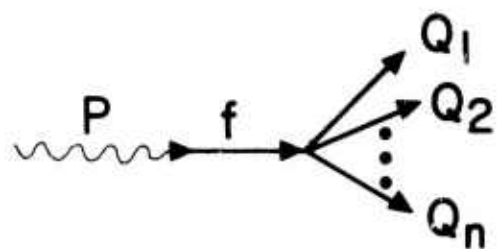
(b)

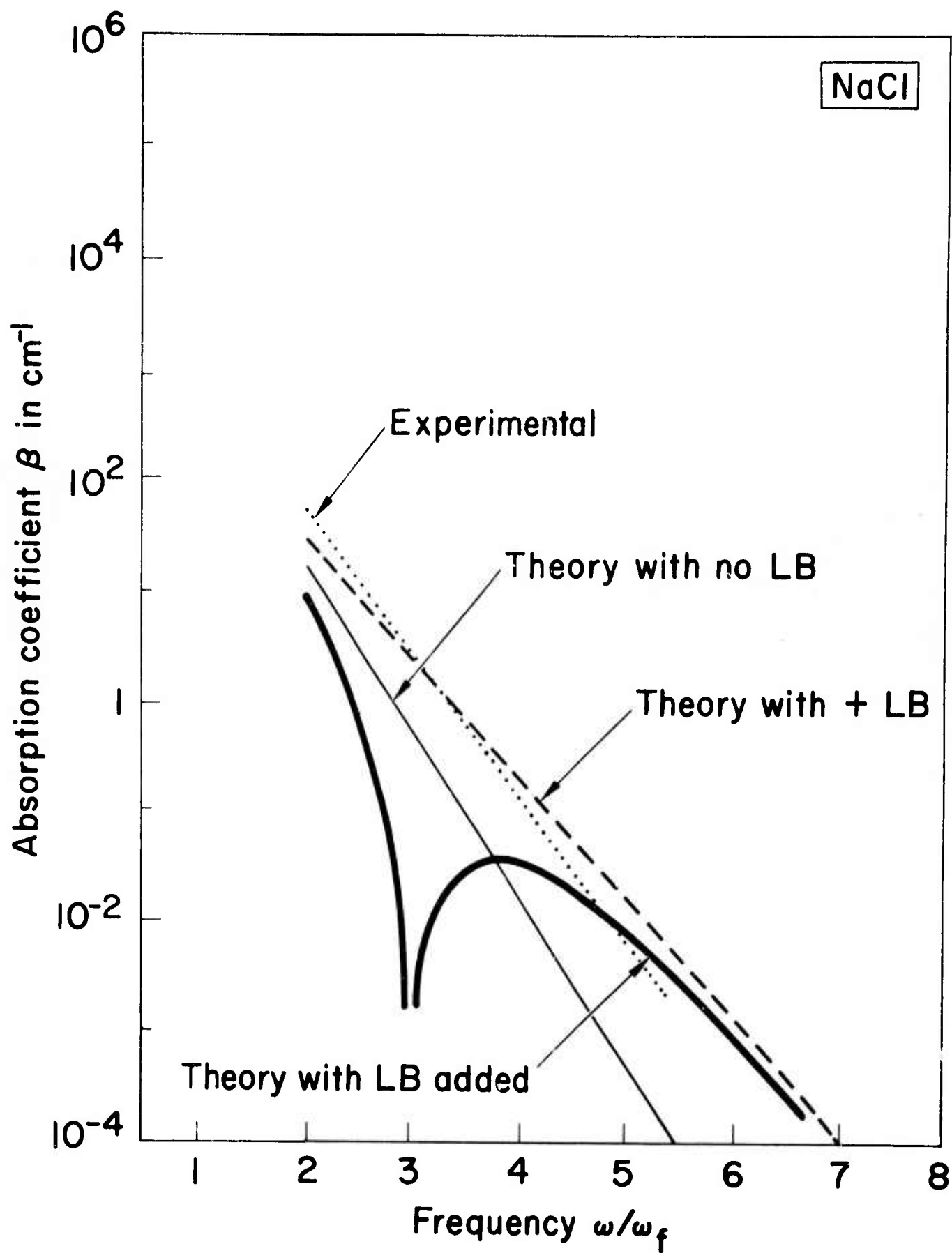


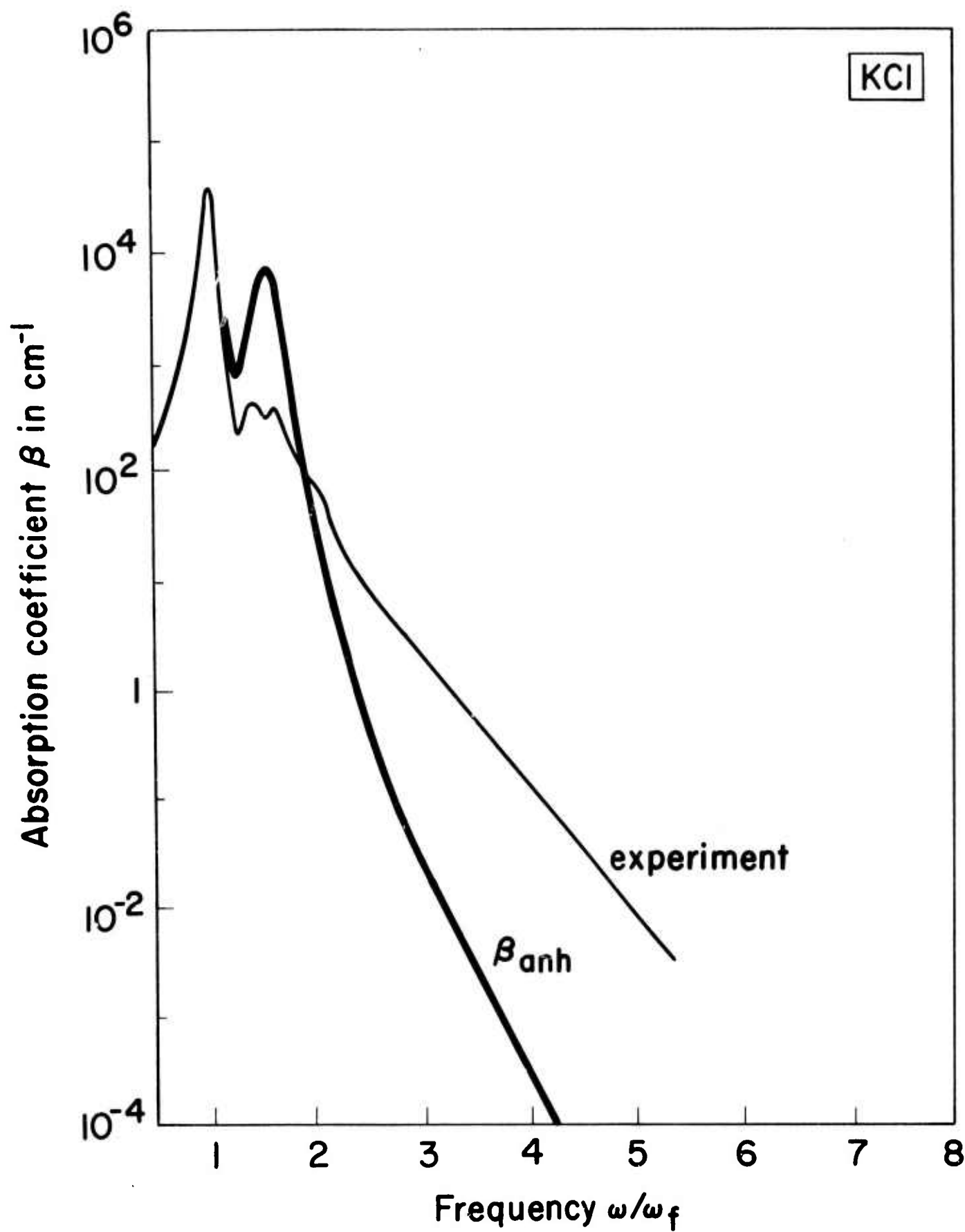


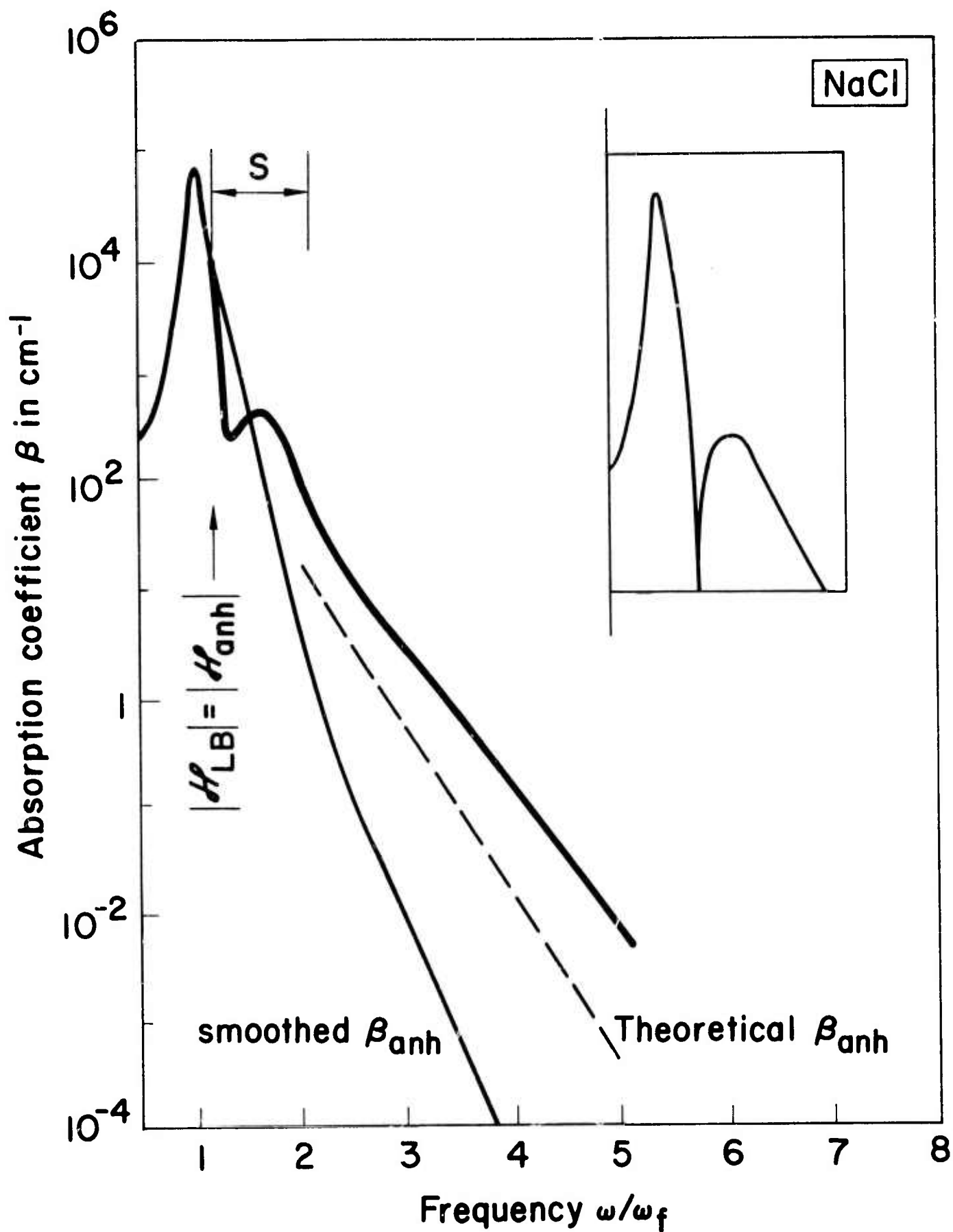
Sec. G

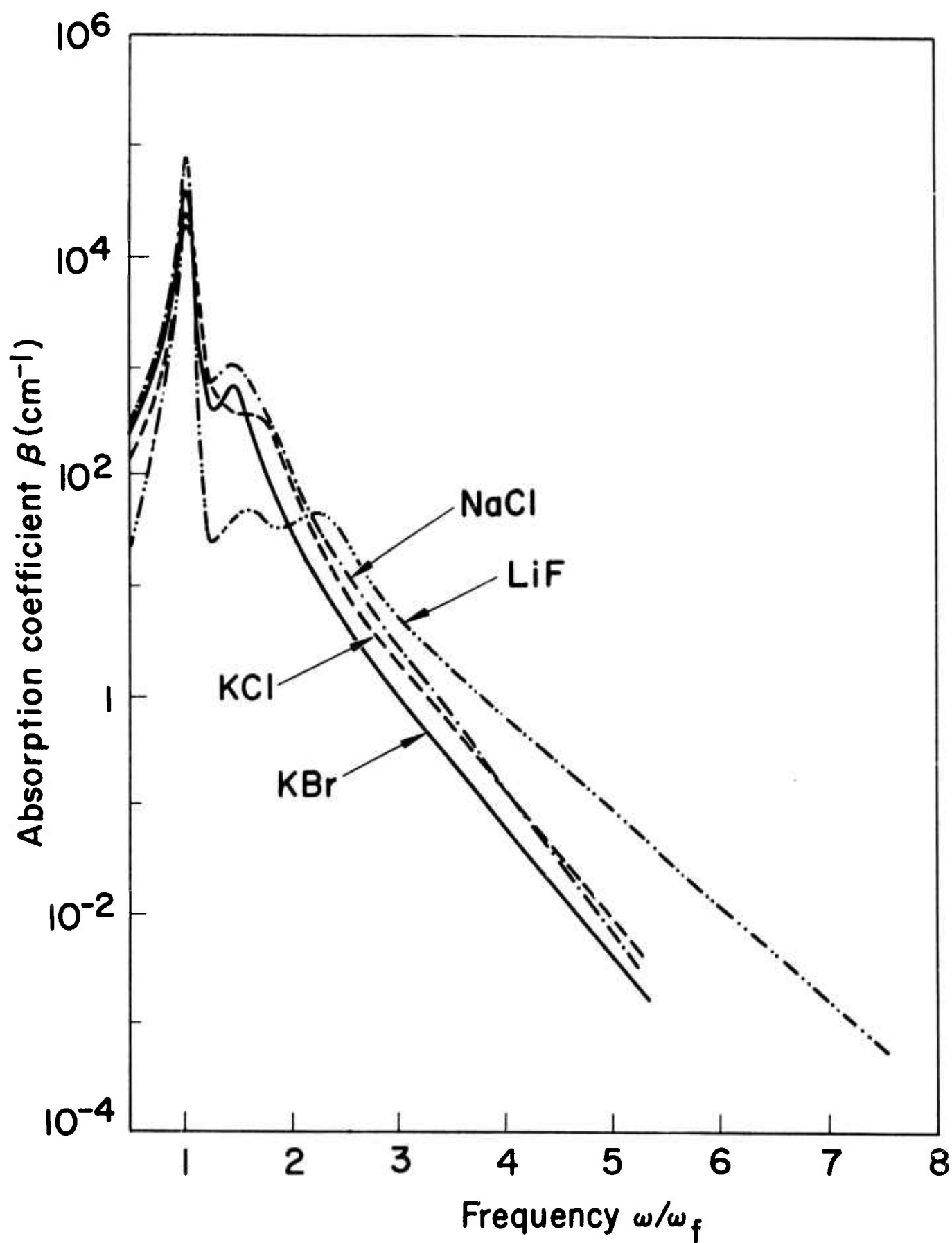












H. STIMULATED RAMAN AND BRILLOUIN SCATTERING: PARAMETRIC INSTABILITY EXPLANATION OF ANOMALIES*

M. Sparks

Xonics, Incorporated, Van Nuys, California 91406

The Raman and Brillouin processes have important sharp-threshold parametric instabilities that afford explanations of long-standing anomalies in stimulated scattering and self-focusing experiments. Below the threshold intensity I_c , the gain is nonexponential and greater than that of previous theories of stimulated scattering, and at the threshold the Stokes intensity increases nearly discontinuously. Typically, $I_c \sim 10^9 \text{ W/cm}^2$ for a number of gases, liquids, and solids. The theoretical results agree well with previous experimental results.

Some of the major problems of the physics of quantum electronics, which concern stimulated scattering, have remained unsolved in spite of numerous investigations. These include "oscillations" observed in a number of systems with insufficient gain to cause oscillations, insensitivity of the "oscillation" threshold to changes in gain, deviations from exponential gain, sharpness of changes in Stokes output, anomalously high gain in a number of systems, a theoretical gain that is orders of magnitude too small to explain the complete conversion to Stokes

radiation in the self-focused forward-moving focal region observed in several liquids, and continued difficulty in explaining the limiting diameter of self-focused beams.

These anomalies are explained in terms of a parametric instability that has been overlooked previously even though parametric instabilities were well known in ferromagnetic resonance, plasma physics, and radio-wave propagation.^{1,2} In ferromagnetic systems, instabilities are observed in samples that are small with respect to the microwave-photon wavelength. The stimulated scattering processes are more complicated since propagation of the photons must be considered.

By using the well known perturbation theory result for the rate of transitions between states, the rate of creation of Stokes photons per volume V by the Raman process can be written down immediately as $C[(n_S + n_Q + V^{-1})n_L - n_S n_Q]$, where $C = 2\pi |V_R/\hbar|^2 V \delta(\tilde{\omega})$, with V_R the Raman matrix element, δ the delta function, $\tilde{\omega} \equiv \omega_L - \omega_S - \omega_Q$, and L, S , and Q denote laser, Stokes, and phonon. The n 's are Boson occupation numbers, which come from the well known three-Boson factor $n_L(n_S + V^{-1})(n_Q + V^{-1}) - (n_L + V^{-1})n_S n_Q$.¹ In gases and liquids, "phonon" means the nearly dispersionless excitation of the system that is excited in the Raman process. The intensities I are related to the n 's by the expressions $I_L = \hbar \omega_L c_L n_L$ and $I_S = \sum \hbar \omega_S c_S n_S$, where the sum is over S and Q in the appropriate solid angle and bandwidth. (Wavevector conservation, which was not displayed explicitly in V_R , eliminates one of the sums.)

By considering the values of n_S and n_Q in a small element dx of the laser beam at position x , we obtain

$$\partial n_S / \partial t = C \left[(n_S + n_Q + V^{-1}) n_L - n_S n_Q \right] - c_S \beta_{\text{loss}} n_S - c_S \partial n_S / \partial x, \quad (1)$$

$$\partial n_Q / \partial t = C \left[(n_S + n_Q + V^{-1}) n_L - n_S n_Q \right] - \Gamma_Q (n_Q - \bar{n}_Q) - v_Q \partial n_Q / \partial x, \quad (2)$$

where $c_S \beta_{\text{loss}}$ and Γ_Q are inverse lifetimes and c_S is the velocity of the Stokes wave. The last term in (2) is negligible since the phonon velocity v_Q is negligibly small, as is easily verified. Previous treatments^{3,4} considered only (1) or neglected the terms $C(n_Q + V^{-1})n_L$ and $-Cn_S n_Q$. By keeping (2) and $C(\bar{n}_Q + V^{-1})n_L$, where the bar denotes the thermal equilibrium value, the solution automatically included "amplification of noise," which was introduced intuitively in the past. By keeping the term $C(n_Q - \bar{n}_Q)n_L$, the parametric instability is obtained, and by keeping the term $-Cn_S n_Q$, the infinity at the threshold of the instability is removed, allowing effects above the threshold to be studied.

Summing (1) over S , adding the result to the analogous equation for n_L , setting the time derivatives equal to zero, neglecting the β_{loss} terms, using $c_S \cong c_L$, and integrating over x gives $n_L = n_{Li} - \sum n_S$, where n_{Li} is the incident value of n_L , and the sum is over Stokes modes. Using this result, setting $\partial n_S / \partial t = \partial n_Q / \partial t = 0$, subtracting (2) from (1) and solving for n_Q , which is substituted into (1), and using the well satisfied approximation $\bar{n}_Q \ll n_{Li}$ gives

$$(n_c - n_{Li} + n_S + \sum n_S) \left(\frac{dn_S}{dx} + \beta_{\text{loss}} n_S \right) = \beta_c (n_{Li} - \sum n_S) (\bar{n}_Q + V^{-1} + n_S) \quad (3)$$

where $\beta_c \equiv \Gamma_Q / c_S$ and $n_c \equiv \Gamma_Q / C$ is the instability-threshold value of n_{Li} as seen below. For values of I_S well below the saturation value $I_{Li} \equiv \hbar \omega_L c_L n_{Li}$, the factors $n_S + \sum n_S$ and $\sum n_S$ are negligible, (3) is linear, and the solution

$$n_S(x) \cong n_{sp} \left(e^{\beta_{\text{tot}} x} - 1 \right) + n_S(0) e^{\beta_{\text{tot}} x} \quad (4)$$

where $n_{sp} = (\bar{n}_Q + V^{-1}) (1 - \beta_{loss} / \beta_{g\ new})^{-1}$, $\beta_{tot} = \beta_{g\ new} - \beta_{loss}$, and $\beta_{g\ new} = \beta_c (n_c / n_{Li} - 1)^{-1}$, is a central result of the paper. The first term on the right-hand side of (4) is the amplified spontaneous emission and the second term is the amplified input Stokes wave. The latter term in the limit $I_{Li} / I_c \ll 1$ is the previously known result for stimulated Raman scattering.^{3,4} The well known expression for the previous gain $\beta_g = \beta_c n_{Li} / n_c = 2\pi c^2 N \sigma_R I_L / \hbar (\bar{n}_Q + V^{-1}) \omega_L \omega_S^2 \Gamma_Q$ at resonance, where σ_R is the Raman cross section and N is the number of molecules in the system, is easily derived from (1) with $\partial n_S / \partial t = 0$, $\partial n_S / \partial x = \beta n_S$, and $\sigma = \beta V / N$.

In order to study the saturation of I_S as I_{Li} is depleted, the divergence in n_S at $n_{Li} = n_c$ in (4) is removed by retaining the nonlinear terms in (3). The gross features of solution⁵ are approximated by formally replacing Σn_S by $\mathcal{N} n_{Sr}$, where n_{Sr} is the resonant value (lineshape factor $\delta(\tilde{\omega}) \rightarrow 1/\pi \Gamma_Q$) of n_S and \mathcal{N} is an effective number of modes. For large values of I_{Li} , $n_{Sr} \gg \bar{n}_Q + V^{-1}$ is typically satisfied, and the solution to (3) is

$$\left(\frac{I_{Li} - I_S}{I_{Li} - I_{S0}} \right)^{\beta_c / \beta_\sigma} \left(\frac{I_S}{I_{S0}} \right)^{1 - I_c / I_{Li}} = e^{-\beta_c x} \quad (5)$$

where $\beta_\sigma \equiv \beta_c / (I_c / I_{Li} + 1 / \mathcal{N})$, $I_S = \hbar \omega_S c_S \mathcal{N} n_{Sr}$, $I_{S0} = \hbar \omega_S c_S \mathcal{N} n_{S0}$ $= (I_{Li} - I_c) \mathcal{N} / (\mathcal{N} + 1)$ for $I_{Li} > I_c$, and I_{S0} is the incident (input) value of I_S for $I_{Li} < I_c$. For $I_{Li} = I_c$, the solution to (5) is $I_S \cong I_c [1 - \exp(-\beta_\sigma x)]$, and for $I_{Li} \gg I_c$ and $\mathcal{N} \gg 1$, $I_S \cong I_{Li} - I_c \exp(-\beta_c x)$. For $I_{Li} \ll I_c$, (5) gives $I_S = I_{Li} [(I_{Li} / I_{S0} - 1) \exp(-\beta_g x) + 1]^{-1}$, which reduces to (4) when $\bar{n}_Q + V^{-1} = 0$ and $I_{S0} \ll I_{Li} \ll I_c$.

These three limiting cases are sketched in Fig. H1. The portion of the lowest curve marked SRS corresponds to the previously studied case of stimulated-Raman-scattering amplification. Note the saturation $I_S \cong I_{Li}$ for $x \gg 1/\beta_c$ in all three cases. As I_{Li} increases, the distance required for saturation decreases, and for $I_{Li} > I_c$, I_S is nonzero at the input surface.⁶ The characteristic distance $1/\beta_c = c_S/\Gamma_Q$ has a typical value of order 10^{-2} to 1 cm. Thus, for $I_{Li} \cong I_c$, large conversion to Stokes radiation occurs near the input face of the sample.

There is evidence for the instability throughout the literature in various types of experiments in gases, liquids, and solids.⁷⁻¹² However, there is little data for which accurate quantitative comparison with experiment can be made, a notable exception being the experiment⁷ on liquid O_2 and N_2 . As the laser power was increased, the Stokes power exhibited successively regions of spontaneous emission, gain, a nearly discontinuous increase by 3-6 orders of magnitude (called the jump), and a saturation region of little further increase. See Fig. H2. There was no self focusing. All known mechanisms for explaining the jump, with the possible exception of oscillations due to feedback by Rayleigh scattering, were ruled out by the authors.

Fig. H2 illustrates the good agreement between the experimental points from Ref. 7 and the theoretical curve, plotted from (4), which is valid for most of the curve ($I_S/I_c < 0.1$), and (5) using the theoretical value of $\beta_c = \Gamma_Q/c_S = 0.51 \text{ cm}^{-1}$ and the observed values of the spontaneous-emission and saturation Stokes intensities and adjusting the value of I_c to position the jump properly. Thus only the scale factors for the axes, and not the shape of the curve, were adjusted to fit the experimental points. Adjusting β_c to smaller values improves the fit, but is

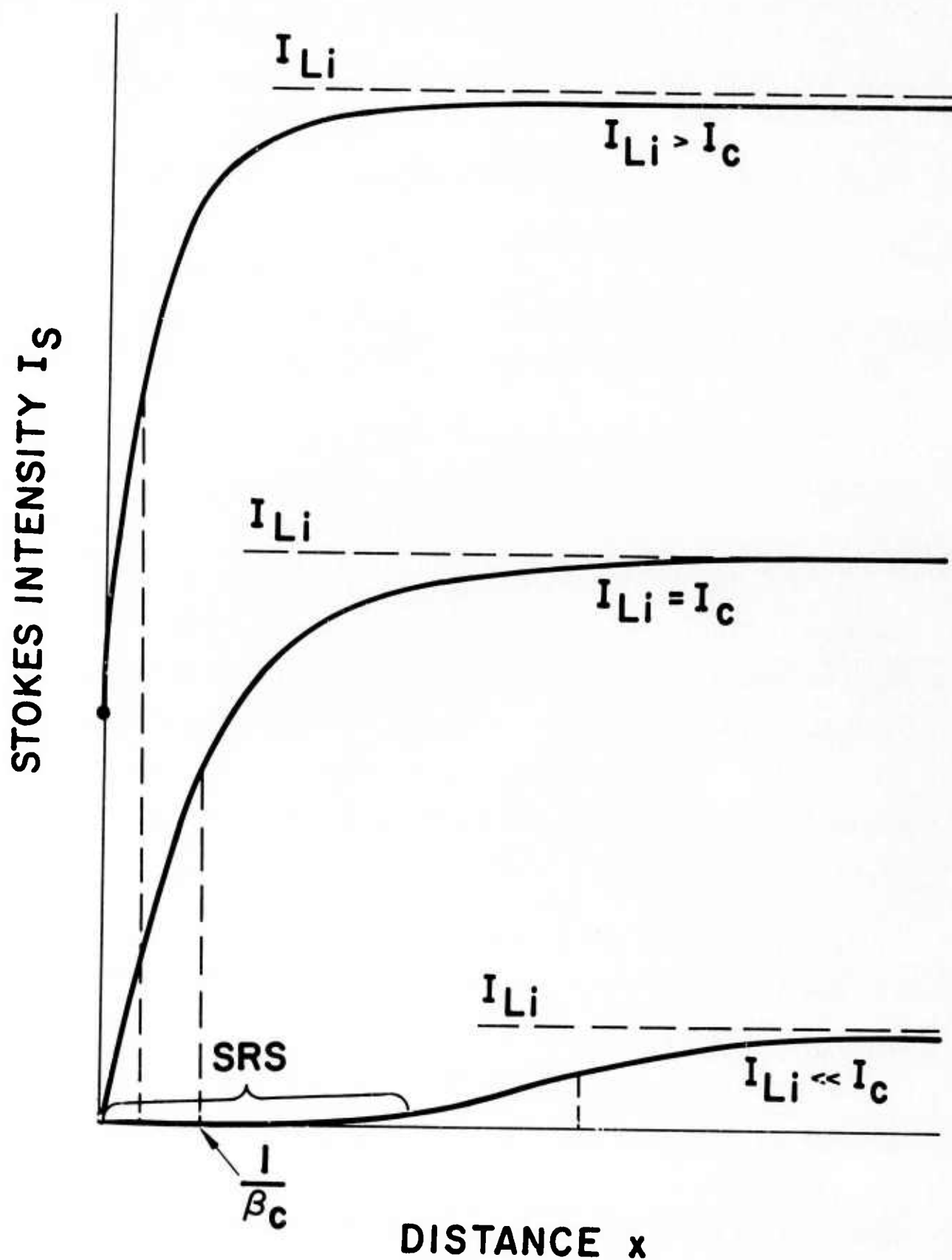


Fig. H1. Schematic illustration of the Stokes intensity I_S for three limiting values of incident laser intensity I_{Li} .

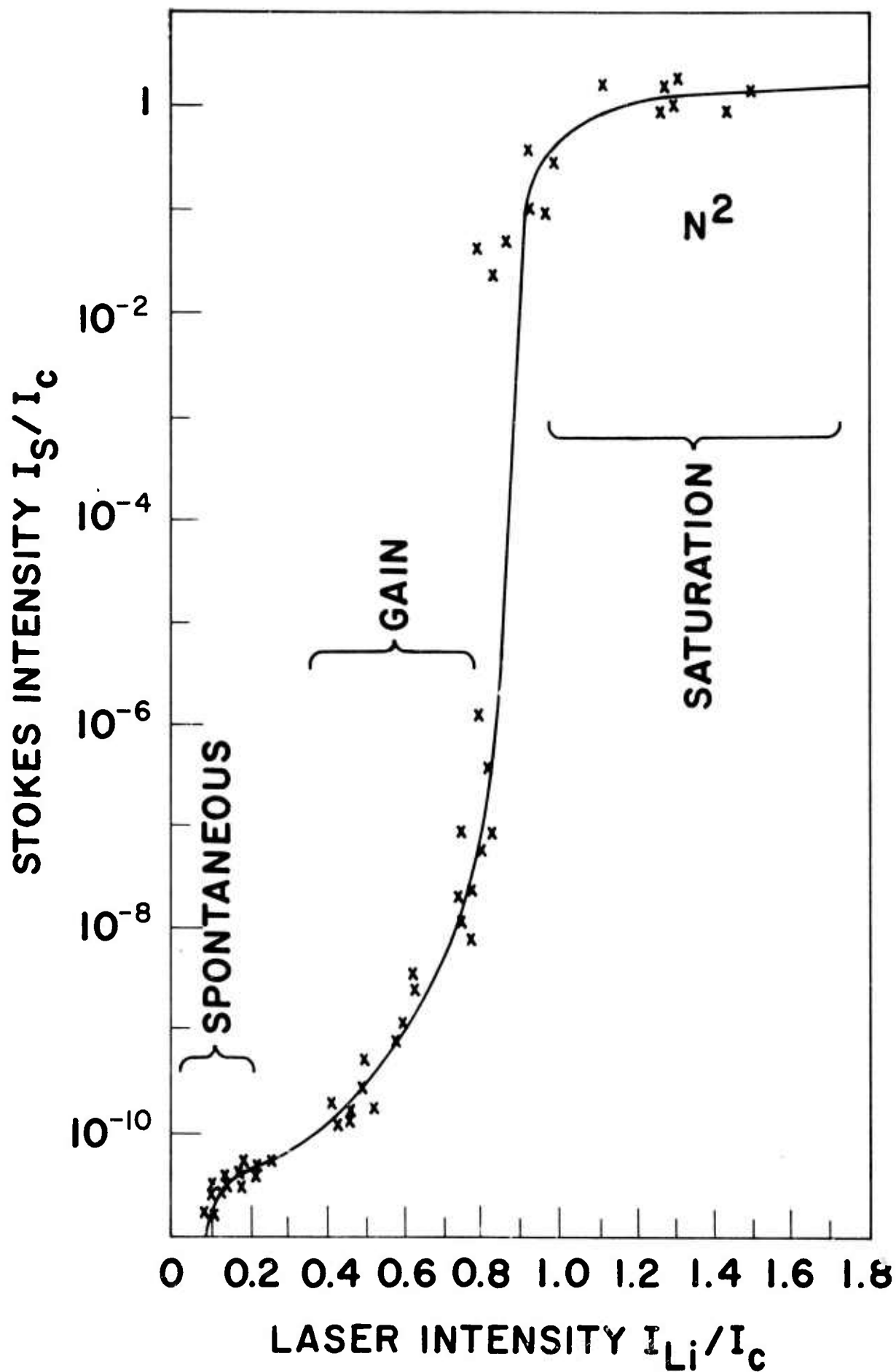


Fig. H2. Comparison of experimental points from Ref. 7 with theoretical curve.

unnecessary in view of the already satisfactory agreement and the scatter in the experimental points. The jump, the saturation at large I_{Li} , the transition from unamplified to amplified spontaneous emission, and the previously unexplained magnitude of β_g and deviation from exponential gain in the gain region $0.3 \lesssim I_{Li}/I_c \lesssim 0.9$ (resulting from $\beta_{g\text{ new}} > \beta_g$), are apparent in the theoretical curve. Second-order Stokes radiation was observed at high intensities, as expected. For $I_{Li} \leq I_c$, which covers the major region of interest in Fig. H2, the steady state is approached in a time of order $\Gamma_Q^{-1} \approx 10^{-10}$ sec, which is short with respect to the pulse duration of $\sim 10^{-8}$ sec.

Similar jumps have been observed in numerous other investigations in gases, liquids, and solids,⁸⁻¹² but focusing and/or self focusing make accurate comparison with the theory difficult. Amplifiers have not reached their expected gains, as the jump could not be suppressed no matter how much the feedback was reduced. The present interpretation of the jump as the parametric instability at $I_{Li} = I_c$ explains the insensitivity to and lack of need for feedback. Hagenlocker and co-workers⁸ observed that the Stokes power generated by a laser beam focused in hydrogen gas at 100 atmospheres and room temperature, where self focusing is not expected, increased by 10 to 11 orders of magnitude as the laser power was increased by a factor of two. Such a sharp increase cannot be explained by normal stimulated Raman gain,⁸ but agrees well with the present theory. The laser intensity at the threshold was of order 250 MW/cm^2 (for $\sim 2.2 \text{ MW}$ in an area of approximately 0.01 cm^2 or slightly less).¹³ From the values of $\Gamma_Q = 2 \times 10^{10} \text{ sec}^{-1}$ and $\beta_g/I_{Li} = 1.5 \times 10^{-9} \text{ cm/W}$, the theoretical value of I_c is $\Gamma_Q I_{Li}/c_S \beta_g = 450 \text{ MW/cm}^2$. The agreement is satisfactory since the experimental value of 250 MW/cm^2 is only an order-of-magnitude estimate in view of the uncertainties in the focused spot size and the value of Γ_Q .

Self-focusing results can be misleading because it is difficult to obtain detailed information on self focusing and experimental results reported in the literature are conflicting. Nevertheless, a number of observed jumps^{4,9-12} undoubtedly result from an increase in intensity by self focusing and the parametric instability in the region of high intensity. Also, Loy and Shen¹⁴ observed that the energy in the forward moving focus in a number of liquids was essentially completely converted to Stokes radiation. Unless the instantaneous length of the focal region is two orders of magnitude greater than the diameter, previous theories cannot explain such great scattering. According to the present theory, if the steady state were attained, complete conversion would occur at $I \cong I_c = 4 \times 10^9 \text{ W/cm}^2$. This value is less than the experimental value of $I = 8 \text{ kW}/(\pi/4)(5 \mu\text{m})^2 = 4 \times 10^{10} \text{ W/cm}^2$, in agreement with the prediction based on (1) and (2) that the steady state is not attained. Preliminary results of an investigation of the transient solution of (1) and (2) indicate that limiting of the focal-spot diameter d_f by conversion to Stokes radiation explains the size of d_f in a number of materials at least as well as other proposed mechanisms.¹⁵⁻¹⁷ Appropriate experiments, important practical consequences of the theoretical results, Brillouin and backward scattering, second- and higher-order Stokes generation, and the time-dependent solution will be discussed in the detailed presentation.⁵

REFERENCES

* This section has been published in the Phys. Rev. Lett. 32, 450 (1974).

1. M. Sparks, Ferromagnetic Relaxation Theory (McGraw-Hill, New York, 1964).
2. Recently M. Sparks and H. C. Chow, to be published, have considered parametric instabilities in infrared absorption.
3. R. W. Hellwarth, Phys. Rev. 130, 1850 (1963).
4. Y. R. Shen and N. Bloembergen, Phys. Rev. 137, A 1787 (1965); N. Bloembergen, Am. J. Phys. 35, 989 (1967); F. De Martini, Phys. Rev. B 4, 4556 (1971).
5. M. Sparks, to be published.
6. In practice, the discontinuity in I_S at the surface will be removed by a higher-order effect, such as the nonlinearity of the vibrational modes.
7. J. B. Grun, A. K. McQuillan, and B. P. Stoicheff, Phys. Rev. 180, 61 (1969).
8. E. E. Hagenlocker, R. W. Minck, and W. G. Rado, Phys. Rev. 154, 226 (1967).
9. G. Bret and G. Mayer, Physics of Quantum Electronics, P. L. Kelley, B. Lax, and P. E. Tannenwald, Eds. (McGraw-Hill, New York, 1966).
10. G. Bisson and G. Mayer, J. Phys. 29, 97 (1968).
11. A. K. McQuillan, W. R. L. Clements, and B. P. Stoicheff, Phys. Rev. A 1, 628 (1970).
12. W. Maier, W. Kaiser, and J. A. Giordmaine, Phys. Rev. 177, 580 (1969).
13. W. G. Rado, private communication.
14. Michael M. T. Loy and Y. R. Shen, J. Quant. Elec. QE-9, 409 (1973).
15. E. Yablonovitch and N. Bloembergen, Phys. Rev. Lett. 29, 907 (1972).
16. J. H. Marburger and E. Dawes, Phys. Rev. Lett. 21, 556 (1968).
17. R. G. Brewer and C. H. Lee, Phys. Rev. Lett. 21, 267 (1968).

I. EXTRINSIC ABSORPTION IN 10.6 μm LASER WINDOW MATERIALS

C. J. Duthler and M. Sparks

Xonics, Incorporated, Van Nuys, California 91406

Two types of extrinsic absorption are discussed. First, our calculations on absorbing inclusions, presented at the 1973 NBS-ASTM Symposium on Laser Induced Damage in Optical Materials, have been extended to explain the cone-shaped surface pits observed by Boling. For a spherical inclusion of radius a located a distance d below the surface, the cone half-angle is $\theta_m = \cos^{-1}(a/d)$. The second type of absorption is that due to polyatomic molecular-ion impurities in alkali halides. A literature survey indicates that concentrations of less than 0.1 ppm of NO_2^- , HCO_3^- , SO_4^{2-} , or CrO_4^{2-} will result in a bulk absorption coefficient $\beta(10.6 \mu\text{m}) > 10^{-4} \text{ cm}^{-1}$.

I. INTRODUCTION

We have previously reported our calculations of infrared absorption and materials damage in transparent materials containing inclusions.¹ We have extended our studies of extrinsic absorption in transparent laser materials to include two new effects. First, the mechanism is described for producing cone-shaped surface damage sites that are observed when certain materials are irradiated with a high-power, short-pulse-length laser at the threshold for damage. Second, certain molecular-anion impurities that substitute for the halide ion in alkali-halide crystals can contribute substantially to the extrinsic 10.6 μm absorption in these materials.

II. CONICAL SURFACE-DAMAGE PITS

At the 1973 NBS-ASTM Symposium on Laser Induced Damage in Optical Materials, Boling, Dube', and Crisp² presented electron micrographs of several materials which suffered pre-plasma surface damage when irradiated with a 30 nsec, $1.06\text{ }\mu\text{m}$ laser pulse of energy from 7 to 25 J/cm^2 . These damage sites are nearly perfectly conical having diameters of a few microns and depths of the order of one micron.

Due to the statistical distribution of the pits on the sample surface, it was proposed that the damage was initiated by an absorbing inclusion located just below the surface. Differing damage thresholds observed when various polishing compounds are used indicate that the inclusions may be polishing grits that somehow become embedded below the surface. Similar damage sites have been observed with thin films by Milam, Bradbury, and Bass.³

During the discussion following the talk by Boling, it was proposed that the conical pit was a crater resulting from the explosion of the inclusion as with conventional explosives. With conventional explosives the crater radius is related to the $1/3$ power of the energy, and it was suggested that this may apply in the case of laser damage.

In a discussion with Dr. Robert Hellwarth after the symposium, we realized that the explosive mechanism is incorrect since it implies that the material in the conical section is completely broken up. A simple calculation reveals that there is only enough energy absorbed by the inclusion to disrupt the chemical bonds along the conical surface and that there is not enough energy available to further disrupt the cone.

Sec. I

Consider a conical pit of $7\text{ }\mu\text{m}$ diameter and $2\text{ }\mu\text{m}$ depth resulting from absorption by a $1\text{ }\mu\text{m}$ radius inclusion. The absorption cross-section of a dielectric inclusion is given by

$$\sigma_{\text{abs}} = A \beta_I \pi a^3, \quad (1)$$

where β_I is the absorption coefficient of the inclusion material, a is the inclusion radius, and A is a constant of order unity.¹ If we use $\beta_I = 10\text{ cm}^{-1}$ and a laser fluence of 15 J/cm^2 , the energy absorbed is $3 \times 10^9\text{ eV}$. Assuming that there is one chemical bond of energy 1 eV per $4 \times 10^{-16}\text{ cm}^2$ of surface, the energy required to remove the conical section is $1 \times 10^9\text{ eV}$.

Therefore a mechanism is needed whereby the conical section is removed intact, or in a small number of fragments. One is led to consider shock waves which, however, can be quickly ruled out by mechanical equilibrium considerations.⁴ In order for a compressive shock propagating outward from the inclusion to be able to produce fracture, the pulse length of the shock must be short compared to the time for sound to travel from the inclusion to the surface. In sapphire the velocity of sound is $1.1 \times 10^6\text{ cm/sec}$. This yields a round-trip time for sound of less than 10^{-9} sec which is less than even the 30 nsec rise time of the compressive pulse. For the sake of completeness, we mention that Fox and Barr⁵ have observed laser-induced shock-wave damage in the back face of aluminum samples.

Hence the inclusion is viewed as acting as a source of quasistatic hydrostatic pressure within the cavity in the host material. The situation is sketched in Fig. 11. Neglecting heat flow out of the inclusion, the pressure P at the inclusion-host interface is found by equating the volume change of the heated and compressed inclusion

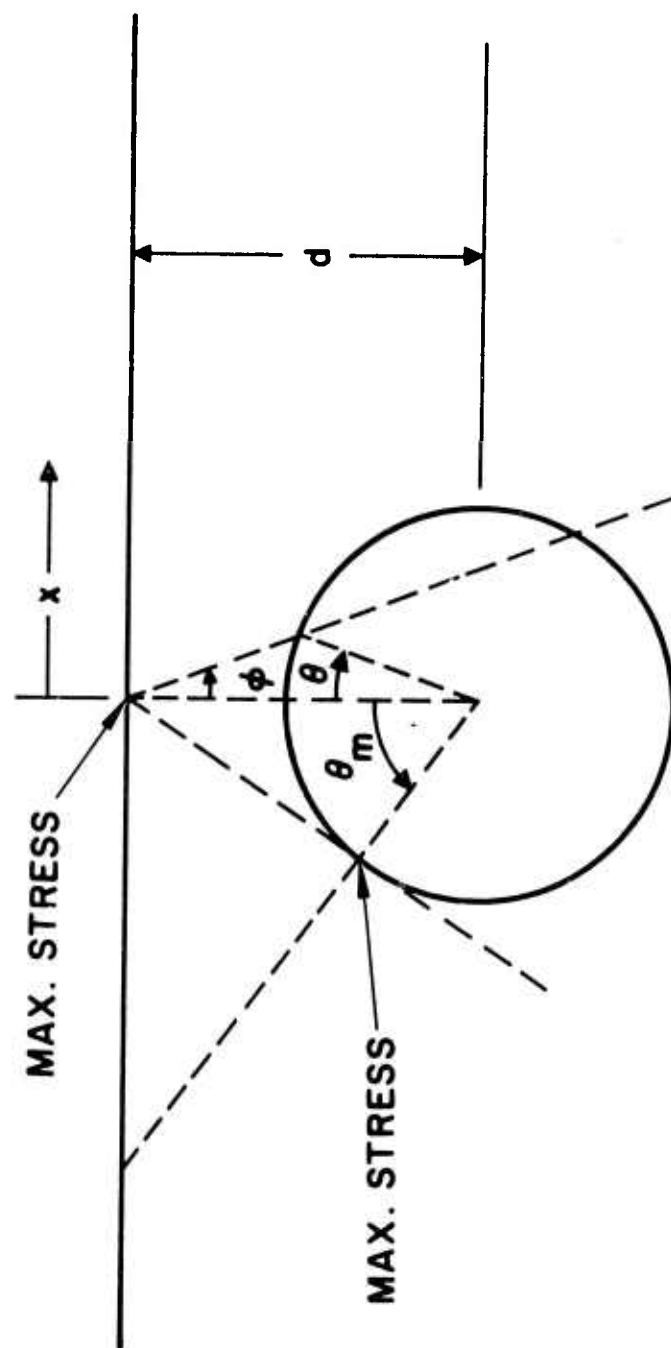


Fig. 11. Sketch of inclusion of radius a at a distance d below the plane surface.

Sec. I

to the volume change of compressed but unheated cavity in the host material, which yields

$$P = 3\alpha_I B_{\text{eff}} T \quad (2)$$

In Eq. (2) T is the temperature of the inclusion, α_I is the linear thermal expansion coefficient of the inclusion, and B_{eff} is an effective bulk modulus given by $B_{\text{eff}}^{-1} = B_I^{-1} + B_H^{-1}$, where I and H denote inclusion and host.

If hydrostatic pressure P is applied within a spherical cavity in an infinite medium, the tensile stress along the spherical surface is given by $\sigma_t = P/2$. However, due to the proximity of the plane surface in the present case, the tensile stress is no longer uniform over the spherical cavity.

The exact solution for the 3-dimensional problem of stresses surrounding a spherical cavity near a plane boundary is very difficult, and approximate solutions converge very slowly. Fortunately, the exact solutions have been obtained for the qualitatively similar problem of a long cylindrical cavity aligned with its axis parallel to the plane surface.⁶ These solutions can be used to gain insight into the present problem.

It is found that the tensile stress along the cylindrical cavity is anisotropic and is enhanced above the value that would be obtained in an infinite medium. The stress along the cylindrical surface σ_t is a maximum at the angle $\theta_m = \cos^{-1}(a/d)$ as is sketched in Fig. 11. Along the plane surface, maximum stress σ_x occurs at $x = 0$.

The dependence of the stresses $\sigma_t(\theta = \theta_m)$ and $\sigma_x(x = 0)$ on the depth of the inclusion is drawn in Fig. 12. For an inclusion near the plane surface ($d/a \rightarrow 1$), the stresses are very much enhanced over the infinite medium

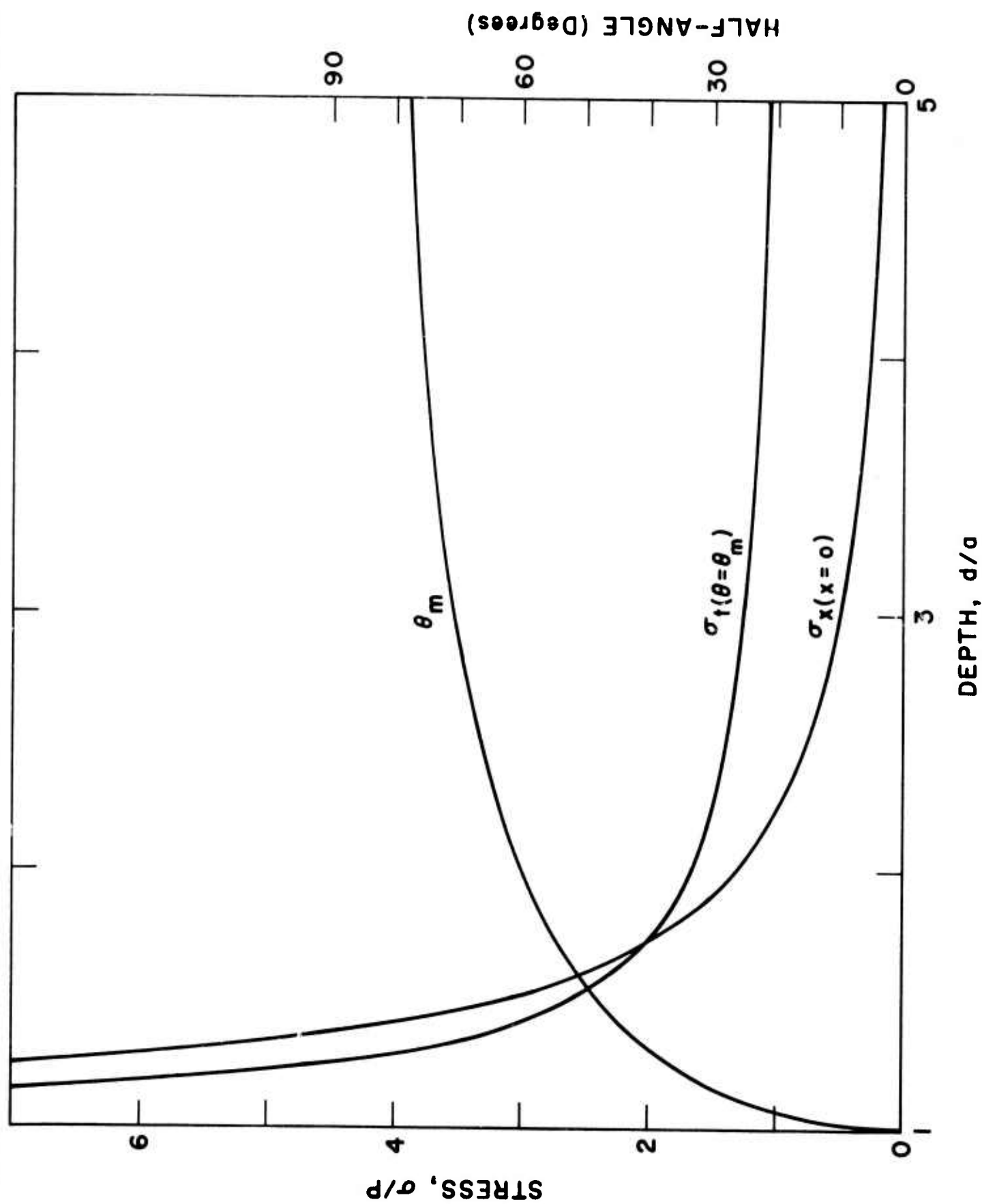


Fig. 12. Tensile stresses and cone half angle as a function of inclusion depth.

values. As d becomes large compared to a , the stresses approach the infinite medium values of $\sigma_t = P$ and $\sigma_x = 0$. The two curves cross at $d = \sqrt{3}a$.

Due to symmetry, the maximum stress along the surface of a spherical inclusion is expected to occur at the same angle θ_m as is shown in Fig. I1. However, the exact dependence of the stress on d/a will be slightly different from those shown in Fig. I2. First, the infinite-medium value for the stress on the spherical surface is $\sigma_t = P/2$. Second, since the stress in the medium surrounding a sphere falls off more rapidly with distance than those surrounding a cylinder, the σ versus d curves are expected to be more strongly peaked near $d/a = 1$ than in Fig. I2.

The mechanism proposed for producing a conical pit is that a crack is nucleated at the point of maximum stress. For d greater than approximately $\sqrt{3}a$, this maximum stress occurs at the angle θ_m on the spherical cavity. The crack then propagates normal to the surface of the spherical cavity until it reaches the plane surface, directly forming a cone-shaped cavity. This is sketched in Fig. I3(a). The half-angle of the cone is θ_m , which is given as a function of d/a in Fig. I2.

Inclusions very close to the surface ($d/a < \sqrt{3}$) will produce maximum tensile stress at the point $x = 0$ on the plane surface. As is sketched in Fig. I3(b), a crack will first propagate from the point $x = 0$ to the cavity surface. Further expansion of the inclusion could result in additional failure near θ_m to produce a cone-shaped damage site.

The following considerations favor fracture first occurring at θ_m as in Fig. I3(a) rather than at $x = 0$ as in Fig. I3(b): Fracture in bulk materials is strongly dependent on surface cracks and imperfections which have the same size as the inclusion.

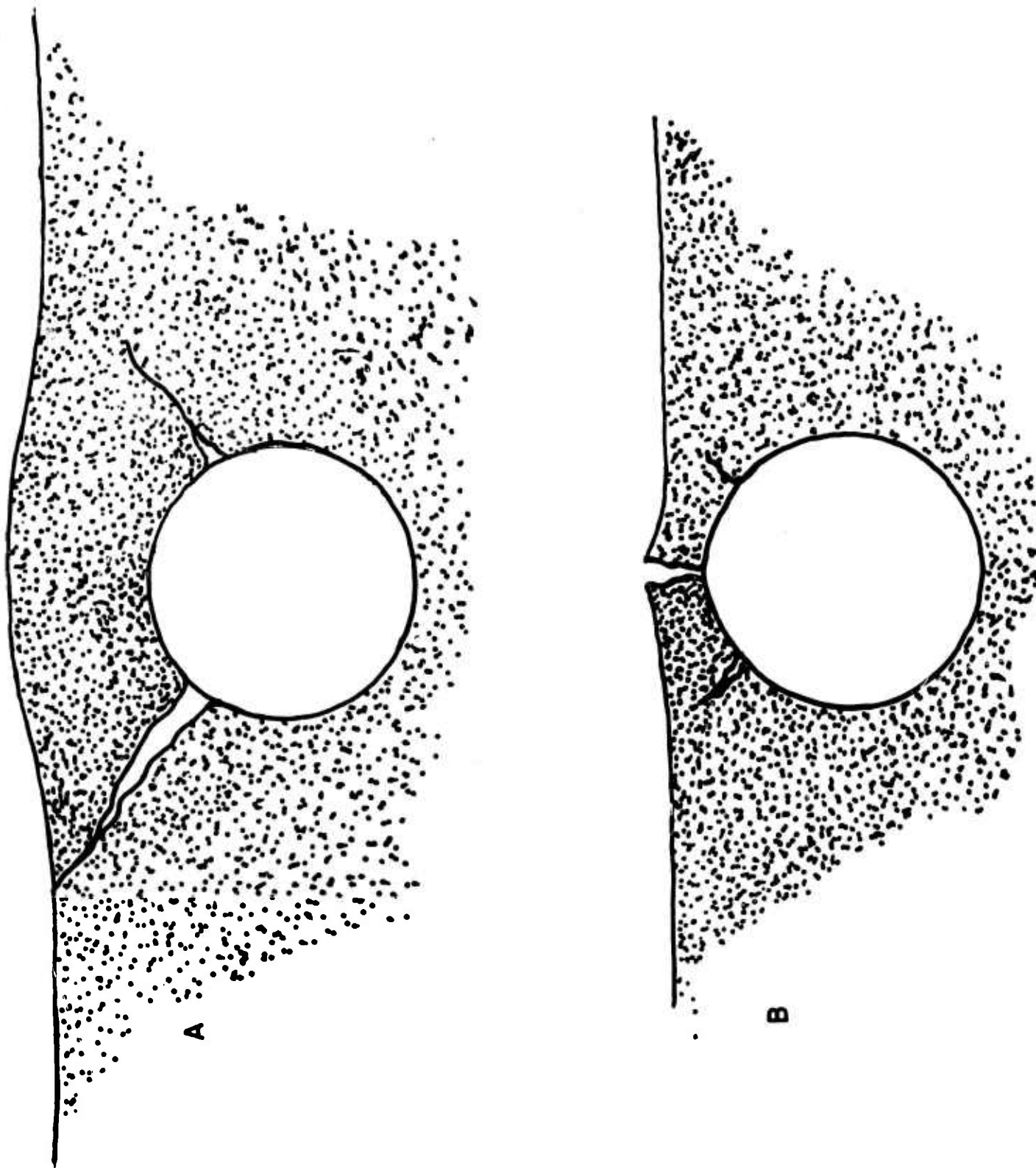


Fig. 13. Cone-producing fracture for crack nucleation at inclusion surface (A) and at plane surface (B).

Similar, but smaller, defects are expected to affect the fracture in the present case. If the inclusion is formed by melting surface material over an embedded polishing grit, more defects are expected on the surface of the inclusion than on the highly polished plane surface. In addition, there is much more surface area, hence more probability of finding a defect, along the circumference of the inclusion at the angle θ_m than at the point $x = 0$.

Calculated laser pulse energies It for failure are very imprecise due to large uncertainties in the failure strength σ_f for the material in the vicinity of the inclusion and in the bulk absorption coefficient β_I of the inclusion material. The failure strength σ_f for sapphire is estimated to be between 6×10^4 psi, observed in bulk samples, and the theoretical strength $\sigma_{\text{theor}} = 6 \times 10^6$ psi estimated from $\sigma_{\text{theor}} = \frac{1}{10} E$, where E is the Young's modulus. Assuming $\sigma_f = 2P$ at the point of failure and using $\sigma_f = 6 \times 10^5$ psi, we estimate that failure occurs at approximately $It = 400 \text{ J/cm}^2$ accurate to only about two orders of magnitude. Pulse energies for damage observed by Boling et al.² are well within the range of reasonable theoretical values.

For the 30-nsec pulse durations used in many experiments, the assumption of no heat transfer to the host material is not valid. It is reasonable to expect that heating has little effect on the failure strength and that the principal effect will be to lower the pressure at the inclusion-host interface, hence increase the required energy for damage, due to thermal expansion of the cavity in which the inclusion is contained.⁷

Apart from the time for the crack to propagate to the surface, with very short pulses $t < \tau_s$, damage could be delayed until the time τ_s after the

Sec. I

laser pulse. This will occur if the initially formed isotropic stresses are insufficient to cause damage but the quasiequilibrium anisotropic stresses, established after the time τ_s for sound to make a round trip to the plane surface, are enhanced sufficiently to cause damage. Delayed surface damage on dielectric mirrors has been observed by Bliss et al,⁸ but it is uncertain whether this is the result of crack propagation or stress enhancement.

III. MOLECULAR-ION IMPURITIES

In this section we consider increases in the overall absorption coefficient due to molecular-ion impurities. This applies mostly to $10.6\text{ }\mu\text{m}$ wavelength cw systems, in contrast to the previous section which was concerned with fracture due to localized heating in pulsed systems. The increased absorption heats the windows and can result in either undesirable thermal defocusing of the beam or fracture of the window.⁹

Among the most promising materials for use with CO_2 lasers are the alkali halides, in particular KCl and KBr. The absorption coefficient as a function of frequency in a typical material is sketched in Fig. I4. At low frequency, the mechanism for absorption is the creation of phonons, with the fundamental Reststrahl peak occurring in the far infrared. It has been well established experimentally¹⁰ and theoretically¹¹ that the intrinsic absorption coefficient decreases exponentially with increasing frequency in the multiphonon region.

In the ultraviolet, the mechanism for absorption is the excitation of an electron across the band gap to create an electron-hole pair. In the Urbach-tail region, β decreases exponentially with decreasing frequency. In between the two exponential regions, the absorption is thought to be dominated by impurities and imperfections. The absorption coefficient β in this region is represented by a wavy line in Fig. I4.

At the CO_2 laser frequency of 943 cm^{-1} ($10.6\text{ }\mu\text{m}$ wavelength), the absorption for KCl and KBr samples is extrinsic, having $\beta > 10^{-4}\text{ cm}^{-1}$. This is to be compared to the extrapolated intrinsic values of $8 \times 10^{-5}\text{ cm}^{-1}$ for KCl and $5 \times 10^{-7}\text{ cm}^{-1}$ for KBr.

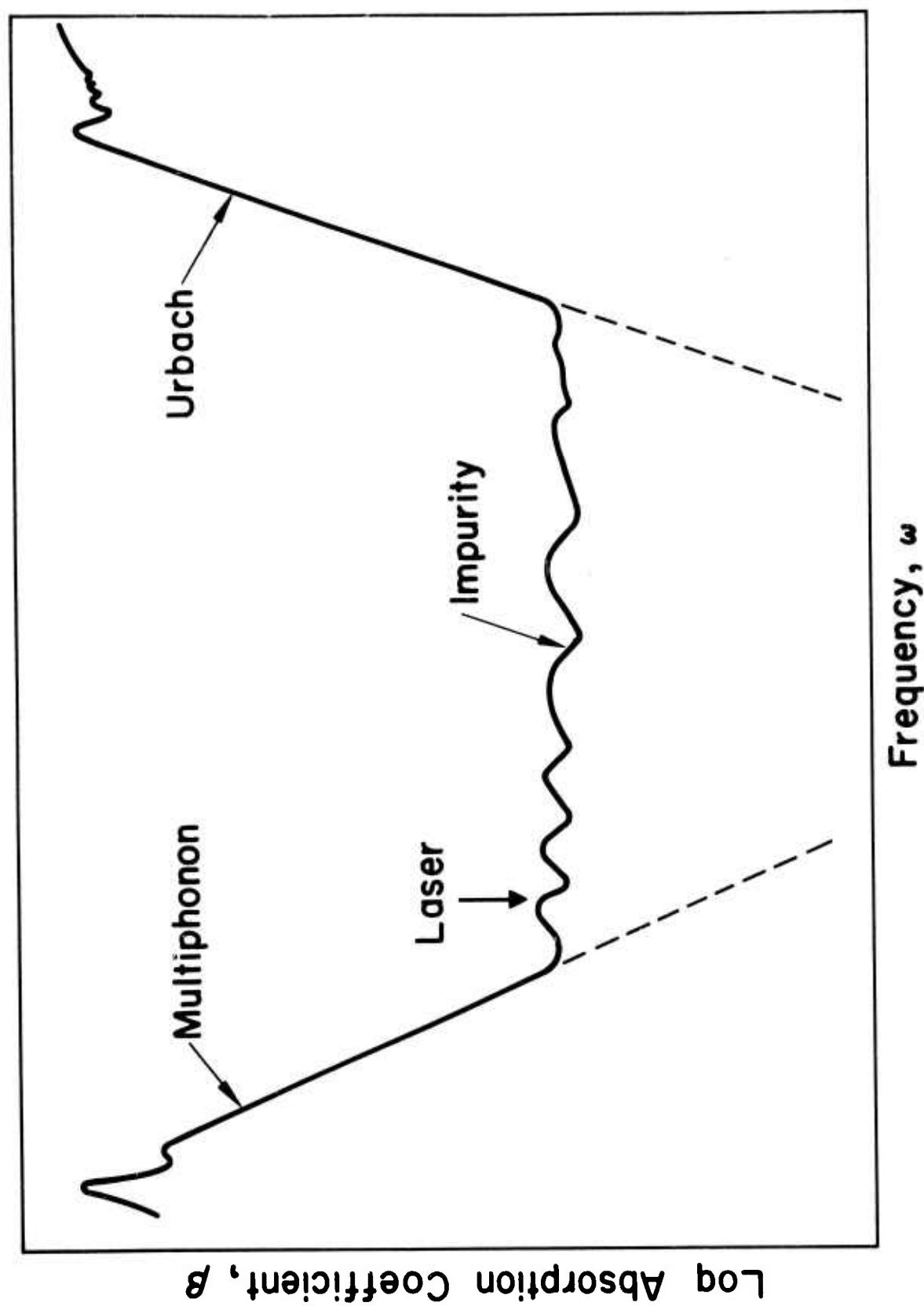


Fig. I4. Semi-log plot of absorption in alkali halides as a function of frequency.

Last year we showed that infrared absorbing inclusions dispersed throughout the crystals can contribute to the overall absorption.¹ In what follows, evidence will be presented showing that another important type of impurity limiting 10.6 μm wavelength transmission in the alkali halides is molecular-ion impurities that substitute for the halide ions in these materials.

As an example, the case of NO_2^- substituting for the Cl^- ion in KCl is drawn to scale in Fig. 15.¹² This ion fits loosely into the lattice and suffers little distortion. Consequently the internal vibrations of NO_2^- and other substitutional anions are only slightly affected by the presence of the host crystal. Frequency shifts of the molecular modes and splittings of degenerate modes are small. Infrared inactive modes may be weakly absorbing in the crystal.

Because of the small interaction with the host crystal, spectroscopists have used the technique of alkali-halide matrix isolation for a number of years to concentrate and isolate ions for convenient study using conventional absorption spectroscopy. A literature survey has been made of those ions that have been studied in KCl and KBr crystals. Those that most severely limit 10.6 μm transmission are presented below.

To estimate the absorption at the laser frequency of $\nu = 943 \text{ cm}^{-1}$ due to an impurity mode at ν_0 , a Lorentzian line shape

$$\beta(\nu) = (\text{const}) \frac{\Delta\nu}{(\nu - \nu_0)^2 + (\Delta\nu/2)^2} \quad (3)$$

is assumed. In Eq. (3), $\Delta\nu$ is the full width at half maximum, which is assumed to be frequency independent. When available, measured line strengths and line widths were used for extrapolation to 943 cm^{-1} . Typically for a crystal with 0.1%

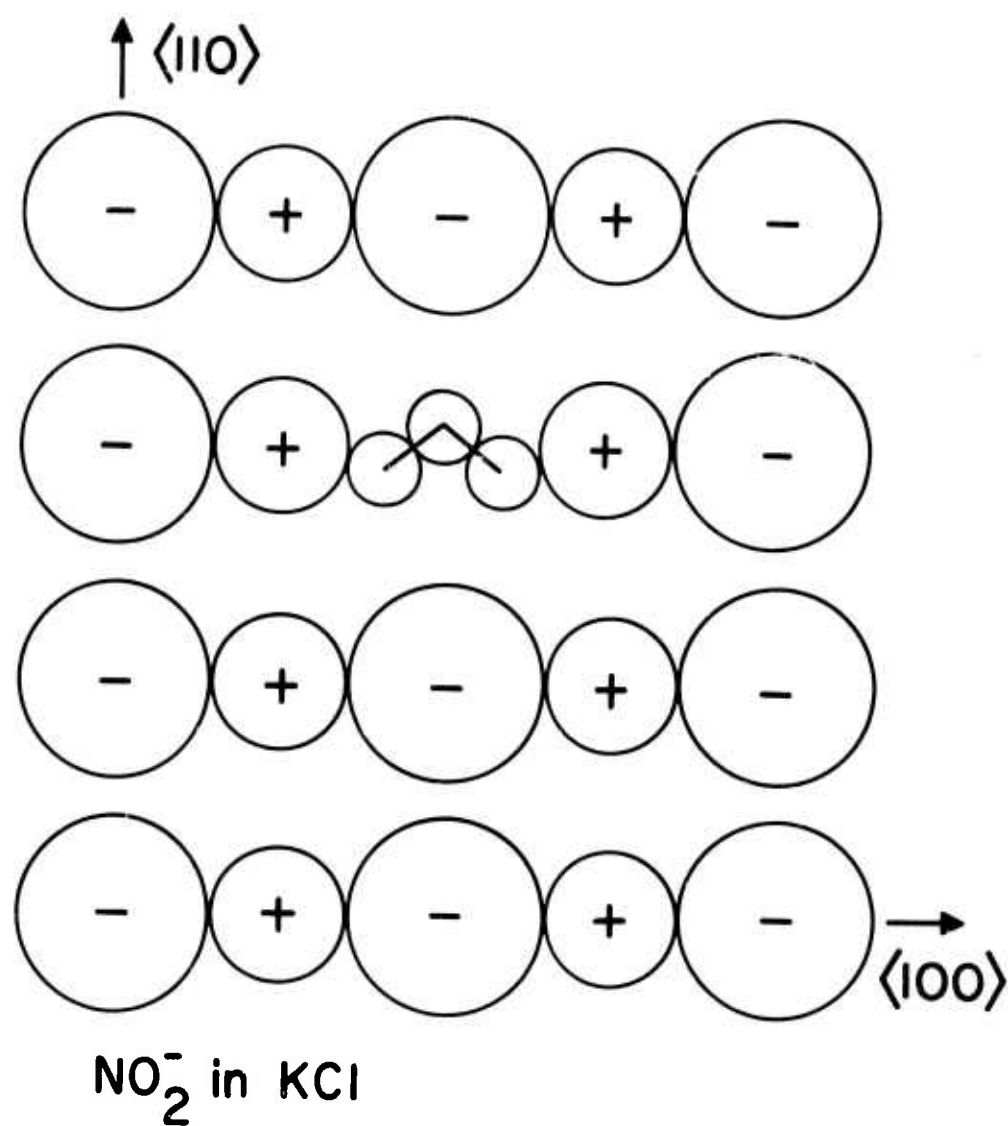


Fig. 15. Orientation of NO_2^- impurity in KCl at low temperature.

impurity concentration, the absorption coefficient $\beta(\nu_0)$ at the center of an allowed transition ranges from 10^2 to 10^3 cm^{-1} , with $\Delta\nu$ ranging from 4 to 50 cm^{-1} depending on the particular molecular species and host.

Impurities that substitute for lattice ions can be grouped into a few general types. First, atomic impurities can either yield an infrared active local mode of the lattice, or can activate normally infrared inactive phonons. However, because the frequencies of these modes are generally small compared to 943 cm^{-1} , little absorption occurs at the CO_2 laser frequency. The U center at 500 cm^{-1} has the highest frequency of this group and we estimate that more than 10 ppm H^- is needed to produce $\beta(\nu = 943 \text{ cm}^{-1}) = 10^{-4} \text{ cm}^{-1}$.¹³

Diatomic ionic impurities that have been studied in KCl and KBr crystals, on the other hand, have absorption frequencies that are too large to result in significant absorption at 943 cm^{-1} in spite of their large line widths. The hydroxyl ion (OH^-) with $\nu = 3640 \text{ cm}^{-1}$, is a member of this group. There has been concern regarding the hydroxyl ion because of the difficulty in removing this ion from alkali-halide crystals.¹⁴ However, using $\Delta\nu = 50 \text{ cm}^{-1}$ in Eq. (3), we estimate that greater than 100 ppm of OH^- at isolated lattice sites is needed to yield $\beta(943 \text{ cm}^{-1}) = 10^{-4} \text{ cm}^{-1}$.¹⁵ At high impurity concentrations, the OH^- may combine with other impurities to absorb more strongly at 943 cm^{-1} .

Polyatomic impurities have several infrared active modes, some of which may occur near 943 cm^{-1} and produce considerable CO_2 laser absorption. This group can be further subdivided into small and large ions. Small polyatomic ions such as NO_2^- fit loosely into the lattice and have large, temperature dependent line widths due to rotational and translational degrees of freedom. Larger ions

Sec. I

such as HCO_3^- fit tightly into the lattice and have several narrow, temperature insensitive lines.

In addition to the above groups, polyvalent ions such as SO_4^{2-} can substitute for the singly charged halide ion. In order to preserve the charge neutrality of the crystal, these ions must be accompanied by a compensating vacancy or by a divalent cation impurity such as Mg^{2+} . The infrared spectrum and 943 cm^{-1} absorption is dependent on the particular compensating species.

Our literature survey indicates that 0.03 ppm of either NO_2^- , HCO_3^- , SO_4^{2-} , or CrO_4^{2-} will result in $\beta(\nu = 943\text{ cm}^{-1}) = 10^{-4}\text{ cm}^{-1}$. Calculated spectra using an assumed Lorentzian line shape along with experimental frequencies and line widths are shown in Figs. I6-I8 for NO_2^- , HCO_3^- , and SO_4^{2-} .¹⁶

In each of the cases shown in these figures, the laser frequency, 943 cm^{-1} , falls at the edge of a small number of peaks representing the infrared active internal modes of the impurity. It would seem from looking at these figures that it would be easy to measure the spectrum of a crystal containing an unknown impurity and hence determine the impurity. However, there are two difficulties. First, the absorption coefficient at the peaks is only 10^{-2} cm^{-1} so that it would be difficult to make high resolution measurements using conventional spectroscopy. Second, and more important, there will be more than one impurity present in a real crystal so that the actual spectrum will look more like that of Fig. I4 than Figs. I6-I8.

In Fig. I9 we represent a real crystal by adding the absorption coefficient in the previous three figures. The individual lines near 1200 cm^{-1} have merged to form a relatively featureless, broad peak. The only distinctive lines remaining are the two HCO_3^- lines at 840 cm^{-1} and 971 cm^{-1} . If in addition we decrease the

Sec. I

amount of HCO_3^- and add different compensating divalent cations such as CO^{2+} along with a small amount of CrO_4^{2-} , even the calculated spectrum would appear featureless from 1000 to 1500 cm^{-1} .

The above examples serve to illustrate the importance of molecular-ion impurities on $10.6\text{ }\mu\text{m}$ transmission in alkali halides. A more complete survey of the ions that have been studied in KCl and KBr crystals will be published elsewhere.¹⁷

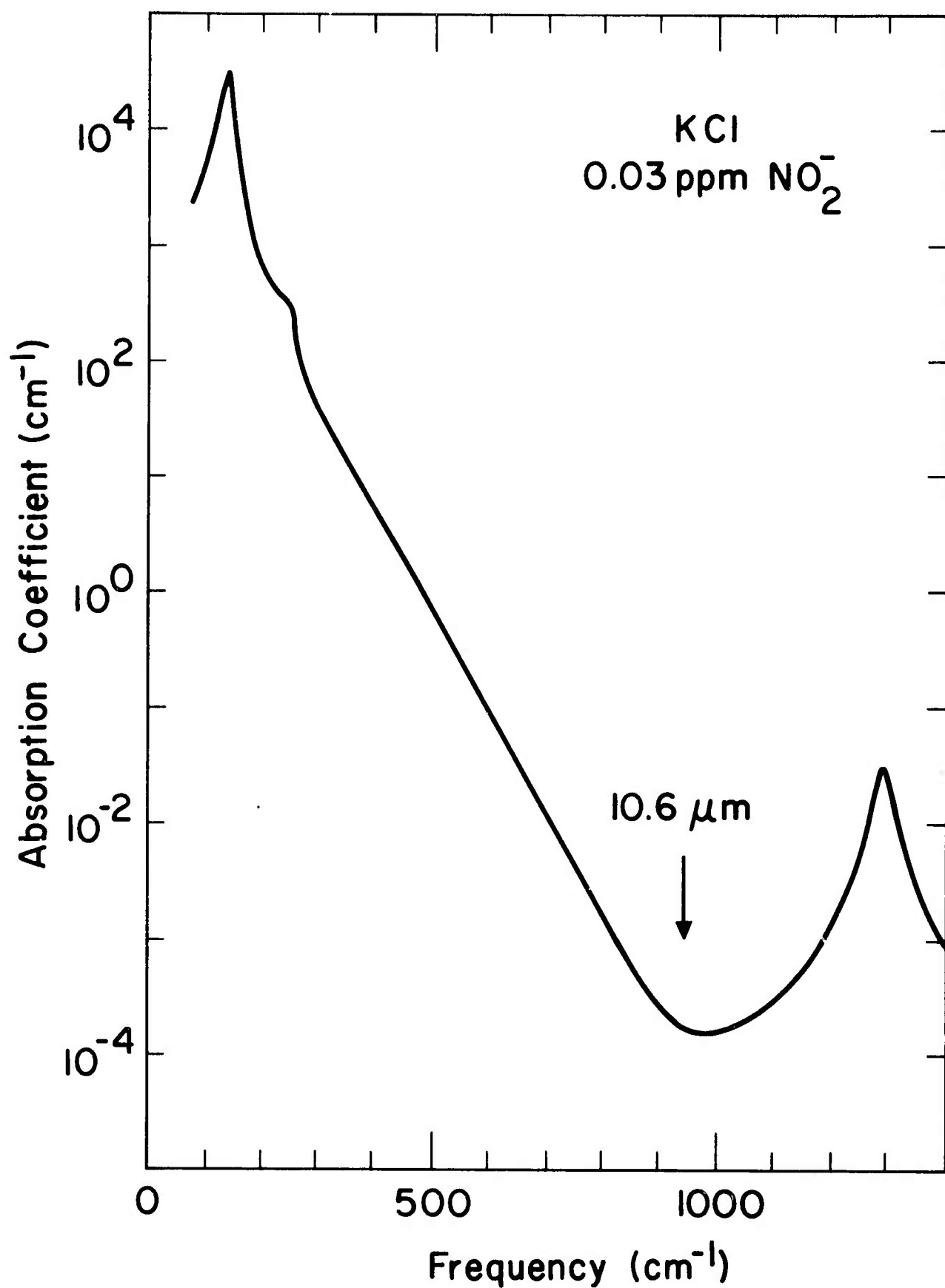


Fig. 16. Calculated absorption coefficient of a KCl crystal containing 0.03 ppm NO_2^- .

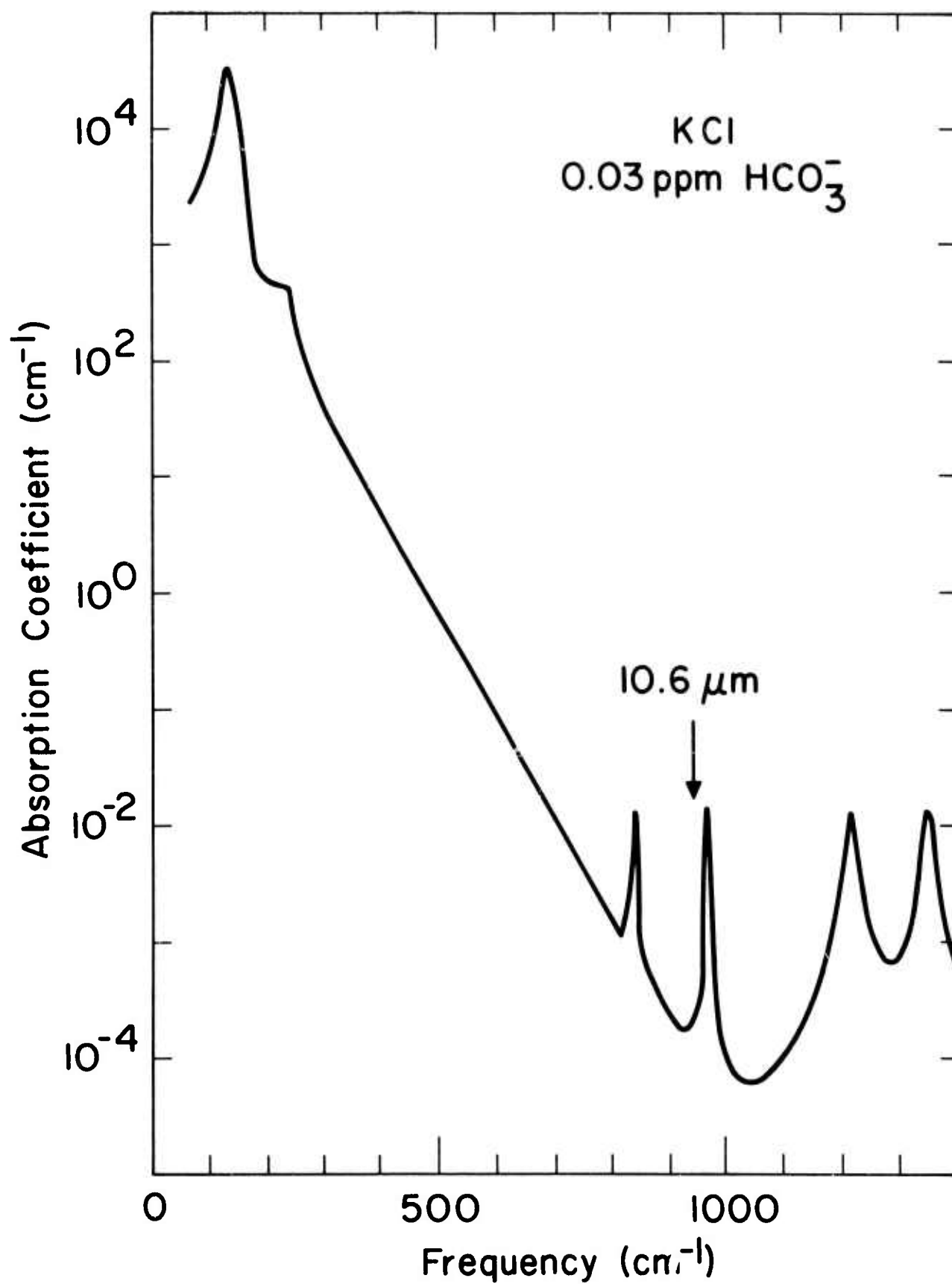


Fig. 17. Calculated absorption coefficient of a KCl crystal containing 0.03 ppm HCO_3^- .

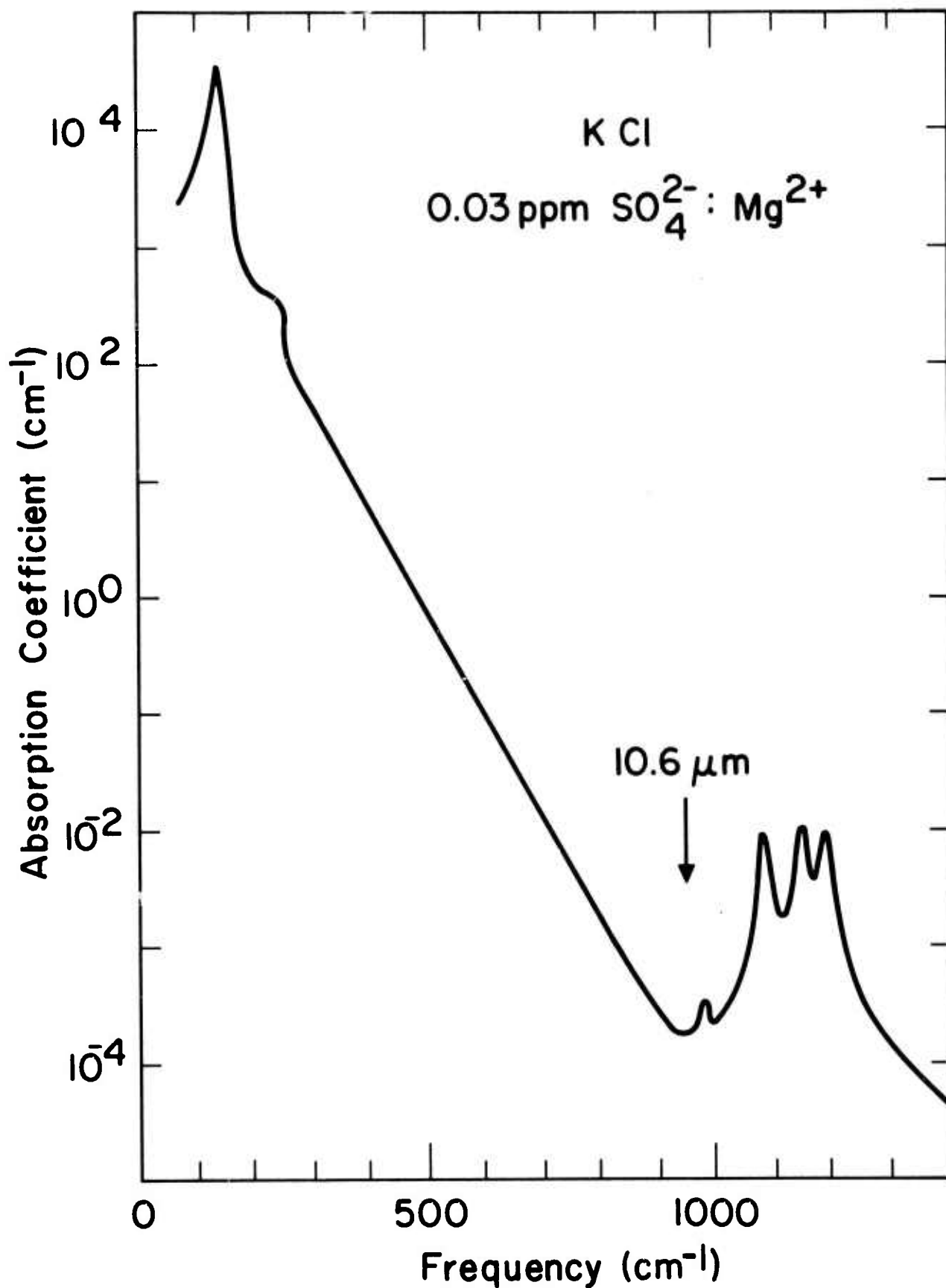


Fig. 18. Calculated absorption coefficient of a KCl crystal containing 0.3 ppm $\text{SO}_4^{2-} : \text{Mg}^{2+}$.

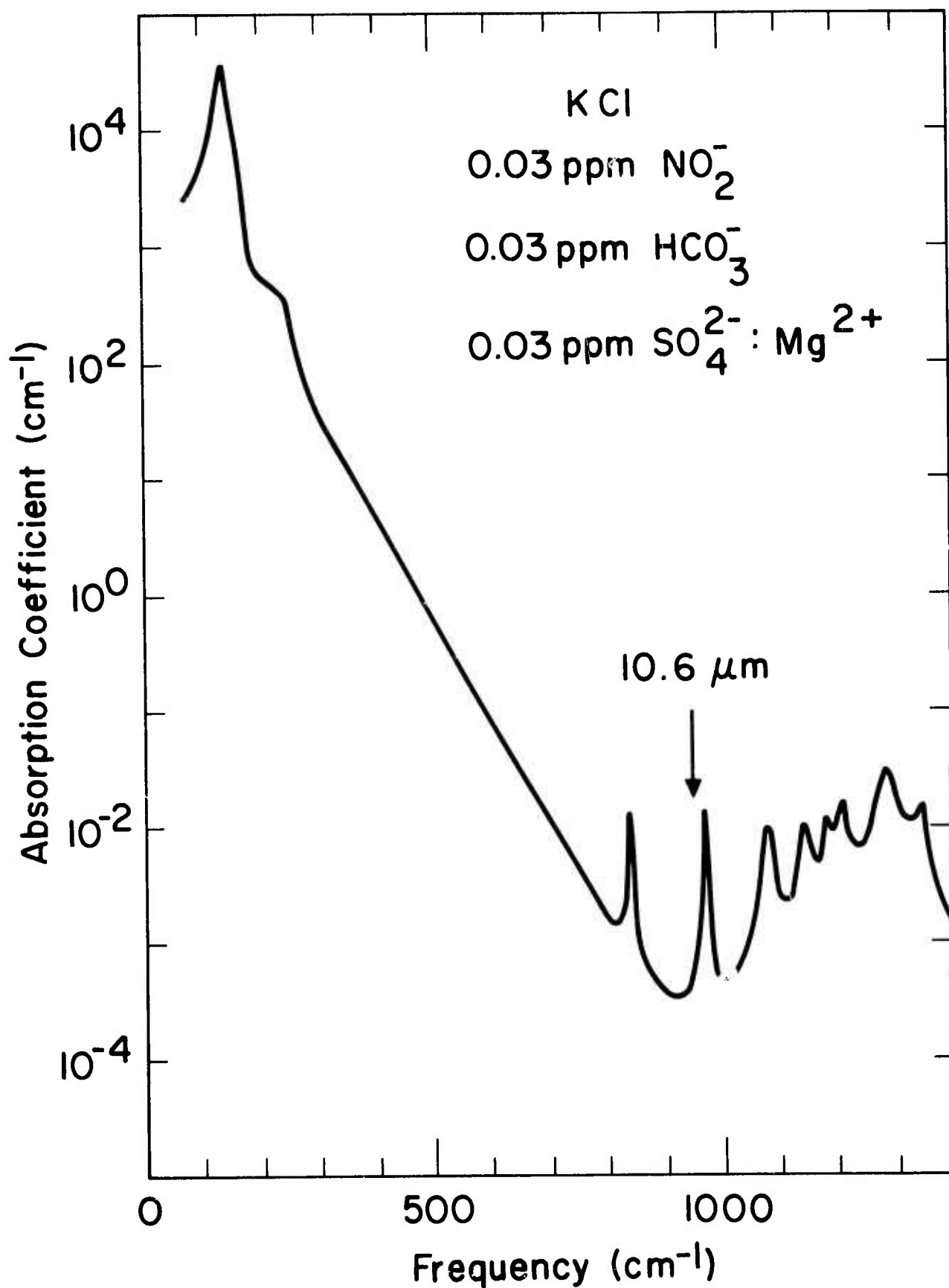


Fig. 19. Calculated absorption coefficient of a KCl crystal containing a few impurities.

REFERENCES

* This section was presented at the ASTM-NBS 1974 Symposium on Damage in Laser Materials, Boulder, Colorado, May 22 and 23, 1974.

1. C. J. Duthler and M. Sparks, Laser Induced Damage in Optical Materials, NBS Spec. Pub. 387, 208 (1973); J. Appl. Phys. 44, 3038 (1973); Appl. Phys. Lett. 24, 5 (1974).
2. N. L. Boling, G. Dubé, and M. D. Crisp, Laser Induced Damage in Optical Materials, NBS Spec. Pub. 387, 69 (1973); Appl. Phys. Lett. 23, 658 (1973).
3. D. Milam, R. A. Bradbury, and M. Bass, Laser Induced Damage in Optical Materials, NBS Spec. Pub. 387, 124 (1973).
4. For a review of shock wave induced fracture see H. Kolsky and D. Rader in Fracture, Vol. I, edited by H. Liebowitz (Academic, New York, 1968).
5. J. A. Fox and D. N. Barr, Appl. Phys. Lett. 22, 594 (1973).
6. G. B. Jeffery, Phil. Trans. Roy. Soc. Lond. 221, 265 (1921).
7. R. W. Hopper and D. R. Uhlmann, J. Appl. Phys. 41, 4023 (1970).
8. E. S. Bliss, D. Milam, and R. A. Bradbury, Appl. Opt. 12, 677 (1973).
9. M. Sparks, J. Appl. Phys. 42, 5029 (1971); M. Sparks and H. C. Chow, J. Appl. Phys. 45, 1510 (1974).
10. T. F. Deutsch, J. Phys. Chem. Solids (to be published).
11. M. Sparks and L. J. Sham, Phys. Rev. B 8, 3037 (1973) and references therein.
12. A. R. Evans and D. B. Fitchen, Phys. Rev. B 2, 1074 (1970).
13. A. A. Maradudin in Solid State Physics, edited by F. Seitz and D. Turnbull (Academic, New York, 1966), Vol. 18, p. 274 and Vol. 19, p. 1.

14. R. C. Pastor and M. Braunstein, Hughes Research Laboratories Technical Report No. AFWL-TR-72-152, Vol. II (1973).
15. B. Wedding and M. V. Klein, Phys. Rev. 177, 1274 (1969); M. V. Klein, B. Wedding, and M. A. Levine, Phys. Rev. 180, 902 (1969); D. F. Smith, J. Overend, J. C. Decius, and D. J. Gordon, J. Chem. Phys. 58, 1636 (1973).
16. The data used for NO_2^- in KCl are obtained from V. Narayanamurti, W. D. Seward, and R. O. Pohl, Phys. Rev. 148, 481 (1966); V. P. Dem'yanenko and Yu. P. Tsyashchenko, Sov. Phys. - Solid State 11, 3043 (1970); R. Kato and J. Rolfe, J. Chem. Phys. 47, 1901 (1967); R. Bonn, R. Metselaar, and J. van der Elsken, J. Chem. Phys. 46, 1988 (1967); A. R. Evans and D. B. Fitchen, Phys. Rev. B 2, 1074 (1970). The HCO_3^- data from D. L. Burnitt, K. O. Hartman, and I. C. Hisatsune, J. Chem. Phys. 42, 3553 (1965). The SO_4^{2-} data from J. C. Decius, E. H. Coker, and G. L. Brenna, Spectrochim. Acta 19, 1281 (1963); E. H. Coker, J. C. Decius, and A. B. Scott, J. Chem. Phys. 35, 745 (1961); D. N. Mirlin and I. I. Reshina, Sov. Phys. - Solid State 10, 895 (1968).
17. C. J. Duthler, J. Appl. Phys. 45, 2668 (1974).

J. ERRATUM

High-power 2- to 6- μ m window material figures of merit with edge cooling and surface absorption included, M. Sparks and H. C. Chow [J. Appl. Phys. 45, 1510 (1974)]

The calculated values of ΔT for SrF_2 and BaF_2 contained errors that were propagated throughout the tables and figures. The corrected values are given below in Table I and Fig. 1. The conclusions of the paper are unchanged, except that the rating numbers on the original Fig. 3 for BaF_2 and ZnSe are reversed for $D = 1 \text{ cm}$. The figure captions for Fig. 1 and Fig. 3 should be interchanged.

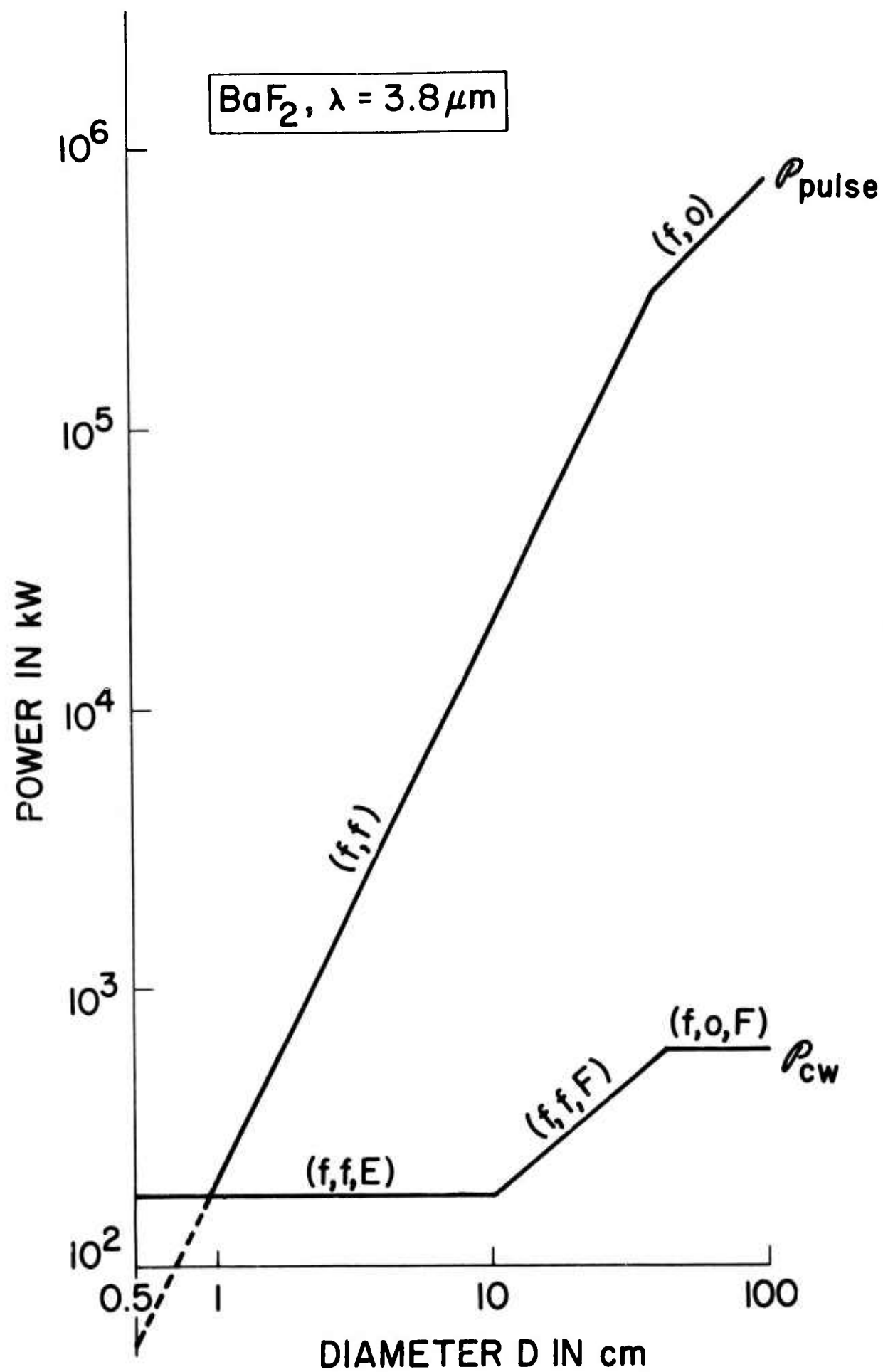
Table Caption

TABLE J1. Corrected values of parameters for SrF_2 and BaF_2 . The subscripts on the materials designate wavelength in μm and diameter in centimeters. An asterisk indicates values calculated with measured absorption coefficient β ($4.1 \times 10^{-5} \text{ cm}^{-1}$ for SrF_2 and $3.0 \times 10^{-5} \text{ cm}^{-1}$ for BaF_2).

Figure Caption

FIG. J1. Corrected diameter dependence of the pulse and cw powers transmitted by BaF_2 at $3.8 \mu\text{m}$.

Material	τ_{less} (sec)	ℓ_{gr} (cm)	ΔT_{less} (K)	$\sigma_{\text{f-o}}$ (10^3 psi)	Bulk Absorption		Surface Absorption	
					ϕ_{pulse} (kW)	ϕ_{cw} (kW)	ϕ_{pulse} (kW)	ϕ_{cw} (kW)
(SrF ₂) ₂ 3.8;100	1200 (F)	4.3 (f)	11 (o)	9.2	2.0×10^6	1.8×10^3	8.6×10^6	7.7×10^3
(SrF ₂) ₂ 3.8;10	100 (F)	0.43 (f)	13 (f)	23	2.4×10^4	2.4×10^2	1.0×10^4	1.0×10^2
(SrF ₂) ₂ 3.8;1		0.043 (f)	13 (f)			1.6×10^2		10
(SrF ₂) ₂ 5.25;100	1200 (F)	4.3 (f)	13 (f)	11	2.4×10^6	2.1×10^3	1.0×10^7	9.0×10^3
(SrF ₂) ₂ 5.25;10	100 (F)	0.43 (f)	13 (f)	26	2.4×10^4	2.4×10^2	1.0×10^4	1.0×10^2
(SrF ₂) ₂ 5.25;100							5.9×10^6	5.1×10^3
(SrF ₂) ₂ 5.25;10							5.9×10^4	5.9×10^2
(BaF ₂) ₂ 3.8;100	1100 (F)	5.3 (f)	4.9 (o)	5.5	7.6×10^5	6.4×10^2	4.1×10^6	3.4×10^3
(BaF ₂) ₂ 3.8;10	100 (E)	0.53 (f)	12 (f)	14	1.9×10^4	1.8×10^2	1.0×10^4	97
(BaF ₂) ₂ 3.8;1		0.053 (f)	12 (f)			1.8×10^2		12
(BaF ₂) ₂ 5.25;100	1100 (F)	5.3 (f)	6.9 (o)	6.2	1.0×10^6	8.8×10^2	5.6×10^6	4.7×10^3
(BaF ₂) ₂ 5.25;10	100 (E)	0.53 (f)	12 (f)	16	1.9×10^4	1.8×10^2	1.0×10^4	97
(BaF ₂) ₂ 5.25;100							3.3×10^6	2.9×10^3
(BaF ₂) ₂ 5.25;10							6.3×10^4	6.0×10^2



High-power 2- to 6- μ m window material figures of merit with edge cooling and surface absorption included*

M. Sparks

Xonics, Incorporated, Van Nuys, California 91406

H. C. Chow

Department of Physics, University of California, Los Angeles, California 90024

and
Xonics, Incorporated, Van Nuys, California 91406

(Received 30 August 1973; in final form 26 November 1973)

Values of the total power ρ that a window can transmit under specified conditions are calculated for use as figures of merit for window materials. New features of the figures of merit are consideration of edge as well as face cooling, treatment of surface as well as bulk absorption, use of ρ rather than intensity as the figure of merit, effects of improving materials, and calculation for 3.8 and 5.25 μ m. New results include the following: For continuous operation, large-diameter windows should be face cooled, but small-diameter window may be edge cooled, and ρ often decreases as the diameter D increases. For pulsed operation, ρ increases as D increases, as was intuitively expected. Values of the diameter D_{FF} , above which face cooling should be used, are surprisingly large, ranging between 7 and 100 cm, typically. For pulsed operation and for $D > D_{FF}$ in cw operation, ρ is independent of thermal conductivity K while for $D < D_{FF}$ in cw operation, $\rho \propto K$. The alkaline-earth fluorides have the greatest figures of merit for large-diameter windows with $\rho = 76$ MW, $\Delta T = 50$ K, and $l = 0.5$ cm for a 1-sec pulse on a 10-cm-diam window of BaF_2 at 3.8 μ m with a bulk absorption coefficient of 10^{-4} cm^{-1} . For small-diameter windows (1-cm diameter), Si, BaF_2 , and GaAs have the greatest values of $\rho = 1.8, 0.94$, and 0.76 MW, respectively, for cw or 1-sec pulse duration.

I. INTRODUCTION

There have been extensive programs within the last three years to obtain materials for high-power infrared systems at 10.6 μ m.¹ Window materials for the 2- to 6- μ m region have received far less attention. However, there is considerable interest in chemical lasers operating in the 2- to 6- μ m range and increasing interest in window materials for this range.

In addition to extending the previous figures of merit²⁻⁴ to 3.8 and 5.25 μ m, the following new features are added: (1) Edge cooling, as well as face cooling, is included for continuously operated (cw) systems. (2) As materials are being improved, surface absorption apparently is becoming relatively more important. Surface absorption may also be of interest in field use where contamination is likely. Thus, surface as well as bulk absorption is included. (3) The total power ρ that a window can transmit under specified idealized conditions is used as the figure of merit. Use of ρ , rather than intensity, is more convenient when considering the effect of changing the window diameter. (4) Effects of improving materials, particularly lowering the absorption coefficient β and increasing the strength σ , are included.

In addition to the new ratings for materials, new results include the following: (a) Edge cooling, which is technically much simpler than face cooling, is more effective than previously realized. Before the importance of thermally induced optical distortion and fracture was realized,³ edge cooling to prevent melting was considered. Subsequently, only face cooling was considered since ΔT must be kept small, and large-diameter windows, which have large values of ΔT for edge cooling, were contemplated to keep the intensity small and to avoid diffraction in long-focal-length systems.

It will be shown that edge cooling can be used for surprisingly large diameters D_{FF} , ranging between 7 and 100 cm, typically. In order to obtain the greatest value of ρ in a cw system, large-diameter windows ($D > D_{FF}$) should be face cooled while small-diameter windows ($D < D_{FF}$) may be edge cooled.

(b) For pulsed operation (pulse length of the order of 1 sec with rapid interpulse cooling) ρ increases as D increases, as was expected intuitively, but for continuous operation ρ often decreases as D increases. Thus, for cw systems that can tolerate small-diameter windows (without excessive diffraction, for example), there are the dual advantages of technically easier edge coolings and often greater ρ . (3) For small diameters, $D < D_{FF}$, the value of ρ_{cw} depends on the thermal conductivity K , whereas, for $D > D_{FF}$, ρ_{cw} is independent of K . For pulse operation, ρ_{pulse} is independent of K .

In considering window materials for high-power infrared lasers, previous theoretical investigations^{3,4} have established the effects of temperature gradients and pressure differentials. Briefly, as a result of the spatial inhomogeneity of the intensity of the incident laser beam, a radial temperature gradient is set up, bringing about radial gradients in the thickness and the index of refraction. The resulting optical distortion may cause significant reduction in the target intensity, especially for long-focal-length systems. Optical distortion may also be caused by deformation of the window under pressure. In addition, both the temperature gradient and pressure can cause fracture of the window.

Application of these considerations to obtain figures of merit for window materials involves the following three distinct factors:

(i) Pressure-induced optical distortion and fracture

TABLE I. Values of material parameters used in calculating figures of merit and values of critical window diameter D_{EF} . The use of symbols, calculation schemes, and the meaning of superscripts accompanying numerical values in this and the following tables are explained in Secs. II and III. The values of the parameters are from Refs. 1-3 unless otherwise stated.

Material	n^a	C (J/cm ³ K)	K (W/cm K)	σ (10 ³ psi)	E (10 ⁶ psi)	α (10 ⁻⁶ /K)	$ \partial n/\partial T ^b$ (10 ⁻⁶ /K)	D_{EF} (3.8 μ m) (cm)	D_{EF} (5.25 μ m) (cm)
Ge	4.02	1.65	0.59	13.5	14.9	5.7	320	40 ^(f)	37 ^(f)
Si	3.43	1.63	1.48	9.0	19.0	2.3	140	105 ^(f)	97 ^(f)
GaAs	3.30	1.42	0.48	20.0	12.3	5.7	160	31 ^(f)	29 ^(f)
CdTe	2.69	1.3	0.06	0.85	5.3	5.9	120	11 ^(f)	11 ^(f)
ZnSe	2.44	2.6 ^c	0.13	7.2 ^d	10.3	7.0	64	8.1 ^(f)	8.1 ^(f)
MgF ₂	1.38	3.14	0.1-0.3	7.6	24.5	13.7	10	12 ^(f)	12 ^(f)
CaF ₂	1.41	2.71	0.09	5.3	11.0	19.7	3.1	6.6 ^(f)	6.6 ^(f)
SrF ₂	1.44	2.37	0.1 ^e	6.1	14.7	15.8	1.0	6.8 ^(f)	6.8 ^(f)
BaF ₂	1.45	1.96	0.12	3.9	7.7	20.3	1.8	10 ^(f)	10 ^(f)
NaCl	1.52	1.84	0.065	0.35	5.8	44	0.66	19 ^(f)	19 ^(f)
KCl	1.47	1.35	0.065	0.33	4.3	36	4.6	19 ^(f)	19 ^(f)
MgO	1.67	3.13	0.6	20	36.1	10.5	26	23 ^(f)	23 ^(f)
Al ₂ O ₃	1.67	3.0	0.45	65	50	5.5	16	11 ^(f)	9.7 ^(f)
Tl 1173 glass	2.60	1.25 ^c	0.003	6.3	3.1	15.0	120	0.2 ^(f)	0.2 ^(f)

^aValues of n at $\lambda = 4 \mu$ m are used in all calculations with the exception of Tl 1173, for which the 10.6- μ m value is used.

^bIn calculating $\partial n/\partial T$, the values of $(\partial n/\partial T)_0$ at $\lambda = 4 \mu$ m are used except for MgF₂ (at $\lambda = 0.7 \mu$ m).

^cSee Ref. 3.

^dP. Miles (private communication).

^eEstimate.

are avoided by making the window thickness l greater than a critical value l_{gr} .

(ii) Thermally induced optical distortion and fracture are avoided by keeping the temperature difference ΔT between the center and rim of the window below a critical value ΔT_{loss} .

(iii) The fact that ΔT must be kept below ΔT_{loss} limits the total power that a window can transmit to values below a critical value ρ_{pulse} for pulse operation or ρ_{cw} for cw operation. The relation between ρ and ΔT depends on the type of operation (pulse or cw), the thermal properties of the window (heat capacity per unit volume C and thermal conductivity K), the type of heating (bulk or surface), and for cw operation the type of cooling (edge or face cooling).

Two of the new features of the figures of merit, sur-

face absorption and edge cooling, pertain to relation (iii) between ρ and ΔT .

II. FIGURE-OF-MERIT ANALYSIS

The figures of merit are obtained as follows^{3,4}: (1) The thickness l_{gr} required to withstand the given pressure P is calculated first. The thicknesses l_f and l_0 required to withstand the pressure without fracturing the window and without causing excessive optical distortion are^{4,5}

$$l_f/D = 0.433(P/SF/\sigma)^{1/2} \quad (2.1)$$

and

$$l_0/D = 0.842[(n-1)(P/E)^2(D/\lambda)]^{1/5}, \quad (2.2)$$

respectively, where σ is the window strength, P is the pressure, the safety factor SF is taken as SF = 4, n is

TABLE II. Figures of merit, values of thermal time constant τ_{loss} , critical thickness l_{gr} , temperature difference ΔT_{loss} , and fracture-to-optical distortion crossover strength σ_{f-o} for the case $\lambda = 3.8 \mu$ m and $D = 100$ cm. In Tables II-VI, the choice of $\beta = 10^{-4}$ cm⁻¹ for all materials except MgO ($\beta = 8 \times 10^{-4}$) and Al₂O₃ ($\beta = 2 \times 10^{-2}$ cm⁻¹) is explained in Sec. III.

Material	τ_{loss} (sec)	l_{gr} (cm)	ΔT_{loss} (K)	σ_{f-o} (10 ³ psi)	Bulk absorption		Surface absorption	
					ρ_{pulse} (kW)	ρ_{cw} (kW)	ρ_{pulse} (kW)	ρ_{cw} (kW)
Ge	860 ^(f)	5.0 ^(f)	0.030 ^(f)	4.3	3.8×10^3	4.5	2.0×10^4	23
Si	690 ^(f)	4.4 ^(f)	0.077 ^(f)	5.7	1.0×10^4	14	4.3×10^4	62
GaAs	760 ^(f)	5.2 ^(f)	0.058 ^(f)	4.1	6.4×10^3	8.6	3.3×10^4	44
CdTe	2400 ^(f)	11 ^(f)	0.039 ^(f)	2.4	3.9×10^3	16	3.9×10^4	16
ZnSe	1500 ^(f)	5.0 ^(f)	0.15 ^(f)	4.3	3.0×10^4	20	1.5×10^5	1.0×10^2
MgF ₂	1300 ^(f)	3.8 ^(f)	1.2 ^(f)	15	3.0×10^5	24	1.2×10^6	94
CaF ₂	1400 ^(f)	4.6 ^(f)	3.4 ^(f)	7.6	7.1×10^5	4.9×10^2	3.3×10^6	2.3×10^3
SrF ₂	1200 ^(f)	4.3 ^(f)	11 ^(f)	11	2.0×10^6	1.8×10^3	8.6×10^6	7.7×10^3
BaF ₂	1100 ^(f)	5.3 ^(f)	4.9 ^(f)	5.5	7.6×10^5	7.2×10^2	4.1×10^6	3.8×10^3
NaCl	6200 ^(f)	14 ^(f)	0.69 ^(f)	4.1	1.0×10^5	16	1.7×10^6	2.8×10^2
KCl	4800 ^(f)	18 ^(f)	0.57 ^(f)	3.4	6.0×10^4	13	1.1×10^6	2.3×10^2
MgO	830 ^(f)	2.6 ^(f)	0.70 ^(f)	16.0	2.2×10^4	26	4.6×10^5	5.4×10^2
Al ₂ O ₃	700 ^(f)	2.3 ^(f)	1.3 ^(f)	21	1.5×10^3	2.1	6.9×10^5	1.0×10^3
Tl 1173 glass	10 000 ^(f)	8.3 ^(f)	0.050 ^(f)	1.6	4.9×10^3	0.46	4.1×10^4	3.8

TABLE III. Figures of merit, values of thermal time constant τ_{less} , critical thickness l_{cr} , temperature difference ΔT_{less} , and fracture-to-optical distortion crossover strength σ_{t-o} for the case $\lambda = 3.8 \mu\text{m}$ and $D = 10 \text{ cm}$.

Material	τ_{less} (sec)	l_{cr} (cm)	ΔT_{less} (K)	σ_{t-o} (10^3 psi)	Bulk absorption		Surface absorption	
					ρ_{pulse} (kW)	ρ_{cw} (kW)	ρ_{pulse} (kW)	ρ_{cw} (kW)
Ge	17 ^(E)	0.32 ⁽⁰⁾	0.47 ⁽⁰⁾	11	6.0×10^2	37	2.0×10^2	12
Si	6.9 ^(E)	0.35 ^(f)	0.96 ⁽⁰⁾	14	1.3×10^3	1.8×10^2	4.3×10^2	62
GaAs	18 ^(E)	0.33 ⁽⁰⁾	0.91 ⁽⁰⁾	10	1.0×10^3	56	3.3×10^2	18
CdTe	140 ^(E)	1.1 ^(f)	0.34 ⁽⁰⁾	6.0	3.5×10^2	2.5	3.9×10^2	2.9
ZnSe	100 ^(F)	0.39 ^(f)	1.9 ⁽⁰⁾	11	3.8×10^3	38	1.5×10^3	15
MgF ₂	98 ^(E)	0.38 ^(f)	11 ^(f)	37	2.8×10^4	2.9×10^2	1.1×10^4	1.0×10^2
CaF ₂	130 ^(F)	0.46 ^(f)	12 ^(f)	19	2.6×10^4	2.0×10^2	1.2×10^4	94
SrF ₂	100 ^(F)	0.43 ^(f)	38 ^(f)	23	7.0×10^4	6.8×10^2	3.0×10^4	2.9×10^2
BaF ₂	100 ^(E)	0.53 ^(f)	50 ⁽⁰⁾	14	7.6×10^4	7.9×10^2	4.1×10^4	4.2×10^2
NaCl	180 ^(E)	1.8 ^(f)	0.69 ^(f)	10	1.0×10^3	5.5	1.8×10^3	10
KCl	130 ^(E)	1.8 ^(f)	1.1 ^(f)	8.4	1.1×10^3	8.6	2.0×10^3	16
MgO	33 ^(E)	0.23 ^(f)	7.9 ⁽⁰⁾	40	2.4×10^3	74	4.6×10^3	1.4×10^2
Al ₂ O ₃	42 ^(E)	0.15 ⁽⁰⁾	21 ⁽⁰⁾	52	2.4×10^2	5.8	7.1×10^3	1.6×10^2
Tl 1173 glass	100 ^(F)	0.53 ⁽⁰⁾	0.78 ⁽⁰⁾	40	7.7×10^2	7.4	4.1×10^2	39

the refractive index, E is Young's modulus, and λ is the optical wavelength. In order to prevent both fracture and excessive optical distortion, the thickness must be greater than both l_f and l_o ; that is, $l > l_{\text{cr}}$, which is defined to be the greater of l_o and l_f .

(2) Next, the temperature difference ΔT between the center and rim of the window that can be tolerated is calculated as follows: If ΔT exceeds ΔT_f or ΔT_o , defined as

$$\Delta T_f = 2\sigma/\alpha E S F \quad \text{and} \quad \Delta T_o = \lambda/8l_{\text{cr}}|\partial_{\text{cr}}T| \quad (2.3)$$

where $\partial_{\text{cr}}T = (\partial n/\partial T)_o + \alpha(1+\nu)(n-1) + S$, in which the derivative is taken at constant stress, α is the linear thermal expansion coefficient, ν is the Poisson ratio, and S is a small stress-optic term,³ then the window fractures from the excessive thermal gradient or causes excessive thermally induced optical distortion,³ respectively. In order to prevent both of these system failures, ΔT must be smaller than both ΔT_f and ΔT_o ; that is, $\Delta T < \Delta T_{\text{less}}$, which is defined to be the lesser of ΔT_f and ΔT_o .

(3) For pulse operation in which the heat diffusion and, therefore, the cooling are negligible during the pulse duration t_{pulse} , the temperature rise at every point is determined by the simple expression $CV = \Delta E/\Delta T$, where V is the volume, C is the heat capacity per unit volume, ΔE is the energy added, and ΔT is the temperature rise. From this expression it is easy to show³ that for intensity $I = I_0 - \frac{2}{3}(\rho/\frac{1}{2}D)^2 I_0$, where ρ is the radial coordinate, the spatially averaged intensity $\langle I \rangle$ and ΔT are related by the expression $\langle I \rangle_{\text{pulse}} = C\Delta T/\beta t_{\text{pulse}}$. The corresponding total power ρ_{pulse} that a window can transmit in the pulse mode of operation is

$$\rho_{\text{pulse}} = \pi(\frac{1}{2}D)^2 \langle I \rangle_{\text{pulse}} = \pi D^2 C \Delta T / 4\beta t_{\text{pulse}}. \quad (2.4)$$

A continuously operated system must be cooled; otherwise, ΔT goes to infinity as t goes to infinity for fixed ρ_{pulse} , as can be seen in (2.4). In this case, (2.4) is valid if t_{pulse} is replaced by τ_{less} , which is the time constant for cooling the window. For edge cooling,

τ_{less} is the time constant τ_E for radial heat flow along the radius $\frac{1}{2}D$:

$$\tau_E = C(\frac{1}{2}D)^2/4K. \quad (2.5)$$

The exact value of τ_E has a weak dependence on the radial distribution of the incident intensity. The value given is for a constant intensity. For I constant inside the circle of diameter $\frac{1}{2}D$ and zero outside this circle, the factor $\frac{1}{4}$ in τ_E is replaced by $1/2.9$.⁸ These results are obtained from trivial solutions to the heat-flow equation.

For face cooling, τ_{less} is the sum of the time constant for heat flow across the window thickness l_{cr} plus that for removal of heat at the interface of the window and coolant³:

$$\tau_F = \frac{Cl_{\text{cr}}}{h} \left(1 + \frac{hl_{\text{cr}}}{3K} \right), \quad (2.6)$$

where h is the heat-transfer coefficient ($\text{W}/\text{cm}^2\text{K}$) at the interface of the window and coolant.

TABLE IV. Figures of merit and related information for small-diameter ($D = 1 \text{ cm}$) windows at $\lambda = 3.8 \mu\text{m}$.

Material	τ_D (sec)	l_{cr} (cm)	ΔT_{less} (K)	ρ_{cw}	
				bulk absorption (kW)	surface absorption (kW)
Ge	0.17	0.029 ^(f)	5.2 ⁽⁰⁾	3.1×10^2	11
Si	0.069	0.035 ^(f)	9.6 ⁽⁰⁾	1.8×10^3	63
GaAs	0.18	0.023 ^(f)	13 ⁽⁰⁾	7.6×10^2	18
CdTe	1.4	0.11 ^(f)	3.4 ⁽⁰⁾	26	2.9
ZnSe	1.3	0.039 ^(f)	19 ⁽⁰⁾	3.1×10^2	12
MgF ₂	0.98	0.038 ^(f)	11 ^(f)	2.8×10^2	11
CaF ₂	1.8	0.045 ^(f)	12 ^(f)	1.4×10^2	6.4
SrF ₂	1.5	0.043 ^(f)	38 ^(f)	4.7×10^2	20
BaF ₂	1.0	0.053 ^(f)	65 ^(f)	9.4×10^2	52
NaCl	1.8	0.18 ^(f)	0.69 ^(f)	5.6	1.0
KCl	1.3	0.18 ^(f)	1.1 ^(f)	8.6	1.6
MgO	0.33	0.023 ^(f)	26 ^(f)	2.5×10^2	46
Al ₂ O ₃	0.42	0.013 ^(f)	120 ^(f)	34	86
Tl 1173 glass	26	0.042 ^(f)	9.9 ⁽⁰⁾	3.7	0.16

TABLE V. Figures of merit, values of thermal time constant τ_{less} , critical thickness l_{cr} , temperature difference ΔT_{less} , and fracture-to-optical distortion crossover strength $\sigma_{T=0}$ for the case $\lambda = 5.25 \mu\text{m}$ and $D = 100 \text{ cm}$.

Material	τ_{less} (sec)	l_{cr} (cm)	ΔT_{less} (K)	$\sigma_{T=0}$ (10^3 psi)	Bulk absorption		Surface absorption	
					ρ_{pulse} (kW)	ρ_{cw} (kW)	ρ_{pulse} (kW)	ρ_{cw} (kW)
Ge	780 ^(F)	4.7 ⁽⁰⁾	0.04 ⁽⁰⁾	4.9	5.3×10^3	6.6	2.6×10^4	31
Si	680 ^(F)	4.1 ⁽⁰⁾	0.11 ⁽⁰⁾	6.5	1.4×10^4	21	6.0×10^4	86
GaAs	710 ^(F)	4.8 ⁽⁰⁾	0.08 ⁽⁰⁾	4.7	2.4×10^3	13	4.6×10^4	64
CdTe	2400 ^(F)	11 ⁽⁰⁾	0.047 ⁽⁰⁾	2.7	4.8×10^3	2.0	5.4×10^4	23
ZnSe	1400 ^(F)	4.7 ⁽⁰⁾	0.22 ⁽⁰⁾	4.9	4.4×10^4	32	2.0×10^5	1.5×10^2
MgF ₂	1300 ^(F)	3.8 ^(f)	1.7 ⁽⁰⁾	17	6.0×10^3	4.7	1.6×10^6	1.3×10^3
CaF ₂	1400 ^(F)	4.6 ^(f)	4.6 ⁽⁰⁾	8.7	1.0×10^6	6.8×10^2	4.6×10^6	3.2×10^3
SrF ₂	1200 ^(F)	4.3 ^(f)	15 ⁽⁰⁾	11	2.9×10^6	2.5×10^3	1.3×10^7	1.1×10^4
BaF ₂	1100 ^(F)	5.3 ^(f)	6.9 ⁽⁰⁾	6.2	1.0×10^6	1.0×10^3	5.6×10^6	5.2×10^3
NaCl	6200 ^(F)	18 ^(f)	0.69 ^(f)	4.7	1.0×10^5	16	1.7×10^6	2.7×10^2
KCl	4800 ^(F)	18 ^(f)	0.79 ⁽⁰⁾	3.8	8.6×10^4	17	1.5×10^6	3.2×10^2
MgO	780 ^(F)	2.5 ⁽⁰⁾	1.0 ⁽⁰⁾	18	1.7×10^3	2.2	6.3×10^5	7.9×10^2
Al ₂ O ₃	660 ^(F)	2.2 ⁽⁰⁾	1.9 ⁽⁰⁾	24	35	5.3×10^{-2}	9.4×10^5	1.5×10^3
Tl 1173	9500 ^(F)	7.8 ⁽⁰⁾	0.073 ⁽⁰⁾	1.8	7.1×10^3	0.75	5.6×10^4	5.9
glass								

In calculating the figures of merit, it is assumed that edge cooling is used if $\tau_E < \tau_F$ and that face cooling is used if $\tau_F < \tau_E$, since larger values of ρ result. Accordingly, the cw figure of merit that will be used is

$$\rho_{\text{cw}} = \pi D^2 C \Delta T_{\text{less}} / 4 \beta \tau_{\text{less}}, \quad (2.7)$$

where τ_{less} is the lesser of τ_E and τ_F .

The critical window diameter D_{EF} that determines whether face or edge cooling is to be used is simply the solution to $\tau_E = \tau_F$. Since the factor $h l_{\text{cr}} / 3K$ in (2.6) is negligible in all materials considered except Tl1173 glass, this term is neglected, which gives $\tau_E = C l_{\text{cr}} / h$. Solving for D gives

$$D_f = \frac{6.93K}{h} \left(\frac{\text{PSF}}{\sigma} \right)^{1/2} \quad \text{and} \quad D_0 = \left[\frac{13.47K P^2 (n-1)}{\lambda^{1/2} h E^2} \right]^{5/4} \quad (2.8)$$

for $l_{\text{cr}} = l_f$ and l_0 , respectively. The critical diameter D_{EF} is the greater of D_f and D_0 .

If the window absorbs the radiation at its surface rather than throughout the bulk, it is easy to show that β in (2.4) and (2.7) is replaced by f/l_{cr} , where f is the fraction of the incident radiation absorbed by the two surfaces. Then (2.4) and (2.7) are replaced by

$$\rho_{\text{pulse}} = \pi D^2 l_{\text{cr}} C \Delta T_{\text{less}} / 4 f l_{\text{pulse}} \quad (2.9)$$

and

$$\rho_{\text{cw}} = \pi D^2 l_{\text{cr}} C \Delta T_{\text{less}} / 4 f \tau_{\text{less}} \quad (2.10)$$

for surface absorption. Since the values of ρ for surface absorption are more strongly dependent on the window size (by a factor of l_{cr}) than are the corresponding values for bulk absorption, ρ_{cw} never decreases with increasing D and the advantages of using large-diameter windows are greater in the case of surface absorption.

Finally, in strengthening materials there is a critical strength $\sigma_{T=0}$ that is of interest. If the strength of the material σ is less than $\sigma_{T=0}$, then $l_{\text{cr}} = l_f$ and increasing

TABLE VI. Figures of merit, values of thermal time constant τ_{less} , critical thickness l_{cr} , temperature difference ΔT_{less} , and fracture-to-optical distortion crossover strength $\sigma_{T=0}$ for the case $\lambda = 5.25 \mu\text{m}$ and $D = 10 \text{ cm}$.

Material	τ_{less} (sec)	l_{cr} (cm)	ΔT_{less} (K)	$\sigma_{T=0}$ (10^3 psi)	Bulk absorption		Surface absorption	
					ρ_{pulse} (kW)	ρ_{cw} (kW)	ρ_{pulse} (kW)	ρ_{cw} (kW)
Ge	17 ^(E)	0.29 ⁽⁰⁾	0.69 ⁽⁰⁾	12	8.6×10^2	53	2.7×10^2	16
Si	6.9 ^(E)	0.35 ^(f)	1.3 ⁽⁰⁾	16	1.6×10^3	2.4×10^2	6.0×10^2	86
GaAs	18 ^(E)	0.31 ^(f)	1.3 ⁽⁰⁾	12	1.5×10^3	86	4.6×10^2	24
CdTe	140 ^(E)	1.1 ^(f)	0.47 ⁽⁰⁾	6.8	4.8×10^2	3.4	5.4×10^2	3.8
ZnSe	100 ^(F)	0.39 ^(f)	2.6 ⁽⁰⁾	12	5.3×10^3	52	2.0×10^3	20
MgF ₂	99 ^(E)	0.38 ^(f)	11 ^(f)	42	4.0×10^2	4.0	1.1×10^4	1.0×10^2
CaF ₂	130 ^(F)	0.46 ^(f)	12 ^(f)	22	2.6×10^4	2.0×10^2	1.2×10^4	94
SrF ₂	100 ^(F)	0.43 ^(f)	38 ^(f)	26	7.0×10^4	6.8×10^2	3.0×10^4	2.9×10^2
BaF ₂	100 ^(E)	0.53 ^(f)	65 ^(f)	16	1.0×10^5	1.0×10^3	5.3×10^5	5.5×10^2
NaCl	180 ^(E)	1.8 ^(f)	0.69 ^(f)	12	1.0×10^3	5.5	1.7×10^3	10
KCl	130 ^(E)	1.8 ^(f)	1.1 ^(f)	9.6	1.1×10^3	8.6	2.0×10^3	16
MgO	33 ^(E)	0.23 ^(f)	11 ⁽⁰⁾	46	1.8×10^3	5.5	6.3×10^3	2.0×10^2
Al ₂ O ₃	41 ^(F)	0.14 ⁽⁰⁾	30 ⁽⁰⁾	59	5.5	0.18	9.4×10^3	2.4×10^2
Tl 1173	95 ^(F)	0.49 ⁽⁰⁾	1.2 ⁽⁰⁾	4.5	1.1×10^3	1.2×10^2	5.6×10^2	5.9
glass								

TABLE VII. Figures of merit calculated from the measured values of absorption coefficient β .

Material	λ (μm)	Measured β (cm^{-1})	$D = 10 \text{ cm}$		$D = 100 \text{ cm}$	
			ρ_{pulse} (kW)	ρ_{cw} (kW)	ρ_{pulse} (kW)	ρ_{cw} (kW)
Ge	4	3.0×10^{-3}	20	0.38	1.3×10^2	0.15
Ge	5.25	1.8×10^{-3}	50	1.0	3.1×10^2	0.41
Si	5.25	5.9×10^{-3}	29	0.5	2.4×10^2	0.36
GaAs	4	9.0×10^{-3}	11	0.24	71	9.4×10^{-2}
CdTe	4	2.0×10^{-3}	17	0.11	2.0×10^2	7.8×10^{-2}
ZnSe	5.25	1.6×10^{-3}	3.3×10^2	3.2	2.7×10^3	2.0
CaF ₂	5.25	5.0×10^{-4}	5.2×10^3	42	2.0×10^5	1.4×10^2
SrF ₂	5.25	4.1×10^{-5}	1.7×10^4	1.6×10^3	7.0×10^6	6.1×10^3
BaF ₂	5.25	$< 3.0 \times 10^{-5}$	3.3×10^5	3.1×10^3	3.5×10^6	3.3×10^2
KCl	5.25	1.5×10^{-5}	7.5×10^3	28	5.6×10^5	1.2×10^2
Al ₂ O ₃	4	4.3×10^{-2}	1.1×10^2	0.26	7.0×10^2	1.0
TI 1173 glass	4	0.20	0.38	3.7×10^{-3}	24	2.3×10^{-5}

the strength allows the use of thinner windows ($l_{gr} \approx \sigma^{-1/2}$). On the other hand, for $\sigma > \sigma_{f-o}$, $l_{gr} = l_0$. Thus, increasing σ does not allow thinner windows to be used since l_0 is independent of σ . The value of σ_{f-o} is obtained by equating l_f and l_0 in (2.1) and (2.2) and solving for σ , which gives

$$\sigma_{f-o} = 0.264 \text{ PSF} \left[\frac{1}{n-1} \left(\frac{E}{P} \right)^2 \frac{\lambda}{D} \right]^{2/5}.$$

III. TABULATION AND DISCUSSION OF RESULTS

Values of ρ , l_{gr} , ΔT_{1000} , τ_{1000} , D_{EF} , and σ_{f-o} are calculated by using the results of Sec. II and are listed in Tables I–VII for various materials of interest for $\lambda = 3.8$ and $5.25 \mu\text{m}$ and $D = 1, 10$, and 100 cm . It is also useful to visualize the results. Thus, Fig. 1 schematically illustrates the D dependence of l_{gr} , ΔT_{1000} , and $1/\tau_{1000}$.

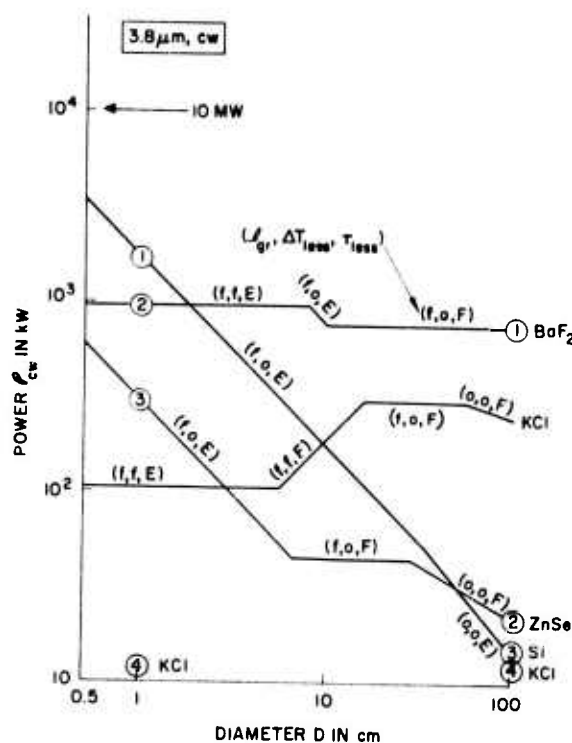


FIG. 1. Schematic illustration of the diameter dependence of thickness, temperature difference, and thermal time constant.

τ_{1000} . The relative positions of the regions of the three curves change from material to material. The tendency for ρ to increase with increasing D caused by the expli-

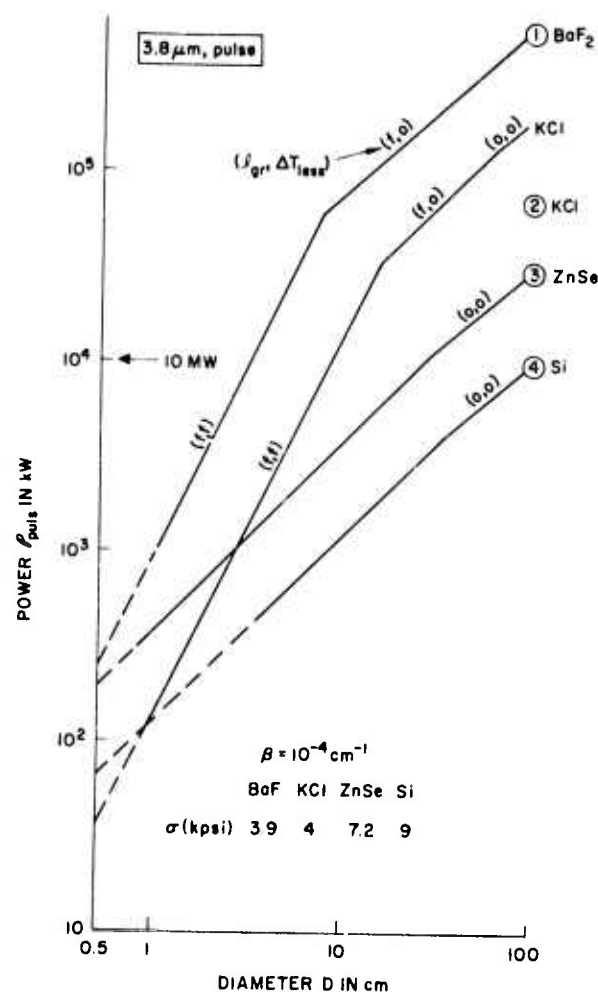


FIG. 2. Diameter dependence of figures of merit ρ_{pulse} at $\lambda = 3.8 \mu\text{m}$. Symbols such as f, o in this figure and f, o, E in Fig. 3 denote the controlling factors for l_{gr} , ΔT_{1000} , and τ_{1000} , respectively: o , optical distortion; f , fracture; E , edge cooling; F , face cooling. Quantities used to obtain the curves are those used for Tables I–IV except KCl ($\sigma = 4000 \text{ psi}$ for curves; $\sigma = 330 \text{ psi}$ for circled numbers). The dashed line indicates that $\tau_{\text{pulse}} > \tau_{1000}$; thus ρ approaches cw value of Fig. 3.

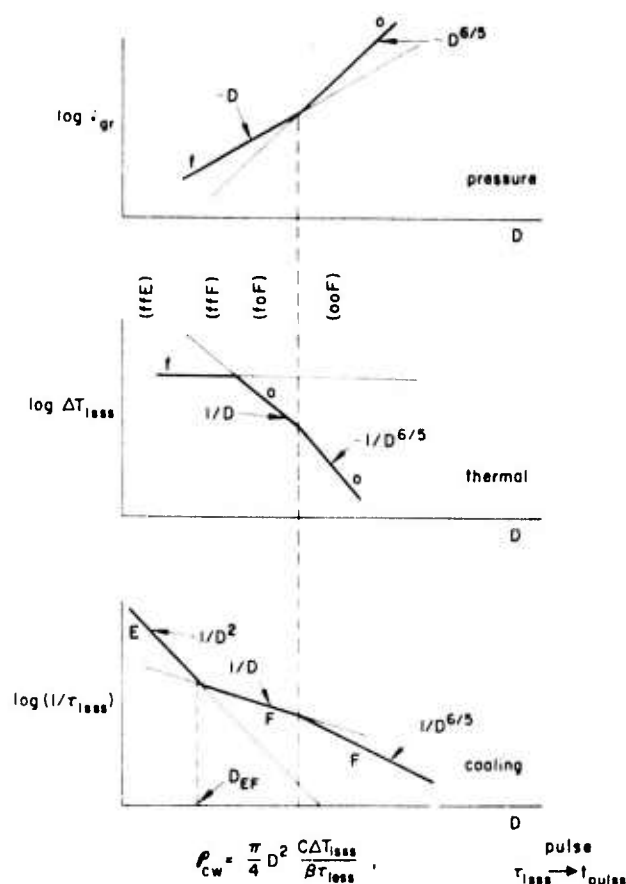


FIG. 3. Diameter dependence of figures of merit ρ_{cw} at $\lambda = 3.8 \mu\text{m}$. (See caption of Fig. 2.)

cit D^2 factor in Eqs. (2.4) and (2.7) tends to be offset by the decreasing factors ΔT_{1000} and $1/\tau_{1000}$ illustrated in Fig. 1. The resulting dependence of ρ and D is plotted in Figs. 2 and 3 for BaF_2 , Si, ZnSe, and strengthened KCl ($\sigma = 4 \text{ kpsi}$). (In the tables, values for unstrengthened KCl, with $\sigma = 330 \text{ psi}$, are given.) Formulas that are useful in scaling and in visualizing the dependence of ρ on variables other than D are displayed in Table VIII.

In the tables and figures all values are computed under the conditions $P = 14.7 \text{ psi}$, $SF = 4$, $h = 10^{-2} \text{ W/cm}^2 \text{K}$, $f = 10^{-4}$, and $t_{\text{pulse}} = 1 \text{ sec}$. The notation f or o designates fracture or optical distortion as the controlling factor, while F or E accompanying τ_{1000} signifies face cooling or edge cooling. Values of ρ in Table VII were calculated by using the measured values of β , while those of Tables II–VI were calculated by using β equal to the greater of 10^{-4} cm^{-1} and the extrapolated intrinsic value.

This choice of β is dictated by the following considerations. There is very little experimental information on the values of β at 3.8 and $5.25 \mu\text{m}$. With the excep-

tion of Al_2O_3 , the experimental values for the materials considered here surely are either extrinsic or characteristic of the experimental calorimetric setup, rather than the material. We have made order-of-magnitude estimates of the intrinsic values of the absorption coefficients by extrapolating from intrinsic values measured at shorter wavelengths. For most materials considered, these intrinsic values are extremely small. As an example, $\beta = 5 \times 10^{-13} \text{ cm}^{-1}$ for BaF_2 at $3.8 \mu\text{m}$. For such small intrinsic values, the observed values of β will be determined by extrinsic processes. In practice, it is difficult to obtain materials with $\beta = 10^{-4} \text{ cm}^{-1}$. It is even difficult to measure such low values. For references we include the measured absorption coefficients that have been reported: at $2.8 \mu\text{m}$, $\beta = 0.027 \text{ cm}^{-1}$ (Ge), 0.018 cm^{-1} (Si), 0.7 cm^{-1} (ZnSe), 0.004 cm^{-1} (CaF_2), 0.001 cm^{-1} (BaF_2), and 0.002 cm^{-1} (TI 1173); at $4.0 \mu\text{m}$, $\beta = 0.003 \text{ cm}^{-1}$ (Ge), 0.009 cm^{-1} (GaAs), 0.002 cm^{-1} (CdTe), 0.043 cm^{-1} (Al_2O_3), and 0.20 cm^{-1} (TI 1173); at $5.25 \mu\text{m}$, $\beta = 0.0018 \text{ cm}^{-1}$ (Ge), 0.0059 cm^{-1} (Si), 0.0016 cm^{-1} (ZnSe), $5.0 \times 10^{-4} \text{ cm}^{-1}$ (CaF_2), $4.1 \times 10^{-5} \text{ cm}^{-1}$ (SrF_2), $3.0 \times 10^{-5} \text{ cm}^{-1}$ (BaF_2), and $1.5 \times 10^{-5} \text{ cm}^{-1}$ (KCl); and at $2.8 \mu\text{m}$, $\beta = 3 \times 10^{-1} \text{ cm}^{-1}$ (BaF_2). From these considerations it is clear that figures of merit based on the estimated intrinsic values of β would be misleading at the present state of the art. In addition to the difficulties in using the experimental values of β already mentioned, the experimental values surely will be decreased as better crystals and better measurements become available, as has been the case at $10.6 \mu\text{m}$.

In small-diameter windows, τ_{1000} ($= \tau_E$) is often less than t_{pulse} , as can be seen in Table IV and Figs. 2 and 3, and the radial heat flow reduces the value of ΔT . Thus, the value of ρ is not increased by using the pulse mode of operation in small-diameter windows. This is indicated in Fig. 2 by the dashed portions of the curves, for which $t_{\text{pulse}} > \tau_{cw}$ (so that $\rho_{\text{pulse}} < \rho_{cw}$ formally). In Table IV, for $D = 1 \text{ cm}$, only the values of ρ_{cw} are given since τ_{cw} is less than or only slightly greater than $t_{\text{pulse}} = 1 \text{ sec}$ for all materials except TI 1173 glass.

The dependence of ρ on the thermal conductivity K is of interest. For pulse operation, thermal diffusion is

TABLE VIII. Formulas useful for scaling ρ to parameters other than D .

ρ	$\Delta T_{1000} \Delta T_f$	ΔT_0
ρ_{pulse}	$\frac{\pi D^2 C \sigma}{2 \beta t_{\text{pulse}} \alpha E S F}$	$\frac{\pi D^2 C \lambda}{32 \beta t_{\text{pulse}} l_{\text{eff}} l_{\text{cr}}}$ ^a
ρ_{cw}	$\frac{8 \pi K \sigma}{\beta \alpha E S F}$	$\frac{\pi K \lambda}{2 \beta l_{\text{eff}} l_{\text{cr}}}$ ^a
	$\frac{\pi D^2 h \sigma}{2 \beta \alpha E S F l_{\text{cr}}}$ ^a	$\frac{\pi D^2 h \lambda}{32 \beta l_{\text{eff}} l_{\text{cr}}^2}$ ^a

^a l_{eff} is the greater of l_f and l_0 ; $l_f = 0.433 D (PSF/\sigma)^{1/2}$; $l_0 = 0.842 D \times [(n-1)(P/E)^2(D/\lambda)]^{1/5}$.

assumed negligible. Thus, ρ_{pulse} is independent of K , as can also be seen in (2.4). For cw operation of small-diameter windows ($D < D_{EF}$), the thermal time constant τ_{less} is equal to $\tau_E \approx 1/K$, from (2.5). Thus, $\rho_{\text{cw}} \approx K$, according to (2.7). For cw operation of large-diameter windows ($D > D_{EF}$), $\tau_{\text{less}} = \tau_F$. The value of τ_F usually is controlled by the heat transfer at the window face rather than by the heat diffusion across the window thickness. In other words, the factor $hl_{gr}/3K$ in (2.6) is much less than unity, one exception being TI 1173 glass in large-diameter windows. For example, for BaF_2 with $D = 10$ cm and $h = 10^{-2}$ W/cm²K, $hl_{gr}/3K = 1.47 \times 10^{-2}$. Thus, ρ_{cw} is independent of K for $D > D_{EF}$.

It should be emphasized that the figures of merit ρ are not the actual powers that windows in real systems can transmit. In this connection, two factors must be stressed. First, the figures of merit apply to specific and idealized conditions.⁴ In spite of this qualification, it is convenient to use ρ as the figure of merit since it does give a rough idea of the power expected and the relative values of ρ for different materials are at least as useful as previous figures of merit. Second, the figures of merit are proportional to $1/\beta$ (or to $1/f$ for surface absorption), and an arbitrary choice of the values of β must be made, as was discussed above.

IV. CHOICE OF MATERIALS

Some materials that have too great an optical absorption at 10.6 μm are expected to have sufficiently small absorption for use in the 2- to 6- μm range. This is important since some of these materials, such as Si, Ge, and the alkaline-earth fluorides, have better physical and thermal properties than most 10.6- μm materials, such as KBr and KCl.

A study of the tables indicates that, of the candidate materials analyzed, the alkaline-earth fluorides have the greatest values of the figures of merit at 3.8 and 5.25 μm and 10- to 100-cm diameters. For diameter $D = 10$ cm, the value of ΔT is controlled by the effect of optical distortion for most materials, but for the alkaline-earth fluorides, which have large values of ΔT , it is controlled by fracture. For $D = 100$ cm, it is the optical distortion effect rather than fracture that limits this temperature difference, with only one exception (BaF_2 at 3.8 μm). For alkaline-earth fluorides, the effects of the temperature dependence of the refractive index and of thermal expansion are opposite and nearly cancel each other [first two terms in δ_{nT} defined under (2.3)], with the result that the optical distortion is smaller than that for other materials. The value of ΔT for BaF_2 with $D = 10$ cm is 50 K, compared with ~ 1 K for the other materials, excluding the oxides and the other fluorides.

In the case of edge-cooled small-diameter windows at 3.8 μm (Table IV), the alkaline-earth fluorides are again relatively good materials because they can toler-

ate large temperature gradients without fracturing. However, in small-diameter windows, radial heat flow is far more important. Specifically, (2.7) with $\tau_{\text{less}} = \tau_{D_{\text{cw}}} \approx 1/K$ shows a linear dependence of ρ_{cw} on the thermal conductivity K . Since silicon has by far the largest value of K , it has the greatest figure of merit for small D .

It has been suggested privately by several investigators that it may be possible to fabricate a mixed alkaline-earth fluoride with $\delta_{nT} \approx 0$, thereby making ρ approach infinity. Unfortunately, for a 10-cm-diam window the value of ρ already is limited by fracture (or nearly so for BaF_2 at 3.8 μm); thus no improvement would result from lowering the value of δ_{nT} unless the crystals were strengthened also. Furthermore, the increase in ρ by decreasing δ_{nT} is a result of increasing the value of ΔT , which already has a value of 50 K in the case of BaF_2 . In addition, the temperature dependence of δ_{nT} would prevent $\delta_{nT} \approx 0$ over the whole window for large values of ΔT .

On the basis of the fact that the multiphonon absorption decreases rapidly with decreasing wavelength λ , for λ less than the wavelength λ_l at which the lattice absorption is maximum, it is sometimes stated that a material that is acceptable for 10.6- μm use will be even better at lower wavelengths. This is not true in general, for several reasons. Diamond, with $\lambda_l < 10.6$ μm , may be useful for small windows at 10.6 μm , but the absorption is too great in the shorter-wavelength region. In other materials, impurities, interband transitions, and possibly deep-gap-level transitions, can give rise to absorption in the 2- to 6- μm region. Since extrinsic processes of unknown origin determine the values of β for most materials of interest, the smaller intrinsic values at the shorter wavelengths have little direct consequence.

Finally, factors other than the figures of merit obviously must be considered in choosing a material for a given application. For example, if programs to obtain improvements in materials are undertaken, the expected difficulty in purifying or otherwise improving a crystal is obviously of interest, and factors such as ease of fabrication, resistance to moisture, hardness, and antireflection and protective coating must be considered. The value of l_{gr} could be so great that the weight of the window could be unacceptably large or the value of ΔT_{less} could be unacceptably high.

ACKNOWLEDGMENTS

Appreciation is expressed to Dr. C.M. Stickley for suggesting this investigation and to Dr. J.A. Harrington for suggesting improvements of the manuscript.

*Research supported by the Advanced Research Projects Agency of the Department of Defense and monitored by the Defense Supply Service, Washington, D.C.

¹See, for example, *Conference on High Power Infrared Laser Window Materials*, edited by C. A. Pitha, Air Force Cambridge Research Laboratory Report No. AFCRL-TR-73-0372 (AFCRL, Cambridge, Mass., 1973), Vols. I and II.

²F. A. Horrigan and R. I. Rudko, Raytheon Research Division Final Technical Report on Contract No. DAAH01-69-C-0038, 1969 (unpublished); F. A. Horrigan, C. Klein, R. Rudko, and D. Wilson, *Microwaves* 8, 68 (1969); F. A. Horrigan and T. F. Deutsch, Raytheon Research Division Final Technical Report on Contract No. DAAH01-70-C-1251, 1971 (unpublished); T. F. Deutsch and R. I. Rudko, Raytheon Research Division Final Technical Report on Contract No. DAAH01-72-C-0194, 1973 (unpublished).

³M. Sparks, *J. Appl. Phys.* **42**, 5029 (1971).

⁴M. Sparks and M. Cottis, *J. Appl. Phys.* **44**, 787 (1973).

⁵*Mechanical Engineers Handbook*, 4th ed., edited by Linell S. Marks (McGraw-Hill, New York, 1941), pp. 447-480.

⁶M. Sparks, Parke Mathematical Laboratories, Inc. Report No. TM-2, 1971 (unpublished).

⁷T. F. Deutsch (private communication).

⁸T. F. Deutsch, Raytheon Research Division Semi-Annual Report, Contract No. DAAH01-72-C-0194, August 1973 (unpublished).

⁹J. Loomis, S. Aikens, L. Marrers, and G. Thompson, Air Force Weapons Laboratory Technical Report No. AFWL-TR-73-131, 1973 (unpublished).

K. LIST OF RECENT PUBLICATIONS

New publications and those whose status has changed since the Second Technical Report of 6 December 1973 are included in the following list:

1. L. J. Sham and M. Sparks, "Explicit Exponential Frequency Dependence of Multiphonon Infrared Absorption," *Phys. Rev. B* 9, 827 (1974).
2. C. J. Duthler and M. Sparks, "Quasiselection Rule for Infrared Absorption by NaCl-Structure Crystals," *Phys. Rev. B* 9, 830 (1974).
3. C. J. Duthler, "Explanation of Laser-Damage Cone-Shaped Surface Pits," *Appl. Phys. Lett.* 24, 5 (1974).
4. M. Sparks and H. C. Chow, "High-Power 2- to 6- μ m Window-Material Figures of Merit with Edge Cooling and Surface Absorption Included," *J. Appl. Phys.* 45, 1510 (1974).
5. M. Sparks, "Stimulated Raman and Brillouin Scattering: Parametric Instability Explanation of Anomalies," *Phys. Rev. Lett.* 32, 450 (1974).
6. D. L. Mills and A. A. Maradudin, "The Absorption Coefficient of Alkali Halides in the Multiphonon Regime: Effects of Nonlinear Dipole Moments," *Phys. Rev.*, in press.
7. C. J. Duthler, "Extrinsic Absorption in 10.6 μ m Laser Window Materials due to Molecular-Ion Impurities," *J. Appl. Phys.* 45, 2668 (1974).
8. C. J. Duthler and M. Sparks, "Extrinsic Absorption in Laser Window Materials," Invited Talk, ASTM 1974 Symposium on Damage in Laser Materials, Boulder, Colorado, May 22 and 23, 1974.
9. M. Sparks and H. C. Chow, "Parametric Instabilities of Phonons: Nonlinear Infrared Absorption," *Phys. Rev.*, in press.
10. M. Sparks, "Infrared Absorption by the Higher-Order-Dipole-Moment Mechanism," *Phys. Rev.*, in press.
11. M. Sparks, "Stimulated Raman Scattering: Enhanced Stokes Gain and Effects of Anti-Stokes and Parametric Phonon Processes," submitted to *Phys. Rev.*
12. A. Karo, M. Sparks, and L. J. Sham, "Infrared Multiphonon Absorption Calculations," in preparation.
13. A. A. Maradudin and D. L. Mills, "The Scattering and Absorption of Electromagnetic Radiation by a Semi-Infinite Crystal in the Presence of Surface Roughness," *Phys. Rev.*, in press.

14. M. Sparks and C. J. Duthler, "Intensity Limits of High-Intensity Vacuum Ultraviolet Materials," to be published.
15. H. C. Chow and M. Sparks, "Calculated Reflectance of Aluminum in the Vacuum Ultraviolet," to be published.